

DISSERTATION

DEVELOPMENT AND IMPLEMENTATION OF NEAR-INFRARED ULTRAFAST LASER SOURCES  
GENERATED BY NONLINEAR FIBER PROPAGATION

Submitted by

Scott R Domingue

Department of Electrical and Computer Engineering

In partial fulfillment of the requirements

For the Degree of Doctor of Philosophy

Colorado State University

Fort Collins, Colorado

Fall 2015

Doctoral Committee:

Advisor: Randy Bartels

Amber Krummel

Diego Krapf

Mario Marconi

Copyright by Scott R Domingue 2015

All Rights Reserved

## ABSTRACT

### DEVELOPMENT AND IMPLEMENTATION OF NEAR-INFRARED ULTRAFAST LASER SOURCES GENERATED BY NONLINEAR FIBER PROPAGATION

This dissertation is broken up into three parts: (I) generating high-quality ultrafast pulses around 1060 nm, (II) using the pulses from part (I) to generate pulses around 1300 nm, and (III) analyzing newly developed experimental theories and methods utilizing these pulses for linear and nonlinear microscopy. The majority of the work in this dissertation is choreographing the dance between nonlinear spectral broadening in optical fiber and the associated complexity in accumulated spectral phase. We have developed and employed several systems which manage to accomplish this task quite elegantly due to our technological contributions, producing high-quality pulses with high oscillator-type pulse energies both at 1060 and 1250 nm. In addition to developing some theory and techniques extending current types of nonlinear microscopy, we have as a capstone an experimental microscope cascading several of our primary source and application technologies to conduct an entirely new form of spectroscopic absorption imaging.

## ACKNOWLEDGEMENTS

*You are the butter to my bread*

Julia Child

This was far from a solitary effort, and I would like to extend thank you's to my lab mates David Winters, David Smith, and Keith Wernsing for their assistance, camaraderie, and encouragement. Also, I would like to thank a second group scientists: Jeff Field, Jesse Wilson, Omid Massihzadeh, Philip Schulp, and Brad Luther; through the years they have lent me advise about lasers and life.

I would also like to thank my brothers and parents for their years of constant support and generosity, especially when it came to picking up the tab. You are all constant examples of how to love and live.

I would like to acknowledge my committee and thank them for taking the time to help shepherd me to the finish line of preparing and defending this dissertation. To my adviser Randy, I want to extend a tremendous thank you; it has been an absolute pleasure to work with and befriend you.

To all of my many lasers, I want to thank you for ridding yourselves of that nasty, annoying habit of catching fire. And to third-order dispersion, I am still coming for you.

And finally, I would like to thank Ms. Stephanie Krueger for her patience, unflagging support, and tenderest friendship. You have made the home stretch of this long journey the warmest and most blessed.

This dissertation is typeset in L<sup>A</sup>T<sub>E</sub>X using a document class designed by Leif Anderson.

## TABLE OF CONTENTS

Abstract .....	ii
Acknowledgements .....	iii
List of Figures .....	viii
Chapter 1. Introduction to the dissertation .....	1
1.1. Part I: Ultrafast fiber sources around 1060 nm .....	1
1.2. Part II: Ultrafast fiber sources around 1300 nm .....	4
1.3. Part III: Novel applications of ultrafast pulses .....	7
Chapter 2. Part I: Utilization of all-normal-dispersion fiber lasers .....	10
2.1. Construction parameters of Yb-doped, double-clad, all-normal-dispersion fiber lasers .....	10
2.2. ANDi Noise .....	13
2.3. ANDi spectral clipping and compression .....	18
Chapter 3. Part I: Nonlinear fiber amplifier with tunable TL pulse duration from a few 100 to sub-100 fs at watt-level powers .....	23
3.1. Nonlinear fiber amplifier with variable output bandwidth .....	23
3.2. Compressibility of the nonlinear amplifier .....	29
3.3. Noise analysis of nonlinear amplifier seeded supercontinuum .....	32
Chapter 4. Part I: Accumulated spectral phase and non-Gaussian/soliton seed pulses in supercontinuum generation in all normal dispersion optical fiber .....	35
4.1. Introduction .....	35

4.2. Spectral phase evolution .....	36
4.3. ANDi Seeded Supercontinuum .....	47
4.4. Conclusion .....	52
Chapter 5. Part I: Polarization instabilities in normal dispersion supercontinuumm	
generation .....	53
5.1. Introduction .....	53
5.2. Weakly birefringent nonlinear fiber .....	54
5.3. Strongly birefringent nonlinear fiber .....	60
5.4. Conclusions .....	62
Chapter 6. Part I: Nonlinear pulse compression systems at 1060 nm: Routes to	
compressing the broadened optical power spectra .....	63
6.1. Introduction to nonlinear pulse compression .....	63
6.2. Optimal fiber coupling via fiber “cocktails” .....	66
6.3. Nonlinear pulse compression with an ANDi laser and a hyper-prism compressor	67
6.4. Nonlinear pulse compression with a pulse shaper in the naive limit .....	70
6.5. Nonlinear pulse compression beyond the naive limit .....	74
Chapter 7. Part I: Nearly transform-limited sub-20 fs pulses at 1065 nm and >10 nJ	
enabled by a flat field ultrafast pulse shaper .....	78
7.1. Our flagship nonlinear pulse compression system .....	78
7.2. Petzval field curvature in pulse shapers .....	79
7.3. Flat-field pulse shaping with a Plössl lens .....	82
Chapter 8. Part I Summary: Modular sources and dispersion control .....	87

Chapter 9. Part II: Generating 1300 nm pulses via soliton self-frequency shifting . . . . .	94
9.1. The marvel that are photonic crystal fibers . . . . .	95
9.2. Soliton self-frequency shifting restricts tuned pulse energy . . . . .	96
9.3. Self-frequency shifting for low energy amplifier seed pulses at 1340 nm . . . . .	102
Chapter 10. Part II: Nonlinear frequency conversion of ultrafast fiber pulses in dual-zero dispersion fiber to 1250 nm . . . . .	105
10.1. Photonic crystal fiber with dual-zero-dispersion wavelengths . . . . .	105
10.2. Nonlinear frequency conversion system using dual-zero-dispersion wavelength photonic crystal fiber . . . . .	108
10.3. Demonstration of 3-photon excitation fluorescence microscopy at 1250 nm . . . . .	113
Chapter 11. Part II: Theoretical design of a Nd-doped fiber amplifier for 1340 nm ultrafast pulses . . . . .	117
11.1. Introduction and background . . . . .	117
11.2. Designing a robust self-frequency shifting system to produce 1340 nm pulses .	120
11.3. Amplifying 1340 nm pulses with a Neodymium-doped ZBLAN fiber amplifier .	122
11.4. Feasibility analysis of potential 795 nm pump powers . . . . .	130
Chapter 12. Part III: Non-impulsive stimulated Raman scattering with chirped supercontinuum pulse pairs . . . . .	133
12.1. Theoretical treatment of nonresonant impulsive vibrational excitation . . . . .	133
12.2. Chirped-pulse excitation in the impulsive-limit . . . . .	139
Chapter 13. Part III: Time-resolved coherent Raman spectroscopy by high speed pump-probe delay scanning . . . . .	152

13.1.	Pump-probe spectroscopy .....	152
13.2.	Impulsive stimulated Raman scattering with the <i>lighthouse</i> .....	153
13.3.	Chemical Imaging with the <i>lighthouse</i> .....	158
Chapter 14. Part III: Hyperspectral imaging via labeled excitation light and		
	background-free absorption spectroscopy .....	163
14.1.	Introduction .....	163
14.2.	LiLa Method .....	166
14.3.	HI-ELF Results .....	171
Chapter 15. A final summary and looking forward .....		
		175
Bibliography .....		
		178
Appendix A. Split-step fiber propagator for the generalized nonlinear Schrödinger		
	equation .....	199
A.1.	The split-step propagator .....	199
A.2.	Fiber properties .....	202

## LIST OF FIGURES

2.1	ANDi schematic .....	11
2.2	Noise amplification from ANDi pulses to SC power spectrum .....	16
2.3	ANDi spectral clipping for temporal pulse clean-up .....	18
2.4	SC noise with improved ANDi compression .....	20
3.1	Schematic of ANDi master oscillator nonlinear power amplifier .....	26
3.2	MOPA seed and amplified pulse energies .....	27
3.3	MOPA performance characteristics .....	29
3.4	MOPA pulse compressibility .....	30
3.5	Modeled cascaded compressor performance .....	32
3.6	Spectral noise in ANDi, MOPA, and SC from either .....	33
4.1	Optical fibers with normal dispersion profiles .....	38
4.2	Phase and Spectral evolution in normal dispersion SC generation .....	39
4.3	Nonlinear pulse compression and peak power enhancement .....	43
4.4	Additional peak power enhancement from nonlinear pulse compression with TOD compensation .....	47
4.5	Nonlinear pulse compression using ANDi seed pulses and how it changes for the level of spectral phase compensation .....	48
4.6	Comparing the power spectra of supercontinuum generated from a Gaussian pulse and ANDi pulses .....	51
5.1	World record SHG-FROG reconstruction .....	55

5.2	Normal dispersion SC polarization instability .....	57
5.3	SC generation in polarization maintaining, normal dispersion nonlinear fiber .....	61
6.1	Hyper-prism compressor schematic .....	68
6.2	Nonlinear pulse compression to 75 fs .....	69
6.3	SC generation in polarization maintaining, normal dispersion nonlinear fiber .....	72
6.4	Wave-breaking lengths for SC generation in normal dispersion optical fibers and the transform-limited pulse durations supported by the SC generated by propagation up to the wave-breaking lengths. ....	75
7.1	Field curvature from an achromatic doublet in a Martinez compressor .....	81
7.2	Field curvature from a Plössl lens in a Martinez compressor .....	83
7.3	Performance of a pulse shaper using a Plössl lens .....	84
9.1	Photonic crystal fiber dispersion profiles .....	96
9.2	Soliton self-frequency shifting a 1060 nm pulse in photonic crystal fiber .....	98
9.3	Shifted soliton spectral overshoot for 25 fs pulses .....	100
9.4	Shifted soliton spectral overshoot for 100 fs pulses .....	101
9.5	Soliton self-frequency shifting to seed Nd-doped fiber amplifier .....	103
10.1	Photonic crystal fiber with dual zero-dispersion wavelengths .....	106
10.2	Nonlinear fiber propagation in a dual-ZDW PCF .....	107
10.3	Experimental schematic for generating pulses at 1250 nm .....	109
10.4	Phantom-FROGs of the 1250 nm pulses .....	110

10.5	Instability in the 1250 nm pulses from dual-zero-dispersion photonic crystal fiber .	112
10.6	Three-photon excitation fluorescence microscope .....	114
11.1	Nd-doped fiber amplifier schematic .....	123
11.2	Optical fibers with normal dispersion profiles.....	124
11.3	Frequency-shifted soliton amplification in a Nd-doped fiber amplifier .....	126
11.4	Chirped- and divided-pulse amplification in a Nd-doped fiber amplifier .....	127
11.5	Negative chirped-pulse amplification in a Nd-doped fiber amplifier .....	129
12.1	The vibrational excitation from chirped beating pulse pairs .....	141
12.2	Tuning the vibrational excitation from chirped beating pulse pairs via pulse delay	143
12.3	Vibrational excitation from non-identical pulse pairs .....	145
12.4	The vibrational excitation spectra for red and blue pulses either half of a Gaussian spectrum .....	146
12.5	Effects of material dispersion on intensity beating and vibrational excitation spectrum between pulse pairs .....	148
12.6	Effects of residual material dispersion on intensity beating and vibrational excitation spectrum between pulse pairs.....	149
12.7	Stimulated vibrational excitation with chirped beating, supercontinuum pulse pairs.....	150
13.1	Experimental schematic of the <i>lighthouse</i> .....	156
13.2	Vibrational signal from <i>lighthouse</i> .....	158
13.3	Rapid averaging of vibrational signals.....	160

13.4 Raman image.....	162
14.1 Concept figure for excitation labeled fluorescence.....	165
14.2 Experimental schematic and light labeling calibration data. ....	167
14.3 Data processing for hyperspectral imaging via excitation labeled fluorescence. ....	173

## CHAPTER 1

# INTRODUCTION TO THE DISSERTATION

*Nobody climbs mountains for scientific reasons. Science is used to raise money for the expeditions, but you really climb for the hell of it.*

Edmund Hillary

This dissertation is broken up into three parts. In Part I we discuss the approach we have taken to generating high quality ultrafast pulses around 1060 nm with sufficient energies to perform a broad range of spectroscopy and microscopy applications. Part II examines ultrafast pulse synthesis in the second biological imaging window around 1300 nm, a highly attractive wavelength region due to the gains in ballistic photon penetration depth but currently missing a simple optical source. Finally, in Part III, we examine some particular application technologies we developed to utilize the pulses from Parts I and II. A more detailed introduction to each Part composes the remainder of this chapter.

### 1.1. PART I: ULTRAFAST FIBER SOURCES AROUND 1060 NM

Ultrafast optical sources are highly potent tools integral to all kinds of marvelous scientific systems: multiphoton microscopes to dynamically capture high resolution micrographs in all three spatial dimensions [1], chemical probes to examine the inner mechanics of molecules [2], and coherent table-top soft X-ray generation platforms [3] to name but a few. While it is such end-applications that drive the development of much modern experimental research, it is the driving laser pulses which are the coner-stone of the experiment's foundation. The quality, energy, cost, and robustness of the ultrafast pulse system serves as the starting point for many research labs; both hindering or enabling work based on the quality of the laser

system. Any improvement to this front-end system improves the entire system, whether it be a reduction in down time or an increase in signal level. To that end, Chapters 2–8 of this dissertation detail our pursuit of producing high-quality ultrafast pulses around 1060 nm utilizing optical fiber systems.

The development of all-normal-dispersion (ANDi) modelocked fiber lasers expanded the parameter space of modelocked oscillators, eliminating the requirement of a conserved soliton for modelocking [4]. This departure from tight cavity dispersion management and constrained pulse energy and duration allows for many different fiber oscillator configurations, including  $> 100$  nJ oscillator pulse energies at high repetition rates [5] and giant chirp oscillators at reduced repetition rates ( $< \text{MHz}$ ) [6, 7] suitable for direct amplification in a chirped-pulse amplifier [8].

The nonlinear polarization evolution (NPE) that acts as a saturable absorber to modelock these fiber lasers is also applicable across a broad range of rare-earth doped fibers lasers. Over the last decade research groups have demonstrated ANDi lasers operating at 930 nm [9], 1030nm[4], 1180 nm [10], 1320 nm [11], 1550 nm [12], and 1900 nm [13]; using Nd-, Yb-, Bi-, Bi-, Er-, and Tm-doped fibers respectively. It is the Yb-doped fibers which we focus on in Part I of this dissertation, as these fibers process high and broad bandwidth gain at 1060 nm [14].

The relative simplicity and ease of maintenance make modelocked, ultrafast fiber lasers using Yb-ion dopants an attractive source of pulses at 1060 nm for applications in spectroscopy, nonlinear optics and imaging, and machining of materials. Yb-doped fibers offer an exceptional platform for ultrafast pulse amplification, as they are efficiently pumped by fiber-coupled multi-mode 980 nm diode lasers and require minimal thermal management.

At oscillator power levels, it turns out to be relatively trivial to construct and maintain an ultrafast Yb-doped fiber laser with  $> 10$  nJ at repetition rates around 60 MHz at low cost ( \$10k) compared to bulk-style oscillators (commercial cost  $\approx$  \$100k).

Ultrafast pulses at 1060 nm have the advantage of penetrating deeper into turbid media, in particular biological tissue, than pulses from the canonical ultrafast laser, a modelocked Ti:sapphire laser operating at  $\sim 800$  nm, due to the reduction in scattering [15–18]. Yb-doped lasers however, lack the exceptional gain bandwidth needed to produce the sub-15 fs pulses possible from a kerr-lens modelocked Ti:sapphire oscillator [19]. In fact, outside of state-of-the-art Yb-doped systems both bulk and fiber based, pulse durations more typically range from 60–200 fs full-width-half-max (FWHM) [20, 4, 21, 22]. Two example state-of-the-art systems that we are aware of produce pulses down to 32 fs FWHM from a bulk oscillator [23] and 22 fs FWHM from a dissipative soliton fiber laser [24], but they are limited in pulse energy to 0.9 nJ and 0.17 nJ, respectively.

Fortunately, the tight mode field confinement of ultrafast pulses in optical fiber is a ready means of increasing the spectral bandwidth of pulses from a Yb-doped fiber oscillator by nonlinear propagation for the purposes of nonlinear pulse compression: synthesizing pulses shorter in duration than the transform-limited (TL) duration supported by the seed pulse bandwidth [25–27]. Dispersion and the nonlinear phase due to the third-order nonlinear optical susceptibility of the optical fiber are the dominant processes in nonlinear propagation [28, 29]. Generating additional spectral bandwidth turns out to be relatively simple, where the few hundred fs pulse durations available from a 1060 nm modelocked ANDi fiber oscillator in combination with a few nJ of pulse energy provide more than enough peak power to drive nonlinear broadening in virtually any single mode optical fiber. The challenge is compressing

the generated spectral bandwidth to near the TL duration supported by the broadened power spectrum since the spectral chirp in the broadened pulses is frustratingly mis-matched to the common devices we can employ to de-chirp them.

Chapter 2 and Chapter 3 discuss both how best to prepare the pulses from an ANDi laser for nonlinear applications as well as an alternative pulse source derived from an master ANDi oscillator an a power amplifier. We then begin to look at how to expand the application range of these pulses by supercontinuum generation using normal dispersion optical fiber in Chapter 4 and Chapter 5. Finally, examine how to manage the spectral phase of the nonlinearly broadened power spectra for nonlinear pulse compression in Chapter 7 and Chapter 6.

Chapter 8 is a survey and summary of the possible sources that come out of the development work in Part I. While some of these solutions are still under investigation, e.g. the cascaded grating-pair compressor and ZnSe prism compressor modeled in Chapter 3.2, we have several fiber laser systems pumping experimental systems; including our flagship laser which incorporates a number of our technical innovations: a nonlinear fiber amplifier (Chapter 3), low-noise spectral broadening (Chapters 4 and 5), and a flat-field pulse shaper (Chapter 7).

## 1.2. PART II: ULTRAFAST FIBER SOURCES AROUND 1300 NM

Laser scanning, multi-photon microscopy (MPM) is widely used to capture rapid, high resolution, three-dimensional micrographs in many biological fields. Nonlinear optical interactions of an intense, short laser pulse with endogenous molecules and tissue structures have been actively pursued for the development of label-free optical diagnostics of tissue, metabolism, and function – enabling quantitative diagnostics of many diseases [30–32]. Several

common endogenous nonlinear interactions are: second harmonic generation (SHG) produced by organized tissue structures [33]; third harmonic generation (THG) produces image contrast at cell and nuclear membrane boundaries and from lipid or protein droplets [34]; and multi photon absorption, fluorescent emission (MPFE) that is used to look at intrinsic fluorophores (e.g. NADH, FAD, and elastin) [35, 36].

MPM imaging is extremely powerful, and offers numerous capabilities for the visualization of cellular and subcellular features, and for observing physiology and pathology of structures deep in tissues of living organisms. Among many applications, MPM has been widely exploited for functional studies [37], with applications to neuroscience [38, 39, 18], skin and skeletal structure, tumor biology, immune cell biology, and embryology [40]. MPM imaging could expand possibilities for real time label free diagnostic capabilities of optical imaging instruments, ideally intraoperatively, such as possibly real-time margin assessment in tumor resection. Indeed, MPM offers better spatial resolution than optical coherence tomography (OCT), which presents insufficient spatial resolution for determining cell morphology for cancer diagnostics [41]. Label-free MPM cancer detection is being investigated for numerous diseases, including skin cancers [42, 43], colon cancer [44–46], prostate and bladder cancers [47, 48], breast cancer [49], and lung cancer [50, 51].

Despite the power and promise of MPM for in vivo optical imaging diagnostics, MPM imaging applications are hindered by the available femtosecond (fs) pulse center wavelengths. Most MPM imaging systems use 800 nm or 1060 nm fs laser pulses. In many applications, the imaging depth is insufficient to study many invasively growing tumors [42], which means that these MPM imaging advances lack diagnostic capabilities for an important class of diseases. Moving to longer wavelength sources reduces optical scattering, because the rate of optical

scattering scales as  $\lambda^{-4}$ . The first MPMs used  $\sim 780$  nm excitation pulses, and were able to image  $700 \mu\text{m}$  into tissue [18, 52, 16]. In the near-infrared, the MPM penetration depth limit is governed by the attenuation of ballistic photons by both tissue scattering and absorption (generally by water), creating additional optimal excitation wavelength “windows” for maximal penetration depth around 1340 and 1700 nm [18, 17, 53]. Using  $\sim 1250$  nm excitation, MPM imaging depths in murine brain and zebrafish increased to 1.6 [53] and 1.5 mm [54], respectively – compared to a few  $100 \mu\text{m}$  at 800 nm [15]. Moving to longer wavelength fs laser pulses also reduces phototoxicity and photodamage [55–57], which avoids radiation DNA damage and greatly improves safety. In both plant and animal cells, the average power cell damage threshold for micro-illumination at 1230 nm ( $> 100$  mW) is nearly an order of magnitude more than at 1047 nm (13 mW) [58] and over an order of magnitude more than at 800 nm (6 mW) [54, 57, 59]. Shifting fs laser sources to a longer wavelength also opens the window for exploiting three photon MPFE, which allows for even deeper imaging depths in live organisms by reducing the background multiphoton fluorescence [60].

The goal of the Chapters 9–11 is to explore, develop, and propose fiber-based ultrafast sources around 1300 nm that will be amenable to facilitating clinical translation of MPM techniques. Chapter 9 looks at the limitations and possibilities of the most obvious nonlinear conversion route of soliton self-frequency shifting 1060 nm seed pulses launched into optical fiber in the anomalous dispersion region. Chapter 10 examines a nonlinear frequency conversion system using 1060 nm ultrafast pulses in optical fibers with dual-zero dispersion wavelengths to directly generate  $> 1$  nJ pulses within the second biological imaging window around 1300 nm, even producing preliminary images. Chapter 11 proposes a hybrid scheme

using nonlinear frequency conversion to generate low energy seed pulses for a master oscillator power amplifier to produce high energy pulses for imaging within the second biological imaging window.

The sources in these chapters are predicated on the frustrating fact that despite all the benefits of  $\sim 1300$  nm excitation, there is a dearth of robust and energetic optical sources in the 1300 nm biological imaging window. The most common sources of ultrafast pulses in this wavelength region are Ti:sapphire pumped optical parametric oscillators, but these systems are expensive and unreliable, preventing possible wide-spread clinical use. Cr:Forsterite lasers produce fs laser pulses at  $\sim 1280$  nm, but also suffer poor reliability, which has confined their use to an extremely limited number of laboratories worldwide. Multiphoton microscope systems employing both sources have been successfully demonstrated [16, 17, 61], but we feel this is an area that is ripe for the development of a robust fiber-based source to reduce the threshold of entry into this highly advantageous biological imaging window.

### 1.3. PART III: NOVEL APPLICATIONS OF ULTRAFAST PULSES

In Parts I and II, we detailed the fiber-based, ultrafast pulsed systems and dispersion management solutions we have developed . The final portion of this dissertation, Part III: Chapters 13–14, transitions from pulse source engineering and management to the applications. These chapters look at both experimental demonstrations of new techniques and a theoretical treatment of a particular spectroscopic technique.

Chapter 12 examines the theoretical strength of vibrational excitation for chirped beating pulse pairs. Illuminating molecules with tightly focused, TL pulses can impulsively excite coherent molecular vibrations, where the ultrafast pulse will excite all the vibrational modes with temporal periods longer than the pulse duration [2]. Delivering TL pulses to the focus of

a laser-scanning microscope, especially the sub-20 fs durations needed to span the fingerprint region ( $500\text{--}2000\text{ cm}^{-1}$ ), is non-trivial, generally requiring a pulse shaper [62, 63, 27]. Within this chapter we examine the possibility of using chirped, broad-bandwidth pulse pairs as a means of coherently exciting vibrations with nuclear displacement amplitudes at nearly the impulsive limit, where the vibrational excitation is now selective (i.e. only coupling to a narrow range of vibrational energies) and dependent on the time delay between the pulse pairs [64]. The end goal being the investigation of the feasibility of using pulses derived from supercontinuum generation around 1060 nm in the normal dispersion region, which are decidedly non-Gaussian in power spectral structure.

Chapter 13 demonstrates a rapid pump-probe delay scanner by measuring time-resolved, impulsive-stimulated Raman scattering (ISRS) [2, 65, 66]. Rapidly averaging pump-probe scans effects white-noise limited signal-to-noise ratio improvements with increasing delay scan number, as opposed to point-averaging (i.e. pump-chopping and lock-in amplification) which is limited by  $1/f^\gamma$  noise from Poynting-vector drift, detector gain drift, air flow induced beam perturbations, and such [67]. The kernel of this chapter is the high-speed delay scanner we created, dubbed the *lighthouse*. This method of rapidly sweeping the pump-probe delay has many potential applications: ISRS (the demonstrated application), transient absorption spectroscopy [68, 69], and other coherent pump-probe spectroscopies. For example, notice how the coherent Raman excitation in Chapter 12 relies on varying the time-delay between a chirped pulse pair; a *lighthouse*-type device could increase the pump-probe delay scan time by a significant magnitude compared to physically translating a retro-reflector.

Chapter 14 introduces and demonstrates a new method of hyperspectral imaging, which involves a technology which is functionally similar to Fourier transform spectroscopy (i.e.

varied time delays between pulses). Functionally, the demonstrated technique moves the spectrometer from the back-end of the experiment to the front, where temporal labels are encoded into the illumination power spectrum, dubbed light-labeling. Capturing spectroscopic data is then a time-domain measurement, much like Fourier-transform spectroscopy but where the temporal dynamics are not governed by the carrier of the optical field but by the carrier of the encoded temporal modulations. This paradigm change in hyperspectral imaging is adaptable to non-array detector based imaging systems such as two-dimensional spatial frequency modulated imaging [70, 71] and fluorescence imaging using radio frequency-tagged emission [72], allowing for a large potential increase in frame rate above state-of-the-art cameras. The method of light labeling we demonstrate (encoding wavelength dependent intensity modulations onto the power spectrum) is also sufficient for spectroscopy on a single element detector at increased signal levels compared to a scanning the illumination wavelength, an improvement that could be particularly useful in spectral regions lacking dense array detectors such as the mid-infrared. In this chapter, we demonstrate background-free absorption spectra imaging by capturing the temporal modulations transferred from absorption into the fluorescent emission intensity.

## CHAPTER 2

# PART I: UTILIZATION OF ALL-NORMAL-DISPERSION FIBER LASERS

*Waiting for perfect is never as smart as making progress.*

Seth Godin

### 2.1. CONSTRUCTION PARAMETERS OF YB-DOPED, DOUBLE-CLAD, ALL-NORMAL-DISPERSION FIBER LASERS

All normal dispersion (ANDi) fiber lasers modelocked using nonlinear polarization evolution (NPE) generating dissipative solitons are an elegant blend of optical fiber and free space optical components [4]. Fig. 2.1 shows a schematic of the ANDi oscillators we use in our laboratory. The Yb-doped double-clad gain fiber is  $\sim 2$  m in length, absorbing  $> 90\%$  of the 980 nm pump light propagating in the multimode core. The other fiber lengths are 10–30 cm in length, putting the oscillator repetition rate between 55–65 MHz. Our ANDi lasers are split into two categories: low and medium power. The low power ANDi lasers operate around 500–750 mW of average power, and the medium power ANDi lasers operate around 1.5 W.

The large group delay dispersion (GDD) present in the phase of the pulse maps the power spectrum into the time-domain, causing a linear sweep in time of the instantaneous carrier frequency of the pulse electric field (what is often called pulse “chirp”). Spectral filtering at the edges of the power spectrum then, affects a reduction in the temporal width of the pulse, since the removed power spectra also composed the edges of the pulse envelope in time. As

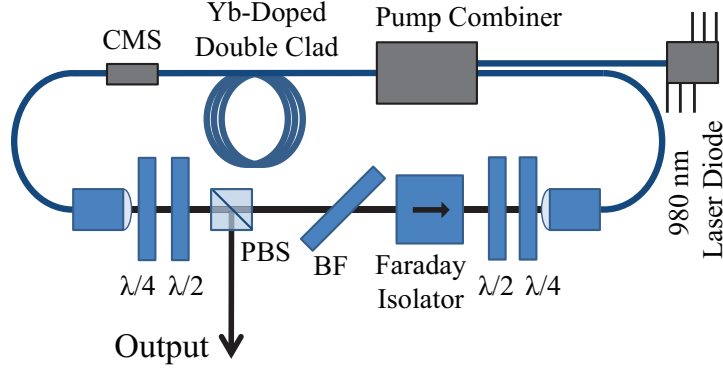


FIGURE 2.1. Schematic of an ANDi oscillator, CMS: cladding-mode stripper, PBS: polarizing beam splitter, BF: birefringent filter.

the pulse traverses the cavity, the filtered spectra is regenerated by nonlinear propagation in the optical fiber again chirped out to assume the space-to-time mapping. This pattern of temporal and spectral reduction in growth, referred to as “breathing”, is critical to the nonlinear polarization evolution (NPE) modelocking dynamics of the ANDi [4].

In the low power ANDi lasers, the spectral filter is a birefringent filter, which is nothing more than a thick quartz plate aligned to Brewster’s angle and the first polarizer in a Faraday isolator. This combination of optics is similar to a Lyot filter [73], where the ordinary and extraordinary axis of the birefringent plate cause a sinusoidal transmission function in the wavelength domain. For the medium power ANDi laser it was necessary to reduce the transmission of competing modes at different wavelengths. To accomplish this, we used two cascaded birefringent filter polarizer pairs or alternatively an angle tuned bandpass filter. The double birefringent filter scheme uses two birefringent plates of differing thickness to reduce the transmission of un-desired secondary modes.

While ANDi lasers are almost trivial to construct and align, there are three features we have found critical to achieving stability at power levels  $> 500$  mW. The first was the introduction of a cladding-mode stripper to eliminate any un-absorbed pump light propagating

in the multimode core after the gain fiber section. If this light pulse remains in the fiber, it will eventually cause the coating in the passive, non-multimode fiber after the gain fiber to catch fire. Or, it will cause the collimator to fail as it will heat the epoxy between the fiber and the ceramic ferrule of the connector. The mode stripper for the low power ANDi lasers is just a high-index re-coat applied to a  $\sim 2.5$  cm section of bare fiber, usually at the fiber splice intersection between the gain fiber and passive fiber. For higher powers, it is necessary to cool the mode stripper. The high power mode stripper is constructed from a water cooled aluminum block (1x1x3 inch, 1/8 NPT tapped 0.25 inch through hole) with a 0.125 inch channel. A 5 cm section of stripped fiber, again the gain-to-passive fiber splice intersection, is potted in the channel using a high-index, high-temperature epoxy (Thorlabs, 353NDPK). The epoxy then takes the place of the usual low-index polymer re-coat. This mode stripper is capable of 50 dB extinction of residual (unabsorbed) pump power with no measured temperature change at 8 W of direct multimode illumination.

The second feature is the usage of collimators with high damage thresholds. For the low power ANDi lasers, the input and output fiber ends are potted into angled-physical contact connectors with the same high-index, high-temperature epoxy used in the cladding-mode stripper. Empirically, we find that at output power levels above 1 W, even these high-temperature connectors eventually fail due to the 3–5 W intracavity power. For the medium power ANDi lasers, we therefore use commercial collimators which glass solder the fiber to the ferrule in addition to utilizing a spatial mode expansion in a short section of coreless termination fiber (purchased from Oz Optics: LPC-04-1030-10/125-LMA-2.3-13.9AS-50-X-1-1-HPC).

The third stability feature is the addition of a half-waveplate within the oscillator cavity. This added waveplate is positioned after the Faraday isolator and second quarter-waveplate. As is discussed in greater detail in Chapter 5, although intended to be perfectly, cylindrically symmetric the fibers used in the cavities do not possess perfect azimuthal symmetry. The latent, and possibly thermally perturbed, birefringence within the fiber means there is an effective fast and slow axis. We find that using the added half-waveplate to tune the re-injected polarization orientation relative to the effective eigen axis of the fiber increases the long term stability of the ANDi oscillator.

## 2.2. ANDi NOISE

One quality common to nearly all ANDi lasers is the necessity to de-chirp the oscillator output pulse to achieve near transform-limited (TL) pulse durations. The large GDD on the pulse results in ANDi oscillator output pulse durations of  $\sim 3$  ps, over an order of magnitude longer than the bandwidth supported TL pulse duration of  $\approx 100$  fs. We need to add some form of pulse compressor then, to the output of the ANDi to pump experiments with pulse durations near the TL.

The broad bandwidth supported by the NPE and the gain bandwidth now becomes something of a problem. As the bandwidth increases, thus decreasing the bandwidth supported TL pulse duration, the output chirp of the pulse becomes ever more sensitive to third- and higher-order spectral phase. The problem lies in the inability of traditional grating and prism compressors to readily compensate the spectral phase beyond the GDD. Generally, the achievable pulse compression is limited by third-order dispersion (TOD) and/or fourth-order dispersion (FOD). The GDD, TOD, and FOD terms are from a Taylor series expansion of the propagation wave vector in angular optical frequency,  $\omega$ , which is the waveguide equivalent

to the free space propagation wave vector  $k = \frac{n\omega}{c}$  where  $n$  is the index of refraction of the propagation medium and  $c$  is the speed of light.

The nonlinear propagation responsible for modelocking these pulses, also contributes to the spectral phase, where the net spectral phase is a combination of the fiber material dispersion, waveguide dispersion, and nonlinear phase. While the pulse duration can still be quite short, with typical pulse durations from Yb-doped fiber oscillators of 150 fs full-width at half-maximum (FWHM), the peak power can be as low as 60% of the TL pulse.

Experiments utilizing second-order nonlinear interactions (e.g. second-harmonic generation or two-photon excitation fluorescence microscopy) are relatively insensitive to a temporal pedestal. Imperfect pulse compression will limit the nonlinear signal to less than the signal from a TL pulse, but these scaling factors are more a nuisance than a catastrophe. Many experiments however, are average power limited by the damage threshold of the sample, so the temporal pedestal from imperfect compression adds to the illumination average power but not the nonlinear signal. Third-order nonlinear interactions (e.g. third-harmonic generation or three-photon excitation fluorescence microscopy), of course, are even more sensitive to this loss in peak power relative to an idealized TL pulse. So, when possible it is desirable to “clean-up” the pulse, i.e. eliminate the temporal pedestal, for which there are two primary sources: all greater than second-order dispersion (i.e. higher-order dispersion (HOD)) and deviations from Gaussian-like power spectra.

The largest contribution to the residual spectral phase occurs at the edges of the power spectrum. One might nominally refer to this phase as FOD, the presence of TOD-like phase too makes defining the phase order a little ambiguous, so we will just refer to this as HOD. Naming aside, the problem remains that standard compressors (grating/prism pair [74],

Martinez compressor [75], or even grisms [76]) are not capable of compensating for this type of spectral phase.

While second- and third-order nonlinearities are not particularly sensitive to the temporal pedestal associated with HOD (aside from a reduction in signal), we are interested in using supercontinuum (SC) generation to produce power spectra much greater than the ANDi oscillator. SC generation is a cascaded, highly nonlinear interaction that takes place over prolonged interaction lengths (typical fiber lengths are 10–100’s of mm) and is highly sensitive to all temporal structure.

Preliminary SC generation efforts yielded an unexpected amount of noise, unexpected because the seed pulse’s were seemingly very quiet ( $< 0.1$  root mean squared noise (RMS-N) defined as  $\text{RMS-N} = \sqrt{\frac{(P_{\text{avg}}(t) - \mu_{\text{avg}})^2}{n}}$ , where  $P_{\text{avg}}$  is the average power captured as a function of time,  $\mu_{\text{avg}}$  is the mean average power over the measurement period, and  $n$  is the number of time points captured). The broad spectral bandwidths generated in nonlinear, all-normal dispersion, polarization-maintaining optical fiber seeded with ANDi pulses contain significantly more spectral noise than the seed pulse. SC generation in an all normal dispersion regime allows for a preserved spectral coherence in the generated power spectrum even at large pulse energies and average powers, according to a scalar model for the nonlinear propagation. As we discuss in detail in Chapter 4, the scalar approximation is only appropriate for polarization maintaining optical fibers. The noise in this case is driven by cascaded nonlinear interactions between the newly generated power spectrum and the temporal pedestal.

To quantify this increase in noise, we introduce a metric that we define as the relative spectral noise (RSN):  $\text{RSN}(\lambda) = \sigma(\lambda)/\mu(\lambda)$ , where  $\sigma(\lambda)$  is the root mean squared noise over a time series within a narrow spectral band,  $\Delta\lambda = 0.5$  nm, located at  $\lambda$  and  $\mu(\lambda)$  is

the mean intensity of the power spectral bandwidth within  $\Delta\lambda$  over the same time interval [26]. The RSN is the spectrally resolved version of the more typical RMS-N – which we will exclusively use in reference to the the standard deviation of the total power fluctuations. We also calculate a total spectral noise metric,

$$(2.1) \quad \Phi_{\text{RSN}} = \frac{\int \sigma(\lambda)\mu(\lambda)d\lambda}{\int \mu^2(\lambda)d\lambda}$$

for direct comparison to the RMS-N. As seen in Fig. 2.2, we find the RMS-N underestimates the noise in the generated power spectrum.

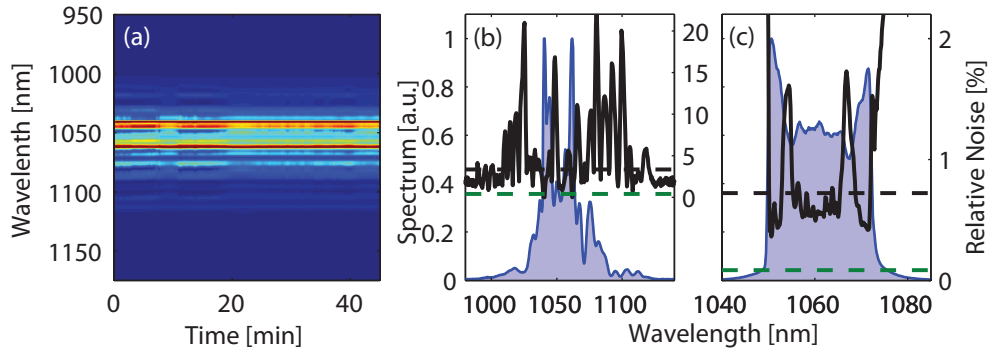


FIGURE 2.2. SC time series (a) and mean power spectrum (shaded blue), RSN (solid-black),  $\Phi_{\text{RSN}}$  (dashed-black), and RMS-N (dashed-green) (b) from 45 minute time intervals from ANDi seeds and 190 mW couple power. The relics of the ANDi cat-ears in (a) and (b) saturated the spectrometer, artificially lowering their power spectral densities. (c) The ANDi oscillator mean power spectrum (shaded blue), RSN (solid-black),  $\Phi_{\text{RSN}}$  (dashed-black), and RMS-N (dashed-green)

Fig. 2.2 shows the amplification of the small RSN in the seed pulse even at the low average power at 190 mW (3 nJ at 61 MHz). The total seed noise is low at a RMS-N of 0.08% and  $\Phi_{\text{RSN}}$  of 0.7%, as seen in the dashed lines of Fig 2.2(c). While these noise metrics are low, the RSN contains two prominent features,  $\text{RSN}(1054 \text{ and } 1067 \text{ nm}) \sim 1.5\%$ , just inside of the “cat-ears” of the power spectrum. The SC RMS-N is also very low averaging 0.08%

for 1 minute intervals and increases to only 0.2% for a 45 minute interval, dashed green in Fig. 2.2(b). The SC's RSN however, is as high as 23% over the full 45 minutes (solid line in Fig. 2.2(b)). The relatively low  $\Phi_{\text{RSN}}$  at 0.8% and 3.4% at 1 and 45 (Fig. 2.2(b) dashed black line) minute intervals respectively, show the spectral fluctuations are concentrated in, if not limited to, areas of low power spectral density.

The ANDi undergoes small spectral mode shifts, the aforementioned 1.5% fluctuations at the inside of the cat-ears, which we attribute to higher-order fiber mode fluctuations and thermally induced changes to the latent fiber birefringence in the ANDi cavity. The small spectral shifts map to large changes in the SC power spectrum. These fluctuations seem intrinsic to ANDi lasers operating with a large normal GDD[77] and ANDi cavities constructed with 10  $\mu\text{m}$  core optical fiber. The mode changes are visible in the SC time series, e.g. see around 10 minutes of the time series shown in Fig. 2.2(a).

To improve the spectral stability of SC generated by ANDi pulses then, it is critical to reduce the influence of the small spectral mode fluctuations on the seed pulse temporal profile. The most obvious route is to simply eliminate the temporal pedestal, which will decouple small spectral mode fluctuations to meaningful changes in the intensity profile. One means of minimizing/eliminating the temporal pedestal is to employ a pulse shaper, which would allow for pseudo arbitrary spectral phase compensation [62, 63, 27]. We avoid that route here, because the critical component of the pulse shaper, the spatial light modulator, costs as much or more as the entire ANDi laser! Luckily, there is one parameter we can easily adjust in the pulse “clean-up” effort: the power spectrum.

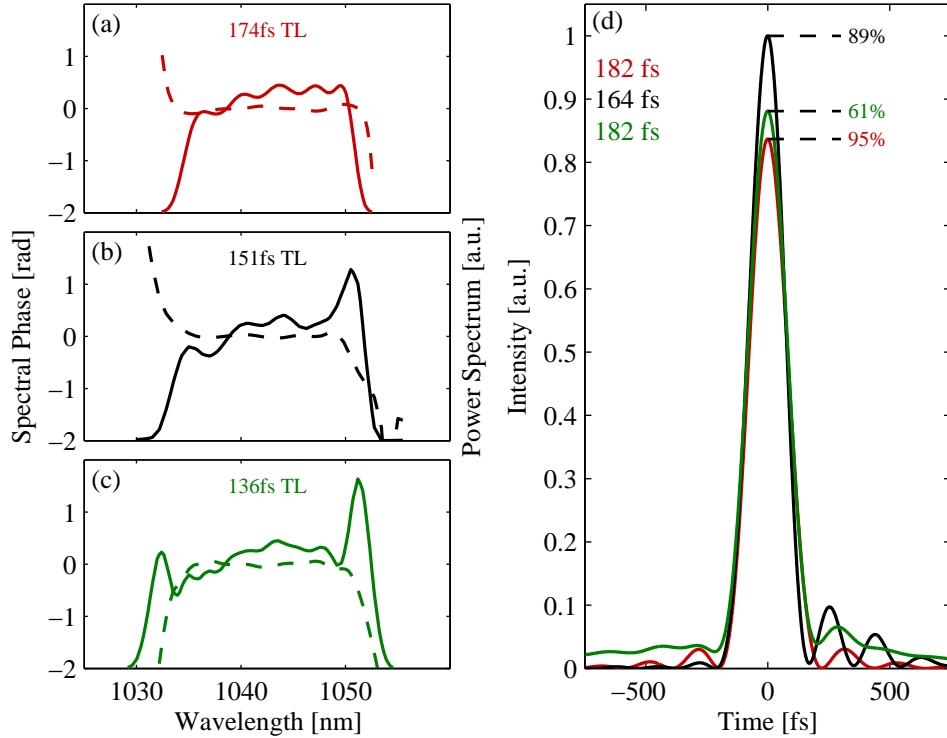


FIGURE 2.3. The effects on ANDi pulses with spectral clipping. The three clipping cases are: (a) heavily clipped with 76% transmission (red), (b) lightly clipped with 87% transmission (black), and (c) un-clipped (green). In (a)-(c) the power spectra (in [a.u.]) are shaded-curves and the spectral phases are solid curves, with the bandwidth supported transform-limits included. (d) The temporal pulse profiles are plotted for the power spectra and phases in (a)-(c) normalized to the lightly clipped pulse (black), the maximum normalized compression intensities and FWHM durations of each pulse are included

### 2.3. ANDI SPECTRAL CLIPPING AND COMPRESSION

By compressing the ANDi pulses in a folded Martinez compressor, we have easy access to the spatially dispersed spectral line focus for the purposes of amplitude modifications. Using an iris, we can clip the edges of the power spectrum which contain the the most significant post-compressor HOD and noise as seen in Figs 2.3 and 2.2, respectively. Another useful metric we introduce here quantifies how close to the TL a pulse is, termed the normalized percent compression. The normalized percent compression is the intensity profile of a pulse scaled to the normalized version of its power spectrum dictated TL. The normalized percent

TABLE 2.1. Spectral clipping pulse energies, average powers, and spectral clipping transmission for a high power ANDi

Clipping	Energy [nJ]	Average Power [mW]	Spectral Clipping Transmission [%]
None	19	1010	100
Lightly Clipped	17	880	87
Heavily Clipped	15	774	77

compression intensity then, is in units of percentage ( $\leq 100\%$ ), relative to the TL peak power. We use this metric because comparisons between the compressed pulse FWHM duration and the TL FWHM duration are misleading in terms of judging the proximity of the compressed pulse profile to its TL.

Fig. 2.3 shows the effects on pulse peak power, normalized percent compression, and pedestal with spectral clipping as measured by second-harmonic generation frequency resolved optical gating [78]. Illustrating the highly deleterious effects of the HOD, the lightly clipped pulse (black power spectrum and intensity) is 87% of the average power of the unclipped ANDi but has the highest peak power at 88 kW in a 164 fs pulse with 17 nJ of energy (i.e. the HOD’s effects are analogous to deconstructive interference). For this particular ANDi, which is our highest power oscillator system and has repetition rate of 53 mHz, the pulse energies, average powers, and spectral clipping transmission are listed in Table 2.1.

It is the reduction in temporal pedestal, however, that is of the most interest to us because it translates into improved SC spectral stability and a more efficient generation of second- and third-order nonlinear signals. By clipping the pulse spectrum, we increase the TL duration to nearly the pulse duration of the compressed pulse, while eliminating the power spectra with HOD. As is most clear for the heavily clipped case (red pulse Fig. 2.3), the pulse is very nearly TL at 95% normalized percent compression due to nearly zero residual spectral phase within the power spectral bandwidth. Fig. 2.3(d) shows how the normalized percent

compression improves and trends towards 100% as more of the HOD is eliminated (and the TL pulse duration increases). Empirically, we find 150 fs TL pulses (16 nm FWHM, albeit with power spectra that is fairly super-Gaussian) to be the duration where we start getting  $> 85\%$  normalized pulse compression.

With spectral clipping, the ANDi pulses become more suitable candidates for highly nonlinear tasks such as SC generation. Where as in Fig. 2.2 we see the amplification of small spectral noise due to poor pulse compression, Fig. 2.4 shows the reduced SC noise resulting from an ANDi seed pulse with improved compression via spectral clipping. Even though the average power coupled into the nonlinear fiber is reduced for the spectrally clipped pulse shown here, 130 mW, compared to the full spectrum ANDi pulse seeded SC, 190 mW. The improved normalized percent compression and reduced temporal pedestal produces nearly as much bandwidth with significantly reduced maxima in the RSN. The RMS-N of the clipped seed pulse is also reduced from the un-clipped case, 0.2 vs 0.4 %, and the amplification of the RMS-N to the  $\Phi_{\text{RSN}}$  is fairly comparable at  $7\times$  and  $8.3\times$ , clipped and un-clipped respectively.

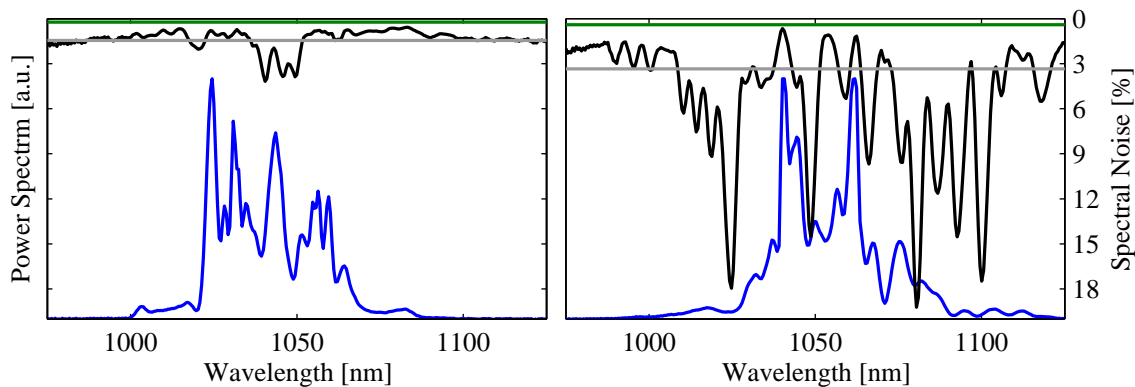


FIGURE 2.4. Spectral SC noise over a 45 min time series for (a) clean ANDi pulses and (b) un-clipped ANDi pulses: power spectrum (blue), RSN (black),  $\Phi_{\text{RSN}}$  (grey), and RMS-N (green)

The reduction in temporal pedestal through modification of the power spectrum and elimination of HOD benefits virtually all downstream nonlinear applications. For most micro-illumination applications involving cells or biological tissue, the illumination average power must be kept below the damage and toxicity level of the sample, which at 1060 nm is  $< 100$  mW [58] for living biological tissue. A major benefit for multi-photon microscopy then, is the improvement in nonlinear signal efficiency (ratio of signal to illumination average power) for nonlinear interactions with an increase in normalized percent compression.

For an  $N^{\text{th}}$ -order nonlinear signal ( $N = 2$  for second-harmonic generation and two photon excitation fluorescence and  $N = 3$  for third-harmonic generation) the ratio between the nonlinear signals driven by two pulses is  $g_N = \frac{\langle I_1^N \rangle}{\langle I_2^N \rangle}$  [79, 80], where  $I$  is the pulse intensity and  $\langle \rangle$  denotes a long time average. Assuming a constant pulse repetition rate, this ratio reduces to  $g_N = \frac{\int I_1^N dt}{\int I_2^N dt}$ . As the remaining average power of even the heavily clipped ANDi pulses are still well above the typical micro-illumination damage threshold for biological samples, it is reasonable to compare the nonlinear signals resulting from the pulses in Fig. 2.3 assuming a constant average power and pulse energy. The increases in nonlinear signal level for both clipped pulses (red and black) relative to the un-clipped ANDi pulse (green) are  $1.5\times$  and  $2\times$  for  $N = 2$  and 3 order nonlinear processes, respectively.

We did not invent or discover the ANDi laser. We have however, developed a particular incarnation of a Yb-doped ANDi oscillator that is exceedingly robust, running up to a year at a time before requiring a few minutes of maintenance. Due to the stringent requirements of SC generation, we developed a means of producing the highest quality pulses possible in the absence of employing a pulse shaper via spectral clipping. The improved normalized percent compression also increases the nonlinear signal scaling factor  $g_N$ , making our ANDi

pulses even more effective pump pulses for multi-photon microscopy. Our ANDi lasers are the foundation on which most of the rest of this dissertation stands.

## CHAPTER 3

# PART I: NONLINEAR FIBER AMPLIFIER WITH TUNABLE TL PULSE DURATION FROM A FEW 100 TO SUB-100 FS AT WATT-LEVEL POWERS

*I have not failed. I've just found 10,000 ways that won't work.*

Thomas Edison

### 3.1. NONLINEAR FIBER AMPLIFIER WITH VARIABLE OUTPUT BANDWIDTH

Ultrafast laser pulses are widely used for applications such as spectroscopy, nonlinear optics, and machining of materials, where their high peak power and short temporal duration are exploited. Many applications are highly sensitive to the pulse duration, and control of the process can be exerted by stretching the pulse to longer than the TL duration without the loss of energy. However, in some systems, such as optimizing molecular two-photon absorption [81], selection of a single high harmonic generation harmonic [3], or two photon absorption in the presence of an intermediate absorption resonance [82], the precise temporal chirp and the temporal duration of the pulse significantly changes the behavior of the laser-matter interaction. This renders simple pulse chirping as inadequate to fully control the laser-matter interaction. While, a narrow region of the spectrum can be selected to increase the pulse duration, this comes at the expense of energy loss and a reduction in the nonlinear interactions exploited in most experiments. Many applications could benefit from a laser source that allows for tuning the output spectrum centroid and width, and thus the TL pulse duration, without sacrificing pulse energy.

In this chapter, we demonstrate such a system, where we tune the output spectrum of a fiber master oscillator power amplifier (MOPA) system, while keeping the amplified pulse train average power nearly constant. This enables us to tune the bandwidth supported transform-limited (TL) output pulse duration from 400 to  $< 60$  fs, each with nearly the same pulse energy. This unique source is enabled by designing a power amplifier to operate in a highly nonlinear regime, so that significant spectral broadening occurs. The highly nonlinear amplifier is leveraged, in combination with tuning the spectral bandwidth of the amplifier seed pulse, to tune the amplifier output power spectral bandwidth. This chapter is based on our work published in Ref [83].

A range of applications for Yb fiber laser sources has driven the development of a number of fiber amplifier architectures: chirped pulse amplification fiber amplifiers [20, 84], similariton amplification [85, 86], and cubicon amplifiers [87]. While similariton and cubicon amplifiers also exploit nonlinear propagation during amplification, the use of pump power tuning for nonlinear phase compensation of third-order dispersion (TOD) results in a single optimal operating condition for the production of pulses with minimal temporal pedestal.

Recent work has revealed that normal dispersion spectral broadening can lead to stable supercontinuum (SC) generation, provided that polarization modulation instability [88] is mitigated through propagation in polarization maintaining (PM) fibers [26]. While the broadening in the amplifier is not as extensive as SC generation in nonlinear optical fiber, the nonlinear phase shifts are still quite large at  $\phi_{nl} \sim (5 - 12)\pi$  [89]. By designing the amplifier with PM gain fiber, and optimizing the launch conditions so that significant nonlinear phase is accumulated, we broaden the seed spectrum in the amplifier by up to  $12\times$ .

Seed pulses for this source are derived from an all-normal dispersion (ANDi) fiber laser [22]. ANDi lasers have attracted significant attention in recent years due to their favorable average power and spectral bandwidth characteristics. The output chirp of an ANDi laser operating with modest average power ( $\sim 500$  mW, 22 nm bandwidth, and 130 fs FWHM TL pulse duration) contains a significant amount of higher-order dispersion (HOD). In combination with small fluctuations in the power spectral density from the ANDi oscillator ( $< 2\%$ , see Fig. 2.2(c)), the temporal structure from the uncorrected HOD on the pulse can drive large spectral fluctuations in all normal dispersion SC generation [26]. Eliminating the influence of spectral fluctuations from the ANDi oscillator during nonlinear broadening in the amplifier is critical, requiring seed pulses with minimal residual cubic chirp after compression. These conditions are met by spectrally filtering the seed pulse spectrum in the focal plane of a compressor before the amplifier. The selected narrow seed bandwidth is centered on a region of the ANDi oscillator with low spectral noise. The narrow spectrum also ensures that we minimize HOD on the seed pulse for the initial stages of propagation in the amplifier. Compared to generating the seed pulse using nonlinear pulse compression [90], our amplifier architecture reduces the number of cascaded nonlinearities – reducing the output spectral noise and relaxing input seed chirp constraints.

The overall amplifier architecture is shown in Fig. 3.1. A folded Martinez stretcher is equipped with an adjustable slit in the Fourier plane to select a narrow spectral band from the oscillator pulse spectrum. The compressor exhibits a transmission efficiency of 91% (with no spectral filtering).

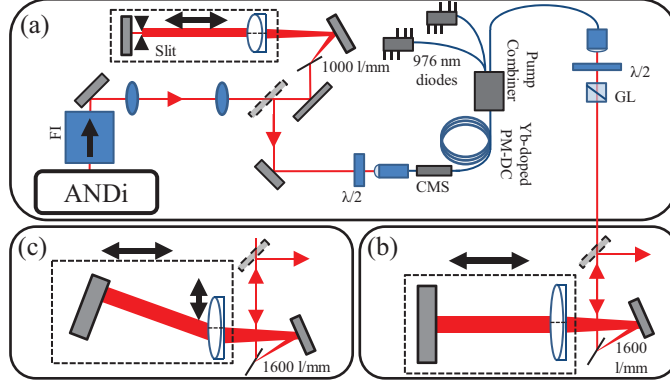


FIGURE 3.1. Schematic of the (a) ANDi oscillator and PM-DC amplifier, and the output compressor (b) without TOD compensation and (c) with TOD compensation. CMS: cladding mode stripper, FI: Faraday isolator, PM-DC: polarization maintaining - double clad fiber, GL: glan-laser polarizer, 1600 l/mm: transmission grating

An APC connectorized entrance segment of  $\sim 2.5$  cm of 980 PANDA fiber is spliced to the double-clad (DC) PM gain fiber; enabling the use of a collimator for simple, efficient ( $\sim 70\%$ ), and robust coupling. The passive entrance fiber is just long enough for a cladding mode stripper at the passive-to-gain fiber splice to remove any residual pump power. The cladding mode stripper is constructed by applying a high-index re-coat over the outer-cladding stripped area of the passive-to-gain fiber splice. Potting the recoated mode stripper into an aluminum housing with high-temperature thermal paste keeps the recoated fiber section from overheating due to absorption. Later versions of the cladding mode stripper actively cool the aluminum housing and pot the stripped fiber using a high-index, high-temperature epoxy. The gain fiber is 2 m of Yb-doped Liekki Yb1200-10/125DC-PM fiber. Two 2.5 W 976 nm fiber-coupled diodes pump the amplifier through a  $(2 + 1) \times 1$  PM pump combiner. The 20 cm long exit fiber includes the pump combiner and is connectorized with an APC connector. Commercial aspheric collimators with APC receptacles are attached to the APC connectors on both the entrance and exit ends of the amplifier.

We investigate the performance of the amplifier by varying the bandwidth of the launched seed pulse from 1.3 – 15 nm full-width-half-max (FWHM). The different seed pulse bandwidths also span a large range fiber coupled seed pulse energies from 0.13 - 1.9 nJ (or 9 - 120 mW at 63 MHz). The input and output pulse energies are shown in Fig. 3.2 and cover small signal gain to deep into gain saturation. The relatively square ANDi power spectra results in linear changes in seed pulse energy with seed pulse bandwidth. The seed pulse temporal durations also change with seed pulse bandwidths ranging from 1.4 ps to < 300 fs.

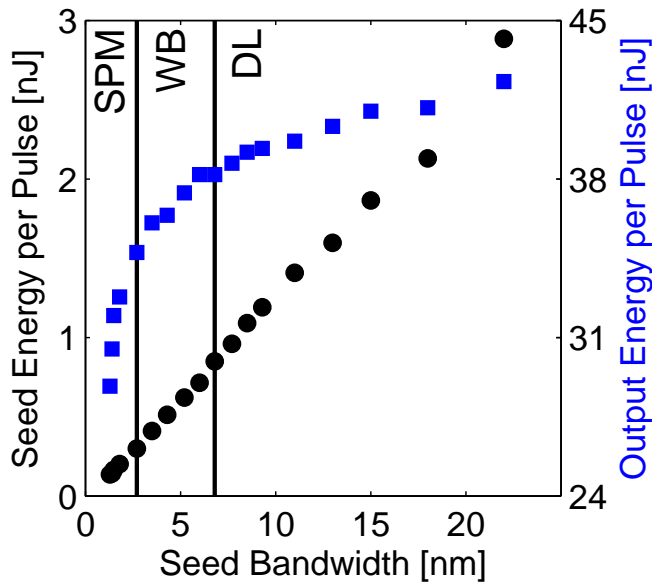


FIGURE 3.2. The seed (black-circles) and amplified (blue-squares) pulse energies as a function of seed pulse bandwidth

The amplifier output, with changing seed and output pulse bandwidth, divides into 3 regions: self-phase modulation (SPM), optical wave-breaking (WB), and dispersion limited (DL). Intensity profiles and power spectra from reconstructed second harmonic generation frequency resolved optical gating (SHG-FROG) measurements [78] are used to characterize the uncompressed amplifier outputs, and are shown in Fig. 3.3. The role of accumulated dispersion in each region is different: being minimal in the SPM region, causing WB in the

second, and substantially disrupting nonlinear propagation in the DL region. Because of the complex temporal structure of the uncompressed amplifier output, FWHM estimates are not meaningful metrics for the uncompressed temporal pulse duration. Instead we use an  $e^{-2}$  relative intensity level in Fig. 3.3(a) for the uncompressed amplifier pulses while employing the typical FWHM for the compressed and TL pulse durations. Similarly, the spectral width estimates in Fig. 3.3(c) use the bandwidth needed to encompass as much energy as a Gaussian spectrum at FWHM, rather than the actual FWHM.

Below seed pulse bandwidths of 2.7 nm FWHM (or temporal durations  $> 700$  fs), the spectra out of the amplifier are highly representative of SPM dominated nonlinear propagation. The input seed energies in the SPM dominated region are below the saturation threshold of  $\sim 0.6$  nJ, but still amplify to  $\sim 30$  nJ [Fig. 3.2]. The uncompressed amplifier output pulse durations and the TL pulse durations supported by the output spectra fall as the seed bandwidth increases [Fig. 3.3(a) and (c)]. The bandwidth increases the most rapidly in the SPM region. The minimum TL pulse duration supported by the amplified pulse bandwidth in the SPM-dominated region is  $\sim 100$  fs FWHM.

We observe a transition from SPM to WB between seed pulses amplified to TL pulse durations of 130 fs and 76 fs FWHM (1.8 and 2.7 nm seed pulse bandwidths, respectively). WB occurs when SPM generated spectra temporally overlaps and beats against the central seed bandwidth as the pulse begins to temporally broaden. In the amplifier, the WB region occupies seed pulse bandwidths from 2.7 to 6.8 nm. The amplifier output reaches its minimum uncompressed temporal duration at the beginning of this region, then begins to broaden again temporally as the integrated dispersion grows with increased seed pulse bandwidth. A spectral side-lobe at 1020 nm from WB by four-wave mixing results in the broadest

amplifier output spectrum supporting the shortest TL pulse duration of 56 fs FWHM, from a 5.2 nm (500 fs) FWHM seed pulse [Fig. 3.3(a)-(c) filled markers]. The seed pulse energies in the WB region cross the saturation threshold, producing amplified pulse energies  $> 35$  nJ.

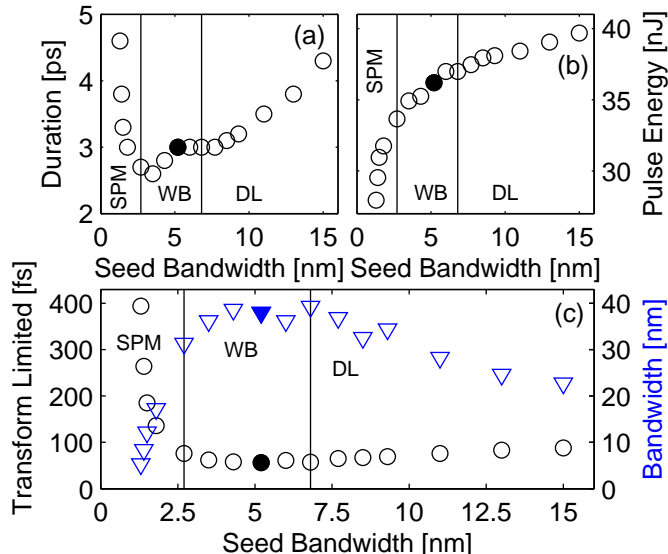


FIGURE 3.3. (a) The amplifiers uncompressed output pulse duration, (b) pulse energy, (c) the TL pulse duration (black circles), and the spectral bandwidth (blue triangles) as functions of amplifier seed bandwidth

The DL region contains the broadest seed pulse bandwidths and therefore also the largest spectral noise from the ANDi seed pulse. The seed pulses in the DL region also contain increasingly complex spectral phase, where on the limit of no spectral filtering the seed pulse is the ANDi oscillator spectrum with significant HOD. As the seed pulse spectral filter/compressor does not produce compressed pulses with minimal temporal pedestal for seeding the amplifier, we focus little attention on this region.

### 3.2. COMPRESSIBILITY OF THE NONLINEAR AMPLIFIER

The spectral phase dictates the compressibility of the amplifier output, which is of the utmost importance. We use SHG-FROG reconstructions to characterize the power spectrum

and intensity profile after transmission through a folded Martinez compressor [Fig. 3.4]. The necessity for TOD compensation further separates the SPM and WB regions, as one would expect by the fundamental division in the significance of dispersion in pulse propagation for each region. In the SPM dominated region, the residual spectral phase without any TOD compensation [Fig. 3.1(b)] is sufficiently small to produce nearly TL pulses, shown in Fig. 3.4(b). As the seed bandwidth increases from 1.8 nm to 3.5 nm and the amplifier output transitions to the WB region, the residual TOD of the compressed amplifier pulse adds an increasingly significant cubic tail to the intensity profile [Fig. 3.4(d)] due to the, now, prolonged fiber propagation at larger bandwidths.

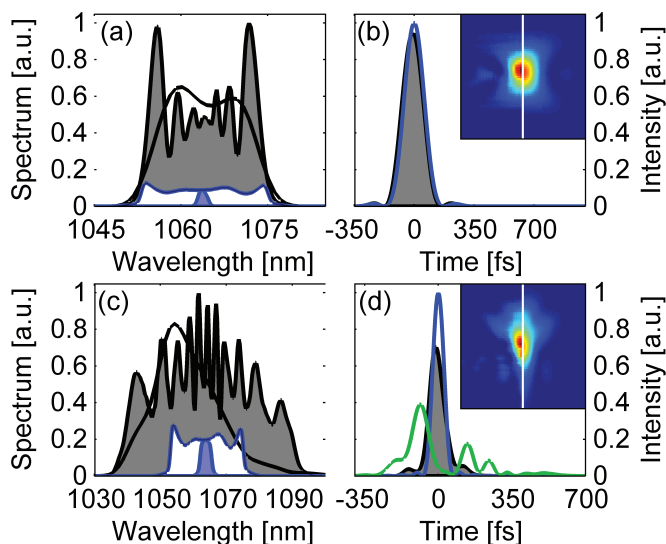


FIGURE 3.4. Pulse characteristics from an amplified 1.8 nm seed pulse (a) and (b), and a 3.5 nm seed pulse (c) and (d). (a)/(c) The reconstructed power spectrum before (black shaded) and after (black line) compression and the ANDi oscillator (blue) and amplifier seed (blue shaded) spectra. (b)/(d) The reconstructed intensity profile of the compressed pulse (black shaded), the supported TL profile (blue), and the pulse without TOD compensation (green, (d) only) with the phantom-SHG-FROG (measured trace left and reconstructed trace right) images inset.

The minimum compressed amplifier output pulse duration in the SPM dominated region is from a 1.8 nm seed pulse (1 ps FWHM), shown in Fig. 3.4(a) and (b). With a Martinez

compressor (82% transmission efficiency) we achieve pulses with 27 nJ (1.7 W at 63 MHz) and 144 fs FWHM, resulting in 180 kW of peak power. This is 95% of the TL peak power, where the TL duration is 136 fs FWHM. Longer, also nearly TL, pulse durations are attainable simply by decreasing the seed pulse bandwidth with the adjustable slit and slight tuning of the output compressor.

In the WB region, the amplified pulses begin to accumulate large amounts of TOD. This dispersion can be partially corrected by laterally displacing the imaging lens in a Martinez compressor [Fig. 3.1(c)], so that coma aberration of the lens maps to third order spectral phase [91]. HOD however, still limits the compressibility of pulses in the WB region. We compressed an amplified 3.5 nm seed pulse to 80 fs FWHM out of a TL duration of 60 fs FWHM. This is a significant improvement over the compression without TOD compensation, where the green-curve in Fig. 3.4(d) shows a significant cubic pedestal. The available peak power is nearly twice as large for pulses with TOD compensation as without; assuming equal pulse energies from either compression architecture. While the coma aberration compensates for the TOD, it comes at a cost of significant apodization of the power spectrum due to the off-axis aberrations, as seen in Fig. 3.4(c) black vs black-shaded curves. Estimating the total transmission efficiency at 60% from both compressor and spectral apodization losses, the peak power of the compressed 80 fs pulse is 215 kW.

An alternative means of compressing the phase in the WB region, is a cascaded compressor scheme: a 1000 l/mm grating compressor and a ZnSe prism compressor. The prism compressor can correct the third order dispersion from the grating compressor and the material dispersion in the amplifier [92], where ZnSe is necessary to achieve the magnitude of TOD to group-delay dispersion. Modeling the compression, we find that a grating separation

of 3.7 mm, a prism separation of 222 mm, and a prism insertion of 15.3 mm would result in the pulse shown in Fig. 3.5. The projection of the spatially dispersed pulse bandwidth onto the second ZnSe prism would be 10 mm, allowing for 15 mm of insertion from a prism with a 30 mm face. Assuming compressor efficiencies of 85% and 95%, for the grating and prism compressors respectively, the 62 fs pulses would reach 350 kW of peak power at 84% of the TL peak power. As in Section 2.2, the increase in peak power and reduced temporal pedestal will increase the efficiency of nonlinear signal generation especially in multi-photon microscopy.

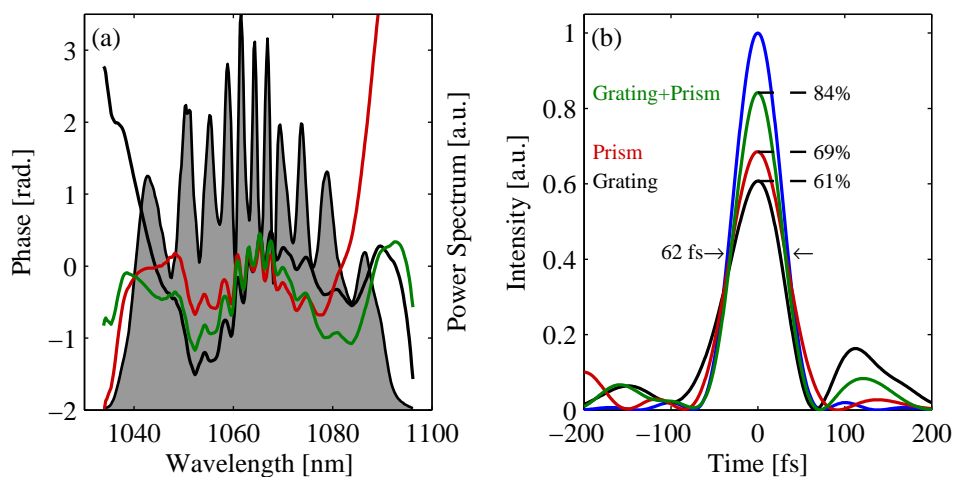


FIGURE 3.5. (a) Residual spectral phases and (b) intensities for an amplified 3.5 nm seed pulse with 3 different compressors: a 1000 l/mm grating compressor (black), a ZnSe compressor (red), and a combination of the two (green), along with the power spectrum (shaded) and the bandwidth supported TL intensity (blue).

### 3.3. NOISE ANALYSIS OF NONLINEAR AMPLIFIER SEEDED SUPERCONTINUUM

SC generation serves as an extremely stringent test of the stability of the intensity profile of an ultrafast pulse source. An ideal SC pump pulse has no relative spectral noise (RSN) in its power spectral density or total spectral noise ( $\Phi_{\text{RSN}}$ ) beyond the root mean squared noise (RMS-N) of the total power fluctuations. These noise characteristics (described in greater

detail in Section 2.2), along with minimal cubic chirp, are paramount in determining the utility of a pulse source for generating SC with low spectral noise.

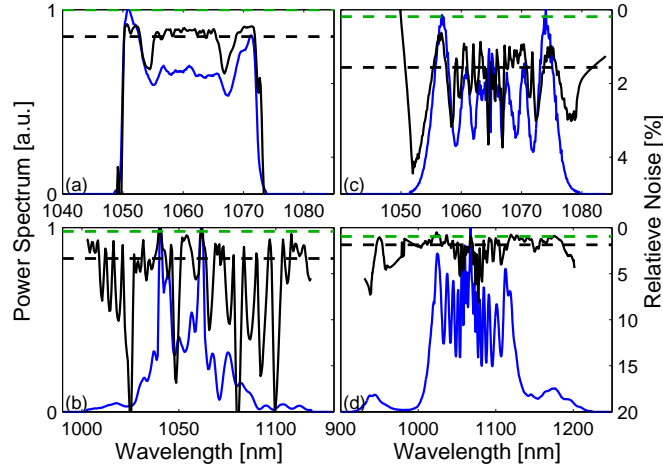


FIGURE 3.6. Spectral stability of the (a) ANDi oscillator, (b) SC generated with the ANDi oscillator, (c) amplified 1.8 nm seed pulses, and (d) SC generated with the amplified 1.8 nm seed pulses: power spectrum (blue), RSN (black),  $\Phi_{RSN}$  (black-dashed), RMS-N (green-dashed).

An Andor iDus spectrometer was used to capture the noise characteristics at 20 Hz over 45 minute time intervals. Previous measurements at up to 100 Hz validated that there was no significant low frequency noise below 20 Hz. These measurement frequencies seek to capture SC noise due to cascaded nonlinear interactions between the newly generated SC and the temporal pedestal, which would fluctuate on the same time scale as spectral mode fluctuations on the ANDi oscillator seed pulse, see Section 2.2 for more details on the ANDi oscillator noise and ANDi oscillator seeded SC noise.

The ANDi oscillator has a low RMS-N and  $\Phi_{RSN}$  of 0.08% and 0.7%, respectively [Fig. 3.6(a)]. The 200 mW of SC generated with the ANDi seed, however, exhibits an increase in spectral noise, as shown in Fig. 3.6(b), with an RMS-N and  $\Phi_{RSN}$  of 0.2% and 3.4%.

In the amplifier, after a gain of 22dB and  $10\times$  spectral broadening (1.8 nm seed pulse) the spectral noise does not significantly increase, with an RMS-N of 0.2% and a  $\Phi_{RSN}$  of 1.6%

[Fig. 3.6(c)]. Beyond the SPM dominated region, the spectral noise remains almost constant; the  $\Phi_{\text{RSN}}$  is 1.8% from an amplified 3.5 nm seed pulse with over twice the output bandwidth as the 1.8 nm seed. The noise characteristics of SC from a PM nonlinear fiber cocktail (fiber details in [26], the same fiber used for the ANDi seeded SC generation) pumped with the amplified 1.8 nm seed pulses are very satisfactory: RMS-N of 1% and  $\Phi_{\text{RSN}}$  of 1.9%. The SC has 500 mW of average power and a spectral width sufficient to support 15 fs FWHM pulses; covering  $> 2500 \text{ cm}^{-1}$  [Fig. 3.6(d)]. The amplifier generated SC is better in every parameter: average power, bandwidth, quality/structure of generated bandwidth, and spectral noise. It is the high quality pulse compression which enables such an increased SC pulse formation.

In conclusion, our fiber amplifier produces a wide range of pulse durations, all with  $> 20$  nJ of energy. The SPM dominated region from the narrowest seed bandwidths produce high power pulses without any need for TOD compensation to realize near TL performance. Marginally larger seed bandwidths produce pulses with  $< 60$  fs FWHM supported transform limits and can be compressed with TOD compensation to attain 80 fs FWHM pulse durations potentially down to 60 fs. Pulses from both regimes exhibit exceptional spectral stability, verified both by direct measurement and through measurements of the spectral stability after SC generation.

## CHAPTER 4

# PART I: ACCUMULATED SPECTRAL PHASE AND NON-GAUSSIAN/SOLITON SEED PULSES IN SUPERCONTINUUM GENERATION IN ALL NORMAL DISPERSION OPTICAL FIBER

*If you can't explain it simply, you don't understand it well enough.*

Albert Einstein

### 4.1. INTRODUCTION

Supercontinuum (SC) generation in the normal dispersion regime has attracted intense interest due to preservation of the seed laser's coherence. The principle effort in SC generation has been focused on anomalous dispersion fibers with low net dispersion. While these fibers generate substantial spectral widths, they suffer from de-coherence mechanisms, such as modulation instability that are not allowed in a normal dispersion regime. Preserving coherence in anomalous dispersion SC generation requires extremely short fiber lengths and/or launching with short input laser pulses with limited pulse energy[28].

Fibers exhibiting normal dispersion relax the constraints on the launched pulse duration, and permit stable SC generation with a much broader range of input pulse parameters. As normal dispersion optical fibers are typically less nonlinear than the designer anomalous dispersion fibers and do not use intrapulse Raman scattering to frequency shift spectra out to low frequencies, more pulse energy or pulse peak power is necessary to achieve spectacularly large power spectral bandwidths.

Photonic crystal fibers (PCF) with all normal dispersion have been used to create few-cycle pulses [93], octave-spanning SC [94], white-light SC [94, 95], and high compression ratio pulses [93, 96, 25, 97]. Solid, ultrahigh-numerical-apertures (UHNA) fibers with all normal dispersion profiles are less frequently used but have generated SC for optical coherence tomography [98]. However, all normal dispersion UHNA fibers are an attractive source for generating SC since they are low cost, relatively easy to splice to other fibers, and can be directly connectorized.

The spectral broadening properties of SC seeded by an ANDi-type, Yb-doped fiber laser [4] are also investigated. ANDi lasers offer an attractive alternative to bulk Yb-doped soliton modelocked oscillators due to the favorable energy and bandwidth scaling properties of the dissipative-soliton modelocking mechanism in addition to their low cost, ease of alignment, and high-quality beam spatial profile. However, the structure of the power spectrum and the complexity of the oscillator’s spectral phase perturbs the nonlinear pulse propagation, leading to SC generation characteristics that are qualitatively and quantitatively distinct from spectra generated by seed pulses from soliton-like modelocking with near-zero net intracavity GDD. Specifically, the steep slopes in the ANDi power spectrum translate into SC generated power spectrum with much more fine structure. This chapter is based on our work published in Ref [26].

## 4.2. SPECTRAL PHASE EVOLUTION

To model and understand the complex parameter space, we implemented a numerical split-step fiber propagator to approximate fiber propagation using the generalized nonlinear Schrödinger equation (GNLSE) [28]. For details on the numerical propagator model see

Appendix A. The evolution of the electric field,  $A(z, t)$ , according to the GNLSE is

$$(4.1) \quad \frac{\partial A}{\partial z} + \sum_{k \geq 2} \frac{i^{k+1}}{k!} \beta_k \frac{\partial^k A}{\partial t^k} = -i\gamma \left( 1 + i\tau_{\text{shock}} \frac{\partial}{\partial t} \right) \left( A(z, t) \int_{-\infty}^{\infty} R(t') \times |A(z, t - t')|^2 dt' \right).$$

The  $\beta_k$ 's are the coefficients of a Taylor expansion of the propagation constant  $\beta(\omega)$ .  $\gamma = \omega_0 n_2(\omega_0) / c A_{\text{eff}}(\omega_0)$  is the fiber nonlinear coefficient, where  $\omega_0$  is the central frequency of the pulse,  $n_2 = 3.2 \cdot 10^{-20} \text{ m}^2/\text{W}$  is the intensity dependent index of refraction of fused silica (the predominant material of the optical fibers),  $c$  is the speed of light, and  $A_{\text{eff}}(\omega_0)$  is the effective mode area at the central frequency. The third-order response function is  $R(t) = (1 - f_R)\delta(t) + f_R h_R(t)$ , where  $\delta(t)$  is the Dirac delta function and  $h_R(t)$  is an analytic representation of the Raman response function.  $f_R$  is the relative strengths of the instantaneous (Kerr) and non-instantaneous (Raman) interactions and following Ref [28] is 0.18 and  $\tau_{\text{shock}} = 1/\omega_0$ . This form of the GNLSE has been shown to accurately model SC generation in Ref [99], and accurately predicts behavior and spectral structure in our systems.

There are quite a few optical fibers suitable for SC generation in the normal dispersion regime. Fig. 4.1 shows the dispersion profile for several such fibers, where the profiles are plotted in units of ps/(nm km), the so-called dispersion coefficient  $D$  (where the normal dispersion region is  $D < 0$ ), and from which the group velocity dispersion of the propagation constant as a function of wavelength,  $\lambda$ , can be calculated from

$$(4.2) \quad \beta_2(\lambda) = -\frac{D 10^{-6} \lambda^2}{2\pi c}.$$

Notice that some of these fibers have a zero-dispersion wavelengths and hence for large enough spectral broadening the red-tails of the SC would slip into the anomalous dispersion region. Such an event would be problematic when trying to smoothly generate SC as it

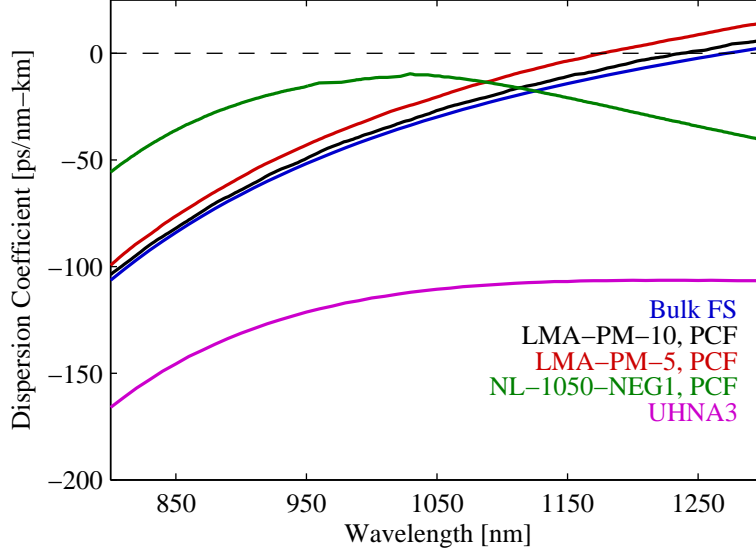


FIGURE 4.1. Dispersion profiles for bulk fused silica (blue) and the photonic crystal fibers LMA-PM-10 (black), LMA-PM-5 (red), NL-1050-NEG1 (green), and a solid core/cladding fiber UHNA3 (magenta), with nonlinear coefficients for the fibers of 0.002, 0.009, 0.037, and 0.029  $1/(W \cdot m)$  respectively

would cause the ejection of a soliton in both the time and frequency domains. There are two fibers in Fig. 4.1, NL-1050-NEG1 and UHNA3, which are specifically all-normal dispersion over the entire possible spectral broadening region. It is these fibers which we will focus on for the remainder of this chapter. But it ought to be noted that the other fibers are good candidates for broadening if either the desired spectral broadening is more modest supporting only  $\sim 20$  fs transform-limited (TL) pulse durations or the central frequency of the seed pulse is of higher frequency than 1030–1060 nm.

Applications where a compressed or shaped laser pulse are desired, the spectral phase of the SC spectrum, its stability, and complexity are critical issues. Here, we study the spectral phase complexity, spectral smoothness, and pulse compressibility in the normal dispersion regime under a wide range of pulse launch parameters by numerical integration of the GNLSE with a split-step propagator. Given that we have found experimentally that PM fibers preserve SC polarization to a large degree [26], we only implement the GNLSE

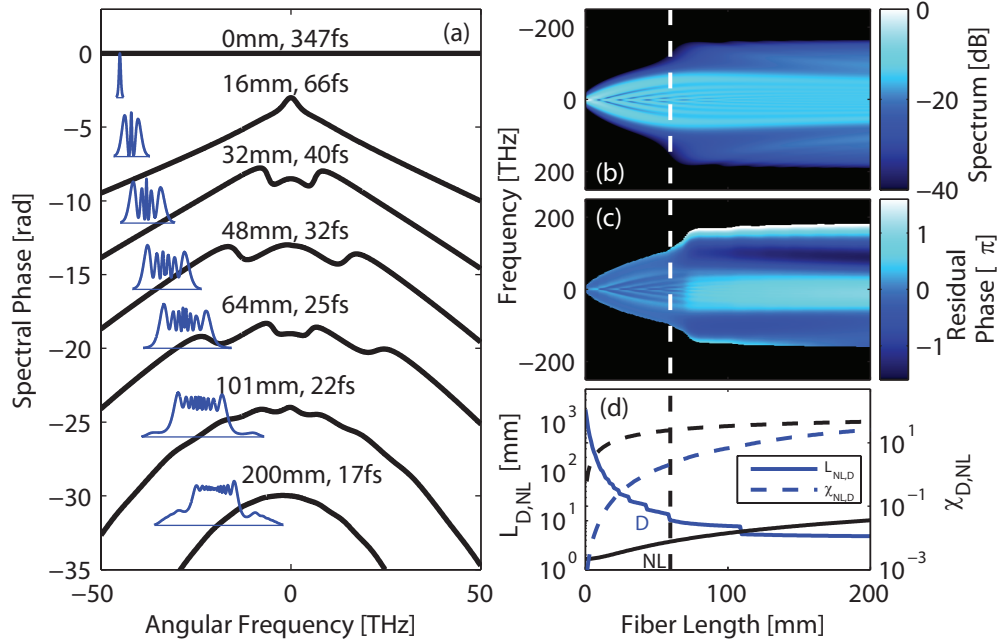


FIGURE 4.2. (a) SC spectral phase from 4 nJ 350 fs seed pulses for different fiber lengths with the power spectrum and numeric TL inset. Evolution of the (b) power spectrum (c) residual spectral phase after GDD compensation (residual phase set to  $-5$  outside of the  $-20$  dB power spectral envelope) and (d) local and accumulated characteristic lengths all as a function of fiber length. The local dispersion length and accumulated dispersion lengths,  $\chi_D$ , are in blue and the local nonlinear length and accumulated nonlinear length,  $\chi_{NL}$ , are in black. The calculated length, 62 mm, for the onset of WB is included as the vertical dashed line in (b)–(d)

for a single eigen polarization of the fiber system, i.e. a scalar electric field. As a reference point, we assume fiber launch conditions that mimic our earliest SC experiments using a bulk Yb:KYW laser: 350 fs hyperbolic secant (sech) seed pulses at 1027 nm, 4 nJ of energy coupled into the nonlinear fiber (or 284 mW at 71 MHz), and Nufern UHNA-3 nonlinear optical fiber (magenta curve in Fig. 4.1). The parameter space in a region around this operating point is explored, providing guidance for the expected behavior over a wide range of ultrafast modelocked laser operating parameters.

The spectral phase (and power spectra as an inset) of the SC spectrum for the pulse energy and bandwidth matching the characteristics from our oscillator for fiber lengths up

to and beyond optical wave breaking (WB) are shown in Fig. 4.2(a). The onset of WB for our example nonlinear system is  $z_{\text{WB}} = 60$  mm. This quantity is based on a definition of WB where new instantaneous frequencies, generated by self phase modulation (SPM), temporally overlap with different instantaneous frequencies from the central bandwidth due to propagation in the presence of group delay dispersion (GDD). The resulting intensity beating is referred to as WB, for which a distance can be computed from the expression [29].

$$(4.3) \quad z_{\text{WB}} = \frac{L_{\text{D}}(z = 0)}{\sqrt{4 \exp(-3/2)N^2 - 1}}$$

Here,  $L_{\text{D}}(z = 0)$  is the dispersion length determined by the bandwidth of the incident seed pulse coupled into the fiber and  $N$  is the soliton number of the seed pulse.

The sinusoidal beating in the pulse intensity following WB coincides with the initiation of four wave mixing (FWM). The spectral phase and envelope modulations characteristic of SPM dominated SC evolution, as seen in Fig. 4.2(a) for fiber lengths  $< 60$  mm, are smoothed out by the subsequent FWM [29]. In addition to the reduction of phase and amplitude structure, FWM generates long spectral tails that further drive down the TL of the pulse supported by the SC spectrum. These spectral tails are slow growing however, since they are a product of WB and, therefore, a diminished pulse peak power. Fig. 4.2(b) illustrates the sudden appearance of these WB/FWM spectral tails after WB, white dashed-line at  $z_{\text{WB}} = 60$  mm. In our example system, the SC's TL decreases from 28 fs at the onset of WB (60 mm) to 17 fs at a 1000 mm fiber length due to this additional bandwidth from WB/FWM.

The large, but smooth, variation in group delay associated with the spectral phase structure post-WB suggests a simple temporal pulse compressor might be sufficient. Counter

intuitively, the pre-WB SPM phase structure barely inhibits a simple compression system from reaching near TL pulses, due partly to the correlation of the spectral phase structure to power spectral nulls. Fig. 4.3(c) plots the simulated residual spectral phase following only GDD compensation as a function of fiber length. Propagation significantly past the WB threshold makes pulse compression acutely more difficult, as seen in the rapid accumulation of residual phase beyond the white dashed line denoting the onset of WB in Fig. 4.3(c).

While the nonlinear fiber propagation characteristics are strongly dependent on the pulse launch parameters such as the spectrum and pulse chirp at the fiber input, we introduce new parameters that track local and cumulative pulse propagation dynamics. These parameters are the spatially (longitudinally) evolving compliments of the common dispersion and nonlinear lengths which are based on the initial launch conditions. We define the local dispersion and nonlinear lengths as

$$(4.4) \quad L_D(z) = \frac{\tau(z)^2}{|\beta_2|}, \quad L_{NL}(z) = \frac{1}{\gamma P(z)},$$

where  $z$  is the local fiber position,  $\tau(z)$  is the full-width-half-max (FWHM) of the TL pulse duration supported by the SC bandwidth,  $\beta_2$  is the group velocity dispersion of the nonlinear fiber, and  $P(z)$  is the peak power. The local characteristic lengths for the example system are plotted in Fig. 4.2(d) solid-curves. The local dispersion length undergoes the more dramatic change falling from 1.9 m at the input to  $< 10$  mm after 200 mm of propagation. The falling local dispersion length is simply a reflection of the shortening TL pulse duration supported by the broadening power spectrum. The local nonlinear length increases due to a drop in the peak power of the pulse from the temporal pulse stretching that occurs with

fiber propagation, e.g. at the onset of WB the peak power has fallen by a  $\frac{1}{2}$ , as reported in Ref [29], and the local nonlinear length increases by a factor of 2.

In addition to the local characteristic lengths, we also introduce a parameter for the accumulated amount of each local length:  $\chi_i(z) = \int_0^z 1/L_i(z')dz'$ , where  $i = \text{D, NL}$ . These parameters are referred to as the accumulated dispersion and nonlinearity for  $i = \text{D}$  and  $i = \text{NL}$ , respectively. The accumulated nonlinear length is analogous to the B-integral [100], and accumulated dispersion length is a measure of the accumulated spectral phase. Increases to either accumulated quantity represents broadening: increasing  $\chi_{\text{D}}$  tracks the chirping of the pulse in time and increasing  $\chi_{\text{NL}}$ , generally, represents increasing power spectral bandwidth. Both accumulated quantities are quantitative handles for interpreting the temporal and spectral phase evolution of sustained nonlinear and dispersive pulse propagation.

Using these new metrics, we re-examine the problem of SC compressibility as a function of fiber propagation. Prior to WB, the SPM generated spectra has not meaningfully sampled the complexity of the fiber dispersion. The fast initial rate of change in the accumulated dispersion in Fig. 4.2(d) reflects the plummeting local dispersion length, but does not introduce significant chirp since the accumulated dispersion is still very small. The accumulated dispersion at the onset of WB is not only low,  $\chi_{\text{D}}(z_{\text{WB}}) \sim 2$ , but it also contains the accumulation of dispersion for the narrower initial spectral bandwidths. At WB however, the local dispersion length has become quite short, 13 mm in our particular example. Propagation beyond this point results in the rapid accumulation of spectral phase with significant higher order dispersion (HOD), due to the short local dispersion length and (now) broad spectra. To reach the shorter TL pulses that accompany propagation past WB, a pulse shaper is required to compensate the HOD.

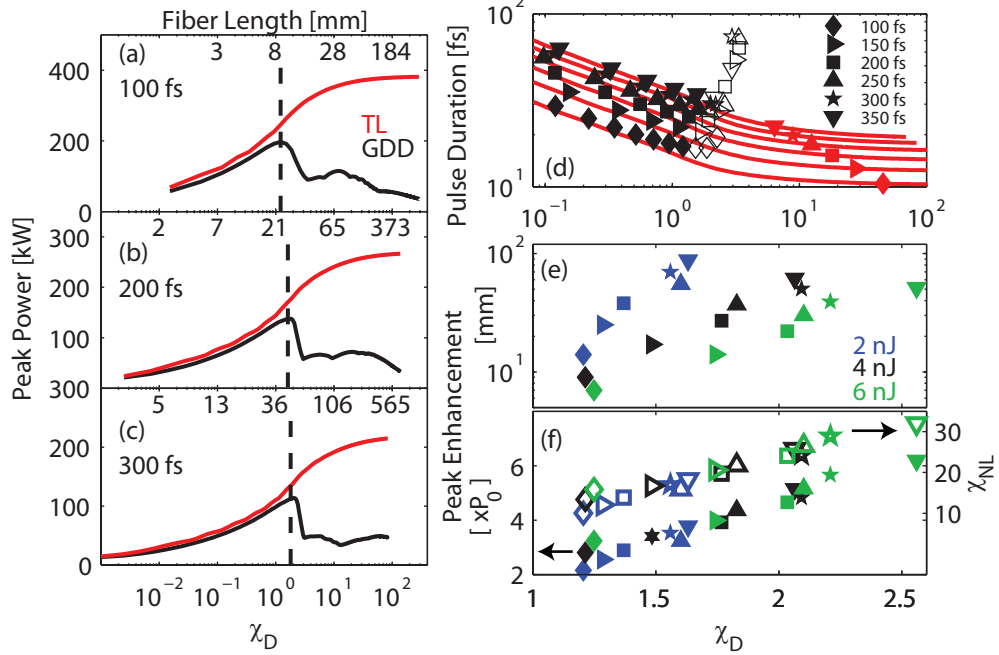


FIGURE 4.3. The peak power evolution with  $\chi_D$  for 4 nJ (a) 100 fs, (b) 200 fs, and (c) 300 fs seed pulses and GDD compensation in black and the TL in red. The onset of WB is plotted in (a)-(c) as a dashed vertical line. (d) The TL pulse duration in red and the pulse duration with only GDD compensation in black markers as functions of  $\chi_D$  for 4 nJ pulses and a suite of seed pulse durations: 100 - 350 fs. The solid black markers indicate the evolution up to the maximum peak power enhancement with GDD compensation, followed by hollow markers for additional propagation. (e) The fiber length corresponding to the maximum peak power enhancement with GDD compensation as a function of  $\chi_D$  for a suite of seed pulses: 2, 4, and 6 nJ shown in blue, black, and green respectively, and pulse durations from 100-350 fs. (f) The maximum peak power enhancement factor with GDD compensation, relative to the incident seed pulses (composed of twice the energy), and the accumulated nonlinear length at peak enhancement.

Moving from the narrow focus of our example nonlinear system to a broader parameter space, we expand our analysis on the evolving SC. Across a whole suite of seed pulses (energies of 2, 4, and 6 nJ and pulse durations of 100-350 fs), it is always the case that around the onset of WB, simple compression systems (e.g. grating or prism compressors) fail to compensate the HOD; resulting in a highly structured intensity envelope. Fig. 4.3(a)-(c) shows the TL and GDD compensated SC peak powers from 4 nJ seed pulses with 100, 200, and 300 fs

pulse durations respectively, as functions of accumulated dispersion. For simplicity, these and the following peak power calculations neglect compressor losses. Propagation beyond WB, dashed vertical lines in Fig. 4.3(a)-(c), causes the broad bandwidth to accumulate fiber dispersion over a larger range, with the spectral phase accumulating significant HOD. The peak power cliff-fall in the black GDD compensation curves of Fig. 4.3(a)-(c), corresponds to the accumulation of enough HOD following WB, to reduce the intensity from a simple compressor.

The point where the GDD compensated peak power reaches a maximum before the cliff-fall, which we will refer to as the peak enhancement, is a critical quantity for practical applications and is plotted in Fig. 4.3(d)-(f). Even though the cliff-edge varies across this parameter space over an order of magnitude in fiber lengths, it peaks very close to the individual WB lengths and in a small region of accumulated dispersion. The hollow markers of Fig. 4.3(d) represent propagation beyond the peak enhancement and are tightly congregated between  $1 < \chi_D < 2$ . A trend of hastening the peak enhancement arrival with falling seed pulse duration begins to manifest itself in Fig. 4.3(d).

The slope and shape of the cliff-fall is highly dependent on the incident seed pulse. At longer duration seed pulses, the GDD compensated peak power has a very sharp enhancement peak. For shorter duration seed pulses however, the GDD compensated peak power begins to diverge from the TL peak power prior to the onset of WB. This results in the rounding of the peak, seen in Fig. 4.3(a), and is a consequence of the increased sensitivity of the shorter incident seed pulse to HOD. The heightened sensitivity to HOD for shorter seed pulses is maintained with seed energy, as seen in Fig. 4.3(e) where the peak enhancement arrives at smaller accumulated dispersion lengths for shorter seed pulse durations.

Fig. 4.3(f) plots the peak power enhancement with GDD-limited spectral phase compensation, relative to the incident seed pulse peak power and the accumulated nonlinearity at peak enhancement. Here, we assume a total transmission efficiency of 50% including the fiber coupling, fiber launch, and compressor efficiencies. The incident seed energy then, is taken to have twice the energy of the GDD compensated SC pulse, giving a strict comparison of peak power enhancement. The SC with the largest accumulated dispersion length at the peak enhancement also has the largest relative peak power enhancement, as seen in the solid markers of Fig. 4.3(f). The larger accumulated dispersion at peak enhancement is accompanied with a larger accumulated nonlinearity, shown in the hollow markers of Fig. 4.3(f). The ratio of GDD compensated SC duration to seed pulse duration increases with seed pulse duration, as expected from the increasing nonlinear length with seed pulse duration.

The previous discussion assumed the luxury of arbitrary fiber lengths. But, it is possible that for particular applications the optimal fiber length is impractically small for connectorizing, splicing, etc. (e.g. the 100 fs, 6 nJ seed pulse in UHNA-3 fiber with a peak enhancement at 8 mm, shown as the green diamonds in Fig. 4.3(e) and (f)). Rather than reducing the seed power to raise the peak enhancement position to a practical length, we provide an alternate solution that keeps the seed power high and relaxes the short fiber requirements for simple compression. An interesting consequence of this work is the realization of the novel gains available from Third Order Dispersion (TOD) compensation. We find that while the GDD and TOD compensated SC peak power still undergoes a cliff-fall after a primary enhancement peak, with the addition of TOD compensation there is a secondary maximum, shown in the green curve of Fig. 4.4(a). The secondary peak enhancement is due to the specific

shape of the UHNA dispersion. The secondary peak enhancement is also only seen for the shorter duration seed pulses.

The inset figures in Fig. 4.4(a) show the progression in compressed SC intensity from the primary peak enhancement, Fig. 4.4(a1), to the bottom of the cliff-fall, Fig. 4.4(a2), to the secondary peak enhancement, Fig. 4.4(a3), and finally at the secondary peak enhancement position with only GDD compensation, Fig. 4.4(a4). Relative to the SC at the primary peak enhancement position, the SC at the secondary peak enhancement has more bandwidth. TOD and GDD compensation is sufficient to produce a pulse with a central temporal lobe shorter in duration than attainable at the primary peak enhancement but with side lobes from quadratic chirp. The two major potential benefits are: 1) the location of the secondary peak enhancement is shifted to an achievable fiber length (51 mm as opposed to 8 mm) and 2) the broadening of the peak enhancement curve. With only GDD compensation, the peak enhancement requires fiber length precisions of  $< 1$  mm, whereas the secondary enhancement with GDD and TOD relaxes this precision requirement to 1 cm.

As convenient metrics of utility, we supplement the peak power computations with the total second harmonic generation (SHG) signal [79] and total third harmonic generation (THG) signal [101] expected from SC seeded with 100 fs 6 nJ pulses compressed with various orders of compensation, assuming samples thin enough to neglect phase-matching. The harmonic signals plotted in Fig. 4.4(b) are normalized to the signal expected from the seed pulse incident on the fiber (where again we are assuming a total efficiency of 50% so the normalization is based on a 12 nJ pulse). The primary GDD compensated peak enhancement, for this particular seed pulse, yields a 1.5 and 5.3 fold improvement in the SHG and THG signals respectively. The secondary peak enhancement harmonic improvements are more

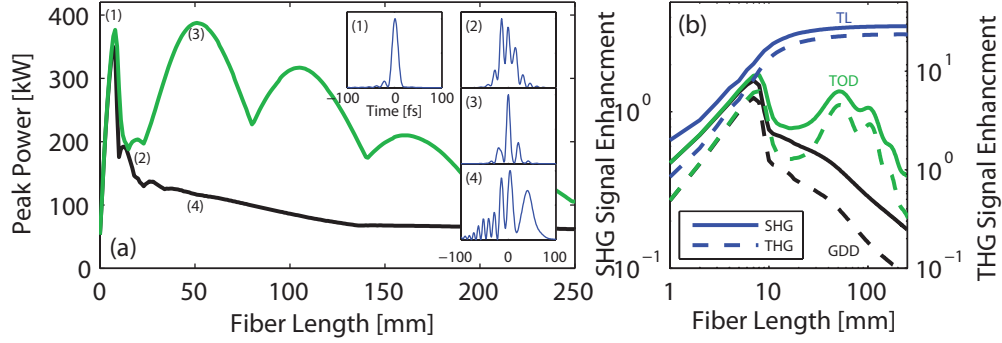


FIGURE 4.4. (a) The peak power evolution as a function of fiber length for 6 nJ 100 fs seed pulses with GDD compensation in black and GDD and TOD compensation in green. The compressed SC intensity is shown at several fiber lengths and compensation orders in inset figures (a1)-(a4). The SHG and THG signal enhancement relative to the incident 12 nJ 100 fs pulse, as a function of fiber length and order of compensation: TL in blue, GDD and TOD in green, and GDD in black.

modest, but still a respectable 1.3 and 4.5 for SHG and THG respectively. For comparison, towards the opposite end of the seed duration/energy spectrum, the pulses simulating our Yb:KYW oscillator of 350 fs and 4 nJ seed pulses yield improvements of 3.2 and 21 for SHG and THG, respectively with GDD compensation of the primary enhancement. These enhancements are potentially artificially low, since any measurement with average power limitations requiring power attenuation (e.g. interrogating a biological sample with a tightly focused beam) will drive up the relative enhancement factors of the compressed SC.

### 4.3. ANDI SEEDED SUPERCONTINUUM

Yb-doped ANDi fiber lasers are a compelling seed source for SC generation, but they are not a direct stand-in for the bulk Yb:KYW (soliton-like) seed pulses. The dissipative-soliton pulses from the ANDi laser have characteristic “cat-ears” in the power spectrum, Fig. 4.5(a) contains a representative power spectrum obtained through an SHG-FROG reconstruction. The cat-ears contribute to a SC power spectrum with much higher structure and noise than

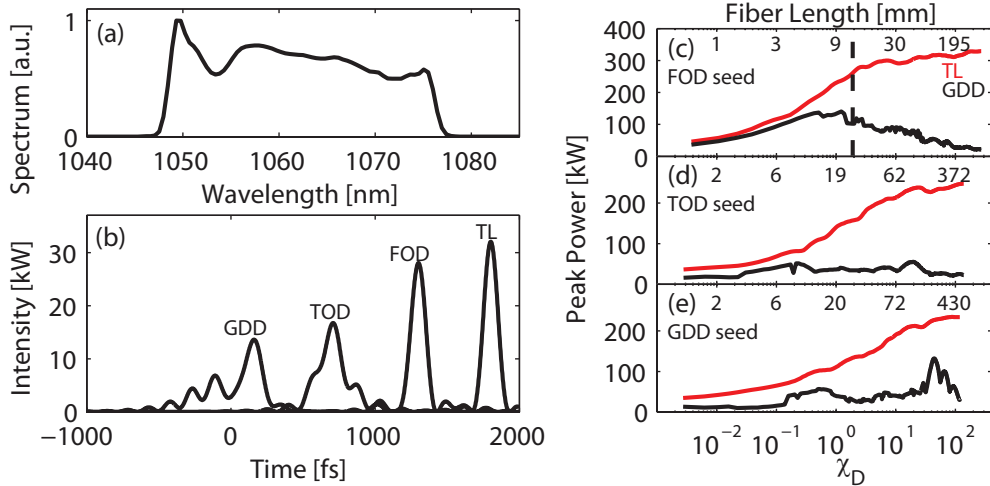


FIGURE 4.5. (a) The power spectrum and (b) intensities for GDD (reconstructed from an second-harmonic generation frequency resolved optical gating measurement [78]), TOD, and FOD compensated pulses along the TL. The peak power evolution with  $\chi_D$  of SC with GDD compensation (black) and the TL SC (red) for the (c) FOD, (d) TOD, and (e) GDD compensated ANDi seed pulses. The onset of WB is plotted in (c) as a dashed vertical line.

that seen from Gaussian or hyperbolic secant pulses, even in the case of a TL ANDi seed pulse.

It is unfortunate, if not surprising, that ultrafast pulses derived from a fiber source around 1060 nm require HOD compensation for clean short pulses, as discussed in Section 2.3. The SC dispersion dynamics developed earlier in this chapter are helpful in explaining why a simple compressor is insufficient. The ANDi pulses come out of the oscillator at  $\sim 5$  ps FWHM, so their accumulated dispersion is  $> 1$  and the  $\sim 100$  fs TL supported bandwidth is sufficient to sample the HOD of the fiber. Fig. 4.5(b) shows ANDi seed pulses with increasing polynomial orders of spectral phase compensation, demonstrating the necessity for HOD compensation to realize a true short pulse with minimum pedestal. Indeed the peak power with GDD and TOD compensation is only 50% of that possible from the TL. Compensating up to Fourth Order Dispersion (FOD) brings the FWHM to 118 fs and the peak power to within 87% of that possible from the 113 fs TL case.

By seeding the fiber propagator with the ANDi pulses in Fig. 4.5(b), we seek to understand how the ANDi seed pulses compare to the simpler sech seed pulses. With FOD compensation, the SC evolution process is quite close to the sech cases studied previously, as seen in Fig. 4.5(c). The peak power enhancement with only GDD compensation of the SC for a FOD compensated ANDi seed pulse occurs with less accumulated dispersion than the SC from a comparable TL sech pulse, e.g. compare Fig. 4.5(c) to Fig. 4.3(a). The slight reduction in the location of the peak enhancement is due to the residual HOD on the incident ANDi seed pulse. This residual HOD on incident ANDi seed pulses, with only GDD and TOD compensation causes an even more dramatic departure in the SC evolution from the sech pulses.

The peak power with compensation below FOD results in an overall reduction in generated SC bandwidths, shown in Fig. 4.5(d) and (e). The TL of the produced SC is comparable to that of a  $\sim 250$  fs sech seed pulses of equivalent energy, e.g. compare Fig. 4.5(d) and (e) to Fig. 4.3(b) and (c), respectively. However, the SC from GDD and TOD compensated ANDi seed pulses experience virtually no peak enhancement effects with only GDD compensation.

Even though the accumulated dispersion length is defined in terms of GDD, it is reasonable to think about the ANDi seed pulses as having  $\chi_D > 0$  at the start of the fiber due to the presence of HOD on the seed pulse. It then follows that the peak enhancement shifts to ever shorter fiber lengths with increasing incident accumulated dispersion (i.e. increasing incident residual HOD). At the extreme, the peak enhancement vanishes, and the SC requires HOD compensation for any fiber length to produce short pulses.

The reduction in SC generation bandwidth and loss of any peak enhancement as a result of HOD present on the ANDi seed pulse shows how critical the ANDi pulse compression is to

SC generation. This is another reason we developed the spectral clipping technique discussed in Section 2.3. By removing the “cat-ears”, we remove all the predominant HOD on the ANDi pulse, allowing nearly TL seed pulses. The improvement in SC generation is two fold then: 1) increasing the compressibility and breadth of the generated bandwidth and 2) reducing the spectral noise in the generated power spectrum by minimizing the temporal pedestal and therefore destabilizing effects of small ANDi spectral mode fluctuations (Section 2.3).

There exists however, another perturbative factor for ANDi seeded SC generation: the non-Gaussian or sech power spectrum. Now, we will look at the qualitative structure of the SC power spectra. Using a different optical fiber than the previous models, we model the nonlinear propagation of pulses through 500 mm of all normal dispersion PCF, NKT Photonic’s NL-1050-NEG-1. The reason we chose this fiber to model is that it has a flattened and reduced dispersion, resulting in remarkably smooth power spectra from a Gaussian seed after significant propagation past WB.

The power spectra for the three TL pulses we model are a Gaussian pulse, a spectrally clipped ANDi pulse (Fig. 2.3(a)), and an un-clipped ANDi pulse (Fig. 2.3(c)). Notice, we are artificially removing all HOD from the ANDi seed pulses to highlight purely power spectra related changes to the generated SC, but as we show in Section 2.3 this is a reasonable approximation for the clipped ANDi pulse. Fig. 4.6 shows the seed power spectra and the SC power spectra at the output of the nonlinear fiber. We set the pulse energy of the clipped ANDi pulse to 4 nJ and then choose the energies of the other two pulses such that all have the same peak power (21 kW), resulting in pulse energies of 3.9 nJ for the Gaussian pulse and 3.2 nJ for the un-clipped ANDi pulse. The duration of the Gaussian pulse was set to coincide with the FWHM of the clipped ANDi pulse of 175 fs.

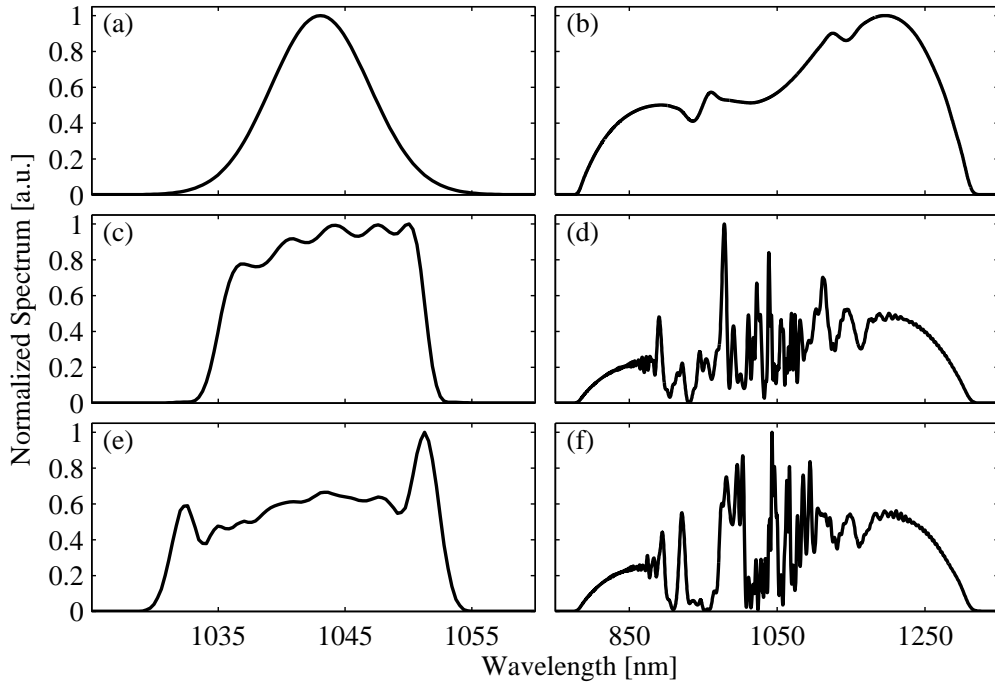


FIGURE 4.6. The normalized power spectra of (a,c,e) seed pulses and (b,d,f) the respective SC after 500 mm of NL-1050-NEG1: (a,b) 175 fs Gaussian seed, (c,d) clipped ANDi, (e,f) whole ANDi. All pulses have the same peak power as the 4 nJ clipped ANDi pulse

The qualitative difference between the SC generated power spectra is large. The Gaussian pulse generates an almost featureless continuum spanning  $> 400$  nm. Inside of the WB generated sidelobes, the SC power spectra from both ANDi pulses is highly structured. The fine structure is highly problematic as it is more sensitive to noise due to small fluctuations in seed energy mapping to small shifts in the peak wavelengths of each spectral modulations.

The cause of all this additional spectral structure are the steep edges in the ANDi power spectrum. These edges cause ringing in the time-domain (temporal pedestal) surrounding the primary pulse peak. With propagation, the temporal sidelobes interfere with the the SC generated power spectrum. The SC power spectral modulations are a mix of beating due to interference between the pedestal and SC and additionally FWM. This structure limits the application space available to SC broadened ANDi pulses. Further work is needed to

appodize the ANDi power spectrum such that there is no secondary temporal structure for the most extreme cases of SC generation.

#### 4.4. CONCLUSION

The introduction of the local and accumulated dispersion/nonlinear lengths have become valuable tools for us in designing nonlinear fiber cocktails and interpreting SC spectral phase. The accumulated dispersion length, in particular, provides a simple explanation for the necessity of a pulse shaper to compress SC generated in fibers with WB. The full study of the spectral phase evolution will serve as a guide for the future design of fiber cocktails.

SC evolution from an ANDi-type laser is also presented. Without compensating for the HOD of the ANDi seed pulses, the generated SC is limited in both bandwidth and compressibility. We also show how the steep sides in the ANDi power spectrum create a much more structured SC power spectrum, potentially limiting their use for nonlinear propagation to more modest spectral bandwidth generation since small noise in the launched ANDi spectra will be amplified in the SC power spectrum.

## CHAPTER 5

# PART I: POLARIZATION INSTABILITIES IN NORMAL DISPERSION SUPERCONTINUUM GENERATION

*In theory, there is no difference between theory and practice. But in practice, there is.*

Yogi Berra

### 5.1. INTRODUCTION

The discussion in Chapter 4 regarding SC generation in the normal dispersion regime assumes fibers with *zero* birefringence. In real fibers, this is an unattainable ideality. We present the discovery that SC generation in all normal dispersion UHNA fibers display a launch power threshold, beyond which the SC is incoherent, a result we published in Ref [26] and which is the basis for this chapter. The level of noise is highly dependent on the launch polarization, indicating even for non-polarization maintaining (PM) fiber the weak, residual stress birefringence plays a critical role in the evolution of SC with propagation. The SC incoherence traces back to a polarization instability driven by this weak intrinsic birefringence in otherwise single mode fibers [102]. Above threshold, polarization modulation instability corrupts the spectral composition of the principal output polarization through energy coupling between the orthogonal polarization modes, even for seed pulses oriented along the effective slow axis of the nonlinear fiber. A combination of low level laser noise and quantum noise from the orthogonal polarization state results in the continuous random fluctuation of the SC output polarization state. Polarization dynamics in birefringent fiber

with pulses launched in the all normal dispersion regime have been widely reported [25, 103–105] however, the reported dynamics primarily deal with the stable coupling of power into spectral sidebands.

Additionally, we observe an instability on long time-scales consistent with thermalization. This suggests that slight temperature drifts change the fiber stresses and perturb the fiber polarization axes, leading to a drift in the polarization state at the fiber output. Moreover, we note that this SC polarization instability produces noise that is highly correlated spectrally. In fact, without directly observing the spectrally-resolved power spectral density fluctuations, the correlated spectral noise averages out in a polarized total power measurement of the SC pulse train leading to a severe underestimation of the total noise.

We discuss the limiting cases of both extremely weak (intrinsic stress-induced) and high (designed) fiber birefringence. We also introduce the spliced fiber “cocktails”, which we use for easy and efficient coupling of seed pulses into the nonlinear PM fiber. The optimal solution for generating stable SC in the all normal dispersion regime is PM nonlinear fibers. SC generated by the PM, nonlinear fiber system exhibits spectral stability comparable to that of the oscillator seed pulse.

## 5.2. WEAKLY BIREFRINGENT NONLINEAR FIBER

The simplest system studied employed the high NA, single mode fiber Nufern UHNA-3. This fiber is both all normally dispersive and highly nonlinear in our spectral operating region. Comparing UHNA-3 to NKT’s PCF NL-1050-NEG1, UHNA-3’s GDD is  $10\times$  greater ( $-110$  ps/nm-km) at 1050 nm,  $10\times$  cheaper, and has comparable mode field diameters at 1050. The fiber cocktail started with a  $\sim 1$  cm length of 1060XP (Nufern) fiber for connecting to the collimator, 1 m of UHNA-3 nonlinear fiber, and then 50 cm of 1060XP exit fiber. The

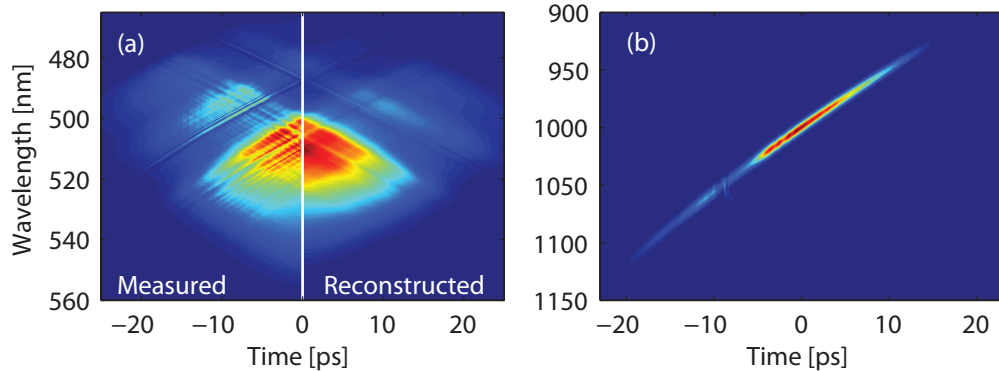


FIGURE 5.1. (a) Phantom SHG-FROG and (b) reconstructed spectrogram

total coupled power efficiency through the fiber is 50%, the splice loss between the nonlinear fiber and the exit fiber is much lower than the entrance splice at -0.3 dB. We use 350 fs transform-limited pulses, generated by a Yb:KYW modelocked oscillator, to seed the fiber cocktail, with a center wavelength of 1027 nm and a power spectrum closely approximating a sech distribution, a repetition rate of 71 MHz, and up to 375 mW of average power coupled into the nonlinear fiber.

We characterized the SC directly out of the fiber using second harmonic generation frequency resolved optical gating (SHG-FROG), using the principal component generalized projection (PCGP) algorithm, which permits the reconstruction of large FROG traces [78]. The large time bandwidth product of the pulse reconstruction required a large vector map to enclose the highly chirped SC ( $2^{13} \times 2^{13}$  for the SHG-FROG presented in Fig. 5.1). The SHG-FROG trace in Fig. 5.1 was captured for SC pulses generated by 200 mW average power coupled through the UHNA-3 fiber cocktail. SHG-FROG traces obtained from unstable laser pulse trains exhibiting stochastic fluctuations in pulse properties does not converge to a unique, low-error FROG reconstruction. Consequentially, reliable FROG reconstructions are a strong indicator of the stability of the ultrafast laser pulse train. The scanning FROG measurement required roughly half an hour to acquire, and its low FROG-error of 0.04

demonstrates the stability of this particular nonlinear broadening system. The described fiber system however, suffered from the unanticipated spectral instability power threshold.

We found experimentally that stable SC were only generated with coupled average powers beneath 200 mw. Fig. 5.2(a) shows a power spectrum time series of stable SC (comparable to the SC shown in Fig. 5.1). Larger coupled powers led to a destabilization in the output polarization state of the generated SC power spectral density making it unusable as a practical source, see Fig. 5.2(a)-(c) for a progression from stable to unstable SC time series.

It is known that in weakly birefringent fiber, polarization modulation instability can lead to coupling between the effective orthogonal polarization modes of the fiber [25, 103–105]. The stability of SC from weakly birefringent fibers is maximized by launching with a pulse polarization orientation that coincides with the highest preserved polarized output power. This corresponds to overlapping the launch polarization with the effective slow axis of the intrinsic, stress-induced birefringence of the fiber. Experimentally, the launch polarization orientation is found by launching at low power and tuning a half waveplate on the fiber launch side and a combination of half and quarter waveplates preceding a polarizer on the collection side of the fiber. To determine the fast axis from the slow axis, we then measured the spectral noise and designated the axis with lower noise the slow axis.

The spectrally resolved noise in the SC power spectrum was measured using an Andor Shamrock spectrometer and Andor iDus detector. Spectra were acquired at 20-100 Hz rates for time intervals ranging from 45-300 minutes. To ensure that this sampling bandwidth fully captured the noise spectrum of the SC de-coherence and depolarization, Relative Intensity Noise (RIN) measurements of the polarized output SC were captured with a photodiode

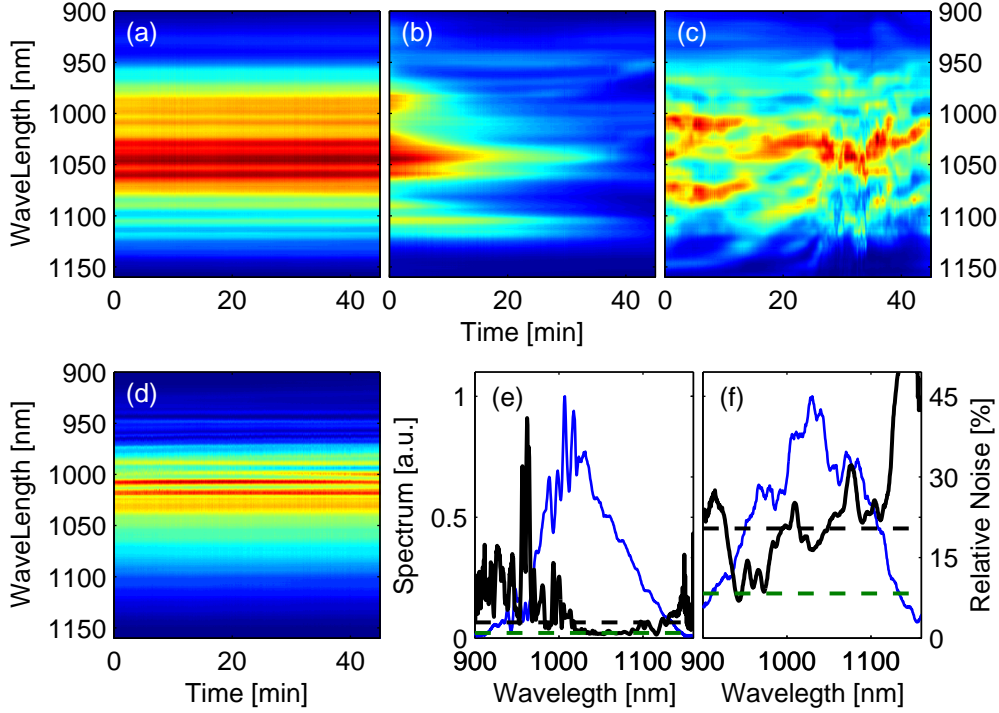


FIGURE 5.2. SC time series for (a) 200 mW, (b) 300 mW, (c) 375 mW, and (d) 300 mW (after 4.5 hours of fiber warm-up) coupled power in UHNA-3. The mean power spectrum (blue), RSN (solid black),  $\Phi_{\text{RSN}}$  (dashed black), and RMS-N (dashed-green) in (e) and (f) from the time series (b) and (c), respectively.

placed at the focal plane of a spectrometer. The RIN measurements demonstrated that the noise spectrum was limited to  $< 20$  Hz.

We define the depolarization as the fraction of the power coupled into the polarization mode orthogonal to the launch polarization:  $P_{\perp}/(P_{\perp} + P_{\parallel})$ , where  $P_{\parallel}$  is the launch polarization. The amount of depolarization is the most easily measured indicator of the stability of the SC power spectrum, as empirically we have found that all other spectral noise parameters increase with increasing depolarization. We will also use the root-mean squared noise (RMS-N), relative spectral noise (RSN), and total spectral noise ( $\Phi_{\text{RSN}}$ ) defined in Section 2.2.

At low power, 200 mW, the depolarization is 25%, even though the SC is very stable as seen in the Fig. 5.2(a) power spectrum time series. The RMS-N and  $\Phi_{\text{RSN}}$  of the laser seed was 0.6% and 1% respectively, over the 45 minute measurement interval (and is typical for all subsequent measurements). The seed RSN is smooth across the spectrum, free of any spectral mode shape changes. The SC RMS-N is 1% over the 45 minute time interval, just above the seed noise. The  $\Phi_{\text{RSN}}$  is in close agreement to the RMS-N at 1.5%, indicating a high spectral stability.

Above 200 mW, the SC is subject to extremely long thermal equilibration times. At 300 mW, the total integrated power decays (nearly linearly) through the first 45 minute measurement; losing 75% of the polarized coupled power to the orthogonal mode, shown in Fig. 5.2(b). The RMS-N for the 45 minute interval would therefore be huge, but less meaningful since it would just be a measure of warm-up dynamics not an equilibrium stability. After 4.25 hours of warm-up and re-tuning the exit waveplates, the SC has improved from the decaying time series of Fig. 5.2(b) to Fig. 5.2(d). Not only is the SC more stable but the mean power spectrum in Fig. 5.2(e) also takes on the roughly triangular form expected from numerical propagation models of the generalized nonlinear Schrödinger equation (Section 4.2 [28]). The depolarization settles to 27% and the RMS-N stabilizes to 1% for both 1 and 45 minute intervals. The RSN for 1 minute intervals is  $\sim 3\times$  less at the peaks than for the full 45 minute interval. While the long time interval RSN has large features (solid black line in Fig. 5.2(e)), the large RSN fluctuations ( $> 10\%$ ) are isolated to regions of low power spectral density as evidenced by the small  $\Phi_{\text{RSN}}$  at 1% and 3% for 1 and 45 minute measurements respectively. The small difference in RSN-N and  $\Phi_{\text{RSN}}$ , dashed green

and black lines in Fig. 5.2(e) respectively, indicates a maintained spectral stability after sufficient thermalization.

At 375 mW there appears to be a phase change, as seen in the Fig. 5.2(c) power spectrum time series. Above this threshold, spectral components continuously drift between the orthogonal polarization modes and do not stabilize, even on timescales of many hours. The spectral fluctuations are highly co-/anti-correlated across the spectrum, resulting in the rough preservation of the total integrated power in the output polarization mode. The RMS-N averages only 1% for any 1 minute interval and 8% for the full 45 minutes, dashed green line in Fig. 5.2(f). The depolarization is around 50%, fluctuating with the RMS-N. The RSN is everywhere higher for the respective 1 and 45 (solid black line in Fig. 5.2(f)) minute intervals. The  $\Phi_{\text{RSN}}$  is also markedly higher than the RMS-N at 3% and 20% for 1 and 45 (dashed black line in Fig. 5.2(f)) minute time intervals, respectively.

In this unstable regime, measurements of the full beam on a photodiode would be an inadequate measure of the SC stability. Significant amounts of spectral noise are masked by the highly correlated nature of the spectral fluctuations, as seen in the  $2.5\times$  higher  $\Phi_{\text{RSN}}$  over the 45 minutes interval compared to the RMS-N. Shorter time-scale measurements of stability are also misleading as the RSN,  $\Phi_{\text{RSN}}$ , and RMS-N are dramatically lower for short time windows. In contrast with the 300 mW case, this is not a thermal relaxation issue. We measured spectra for 4.5 hours without ever seeing a change from the continuously evolving spectra of Fig. 5.2(c).

Our experiments also indicate that this instability threshold is not explainable as fiber degradation. The same fiber repeatedly returns to the same spectra below threshold after prolonged pumping above threshold. Also the highest coupled average powers are well below

the damage threshold reported for these fibers in Ref [106]. This destabilization transition sets a sharp limit on the power that can be used for a SC-broadened source. In order to scale to higher average power SC sources with normal dispersion fibers, a larger and more stable fiber birefringence is required.

### 5.3. STRONGLY BIREFRINGENT NONLINEAR FIBER

In strongly birefringent fibers, the large contrast in orthogonal indices of refraction eliminates the phase-matching condition that gives rise to the polarization modulation instability. While attempts have been made to induce birefringence through high stress levels [25, 107], the optimal solution is PM, all normal dispersion, nonlinear optical fiber. In the absence of such a PM nonlinear fiber, one can potentially induce enough asymmetrical strain in the fiber to create strong birefringence. Tu et al. used a pinch plate along a 27 cm length of PCF fiber and largely eliminated the polarization modulation instability defects from the measured power spectrum and reduced the depolarization from 60% to 20% [25]. For fibers where longer lengths and WB are desired, a small expandable spool could be employed. We found mixed results with this strategy using 1 m of UHNA-3 wrapped onto a 12 mm diameter spool and 2 – 4% strain. We were able to reduce the depolarization from 26% to 20% at 300 mW average power, in comparison to Fig. 5.2(d) and (e). It was unclear however, if this was not purely a result of thermal relaxation after significant fiber warm up time.

Fibers with designed high birefringence disallow polarization modulation instability and therefore polarization instabilities for seeds aligned to the slow axis. The polarization eigenaxes of such a PM fiber are also insensitive to the environmental perturbation seen in stress induced birefringent fibers: thermal relaxation and long-term strain relaxation.

CorActive offers a suitable, commercially available, UHNA PM-nonlinear fiber: SCF-UN-3/125-25-PM. Theoretically, the strong birefringence should eliminate polarization modulation instability; however, a direct comparison between the CorActive and Nufern UHNA-3 fibers is limited by the fact that the CorActive fiber nonlinearity is 40% of the Nufern value, due to the lower confinement in the larger CorActive core.

We tested the SC stability from the CorActive PM UHNA fiber with a long fiber cocktail: 12 mm Panda-type fiber and 2 m of nonlinear PM fiber. At 375 mW average power coupled into the PM nonlinear fiber cocktail, the SC depolarization is 10% and required no thermal equilibration time. The stable time series is shown in Fig. 5.3(a). The RMS-N averages 0.3% over any 1 minute interval and 0.7% for the full 45 minute measurement (Fig. 5.3(b) dashed green line). The RSN (Fig. 5.3(b) solid black line) is  $< 1\%$  across the power spectrum for both 1 and 45 minute intervals, and the  $\Phi_{\text{RSN}}$  is close to the RMS-N at 0.5% and 0.8% for 1 and 45 minute (Fig. 5.3(b) dashed black line) intervals respectively, a tremendous improvement over the SC from the non-PM UHNA fiber.

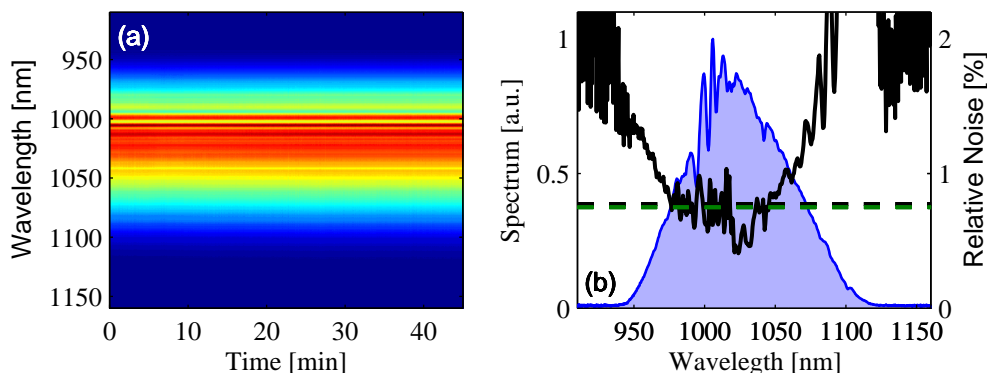


FIGURE 5.3. (a) SC time series and (b) power spectrum (blue), RSN (solid black),  $\Phi_{\text{RSN}}$  (dashed black), and RMS-N (dashed-green) from a 45 minute time interval from Yb:KYW oscillator seeds and 375 mW coupled power.

#### 5.4. CONCLUSIONS

We identify a polarization instability in the generation of SC in weakly birefringent, all normal dispersion, UHNA fiber. Unlike previous work regarding polarization modulation instability, we focus on the temporal dynamics of the instability. We report an instability power threshold, above which, the output SC's spectral polarization state is seeded from noise. Large fluctuations in power spectral density within the analyzed output polarization are highly correlated which masks the magnitude of the spectral instability when characterized by the total integrated power. The use of a PM, all normal dispersion, optical fiber eliminates the spectral instability when seed pulses are oriented along the slow axis of the fiber.

## CHAPTER 6

# PART I: NONLINEAR PULSE COMPRESSION SYSTEMS AT 1060 NM: ROUTES TO COMPRESSING THE BROADENED OPTICAL POWER SPECTRA

*I wish I had an answer to that because I'm tired of answering that question.*

Yogi Berra

### 6.1. INTRODUCTION TO NONLINEAR PULSE COMPRESSION

Unlike the canonical ultrafast laser, a modelocked Ti:sapphire laser, Yb-doped lasers lack the exceptional gain bandwidths to readily produce sub-20 fs pulses. In fact, outside of state-of-the-art Yb-doped systems both bulk and fiber based, pulse durations more typically range from 60–200 fs full-width-half-max (FWHM). Two such systems produce pulses down to 32 fs FWHM from a bulk oscillator [23] and 22 fs FWHM from a 915 nm pumped ANDi fiber laser [24], but they are limited in pulse energy to 0.9 nJ and 0.17 nJ, respectively.

Fortunately, the tight mode field confinement of ultrafast pulses in optical fiber is a ready means of increasing the spectral bandwidth of a Yb-doped fiber oscillator by nonlinear propagation [28, 29] for the purposes of nonlinear pulse compression [25–27]. But, unless the nonlinear fiber lengths are kept exceptionally short or only modest lengths of dispersion-decreased photonic crystal fiber are used, higher-order spectral phase severely limits the compressibility of these pulses; keeping the compressed duration far above the bandwidth supported transform-limit (TL) [26].

The higher-order dispersion (HOD), particularly third-order dispersion (TOD), imparted by spectral broadening in optical fiber is quite difficult to eliminate, but without compensation the additional spectral bandwidth is un-utilized. The problem with traditional grating compressors is that they possess the wrong sign between GDD and TOD: typical normal dispersion bulk material at 1060 nm is +GDD and +TOD and grating compressors are -GDD and +TOD [76].

Prism pair compressors do, in fact, have the appropriate relative sign between GDD and TOD to compensate for material dispersion, and for cases of phase compensation of small lengths of bulk optics can reach fourth-order dispersion (FOD) limited intensity profiles [92]. The possible intraprism length, or prism insertion length, is what limits prism compressors from compensating for arbitrary ratios GDD and TOD, since prisms have a finite aperture size.

Pulse shapers can compensate for pseudo-arbitrary spectral phase [62, 63, 27], but are limited in the total magnitude of phase they can impart. Pulse shapers are also not always an economical solution. Another method of compensating for TOD, in addition to GDD, is a grism [108, 109, 76]: an optical element formed from a grating and a prism. The grism design parameters allow for the selection of the relative ratio and sign between GDD and TOD. The primary limitation of grisms is their lack of commercial availability, and the efficiency of the diffraction grating necessary to achieve the right GDD:TOD ratio for prisms of standard optical glasses.

And lastly, the nonlinear fibers themselves pose challenges. The first challenge is the divide between nonlinear fiber propagation in the presence of normal or anomalous dispersion. Launching energetic seed pulses into fibers in a predominantly anomalous dispersion regime

initiates a complex series of soliton driven dynamics. These soliton dynamics put strict limitations on the pulse energy and duration to maintain the coherence in the generated supercontinuum (SC) [28]. Using optical fibers that are all normal dispersion eliminates the soliton-driven seed pulse energy/duration restrictions [29], but instead there is a polarization instability threshold (Chapter 5)[25, 26].

Preserving the polarization state during nonlinear propagation through the optical fiber is the second optical fiber challenge. So there are several routes one might take with regard to preserving the polarization state during the nonlinear propagation through the optical fiber: (1) non-polarization maintaining, highly nonlinear optical fibers and low pulse energies; (2) polarization-maintaining (PM), highly nonlinear optical fibers and medium pulse energies; (3) or PM, telecom-like, and therefore normally dispersive optical fibers and high pulse energies (where we have lumped large mode area fibers into the telecom-like category). The limiting factor in route (1) in the normal dispersion region is polarization mode instability, discussed in detail in Chapter 5, where the polarization instability threshold in normal dispersion fibers is much higher than the soliton-based restrictions in anomalous dispersion fibers. For route (2), PM highly nonlinear fiber is not only limited in availability but also has a much lower damage threshold than telecom fibers [106], where we have seen empirically a reduction in the polarization maintenance of PM ultrahigh numerical aperture optical fibers (solid core and cladding) at average powers of  $< 500$  mW. Similarly, we have heard anecdotal reports of PM-damage well below the optical fiber damage threshold for PM PCF nonlinear fibers as well. Leaving route (3) as the only option when designing a system for high average powers. Route (3) consists of the least nonlinear group of fibers, so to generate comparably

broad power spectra as is possible from route (2), for example, much higher pulse energies are necessary.

## 6.2. OPTIMAL FIBER COUPLING VIA FIBER “COCKTAILS”

End coupling (focusing into a suspended, cleaved optical fiber face) is often used to launch laser pulses into PCF and high numerical aperture (NA) fibers. End coupling is an unreliable method of fiber coupling because it is subject to optical degradation of the end face and coupling drift due to tight coupling tolerances on beam size and alignment. These sensitivities and damage mechanisms lead to challenges for long-term stable operation of SC fiber sources. To avoid end-coupling into high NA fibers as well as to improve the long-term experimental stability, we have designed a fiber cocktail system that provides long term coupling stability in addition to ease of implementation. Splicing high NA optical fiber to standard optical fiber ( $\sim 7$  micron core), leverages the ease of coupling pulses into standard fiber using commercially available aspheric collimators and the back-reflection eliminating angled-physical contact (APC) connectors to easily, efficiently, and robustly get light into the nonlinear fiber. We connectorize the fiber cocktail to keep the entrance fiber (the standard fiber) short (5-10 mm). Splices between the standard fiber and UHNA fiber are robust and relatively low loss ( $< 1$  dB optical fibers with  $\sim 50\%$  mismatch in mode-field diameter). The total coupling efficiency into the nonlinear fiber is typically  $> 50\%$  (depending on the fiber cocktail) and often as high as 70%, which is a significant improvement over typical reported coupling efficiencies using objectives (or aspheres) and bare fibers [98]. The connector/collimator unit also serves to protect the fiber face as well as minimizing coupling loss due to fiber drift. For applications involving short pulse compression, the

output would ideally be directly from the nonlinear fiber, connectorized and collimated by another aspheric collimator or an off-axis parabolic mirror collimator.

Systems involving only telecom-like optical fibers are much simpler, since no intermediate optical fiber is needed. Such systems just use short, custom patch-chords with APC connectors. In both fiber system types, the APC style connector greatly reduces back-reflections.

### 6.3. NONLINEAR PULSE COMPRESSION WITH AN ANDI LASER AND A HYPER-PRISM COMPRESSOR

In this section, we demonstrate a basic version of nonlinear pulse compression. The pulse compression ratio is  $\sim 2\times$  using large-mode area fiber and a prism compressor. The efficiencies in the system are such that the peak power of the nonlinearly compressed pulse is in fact, a bit higher than the seed pulse. The major benefits of this system are its low cost and simplicity in components.

To compress the broadened power spectra, we utilize a specialized prism compressor built in a hyper-prism geometry [110], where each prism is double-passed. Fig. 6.1 is a reference schematic of the hyper-prism compressor. Usually, the second pass through a prism collimates the dispersed beam, here the second pass is anti-parallel to the usual geometry increasing the angular dispersion.

This compression scheme was born from the inability to otherwise compensate for the residual TOD of fiber broadened power spectra, limiting the pulse durations above the TL durations supported by the largest spectral bandwidths that we can generate. Preliminary modeling indicated a prism compressor could compensate for the measured residual TOD, but only for very large prism insertions. As opposed to ordering a custom large-format prism, we instead conceived of the hyper-prism design in Fig. 6.1. The hyper-prism configuration

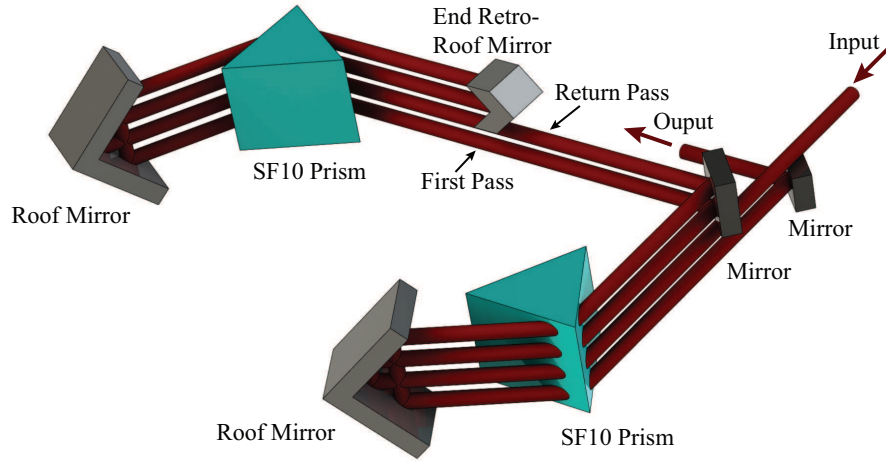


FIGURE 6.1. Hyper-prism schematic

also has the effect of roughly doubling the angular dispersion of the beam after double-passing each prism, which effects a  $\sim 4\times$  increase in the GDD allowing for a much shorter prism separation. The limitation here, is the clear aperture of the second prism which prevents endless prism insertion lengths and arbitrarily large GDD compensation.

To generate the broadened power spectra, the pulses described in Section 2.3 are injected into a  $10\ \mu\text{m}$  core, large-mode area fiber 150 mm in length with 83% coupling efficiency, resulting in  $\sim 12\ \text{nJ}$  of coupled pulse energy. The output pulses are then compressed in a hyper-prism compressor. The resultant pulses measured with second-harmonic generation frequency resolved optical gating [78] are shown in Fig. 6.2. The highest peak power pulses achieved are 116 kW in a 10 nJ, 72 fs pulse, Fig. 6.2(c,d), from a 17 nJ, 160 fs seed pulse with 88 kW of peak power (including the combined the 83% fiber coupling and 80% hyper-prism compressor!). As we have seen elsewhere (Section 2.2 and Section 4.3), failure to fully compress the un-clipped ANDi spectra results in a reduction in the system performance, in spite of the broader initial seed bandwidth. The compressed pulse energies for the pulses shown in Fig. 6.2(a)/(b) and (e)/(f) are 11.5 and 9 nJ, respectively.

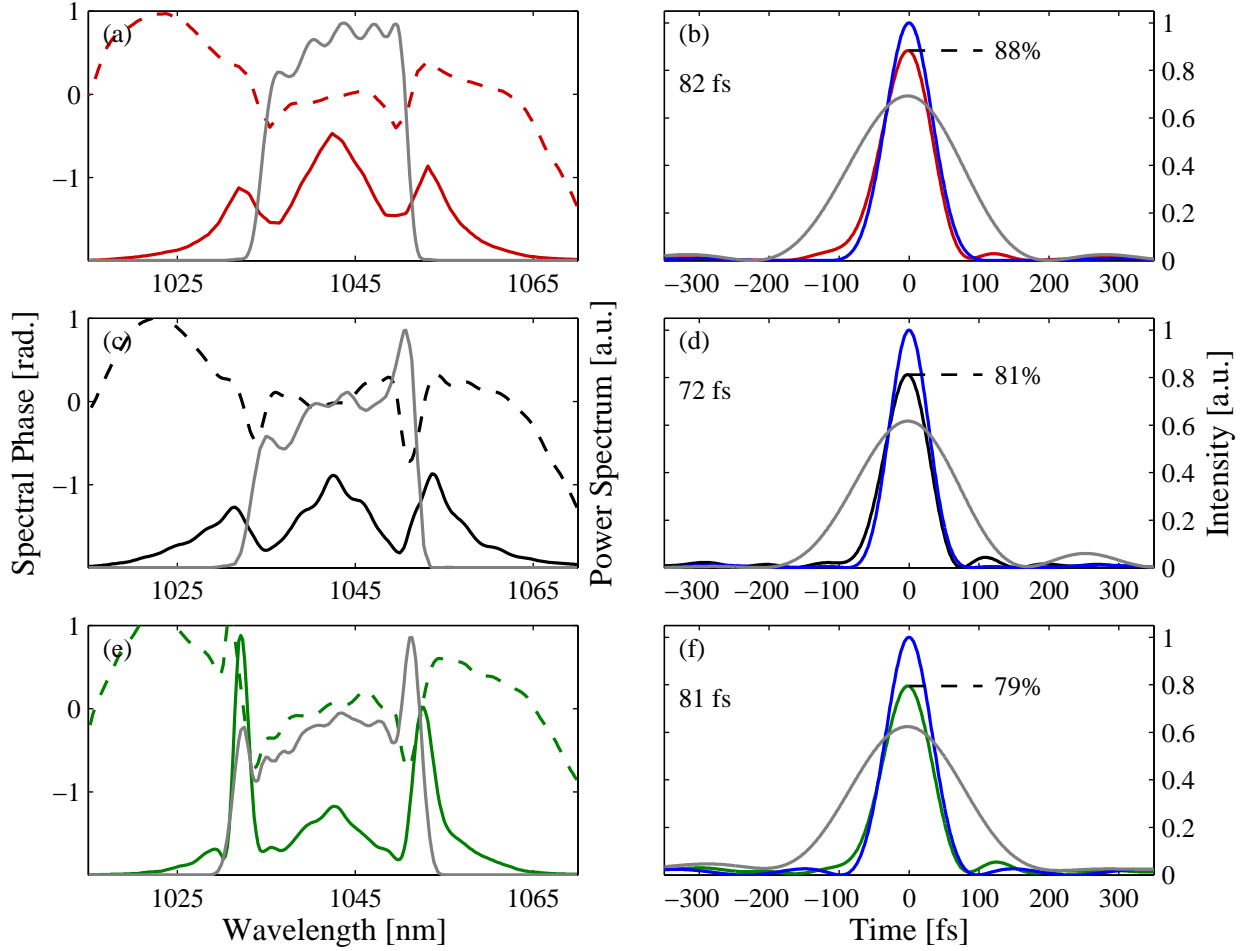


FIGURE 6.2. Nonlinear pulse compression for a series of ANDi pulses: (a,b) high spectral clipping (red), (c,d) medium spectral clipping (black), and (e,f) no spectral clipping (green). (a,c,e) show the seed power spectra (gray), broadened power spectra (solid), and residual spectral phases (dashed). (b,d,f) show the intensities of the seed pulses (gray), compressed pulses, and the bandwidth supported TL pulses (blue)

While the peak power enhancement is relatively minor (116 vs. 88 kW), the reduction in pulse duration from 160 fs to 72 fs has a huge potential to increase the generated nonlinear signals for applications such as multi-photon microscopy. As discussed in Section 2.3, the nonlinear signal will scale as  $g_N$ , where  $g_N = \frac{\int I_1^N dt}{\int I_2^N dt}$ ,  $I$  is the pulse intensity, and  $N$  is the order of the nonlinear process. In microscopes interrogating biological media, the damage threshold of the sample limits the total micro-illumination average power well below the average power of these sources, meaning the illumination average power for the ANDi pulse

and the nonlinearly compressed pulse would be equivalent. In the case of equivalent average power, the increase in nonlinear signal for the 72 fs pulse (Fig. 6.2(c) and (d) black-curves) relative to its 160 fs seed pulse (Fig. 6.2(c) and (d) grey-curves) and the un-clipped ANDi pulse (Fig. 6.2(e) and (f) grey-curves) would be  $2\times$  and  $3\times$  for an  $N = 2$  nonlinear process and  $4.4\times$  and  $9\times$  for an  $N = 3$  order process. What we can say then, for these non-Gaussian pulses a second-order nonlinear signal will increase linearly in pulse duration reduction when both pulses have a high percent compression. Reducing the pulse duration and increasing the percent compression yields still further gains in nonlinear signal level.

#### 6.4. NONLINEAR PULSE COMPRESSION WITH A PULSE SHAPER IN THE NAIVE LIMIT

We will use this section, as a case study of how you might naively go about constructing a nonlinear pulse compression system with a pulse shaper. This effort, our first pulse shaping effort [26], highlights some of the features characteristic of the nonlinear pulse compression systems that we work with: an optimal free-space to nonlinear fiber coupling strategy discussed in Section 6.2, compression factors  $> 2\times$ , appreciable amounts of HOD, and sensitivity to spatio-spectral aberrations (spatial chirp, angular chirp, etc.). Notably, the results of this first pulse shaping effort illustrate how a naive approach to the optical systems involved produce limited results.

One of the primary goals of nonlinear fiber broadening is the production of compressed pulses much shorter than the seed pulse, which more effectively drive subsequent nonlinear optical interactions. As discussed in Section 4.2, nonlinear fibers with sufficient length for optical wave-breaking (WB) require a pulse shaper to completely compensate the complex spectral phase. Propagation well beyond the onset of WB leads to spectral phases with

significant amounts of HOD, because the pulse propagation at this point is specifically dispersion dominated. So, the length for the onset of WB also represents when a nonlinear pulse compression system will begin to require a pulse shaper or some other form of HOD compensation. The attraction of WB is the smoothing effect it has on both the power spectrum and the spectral phase, yielding somewhat shorter pulse durations and a reduction in the bandwidth dictated temporal pedestal.

The fiber system used in this example contains a 12 mm Panda-type entrance fiber, 25 cm CorActive's PM nonlinear fiber, and 13 mm of a custom Nufern PM fiber similar to UHNA-4 all spliced together. The custom Nufern PM fiber had the appropriate cladding size for APC connectorization and minimized losses at the splice compared to standard core-sized PM fibers (the CorActive cladding is unfortunately just over the standard 125 microns). The length of nonlinear fiber is much greater than the WB threshold, determined experimentally by the presence of WB/four-wave mixing sidebands in the power spectrum measured directly out of the fiber (Fig. 6.3 black-dashed, the WB/four-wave mixing sidebands occupy roughly all the spectra outside of 990–1075 nm and in the plot appear just as the sides of the power spectrum due to being filled in). We were unable however, to obtain specific dispersion data for the CorActive fiber to calculate the length for the onset of WB. The fiber length was kept short to aid in pulse compression by reducing the opportunity for a broad spectrum to sample the fiber dispersion map. The total transmission of the short pulse fiber is 48%.

For our particular short pulse fiber, the large group-delay dispersion (GDD) overwhelms the dynamic range of our spatial light modulator (SLM), so we had to add a grating compressor to the output of a  $4-F$  pulse shaper. This is unfortunate as the secondary compressor reduces the transmission efficiency of the total system. Consequently, this also begins to hint

at the potential false narrative about pulse shapers: that they are a cure all for virtually any pulse duration issue.

The pulse shaper was calibrated using the in-line spectral interferometry technique [63]. As our modulator is designed and coated for operation in the Ti:sapphire spectral region, we suffer from a thin-film dispersion resonance in the AR coating of the modulator in the region of 1050 nm. Errors in the calibration of the shaper response, introduced by the thin-film coating resonances, prevented a direct inversion of the spectral phase recovered from an SHG-FROG reconstruction to quickly obtain TL pulses, as is possible when the resonances are absent.

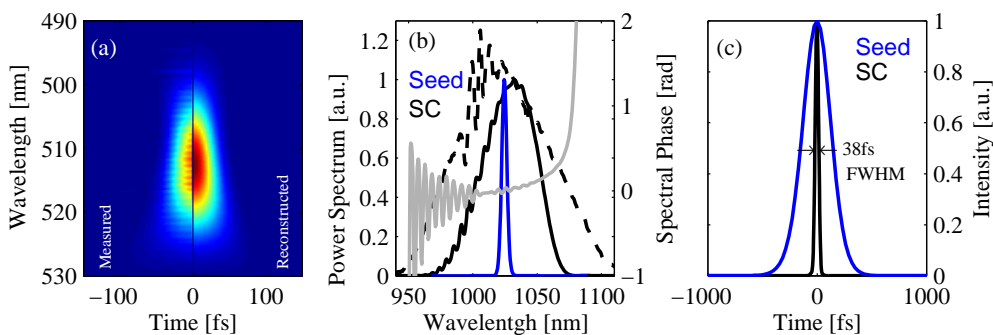


FIGURE 6.3. (a) The Phantom SHG-FROG, (b) the SC reconstructed power spectrum (black), the SC power spectrum out of the fiber (black-dashed), and spectral phase (grey), and seed power spectrum (blue). (c) The normalized seed intensity (blue) and the reconstructed SC intensity after a two stage compression system.

With most of the GDD eliminated by the grating compressor, an SHG-FROG measurement determined an initial phase mask to apply to the pulse shaper. We then used a simple genetic algorithm to improve the  $2\pi$ -wrapping points and secondarily too improve the shape of the phase mask itself. The resulting pulse is shown in Fig. 6.3(a)-(c), with remnants of the phase mask itself. The resulting pulse is shown in Fig. 6.3(a)-(c), with remnants of the  $2\pi$ -wrapping point error seen in the rippling power spectrum and spectral phase in Fig. 6.3(b).

The power spectrum directly out of the fiber, supporting a 20 fs pulse, is broader than the spectra we reconstruct from an SHG-FROG trace. This is not a phase-matching limitation in the Type-I KDP crystal, as we previously measured a broader bandwidth SC pulse (see Fig. 5.1) with the same SHG-FROG apparatus.

Even with the lost power spectral wings, the reconstructed pulse, with 0.004 FROG error, is 37.6 fs FWHM, compared to a bandwidth supported TL of 36 fs FWHM. The  $9\times$  compression ratio is shown in Fig. 6.3(c). SHG-FROG is an excellent means of characterizing pulses for this reason, it demonstrates the actual spectral bandwidth one might deliver to the focus of a nonlinear experiment.

When this compression experiment was first conducted, we suspected two major contributing factors to the lost spectra: spatial chirp from the pulse shaper and wavefront error introduced by the SLM modulator. The SLM is a 2005 model Cambridge Research Inc 640 pixel unit, that exhibits a wavefront error of  $> 3\lambda$  when double passed.

We realized however, the  $4-F$  Martinez imaging system, which is the back-bone of the pulse shaper, severely deviates from a paraxial system. Pulse shaping with transmissive optics (beyond the naive limit) is the focus and motivation of our published paper Ref [27] and Chapter 7. Briefly, by carefully modeling the  $4-F$  Martinez imaging system in Zemax, we discovered that using a single achromatic doublet lens will impart substantial field curvature to the angularly dispersed spectral bandwidth. It is the field curvature that dominates all other aberrations, where the wings of the spectral line focus at the joint Fourier plane of the Martinez are out of focus by  $\sim 10\times$  their respective Rayleigh lengths. The field curvature is thus responsible for the diminished spectral bandwidth at the focus of the SHG-FROG measurement.

TABLE 6.1. The nonlinear coefficients ( $\gamma_0$ ), group velocity dispersion ( $\beta_2$ ), dispersion coefficient ( $D$ ), and the third-order dispersion ( $\beta_3$ ) at 1060 nm of fused silica and several all normal dispersion optical fibers.

Fiber	$\gamma_0$ [1/(W m)]	$\beta_2$ [fs <sup>2</sup> /mm] / $D$ [ps/(nm km)]	$\beta_3$ [fs <sup>3</sup> /mm]
bulk Fused Silica	n.a.	16.8 / -28.1	39
LMA-PM-10	0.002	15.0 / -25.3	47
SMF 6 $\mu$ m MFD [111]	0.004	23.0 / -39	25
LMA-PM-5	0.009	11.0 / -18.6	54
UHNA3	0.029	66.9 / -112.4	-51
NL-1050-NEG1	0.037	6.8 / -11.3	-33

In the absence of such large field curvature the system could have achieved nearly twice the compression factor as realized at the time, or  $17\times$ . As we demonstrate in Chapter 7, the effort to design flat-field pulse shapers can be quite fruitful, resulting in  $< 20$  fs pulse durations while maintaining high transmission efficiency.

## 6.5. NONLINEAR PULSE COMPRESSION BEYOND THE NAIVE LIMIT

In the previous sections, we looked at two particular cases of nonlinear pulse compression. One with modest bandwidth generation and a prism compressor achieving a  $\sim 2\times$  compression factor and a second requiring a pulse shaper but achieving a  $9\times$  compression factor. The latter we used to illustrate how these systems can deviate from paraxial behavior in a problematic manner. We would like to conclude this chapter with a broader discussion on the nonlinear pulse compression landscape.

There are as many possibilities as there are pulses and optical fibers. As a starting point, we show in Table 6.1 the nonlinear and dispersion properties for a sampling of the commercial fibers one might use to broaden the power spectrum of a 1060 nm pulse. Depending on the actual combination of pulse and fiber, as discussed briefly in Section 6.4 and in detail in Section 4.2, the compression system necessary to generate nearly TL pulses will depend on the total fiber propagation length beyond WB. We show in Fig. 6.4 the onset of WB lengths

for 200, 150, and 100 fs Gaussian seed pulses with 5 to 25 nJ of energy for 4 of the optical fibers in Table 6.1. Fig. 6.4 also shows the TL durations supported by the SC at these predicted WB lengths. Very interestingly, we see that though the UHNA3 fiber has a  $3\times$  higher nonlinearity than the LMA-PM-5 PCF, it's much larger dispersion causes the spectral broadening in the LMA-PM-5 PCF to exceed that from the UHNA3 for fiber lengths limited to the WB onset lengths.

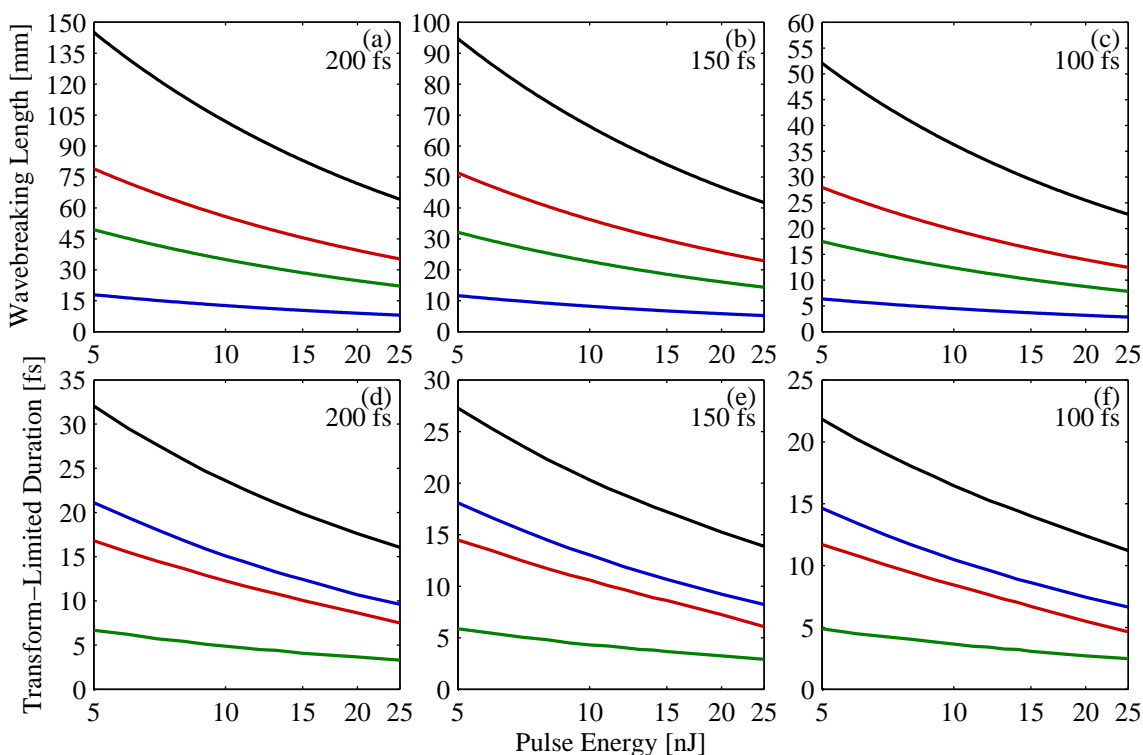


FIGURE 6.4. (a-c) WB lengths for SC generation in normal dispersion optical fiber and (d-f) the TL pulse durations supported by the SC generated by propagation up the WB lengths for (a/d) 200, (b/e) 150, and (c/f) 100 fs FWHM Gaussian seed pulses as a function of pulse energy for LMA-PM-10 (black), LMA-PM-5 (red), NL-1050-NEG1 (green), and UHNA3 (blue) optical fibers.

A general scaling relationship for the onset of WB length is found using Eqn.s 4.3, 4.2, and approximating the pulse peak power as  $P_0 = E/T_0$  where  $E$  is the pulse energy and  $T_0$

is the pulse width:

$$(6.1) \quad z_{\text{WB}} \propto \sqrt{\frac{T_0^3}{\beta_2 \gamma_0 E}}$$

where  $\beta_2$  is the fiber group velocity dispersion and  $\gamma_0$  is the fiber nonlinear coefficient. As you can see from Eqn. 6.1 and Fig. 6.4, the WB onset length is most sensitive to the pulse duration which represents both the power spectral bandwidth and the pulse peak power (i.e. the presence of any chirp on the seed pulse). The other parameters ( $T_0$ ,  $\beta_2$ , and  $\gamma_0$ ) are equally weighted, which is a rather interesting reduction.

This scaling relation can guide the design of new systems. For example, using the seed pulses in Section 6.3 (Section 2.3 (a)) with 15 nJ of energy coupled into the LMA-PM-5 PCF, we would need to keep the fiber length below 37 mm to prevent WB. While Fig. 6.4, Eqn. 4.3, and Equations 6.1 more generally presume pulses with smooth spectra (Gaussian or hyperbolic secant), the 37 mm estimate for WB is quite close to the numerically modeled length of  $\approx 34$  mm (see Appendix A for model details). Adding  $3 \cdot 10^3$  fs<sup>2</sup> of GDD to the pulse to reduce the duration to 188 fs from the TL of 175 fs has the desired effect of pushing the onset of WB back to 37 mm ( $37 = (188/175)^{1/3} \cdot 34$ ), in agreement with the scaling approximation.

When trying to design a new broadening and compression system, we have come to find the mantra, “everything matters” to be a concise summary of what details need to be addressed. The total net bandwidth generated in fiber will depend on all the factors discussed above. The approximation  $P_0 = E/T_0$  in in Eqn. 6.1 is only accurate for nearly TL pulses, and so is not an accurate predictor of how adding large chirp to the pulse will cause changes in the WB onset length. However, between the Fig. 6.4 and Eqn. 6.1, an

outline of the fiber/pulse combinations for nonlinear pulse compression landscape begins to come into focus.

## CHAPTER 7

# PART I: NEARLY TRANSFORM-LIMITED SUB-20 FS PULSES AT 1065 NM AND $>10$ nJ ENABLED BY A FLAT FIELD ULTRAFast PULSE SHAPER

*If opportunity doesn't knock, build a door.*

Milton Berle

### 7.1. OUR FLAGSHIP NONLINEAR PULSE COMPRESSION SYSTEM

The goal of this work was to design a nonlinear pulse compression system with power spectral bandwidths beyond the typical Yb-ion gain bandwidth while maintaining high pulse energies (10 nJ). Our seed source is nonlinear fiber amplifier described in Chapter 3 [83] seeded by a Yb-doped all normal dispersion (ANDi) fiber oscillator [4]; generating 100 fs pulses with highly stable temporal features. Due to the high pulse energy and the fiber/pulse restrictions outlined in Chapters 5 and 6, we utilize a relatively low-nonlinearity, all normal dispersion, polarization-maintaining (PM) fiber with a 10  $\mu\text{m}$  core: Leikki Passive-10/125-PM fiber. The nonlinear propagation of these high energy and short duration seed pulses in the PM 10  $\mu\text{m}$  core optical fiber is such that it allows for a short length of optical fiber (142 mm which is 2–3 $\times$  the fiber length for the onset of optical wave-breaking). For long term stability, the 10/125-PM fiber has angled physical contact connectors; commercial aspheric lens collimators with connector receptacles couple the pulses into and out of the optical fiber. The power transmission efficiency through the fiber is 84%. The power spectral bandwidth

out of the fiber supports TL durations from 100 fs down to 19 fs FWHM, based on the seed pulse chirp.

The pulses out of the fiber have a group delay dispersion of 1000's fs<sup>2</sup>, with significant amounts of higher-order dispersion. The most common tool to compensate such complicated spectral phase is a 4- $F$  Martinez compressor with a liquid crystal spatial light modulator (SLM), termed a pulse shaper; allowing semi-arbitrary spectral phase compensation [62, 63]. Other nonlinear pulse compression systems around 1060 nm have used pulse shapers to produce nearly TL pulses [112, 97]; reaching durations as short as 6.4 fs [97]. These systems, however, have low transmission efficiencies (< 20%) due to the use of diffraction gratings with low ruling densities to allow for long focal length reflective optics. The key technology we introduce here is a high efficiency pulse shaper using a Plössl lens with up to 80% transmission efficiency. The total nonlinear pulse compression efficiency of our system is 66%, including both fiber and pulse shaper losses. This hardware was first published in Ref.s [113, 27], the latter of which forms the basis for this chapter.

## 7.2. PETZVAL FIELD CURVATURE IN PULSE SHAPERS

Our pulse shaper has three primary design parameters: large spectral bandwidth, high transmission efficiency, and a small SLM active area. The latter two requirements are based on the availability of commercial components. We are partial to the broad bandwidth, high diffraction efficiency, and inexpensive 1000 l/mm transmission gratings from LightSmyth Technologies and a 1x12,288 pixel SLM by Boulder Nonlinear Systems (19.66 mm active area). These two components plus a broad bandwidth pulse necessitate a fast focal length optic.

There is a fundamental difference when designing pulse shapers for 1060 nm than at 800 nm: the bandwidth in wavelength (referred to here as the spectral bandwidth) scales as  $\lambda_0^2$ , where  $\lambda_0$  is the central wavelength. Meaning for the same pulse duration, a 1060 nm pulse will have  $1.76\times$  the spectral bandwidth than an 800 nm pulse. The increase in spectral bandwidth maps to an increase in the first order diffraction angles of the spectral bandwidth, where we will refer to the diffraction angles as field angles while discussing their effect of aberrations to an optical system. The increase in field angles leads directly to an increase in the Petzval field curvature at the SLM after focusing through an achromatic lens: a frequency dependent de-focusing across the power spectrum illustrated in Fig. 7.1(a). Using ray tracing calculations generated in Zemax, we plot in Fig. 7.1(b) the spectral bandwidth to field curvature coupling in a Martinez compressor, and how it changes for Gaussian pulses centered at 800 nm and 1060 nm. The increased field curvature across the edges of the power spectrum results in both a decrease in the spectral resolution at the SLM and an increase in divergence; apodizing the power spectrum in the focal spot of any subsequent optical system. A common alternative approach is using reflective concave optics. However, for large spans of field angles (due to large spectral bandwidths) and the need for  $< 100$  mm focal length optics, reflective optics become untenable due to physical space constraints and the mounting astigmatism due to high off-axis alignment.

Interestingly, Fig. 7.1(b) shows the curvature is not due to chromatic aberration, as the same lens produces very similar tangential and saggital focal curvatures as a function of field angle for both 800 nm and 1060 nm pulses. Another means of illustrating this, is to note that the same field angle to field curvature calculation performed for a single wavelength, such as a galvo scanner and a 1060 nm beam, results in a deviation from the red curves in Fig. 7.1(b)

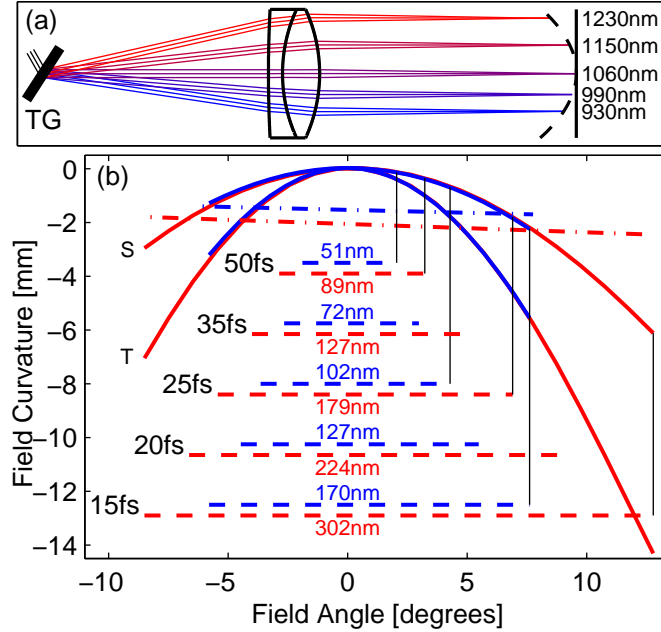


FIGURE 7.1. (a) Illustration of the field curvature at the focus of a folded 4- $F$  Martinez compressor from a 100 mm focal length achromatic lens. TG is a 1000 l/mm transmission grating. (b) The field curvature of the tangential (t) and saggital (s) planes from a 100 mm focal length achromatic lens for Gaussian pulses with 2.5 mm mode field diameters centered at 800 nm (solid-blue, 1208 l/mm grating and  $30.7^\circ$  angle of incidence) and 1060 nm (solid-red, 1000 l/mm grating and  $31^\circ$  angle of incidence) as a function of field angle. The field angles spanned by the  $e^{-5}$  bandwidths for 15 - 50 fs FWHM pulses at 800 nm (blue-dashed) and 1060 nm (red-dashed) are shown. The Rayleigh lengths are also shown for the 800 nm (blue-dash-dot) and 1060 nm (red-dash-dot) pulses. For ease of comparison, the largest field angles for several pulse durations are marked by black vertical lines.

of less than  $125 \mu\text{m}$ . The field curvature is driven by field angle, which is wholly dependent on the spectral bandwidth and dispersive element. While an optimal system would make the field angles symmetric by shifting the zero field angle wavelength away from the central frequency, pulses beneath 25 fs in duration at 1060 nm would still have field curvatures larger than the Rayleigh length of the focus,  $z_R$  (at least within the parameter space shown in Fig. 7.1).

Another means of flattening the line focus is to move to longer focal length achromatic lenses. In terms of absolute defocusing with field angle,  $z_f$ , the field curvature does not

actually improve for longer focal lengths lenses. But rather, the field curvature relative to the Rayleigh length of the focus improves with increased focal length. It is this property,  $z_f/z_R$ , which meaningfully accounts for the increase in field angle dependent spectral divergence out of the pulse shaper.

In Fig. 7.2, we plot the relative field curvatures for Martinez compressors composed of different focal length achromatic lenses, showing only the tangential relative field curvatures of a 1060 nm Gaussian pulse with a 2.5 mm mode field diameter diffracted by a 1000 l/mm transmission grating at a  $31^\circ$  incidence angle (calculations performed in Zemax). The maximal extent of the field angles in Fig. 7.2(b) corresponds to the  $e^{-5}$  spectral bandwidth of a 15 fs FWHM pulse. For comparison, the solid-red line in Fig. 7.2(b) is the same tangential field curvature as the solid-red line plotted in Fig. 7.1(b). The longer focal length achromatic lenses are not a viable solution, however, as the line focus exceeds the active area of the SLM when combined with the diffraction grating used here.

### 7.3. FLAT-FIELD PULSE SHAPING WITH A PLÖSSL LENS

What we desire then, is an optical component that manages high field angles while maintaining a flat field curvature for focal lengths  $\leq 100$  mm. This is solved by borrowing a simple compound lens design from astronomy and more recently used in microscopy [114]: the Plössl lens [Fig. 7.2(a)]. These simple compound lenses reduce the field curvature when used as a scan lens in laser scanning microscopy; increasing the field-of-view. As seen in Fig. 7.2(b), the relative field curvatures predicted by Zemax are much better than a single achromatic lens, especially for small focal lengths. Here, we make use of the flat field to extract large field angles (large spectral bandwidths) from a folded  $4-F$  pulse shaper with minimal spatial pulse degradation, an example of which is shown in Fig. 7.3(a).

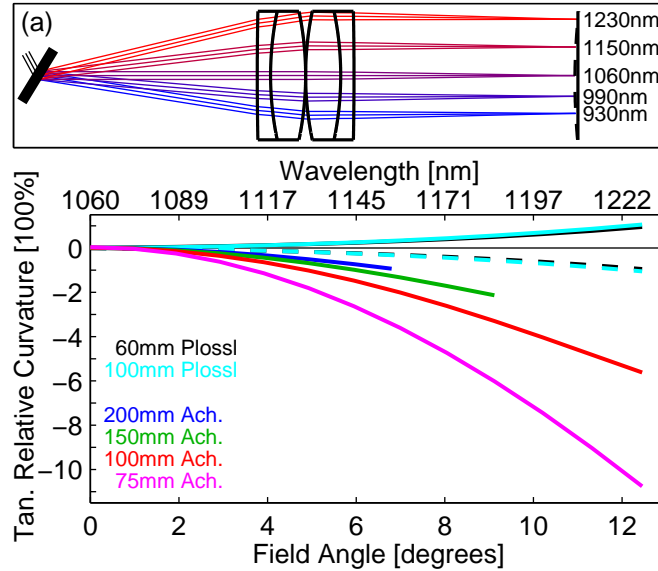


FIGURE 7.2. (a) Illustration of the field curvature at the focus of a folded 4- $F$  Martinez stretcher from a 100 mm EFL symmetric Plössl lens and a 1000 1/mm transmission grating. (b) The field curvature of the tangential foci relative to the Rayleigh lengths,  $z_f/z_R \cdot 100$ , as a function of field angle for several achromatic and Plössl lenses. The dashed lines shows the negative of the field curvatures of the Plössl lenses, for ease of comparison. The clear apertures of the 150 and 200 mm focal length achromatic lenses limits the transmitted field angles.

Another benefit of using a Plössl lens is the design freedom provided by symmetric and asymmetric lens pairings. When two 200 mm achromatic lenses are combined as a Plössl lens, they function as a compound lens with an effective focal length (EFL) of 100 mm. A 100 mm and 150 mm focal length achromatic lens pairing functions as a 60 mm EFL Plössl lens. With this design flexibility, one can more readily tailor the width of the line focus from a particular spectral bandwidth and diffraction grating to the active area of an SLM than with standard optical components.

We illustrate that flexibility here, using the 100 mm and 60 mm EFL Plössl lenses in pulse shapers designed for a 28 fs pulse and a 19 fs pulse, respectively. With the flat field pulse shapers, we achieve nearly TL compression of both the 28 fs and 19 fs FWHM pulses at 1065 nm, as measured by second-harmonic generation frequency resolved optical gating

(SHG-FROG) [78] and shown in Fig. 7.3 (b)-(e). The total transmission efficiency of the two shapers is 80% and 79%, for the 28 fs and 19 fs shapers, respectively. The total power transmission efficiency of the fiber-shaper systems are 67% and 66%. The high efficiency of this nonlinear pulse compression system results in short pulses with 11.5 nJ of energy (700 mW average power), achieving peak powers of 370 kW and 450 kW for the 28 fs and 19 fs pulses.

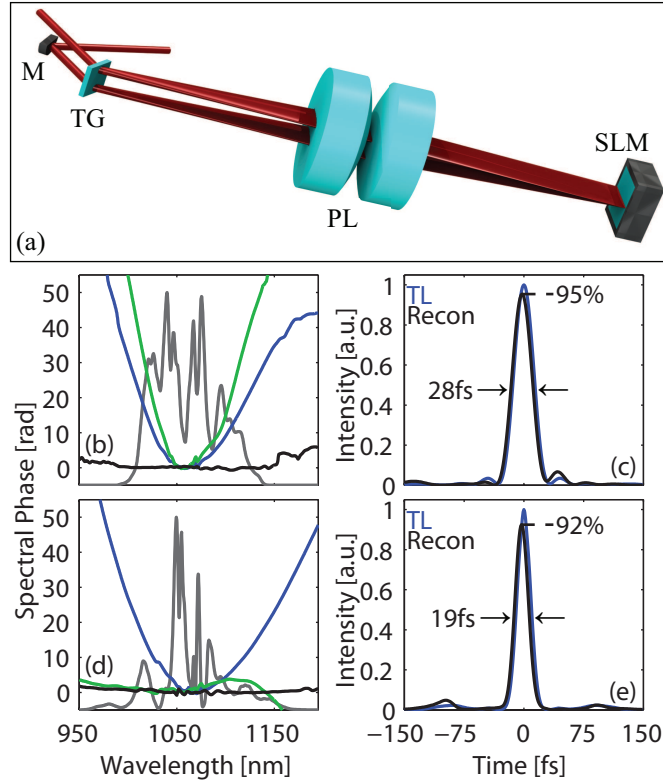


FIGURE 7.3. (a) The flat-field, Plössl pulse shaper. M: mirror, TG: transmission grating, PL: Plössl lens, and SLM: spatial light modulator. The SHG-FROG reconstructed 28 fs (b-c) and 19 fs (d-e) pulses. (b)/(d) The spectral phases before the pulse shaper (blue), after the pulse shaper with the shaper phase set to zero (green), and with compensation of the zero state phase (black) as a function of wavelength, the power spectra (gray) are also plotted in a.u. (c)/(e) The temporal intensity profiles of the bandwidth supported TL (blue) and the shaper compressed pulse (black).

The spectral phases in Fig. 7.3(b) and (d) show a distinct difference in the operation of the two different pulse shapers. The shaper with the 100 mm EFL Plössl lens requires

the grating-lens distance be less than the focal length to eliminate output spatial chirp, imparting positive GDD (i.e. it is configured as a Martinez stretcher). The spatial chirp at  $4F$  results from rays with non-zero incident field angles leaving the Plössl lens non-parallel to the optical axis. A small reduction in the grating-lens distance from  $4F$  ( $\sim 0.5$  mm) eliminates this angular deviation away from the optical axis. The shaper with the 60 mm EFL did not require this correction, allowing some tuning of the grating-lens distance around the focal length without accumulating significant spatial chirp. So, the 60 mm EFL shaper is set to act as a Martinez compressor; compensating for the bulk of the spectral phase from the fiber and the glass of the Plössl lens. The residual spectral phase, green curve of Fig. 7.3(d), is still sufficient however, to reduce the peak power to 25% of the TL.

To calibrate the pulse shaper, we use the common-path spectral interferometry technique described in Ref [115]. First, the pulse polarization before the pulse shaper is set to  $45^\circ$ . After the pulse shaper, a 5 mm calcite beam displacer separates the orthogonally polarized pulses in time by a few ps. Uniformly raising the voltage across all the pixels and recording spectral interferograms through a  $45^\circ$  polarizer generates (after processing) a “waterfall” of the voltage-to-phase mapping as a function of wavelength, since the SLM only acts on the p-polarized light.

After calibrating the pulse shaper, SHG-FROG measurements with the pulse shaper mask set to zero phase determines the spectral phase to compensate [green curves Fig. 7.3(b) and (d)]. The 28 fs pulse shaper compensates for a group delay dispersion of  $\beta_2 = 9000\text{fs}^2$ , where the spectral phase is taken as  $\exp(-i\beta_2\Omega^2/2)$  and  $\Omega$  is angular frequency. The nearly TL performance at 28 fs is from the inversion of the reconstructed spectral phase of a single SHG-FROG measurement with the shaper phase set to zero. The 19 fs pulse required

two iterations due to the increased sensitivity of the shorter pulse to small spectral phase perturbations, where the recovered spectral phases of each step are added to create the most accurate spectral phase compensation mask. The compression is such that the reconstructed pulses are at 95% and 92% of the respective TL peak powers.

The work presented here is a demonstration of state-of-the-art nonlinear pulse compression at 1065 nm, where the whole system operates in a near turn-key manner day-to-day. The unique combination of temporal duration, wavelength, pulse energy, and average power make this an ideal source to pursue novel research in nonlinear and ultrafast optics. We have already used the 28 fs pulses to seed another nonlinear fiber stage composed of a photonic crystal fiber with two zero dispersion wavelengths; generating 26 fs pulses at 1250 nm for use in a three-photon excitation fluorescence microscope [113]. Additionally, the method of nonlinear pulse compression shown here is highly scalable. As we have decoupled ourselves from highly nonlinear fibers and instead rely on short pulses and large oscillator pulse energies, this approach should remain viable for much higher pulse energies.

## CHAPTER 8

# PART I SUMMARY: MODULAR SOURCES AND DISPERSION

## CONTROL

*The most dangerous poison is the feeling of achievement. The antidote is to every evening think what can be done better tomorrow.*

Ingvar Kamprad

We have come to think of the methods and technology developed in Part I as modular components. Combining these components, we can create (and have created) a wide range of pulse energies and durations around 1060 nm. The purpose of this chapter is to provide a summary of what sort of systems can be constructed from the technologies and ideas in Part I, along with an over-arching narrative about how we have come to think of the problems and solutions in generating energetic pulses at 1060 nm at and beyond the gain bandwidth of Yb-ion doped optical fiber.

As a starting point, we have systems pumped by a stand-alone ANDi fiber laser oscillator. The ANDi lasers, in the configuration we construct them, produce:

- 150 fs pulses after compression with a grating compressor
- average powers of 500 mW up to 1.5 W at 50–60 MHz repetition rates, analogously  $\sim 10$  nJ pulse energies and  $\sim 60$  kW of peak power (we have built only one ANDi capable of producing  $> 1$  W of average power and it still in development)
- significant fourth-order spectral phase over the “cat-ears” portion of the power spectrum

- small power spectral mode fluctuations at the “cat-ears”, which map to small changes in the temporal pedestal.

As stand-alone ultrafast pulse sources, these lasers outperform all but the most cutting-edge 1060 nm bulk oscillators. As examples of the utility of these sources, we will highlight two of our ANDi pumped systems dubbed Negato (for the robustness of the downstream microscope’s construction) and K-ANDi (as it resides within the Keck laboratory for ultra-sensitive Raman detection). Negato has operated as a user-facility-like multiphoton laser-scanning microscope for a couple years now[116], generating images in multiple modalities: second-harmonic generation, third-harmonic generation, and two-photon excitation fluorescence. K-ANDi, which is towards the end of its development phase, is being used to generate visible pulses simultaneously at 488 nm and around 530 nm. To do this, we use the clipped power spectra compression scheme (Chapter 2.3) to generate low noise supercontinuum (Chapter 2.2) from which we carve out narrow-band seed pulses for dual Yb-doped amplifiers. The output of the amplifiers are then up converted in second-harmonic generation stages.

The next step up in source complexity relies on broadening the power spectrum of the 150 fs optical pulses in normal dispersion optical fiber. Normal dispersion fibers were supposed to be a straight-forward solution for spectral generation, as they they do not support soliton propagation and a number of de-stabilizing mechanisms that are associated with nonlinear soliton propagation. However, it turns out the latent birefringence of a non-polarization maintaining optical fiber causes a significant deviation in the pulse evolution from a scalar model of the nonlinear fiber propagation, namely that polarization modulation instability couples the two effective eigenaxis of the fiber as illustrated and discussed in Chapter 4 [26]. These destabilizing mechanisms were explored in so much as we desired a robust

solution, which proved to be polarization-maintaining optical fiber where the high designed birefringence prevents phase matching for polarization modulation instability.

We use both active fibers and passive fibers for spectral broadening, using optical fibers with relatively large modefield diameters in both cases. By relying on standard telecom optical fibers and large mode area optical fibers, we reduce the nonlinearity of the spectral broadening process. This may seem counter-intuitive, but it stems from our desire for spectral generation with the lowest noise at relatively high oscillator-type average powers ( $> 500$  mW) which rules out anomalous dispersion fibers, non-polarization maintaining highly-nonlinear all normal dispersion photonic crystal fibers and ultra-high numerical-aperture fibers. Non-linear photonic crystal fibers are not suitable since they have been shown to suffer from the same polarization fluctuation effects we experienced with nonlinear step-index fibers (the so-called ultra-high numerical aperture fibers), in spite of an order of magnitude higher latent birefringence over non-polarization maintaining telecom fiber [25]. The ultra-high numerical aperture fibers are available in polarization maintaining versions, but the polarization maintaining structures have a lower damage threshold than the bulk fiber; reducing their damage threshold to  $< 500$  mW of average power. Additionally, for many of these systems we are not seeking to generate the exceptional bandwidths that characterize typical supercontinuum generation (e.g. power spectral bandwidths supporting transform-limited (TL) durations of  $\ll 20$  fs), since the higher-order dispersion of such pulses requires much more complicated compression schemes which aside from pulse shapers remains an area of investigation.

The step away from highly nonlinear fiber for power spectral broadening however, is quite liberating in there are many more telecom or large-mode area fibers than nonlinear fibers. For example, moving to a large mode area, endlessly single-mode photonic crystal

fiber would enable very similar spectral broadening to what we demonstrate in Chapter 7 but for pulse energies  $> 100$  nJ and average powers  $> 20$  W (peak powers in excess of a MW!). Such pulse durations and energies would open up the possibility of using some techniques from the high-power community such as cross-polarized wave generation, leading to pulses at 1060 nm that would start to compete with amplified Ti:sapphire pulses in terms of not only duration but, equally important, a power spectrum which dictates a minimal TL temporal pedestal.

Merely, generating additional power spectrum in optical fiber turns out to be relatively trivial, as all pulses below a ps in duration have very high peak powers even for modest pulse energies of a few nJ. Maintaining stability and compensating the associated spectral phase of the broadened power spectrum however, is **not** trivial. The residual spectral phase not only reduces the peak power but effectively reduces the potency of the nonlinear pulse compression. One auxiliary reason for this limitation is our current inability to fabricate very short ( $< 40$  mm) optical fiber systems. In general, the uncompressed temporal tails only add to the average power (e.g. heating of a biological sample) without contributing to the nonlinear signal.

We have spent almost equal amounts of effort working on various pulse compression schemes as we have on the pulse broadening systems: using coma aberrations in a Martinez compressor to compensate for third-order dispersion (Section 3.2 [83]), modeling cascaded compressors using specific combinations of grating compressors and prism compressors (Section 3.2), a hyper-prism architecture enabling large prism insertions (Section 6.3), and perhaps our most notable development the flat-field pulse shaper (Chapter 7 [27]).

For spectral broadening in an active fiber, we are seeding only a portion of the ANDi oscillator power spectrum ( $< 4$  nm) into a fiber amplifier and broadening by roughly  $15\times$  (Chapter 3). These master oscillator nonlinear and power amplifier sources have the following benefits over a stand-alone ANDi:

- reduction in the inherent power spectral noise in dissipative soliton ANDi fiber laser oscillators
- reduction in the magnitude of the third- and fourth-order dispersion in the spectral phase, allowing for pulse compression down to 100 fs in a traditional compressor
- generation of power spectral bandwidths supporting  $< 60$  fs TL pulse durations, but which do require third-order dispersion compensation to realize near TL pulse intensities
- highly tunable power spectral bandwidths
- higher average powers of 1.5–3 W.

We have three such systems in operation: B-laser (named after Beau Domingue who designed it), M-ANDi (a system operating in Dr. Omid Masihzadeh's laboratory at the University of Colorado Denver at the Anschutz medical campus), and our flagship system BI-ANDi described below. These turn-key laser systems are being used to do fundamental research on CdTe photovoltaic cells using a newly developed super-resolution imaging technique (B-laser) and unlabeled functional imaging of mammalian retinas (M-ANDi) [34].

The next step in source complexity is using energetic (high oscillator pulse energies), compressed pulses to pump a nonlinear pulse compression stage composed of passive optical fiber and some form of pulse compressor. The broadening factors are  $2\text{--}5\times$  producing spectral bandwidths supporting TL pulse durations of  $< 100$  fs. Again, these spectral bandwidths

are in part dictated by the systems we have to compensate for the associated spectral phases. As an example of a system from the low end of spectral broadening factors, we broaden an ANDi operating at over 1.5 W of average power in a 10  $\mu\text{m}$  core large-mode area fiber and then compress the broadened power spectra in a hyper-prism compressor; producing nearly TL 72 fs pulses with 10 nJ of energy (Fig. 6.2).

The final example system is our flagship 1060 nm laser system, BI-ANDi (the laser with no name, a deep Sergio Leone reference), which combines nearly all of the components in Part I:

- An ANDi fiber laser for the master oscillator (Chapter 2)
- A nonlinear and power fiber amplifier seeded by the Andi (Chapter 3)
- The output of the amplifier is compressed and broadened in optical fiber following in a manner that minimizes noise in the resulting power spectrum and phase (Chapter 5)
- The broadened optical spectrum is then compressed to virtually the TL (95%) in a flat-field pulse shaper (Chapter 7)
- The final pulses are between 19–28 fs in duration (set by the seed chirp) with  $> 10$  nJ of energy for  $> 400$  kW of peak power (Fig.s 7.3)
- to the best of our knowledge, this is the most efficient pulse compression system of its kind in the world at a net efficiency of 66% (for comparison, other systems efficiencies are 18% [112] to 20% [97], this is largely due to the  $\leq 50\%$  efficiency of the MIIPS commercial pulse shaping system supplied by Biophotonics).

To date, BI-ANDi has been utilized in two very different experimental applications: synthesis of 1250 nm pulses for three-photon excitation fluorescence microscopy in the second

near-infrared biological imaging window [18, 113] (Chapter 10) and generating green pulses spanning 500–570 nm via second-harmonic generation for a new method of hyperspectral imaging capturing back-ground free absorbed spectra through excitation labeled fluorescence (Chapter 14).

One limitation to our systems is the seed power spectrum, both the steep-edged spectrum of an ANDi and/or the steep and modulated spectrum from the master oscillator nonlinear and power amplifiers. These spectrum produce ultrafast pulses of high utility for second- and third-order nonlinear applications, but in highly nonlinear environments the steep edges in the power spectra are preserved in an increase in the structure of the nonlinearly generated power spectra. The increase in structure limits the utility of the broadest possible spectral bandwidths (supporting TL durations  $< 20$  fs). For example, in non-impulsively stimulated Raman scattering using chirped supercontinuum pulses like those in Fig. 4.6(b)and(c), the vibrational excitation profiles are significantly degraded compared to ultra-broad Gaussian pulses or the pulses in Fig. 4.6(a) (discussed in detail in Chapter 12).

Taken together, we have a number of established ultrafast sources we can employ for myriad experimental applications. They vary in degree of sophistication and corresponding potency, where our system with the most bells-and-whistles (Bl-ANDi) is a world-class laser system. The Bartels ultrafast research group now has a small army of ultrafast sources to conduct all the research we conjure up.

## CHAPTER 9

# PART II: GENERATING 1300 NM PULSES VIA SOLITON

## SELF-FREQUENCY SHIFTING

*If you shoot for the stars and hit the moon, it's okay. But you've got to shoot for something. A lot of people don't even shoot.*

Confucius

We now transition from 1060 nm source development to synthesizing ultrafast pulses at 1300 nm out of the suite of 1060 nm pulses we developed in Part I. As discussed in Section 1.2, pulses at 1300 nm benefit from a deeper penetration of ballistic photons into turbid media than 800 or 1060 nm pulses due to reduced scattering, hence the designation the second biological imaging window. None of the most common ion dopants in a fused silica host fiber produce gain around 1300 nm. We seek then to use nonlinear frequency conversion in optical fibers to shift energy from pump pulses at 1060 nm into pulses in this imaging window at 1300 nm.

The three types of fiber that have the necessary nonlinear and dispersion characteristics are hollow-core photonic bandgap fibers, photonic crystal fibers (PCF) with a single zero-dispersion wavelength (ZDW), and fibers with two ZDWs straddling the seed pulse frequency and an approximately parabolic (concave down) dispersion coefficient curve. The low nonlinearity of air-core photonic bandgap fibers require many 10's to 100's of nJ pulses to launch solitons [117]. In this dissertation, we examine processes utilizing oscillator level energies, which are far below the requisite energies of the photonic bandgap fibers.

As a starting point we look at the simplest fiber-based nonlinear conversion scheme: soliton self-frequency shifting (SSFS) in optical fibers with a single ZDW at a higher frequency than the 1060 nm seed pulse [118]. On the surface, SSFS seems like an attractive method of converting 1060 nm pulses into 1300 nm pulses, but as we will show, the high fiber nonlinearity also causes shifted solitons with  $> 1$  nJ of energy to “overshoot” the target wavelength region. The analysis for the limitations of generating frequency shifted solitons at pulse energies  $> 1$  nJ is based on our publication Ref [113].

### 9.1. THE MARVEL THAT ARE PHOTONIC CRYSTAL FIBERS

The novel guiding structure of photonic crystal fiber (PCF) allows researchers (and now the company with the patents, NKT Photonics) to tune the zero-dispersion wavelength (ZDW), where the material switches from normal to anomalous dispersion, to a higher frequency than that of bulk silica [119]. This is because both the material dispersion and the waveguide dispersion contribute to the total propagation wavevector, and the waveguide dispersion in PCF can dominate the material dispersion. Fig. 9.1 shows dispersion curves for several such PCFs with increasingly small core diameters and correspondingly higher frequency (shorter wavelength) ZDWs. Several commercial PCFs exist with a ZDW shorter than 1060 nm (e.g. NKT Photonics’ SC-3.7-975 and NL-33-890). Fig. 9.1 shows the scope of fibers with ZDW’s at higher optical frequencies than the ZDW of bulk fused silica (blue curve in Fig. 9.1) all of which are PCF. The anomalous dispersion and high nonlinearity of these fibers supports solitons at low pulse energies ( $< 0.1$ – $1$  nJ). A soliton propagating in PCF will undergo soliton self-frequency shifting (SSFS) induced by intrapulse Raman scattering. Sub-ps pulses will undergo significant frequency shifting in PCF lengths of  $< 1$  m [118].

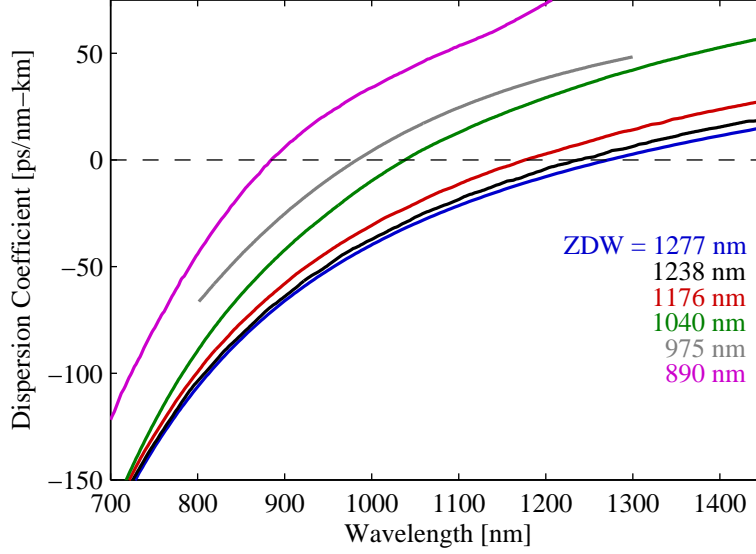


FIGURE 9.1. Dispersion files for bulk fused silica (blue) and the photonic crystal fibers LMA-PM-10 (black), LMA-PM-5 (red), SC-5.0-1040 (green), SC-3.7-975 (grey), and NL-3.3-890 (magenta), with the nonlinear coefficients for the fibers of 0.002, 0.009, 0.011, 0.016, 0.04 1/(W m) respectively.

The large-mode area PCF (black and red curves in Fig. 9.1) are not suitable for generating 1300 nm pulses through SSFS 1060 nm seed pulses since the ZDW is at a lower optical frequency than the seed pulse central frequency. The other PCFs however, were made for the express purpose of having a ZDW at a higher optical frequency than a pulse from a Yb-doped laser source (green, gray, and magenta curves in Fig. 9.1), and it is this group of PCF that we can utilize for SSFS 1060 nm pulses out to the second biological imaging window at 1300 nm.

## 9.2. SOLITON SELF-FREQUENCY SHIFTING RESTRICTS TUNED PULSE ENERGY

A seed pulse with more energy than required to support a single soliton becomes a higher-ordered soliton inside the PCF [28]. The low constituent soliton number required to maintain coherence (stable amplitude and phase) and conversion efficiency sets a threshold on the seed pulse energy as a function of pulse duration, fiber nonlinearity, and fiber dispersion [28]. The

constituent soliton number is given by  $N^2 = L_D/L_{NL}$ . The characteristic dispersion and nonlinear lengths are  $L_D = T_0^2/|\beta_2|$  and  $L_{NL} = 1/\gamma P_0$ , where  $T_0$  is the transform-limited (TL) pulse duration (defined below),  $\beta_2$  is the group velocity dispersion,  $P_0$  is the maximum pulse peak power, and all of which are based the input pulse.  $\gamma = \omega_0 n_2(\omega_0)/cA_{\text{eff}}(\omega_0)$  is the fiber nonlinear coefficient, where  $\omega_0$  is the central frequency of the pulse,  $n_2$  is the intensity dependent index of refraction,  $c$  is the speed of light, and  $A_{\text{eff}}(\omega_0)$  is the effective mode area at the central frequency.  $T_0$  is defined for an electric field with a hyperbolic secant temporal envelope,  $A'(t) = \sqrt{P_0} \text{sech}(t/T_0)$ , where  $t$  is a time frame moving with the envelope group velocity of the pulse. As the pulses generated in our fiber laser are not from a laser with conserved soliton modelocking and are somewhat more Gaussian than hyperbolic secant, we numerically model Gaussian pulses,  $A(z = 0, t) = \exp(-2 \ln(2)(t/\Delta\tau)^2)$ , where the fiber is assumed to start at  $z = 0$  and  $\Delta\tau$  is the full-width at half-maximum (FWHM) pulse duration. The equivalent  $T_0$  for a hyperbolic-secant having the same FWHM pulse intensity,  $\Delta\tau$ , as the Gaussian seed pulse is  $T_0 = \Delta\tau/(2 \ln(1 + \sqrt{2}))$ .

A common interpretation of the soliton order limitation is that by decreasing the pulse duration SSFS is once again a viable option for frequency conversion out to the 1300 nm spectral region. To examine this, we numerically model pulse propagation using a split-step fiber propagator separately integrating the linear and nonlinear components of the generalized nonlinear Schrödinger equation (GNLSE), Eqn. 4.1 [28]. For more details on the propagator model see Appendix A. Fig. 9.2 shows the temporal and spectral dynamics from nonlinear propagation in a PCF with a ZDW at 890 nm (Thorlabs/Blaze Photonics NL-3.3-890-02) for a 50 fs FWHM Gaussian seed pulse at 1065 nm with a constituent soliton number of 3.

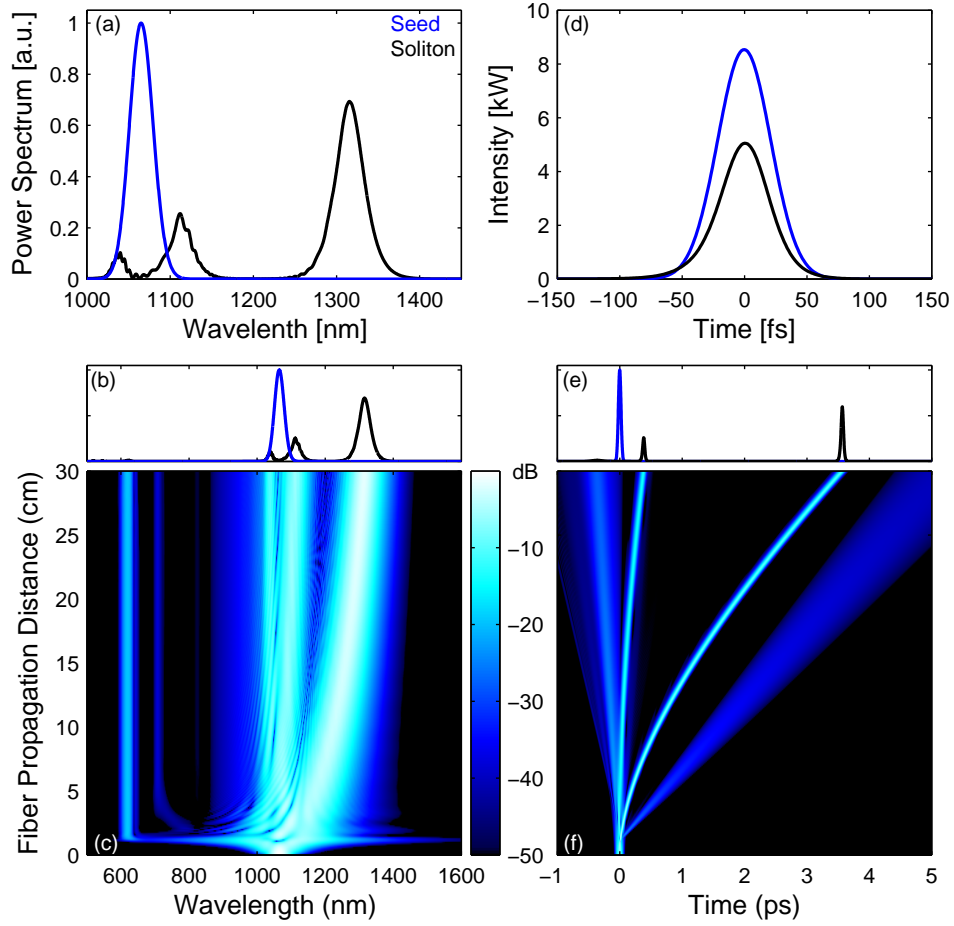


FIGURE 9.2. (a/b) The input (blue) and output (black) power spectra of a 50 fs Gaussian seed pulses with  $N = 3$  at 1065 nm after 30 cm of PCF fiber with a ZDW of 890 nm. (c) The evolution of the power spectrum with nonlinear fiber propagation. (d/e) The input (blue) and output (black) pulse intensities, where in (d) the output frequency shifted soliton is time shifted to overlap with the seed pulse. (f) The evolution of the pulse intensity with nonlinear fiber propagation.

The higher-order dispersion (HOD) of the fiber and stimulated Raman scattering disrupt the cyclical spectral-temporal breathing of the multi-order soliton. Instead of compressing in the frequency domain back to the seed bandwidth the pulse fractures, ejecting the constituent solitons one-by-one starting with the most energetic soliton in a process called soliton fission [28]. Fig. 9.2(c) and (f) shows two ejected solitons within the fiber length shown, where the amount of frequency shifting situates the highest energy soliton right in our desired

TABLE 9.1. SSFS conversion efficiency by seed pulse duration and soliton number.

$\Delta\tau$ [fs]	N=4			N=5			N=6		
	seed [nJ]	sol. [nJ] (%)		seed [nJ]	sol. [nJ] (%)		seed [nJ]	sol. [nJ] (%)	
100	0.32	0.17 (53%)		0.49	0.23 (46%)		0.71	0.29 (40%)	
50	0.63	0.33 (53%)		0.99	0.44 (45%)		1.42	0.57 (40%)	
25	1.26	0.64 (51%)		1.98	0.82 (42%)		2.84	1.15 (40%)	

wavelength region. It is the ejected, frequency-shifted, highest energy soliton which we would filter out and use for experiments. The energy of the highest-energy soliton generated in a nonlinear fiber from a 1060 nm seed pulse with duration  $T_0$  and constituent soliton number  $N$  is constrained by the relationship  $E \propto \frac{(|\beta_2|(2N-1))}{(T_0\gamma)}$  [28]. This expression shows that in order to support a high energy soliton in optical fibers with high nonlinearity we need a combination of the following: a large magnitude of anomalous dispersion, a large constituent soliton number, and/or a short pulse duration. For the range of fiber properties, seed pulse energies, and seed durations the energy conversion efficiency from the seed to the highest energy soliton is  $\sim 50\%$ . Table 9.1 contains the energies of seed pulses and the first ejected soliton as modeled by the numerical propagator, for several pulse durations and soliton numbers for pulses centered at 1060 nm.

From the model, SSFS scaling with energy seems promising:  $N = 6$  and 25 fs FWHM seed pulses generate shifted solitons with  $> 1$  nJ of energy. Table 9.1, however, does not account for the power spectra of the shifted soliton. Fig. 9.3 plots the evolution of the power spectra with fiber propagation of  $N = 4-6$  for 25 fs FWHM Gaussian pulses. While the shifted soliton contains over 1 nJ of energy for  $N = 6$ , it is beyond the target wavelength region once it is spectrally isolated. The 25 fs seed pulse generates a spectacular bandwidth during the first few mm of propagation and remains broad up to soliton fission ( $\sim 1$  mm). Supercontinuum (SC) generation is a more accurate characterization of the nonlinear propagation shown

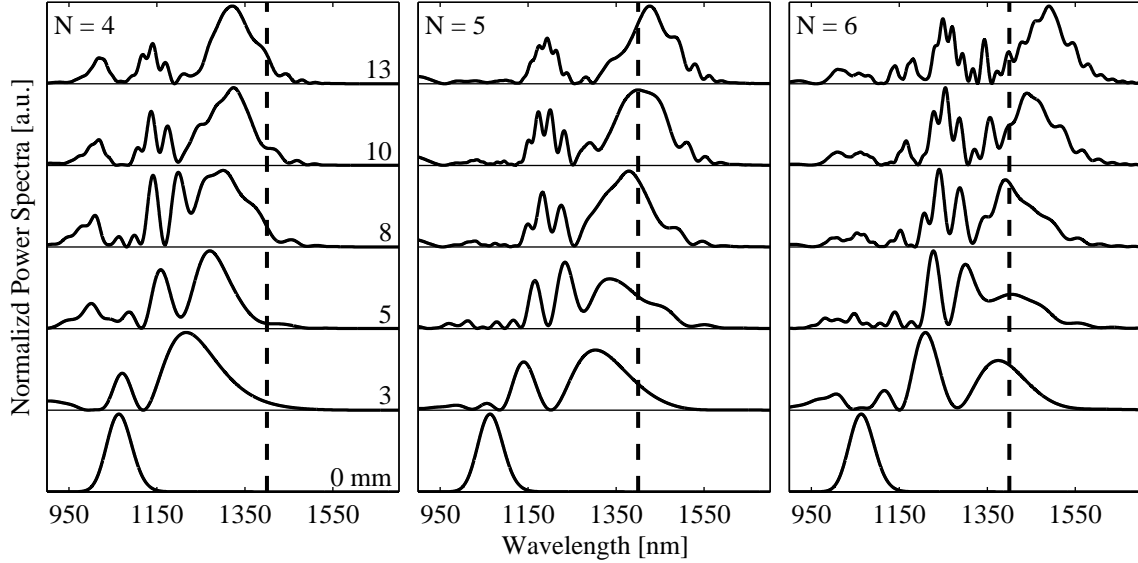


FIGURE 9.3. The modeled SC power spectra from a 25 fs seed pulse at 1065 nm with  $N = 4-6$  at various positions within an 890 nm ZDW PCF. Vertical dashed-lines correspond to 1400 nm, the edge of the spectral region of interest.

in Fig. 9.3(c) than SSFS, even though SSFS is the dominating effect for continued fiber propagation well beyond soliton fission. The power spectrum of the first ejected soliton, from the point of soliton fission onward to where it is spectrally and temporally isolated,  $\sim 10$  mm of propagation for the  $N = 6$  seed, is well beyond the desired 1250-1350 nm spectral range. Fig. 9.3 includes a vertical reference line at 1400 nm, to ease comparison of the frequency shifted solitons to the spectral region of interest. To circumvent the spectral over-shoot, one would add chirp to the seed pulse. Effectively exchanging the 25 fs and  $N = 6$  seed pulse for a pulse with a longer duration and larger soliton number, which reduces the efficiency of conversion into the highest energy ejected soliton; leading directly to  $< 1$  nJ of energy in the shifted soliton.

The same spectral overshoot issue plagues longer seed pulses,  $\sim 100$  fs, as well. From Table 9.1, the conversion efficiency levels-off for increasing  $N$ ; leaving open the possibility of achieving increased pulsed energies in the highest-energy ejected soliton while keeping  $N$

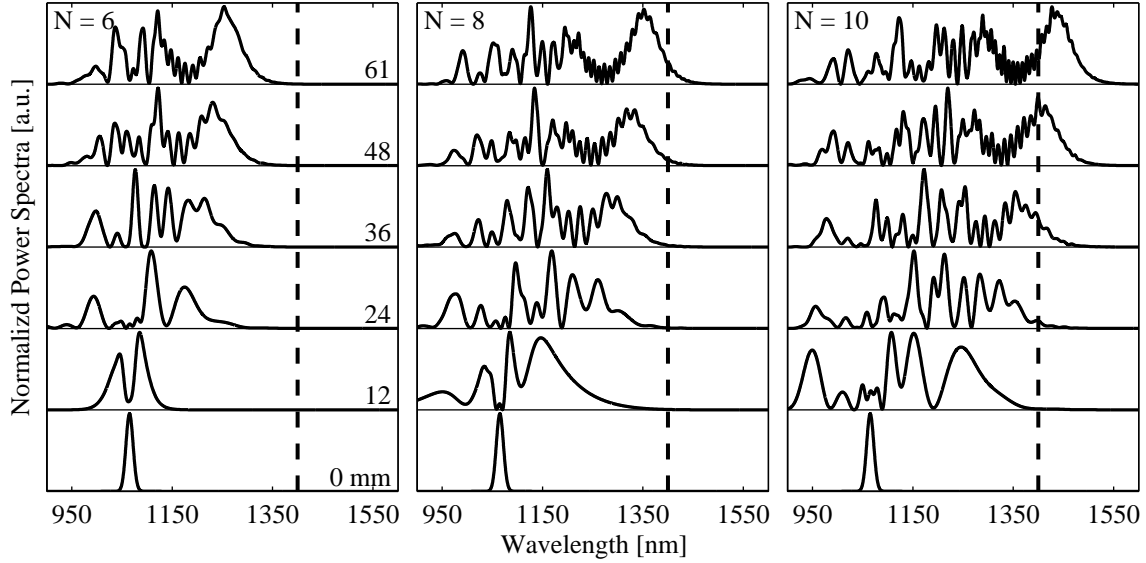


FIGURE 9.4. The modeled SC power spectra from a 100 fs seed pulse at 1065 nm with  $N = 6, 8,$  and  $10$  at various positions within an 890 nm ZDW PCF. Vertical dashed-lines correspond to 1400 nm, the edge of the spectral region of interest.

in the low teens. Again however, one must expand the scope of this particular investigation to include the power spectra of the highest energy ejected soliton. Doing so, results in the same situation as the 25 fs seed pulse: spectral overshoot by the highest energy frequency shifted soliton. Fig. 9.4 explicitly shows this spectral overshoot, where the highest energy ejected soliton is  $< 1$  nJ.

The SSFS conversion route may still be a viable method of converting  $\sim 1060$  nm pulses out into the infrared spectral region beyond 1300 nm, but as a means of producing  $> 1$  nJ pulses at 1300 nm it falls short (in this case by overshooting). In the event a suitable 1300 nm fiber amplifier were available, SSFS would be a strong candidate for generating seed pulses for amplification. But, short of amplification, the pulse energies around 1300 nm are not large enough for to pump a complex multi-photon microscope.

### 9.3. SELF-FREQUENCY SHIFTING FOR LOW ENERGY AMPLIFIER SEED PULSES AT

1340 nm

By themselves, these SSFS seed pulses do not have sufficient energy to drive a multi-photon microscope at 0.25–0.5 nJ; they are, however, great candidates to seed an amplifier with possible root-mean squared power noise equivalent to the initial 1060 nm pulses [120] and enough initial energy to only necessitate 12.5–13 dB amplification for maximal penetration-depth in multi-photon imaging applications [53]. This section looks at a theoretical survey of possible seed pulses for a Nd-doped fiber amplifier (peak gain at 1340 nm), which we discuss further in Chapter 11.

The 1060 nm pulse used to seed the SSFS nonlinear fiber will come from one of the pulse sources discussed in Chapters 2, 3, 6.1, and 7. As these systems span from 20–100s of fs in duration, we can choose the seed pulse duration and energy to coincide with the numerical propagator model guided optimal seed pulse. Fig. 9.5 illustrates a typical example of the nonlinear propagation computed with our code that gives rise to a frequency-shifted soliton at 1340 nm. At  $\sim 3$  cm of propagation (Fig. 9.5(c) and (d)), the pulse fractures in time and frequency ejecting the highest energy constituent soliton. After 30 cm of propagation, this soliton (marked by arrows in Fig. 9.5(a) and (b)) has frequency shifted to the peak gain of Nd-doped ZBLAN fiber at 1340 nm. A preliminary survey of some pulse parameters indicates there are strong candidates within the PCF and 1060 nm pulse space to meet our performance goals, shown in Table 9.2. For example, the 75 fs pulse with  $N = 6$  in the 975 nm ZDW exceeds our seed pulse energy target.

The rate of frequency shifting determines the total length of PCF, and will map small fluctuations in the 1060 nm seed pulse to timing jitter in the 1340 nm output pulse, as it

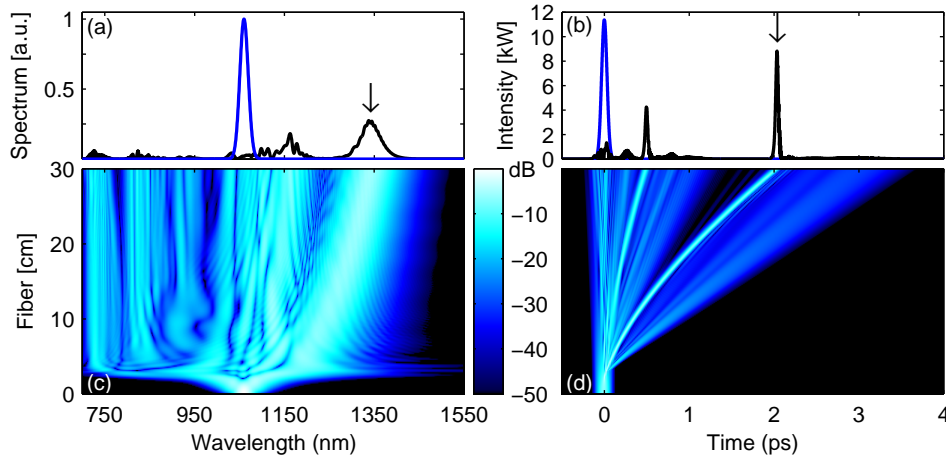


FIGURE 9.5. The modeled SC power spectra from a 75 fs seed pulse at 1065 nm with  $N = 6$  propagating in 30 cm of 975 nm ZDW PCF. Arrows indicate the highest energy ejected soliton, frequency shifted to 1340 nm.

TABLE 9.2. Survey of pulses and fibers for 1350 nm SSFS source.

Seed FWHM [fs]	N	ZDW [nm] / $\gamma$ [1/W-km]	Fiber [cm]	Sol. [nJ]	Sol. FWHM [fs]	Overlap Sol. /Nd Gain [%]	$\Delta\lambda$	Timing Jitter [fs]
125	6	975 / 18	92	0.24	50	88		32
125	8	975 / 18	37	0.35	40	77		10
100	6	975 / 18	57	0.29	44	83		15
100	8	975 / 18	25	0.39	36	72		7
100	6	890 / 37	15	0.38	38	76		12
75	6	975 / 18	28	0.38	37	74		7
75	8	975 / 18	11	0.56	28	60		4
50	6	975 / 18	10	0.56	29	60		3

causes small perturbations to the exact location of soliton fission (temporal and spectral ejection). Preliminary modeling of 1060 nm seed pulses with 0.5% root-mean-squared noise over 150 pulses shows that the SSFS pulses will have jitter between 3-32 fs depending on the PCF and 1060 nm seed pulse. Our proposed NDFA system will be insensitive to a few fs timing jitter as would a downstream imaging platform. But, this jitter could be a potential problem for an optical parametric amplification system, an alternative means of 1340 nm amplification.

While the parameter space is broad, a preliminary survey of a few pulse/PCF combinations indicates a few trends. For example, from the same PCF and 1060 nm pulses with the same constituent soliton number, a diminishing 1060 nm pulse duration produces more energetic solitons. Likewise, holding the PCF and 1060 nm pulse duration constant, seed pulses with increasing constituent soliton numbers (i.e. more energetic 1060 nm pulses) produce more energetic solitons. However, the more energetic solitons are broader in bandwidth and reduce the spectral overlap between their power spectrum and the Neodymium-doped ZBLAN gain bandwidth. And, as discussed in the previous section, a 1060 nm launched pulse that is too short or energetic will not produce a spectrally isolated soliton within the target wavelength region but instead the highest energy ejected soliton will only separate from the background spectra surrounding the 1060 nm seed pulse beyond 1340 nm and the NDFA gain bandwidth. These competing considerations require careful design and optimization to achieve the most robust and reliable performance.

In this chapter, we outlined the problems inherent in generating 1300 nm pulses from 1060 nm seed pulses by SSFS in highly nonlinear PCF. The problem is two-fold, one is the low energies required ( $< 1$  nJ) of  $\sim 100$  fs seed pulses to form small numbered higher-order solitons. The second is that even for seed pulses at 25 fs which can generate shifted solitons with  $> 1$  nJ of energy, the shifted solitons over-shoot the target spectral region. SSFS generated pulses are strong candidates however, at the reduced pulse energy requirements for seeding a 1300 nm amplifier. Preliminary numerically modeled results show there are a number of promising pulse/PCF combinations for generating 1340 nm seed pulses with 0.3–0.5 nJ of pulse energy, which with  $\sim 13$  dB amplification should achieve fundamental multi-photon penetration depth limit at 1340 nm.

## CHAPTER 10

# PART II: NONLINEAR FREQUENCY CONVERSION OF ULTRAFAST FIBER PULSES IN DUAL-ZERO DISPERSION FIBER TO 1250 NM

*A ship in harbor is safe, but that is not what ships are built for.*

John A. Shedd

As in Chapter 9, we are still pursuing nonlinear frequency conversion as a means of generating  $\sim 1300$  nm pulses from 1060 nm seed pulses. In this chapter, we look at a different type of nonlinear fiber which has two zero-dispersion wavelengths (ZDW) surrounding the central frequency of the seed pulse. The results and analysis in this chapter are based on our publication Ref [113].

### 10.1. PHOTONIC CRYSTAL FIBER WITH DUAL-ZERO-DISPERSION WAVELENGTHS

Not only does the novel guiding properties of PCFs allow designers to blue-shift the silica ZDW, it allows the design and manufacture of PCFs with closely spaced ZDWs. Fig. 10.1 compares the dispersion profiles of various types of nonlinear PCF fibers, including a dual-ZDW fiber (magenta curve). Injecting seed pulses with a central frequency which resides in between the ZDWs (in an anomalous dispersion region) generates dual-band SC, without intrapulse Raman scattering. A commercially available PCF with such a dispersion profile is NKT Photonics NL-1050-ZERO-2 with ZDWs at 1020 and 1076 nm (per the manufacturer, magenta curve in Fig. 10.1). Seeding the NL-1050-ZERO-2 fiber with ultrafast pulses at

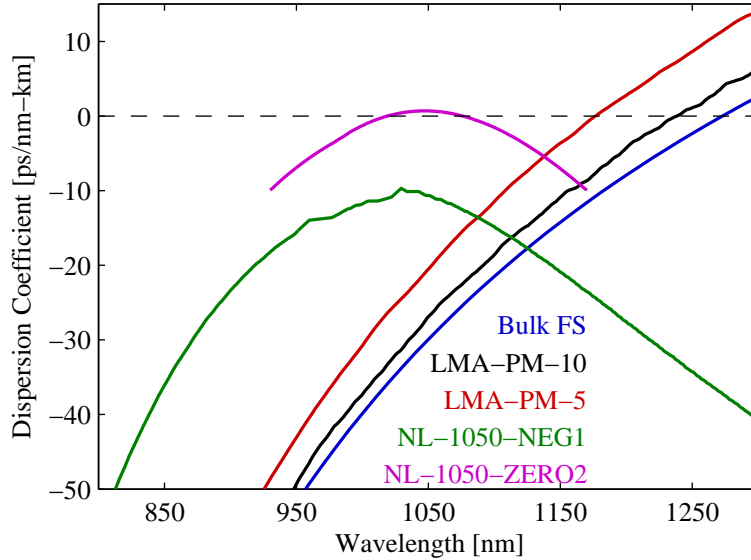


FIGURE 10.1. Dispersion files for bulk fused silica (blue) and the photonic crystal fibers LMA-PM-10 (black), LMA-PM-5 (red), NL-1050-NEG1 (green), and NL-1050-ZERO2 (magenta).

1060 nm generates a bi-modal supercontinuum spectra around 800 nm and 1250 nm, an example of the spectral evolution is shown in Fig. 10.2(a).

Optical coherence tomography (OCT) was the original application of the dual-band spectra from the dual-ZDW PCF [121, 122]. The smoothness of the generated SC power spectra was of the utmost importance to minimize the OCT point spread function pedestal, and so the PCF lengths were quite long ( $\sim 1$  m); introducing significant higher-order dispersion effects. Another study pursuing  $\sim 1250$  nm pulses with  $> 1$  nJ of energy used a higher-order mode fiber with a similar dispersion curve containing two ZDWs but  $\sim 10\times$  lower nonlinearity [123]. Coupling 1.39 nJ and 200 fs pulses at 1064 nm into higher-order mode fiber, van Howe et al. produced 0.8 nJ pulses around 1150 and a pulse duration of 49 fs. In related work, the wavelength of SC from higher-order mode fibers was extended to 1350 nm by Čerenkov radiation; producing 0.66 nJ and 106 fs pulses [124].

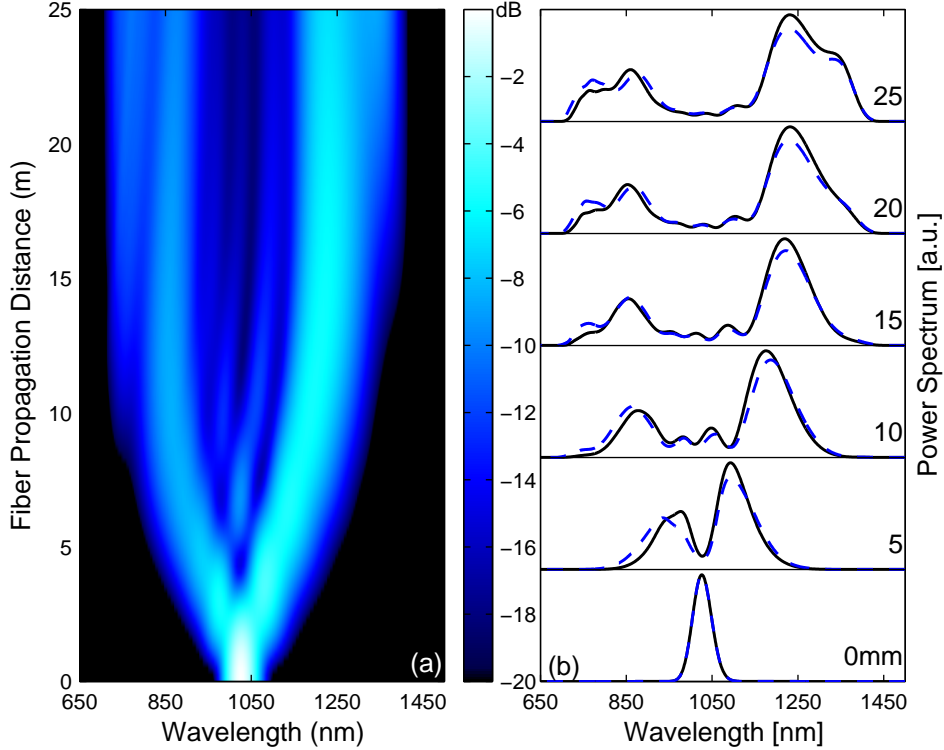


FIGURE 10.2. (a) The modeled spectral and temporal evolution from nonlinear fiber propagation of a 0.5 nJ, 30 fs Gaussian seed pulse. (b) A theoretical comparison of the effects of Raman scattering on the dual-band spectra formation in dual-ZDW PCF. For the same seed pulse as in (a), power spectra at intermittent fiber lengths are shown with (black-solid) and without (blue-dashed) Raman scattering.

Dual-ZDW PCF fiber generates SC with a dual-band power spectrum through the unique dispersion profile and low order nonlinearities, predominantly self phase modulation. Unlike in soliton self-frequency shifting (SSFS), the Raman effect does not play a role in the generation of the red-shifted light. We demonstrate this here by modeling the propagation of a 1 nJ and 30 fs FWHM Gaussian seed pulse at 1060 nm in NL-1050-ZERO-2 PCF with and without the Raman effect, using the generalized nonlinear Schrödinger equation (Eqn. 4.1) and our numerical propagator model. We do this by “turning off” the non-instantaneous component of the response function in Eqn. 4.1 by setting  $f_R = 0$ . The results in Fig. 10.2(b)

clearly show that the splitting of the power spectra happens in the absence of Raman scattering. Critically, that the frequency shift is not a SSFS process (or for that matter another soliton-driven process like soliton fission or a superposition of higher-order solitons) indicates dual-ZDW PCF avoids the SSFS energy restrictions.

Using 29 mm of NL-1050-Zero-2 PCF, we report here 1250 nm pulses having up to 2nJ of energy and for less energetic pulses (0.6 nJ) durations as short as 26 fs full-width at half-maximum (FWHM). To extract fully separated power spectra from the short length of PCF, we use a 28 fs FWHM seed pulses centered at 1075 nm. To the best of our knowledge, the 26 fs FWHM pulse is the shortest reported nonlinear fiber derived pulse in the 1250 nm wavelength range.

## 10.2. NONLINEAR FREQUENCY CONVERSION SYSTEM USING DUAL-ZERO-DISPERSION WAVELENGTH PHOTONIC CRYSTAL FIBER

The source of the ultrafast seed pulses is the home-built system shown in Fig. 10.3 (BLANDi of Chapters 8 and 7). An all normal dispersion fiber oscillator and a narrow-band, nonlinear fiber amplifier produce 140 fs FWHM pulses with over 25 nJ of energy at 61 MHz [83]. The 140 fs amplifier pulses seed a fiber broadening stage composed of 142 mm of Leikki Passive-10/125-PM fiber, with 84% total transmission efficiency through the APC connectors and aspheric collimators. A custom folded 4-F pulse shaper [27] compresses the spectrally broadened pulse. A half waveplate and polarizer attenuate the seed pulse down to between 2-6 nJ and a telescope sizes the beam appropriately for fiber coupling.

Since multiphoton excitation improves with shorter pulse duration [15], one of our primary concerns was minimizing the SC pulse duration. To minimize the effects of higher-order dispersion and de-polarization during propagation [26, 25], we constructed a short 1250 nm

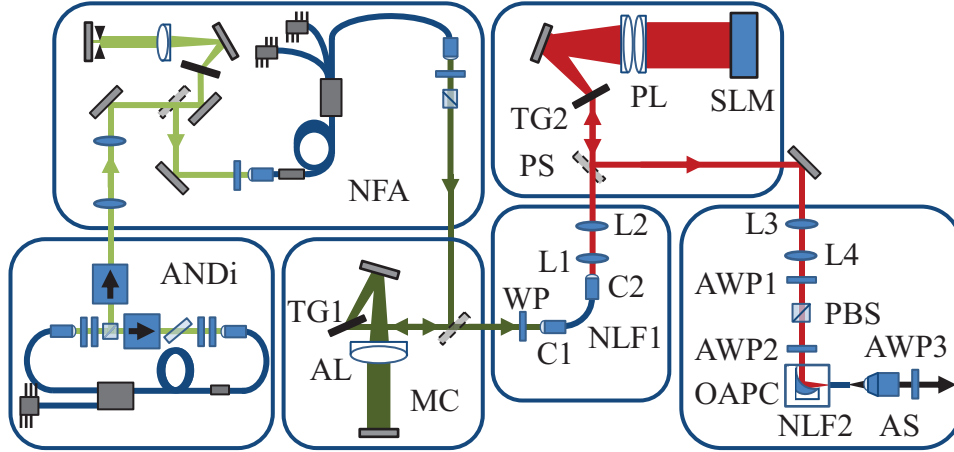


FIGURE 10.3. Setup for the 1075 nm pulse generation and subsequent 1250 nm pulse generation. ANDi: all normal dispersion laser, NFA: nonlinear fiber amplifier; TG1 and TG2: transmission gratings 1600 l/mm and 1000 l/mm respectively; AL: achromatic lens, MC: Martinez compressor; WP: half-waveplate; C1 and C2: aspheric fiber collimators with APC receptacles; NLF1: nonlinear fiber (10/125-PM), L1, L2, L3, and L4: lenses; PS: pulse shaper; PL: Plössl lens; SLM: spatial light modulator; AWP1, AWP2, and AWP3: achromatic half-waveplates, PBS: polarizing beam splitter; OAPC: off-axis parabolic fiber collimator with APC receptacle; NLF2: nonlinear fiber (NL-1050-ZERO-2); AS: aspheric lens.

nonlinear fiber cocktail, or segmented fiber, from 8 mm of HI1060 spliced to 29 mm of NL-1050-ZERO-2, referred to here as the 1250 nm nonlinear fiber. Epoxying and polishing the 1250 nm nonlinear fiber into an angled physical contact (APC) fiber connector makes a robust entrance coupling platform, where the larger mode-field diameter of the HI1060 entrance fiber acts as a bridge fiber to increase the coupling efficiency into the smaller core PCF. The splice loss at the fiber intersection is 0.67 dB. An off-axis parabolic collimator (Thorlabs RC02APC-P01) couples the seed pulses into the fiber cocktail. Pulses exit the fiber cocktail via a cleaved face of the PCF and an anti-reflection coated aspheric lens (4.5 mm effective focal length, Newport 5723-H-C) collimates the output beam. The total power transmission efficiency of pulses incident on the off-axis parabolic collimator through the

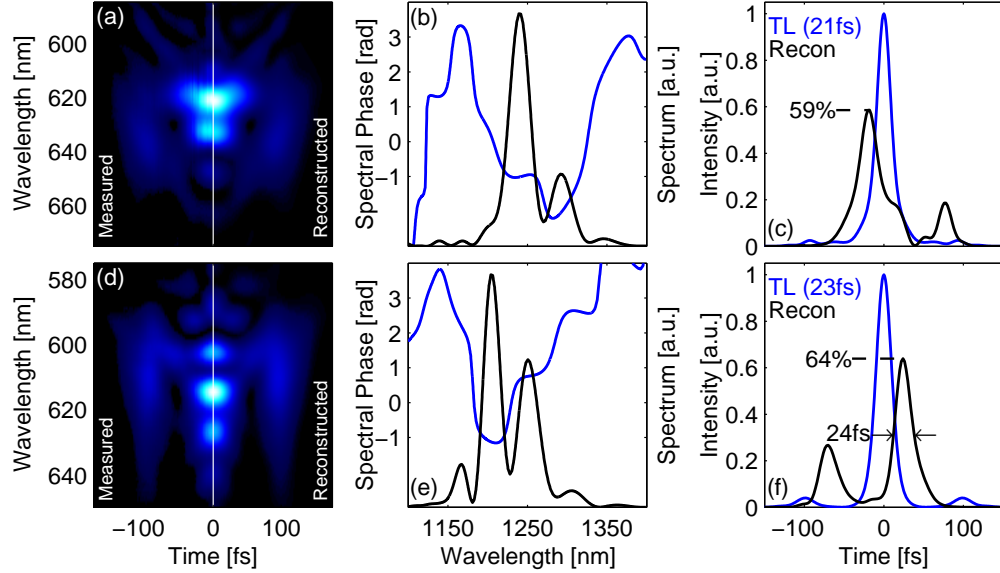


FIGURE 10.4. 1250 nm pulses at 2 nJ pulse (top) and 0.6 nJ (bottom). (a,d) Phantom-FROG: comparison of the measured (left) and reconstructed (right) SHG-FROG traces, (b,e) spectral phase (blue) and power spectrum (black), and (c,f) the temporal profile of the bandwidth supported transform-limited pulse (blue) and the reconstructed pulse (black).

output aspheric lens is 59%. An achromatic half waveplate before the entrance fiber collimator matches the seed pulse polarization orientation to the weak birefringence induced slow axis of the PCF [26, 25].

Generating pulses at 1250 nm containing 0.6 nJ and 2 nJ of energy, we are able to demonstrate both power scaling and the effects of increased energy on the pulse intensity profile. The two 1250 nm pulses are shown in Fig. 10.4. We rely on SHG-FROG reconstructions to determine the pulse structure and power spectrum. At 2 nJ, the nonlinear spectral phase causes a double peak structure in the intensity profile; limiting the pulse to 30 fs FWHM where the transform-limited duration is 21 fs FWHM. The main temporal peak in the 2 nJ pulse contains 84% of the total energy. It is possible to generate enough bandwidth at 2 nJ to support  $< 20$  fs pulses by tuning the seed chirp, but the increase in nonlinear spectral phase limits the pulses to  $\sim 35\%$  of the transform-limited peak power. At 0.6 nJ, the main

temporal peak is exceptionally short at 26 fs FWHM out of a transform-limited duration of 22 fs FWHM and contains 73% of the total pulse energy.

The presence of the satellite pulses at both energies is unfortunate, as they are caused solely by nonlinear spectral phase and fiber dispersion. It seems to us, metrics like the FWHM do not fully capture the complexity of the pulses in Fig. 10.4(c) and (f). To try and estimate the effectiveness of a structured temporal profile, e.g. as an excitation source for multiphoton microscopy, we think there is some merit to comparing them to a square pulse. The temporal duration of a square pulse is quite simple:  $\Delta\tau_{\text{square}} = E/P_0$ , where  $E$  is the energy in the pulse and  $P_0$  is still the maximum peak power. For comparison, a true Gaussian pulse with an intensity FWHM duration of 50 fs has a square pulse duration of 53 fs, only a factor of  $1.06\times$  longer. The square pulse comparison is a straightforward means of quantifying pulse structure into the common language of pulse duration. Applying this to our 2 nJ and 0.6 nJ pulses, the effective square pulse durations are 49 fs and 42 fs, respectively.

Defining the depolarization as  $I_{\perp}/(I_{\perp} + I_{\parallel})$ , where  $I_{\parallel}$  and  $I_{\perp}$  are the intensities in the slow and fast axes, respectively, and the seed pulse is oriented along the slow axis. The 1250 nm SC is only 10% and 5% depolarized for the 2 nJ and 0.6 nJ pulses, respectively; meaning both are largely free of polarization instabilities. Of the light coupled through the dual-ZDW PCF, the conversion efficiency into short pulses near 1250 nm, including depolarization, is 60%; meaning the greater depolarization in the higher energy pulse is actually offset by a larger power conversion efficiency into the 1250 nm spectral region. The total conversion efficiency from the 1075 nm seed pulse to 1250 nm pulses then, including coupling losses and depolarization, is 35%.

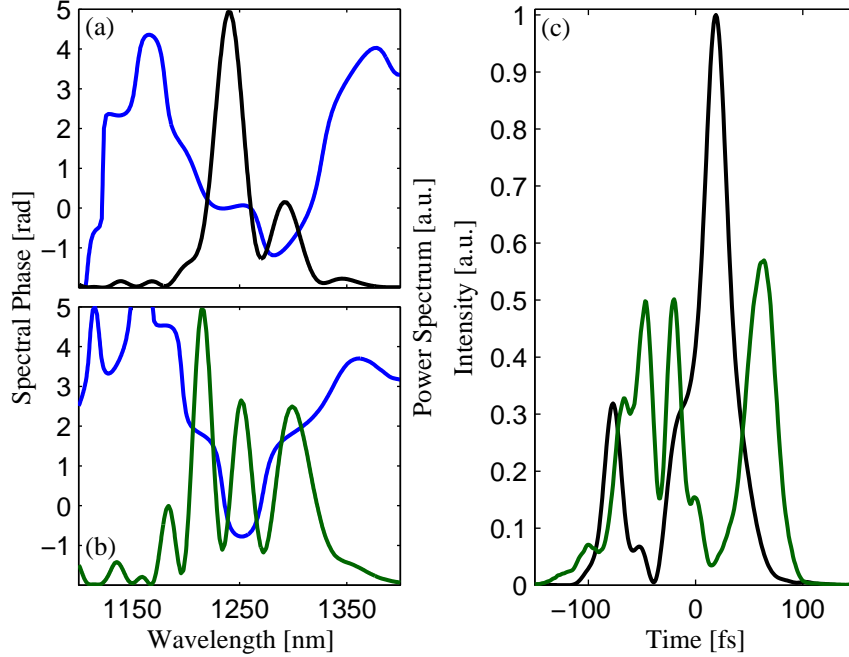


FIGURE 10.5. 2 states of the 2 nJ 1250 nm pulses. (a,b) The spectral phase (blue-curves) and power spectrum for two different pulse states. (c) The intensity profiles from (a) and (b) in black and green, respectively, normalized to the pulse from (a).

There exists however, a problematic instability in the SC generation of 2 nJ pulses at 1250 nm within our setup. For undetermined reasons, the output 1250 nm pulses undergo seemingly binary changes of state. The pulse energy is invariant (within a few percent) but the power spectrum and spectral phase both change. Fig. 10.5 shows a 2 nJ pulse in the “good” state (the same pulse shown in Fig. 10.4(a-c)) and a “worse” state. The pulse in the worse state drops in peak power, relative to the good state, by 57%! The resulting degradation in signal from two- and three-photon nonlinear interactions would be 65% and 38%, based on the  $g_N$  factor defined in Section 2.3. At 0.6 nJ, the system does not exhibit this instability.

We suspect feedback from the cleaved PCF end into the amplifier broadening fiber and amplifier itself is the source of these state changes. Extinguishing the feedback into the

amplifier should eliminate these changes of state and enable an increase in the injected seed pulse energy. A Faraday-isolator would extinguish this feedback but broadband Faraday-isolators at 1075 nm are not yet a common commercial component. Alternatively, angle cleaving the exit face of the PCF fiber would also diminish the back reflected parasitic light but is outside of our current fabrication capabilities.

There are a few additional improvements which would increase the robustness of the the 1250 nm source, such as hermetically enclosing the PCF exit face, as the system did experience a degradation in output beam quality and transmission over time. Potentially the most dramatic improvement however, would involve having the NL-1050-Zero-2 PCF re-designed incorporating polarization maintaining structures. As studies [26, 25] and Chapter 5 have shown, polarization maintenance within nonlinear fibers is of the utmost importance when scaling to higher pulse energies.

### 10.3. DEMONSTRATION OF 3-PHOTON EXCITATION FLUORESCENCE MICROSCOPY AT 1250 NM

We built a stage-scanning microscope, illustrated in Fig. 10.6(a), as opposed to a laser scanning microscope, in an effort to preserve pulse energy. Since the stages move, the incident beam is always co-axially directed into the focusing objective. We can therefore use a highly transmissive, aspheric lenses and still produce a diffraction-limited focus at each pixel in the two-dimensional (2D) section scanned by the stages. Epi-fluorescent light is detected in the traditional manner: with a longpass dichroic mirror (Semrock FF775-Di01-25x36) and filters isolating the fluorescence light from residual fundamental and harmonic frequencies (Thorlabs FGS900-A and Thorlabs MF525-39).

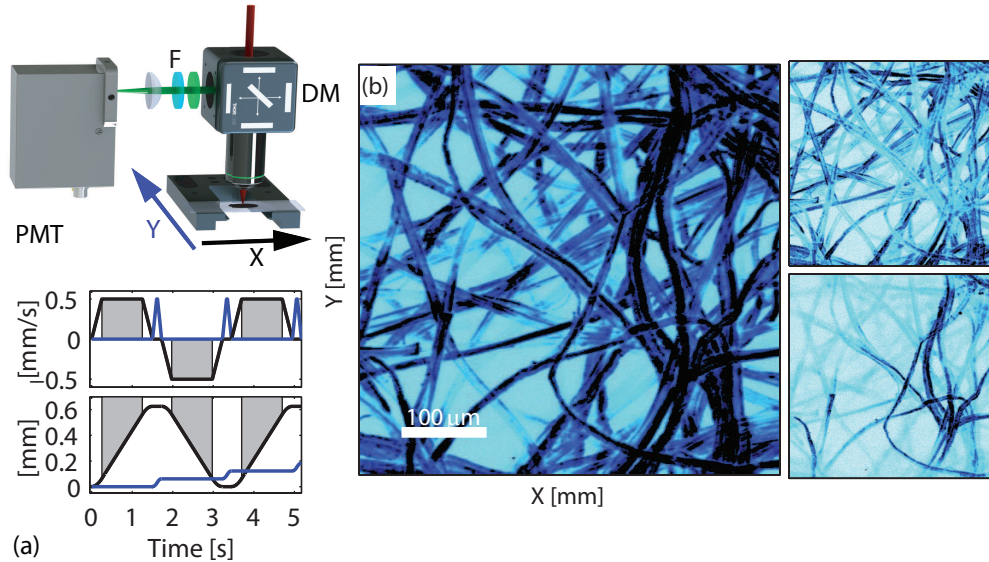


FIGURE 10.6. (a) Setup of the 3-photon epi-detected stage-scanning microscope (top) and an example of the position and velocity curves of both x (black) and y (blue) stages used to acquire sectioned 2D images (bottom). The shaded areas indicate regions of constant velocity where pixel data is captured. PMT: photomultiplier tube, F: filters, and DM: dichroic mirror. (b) An integrated image stack of fluorescein-dyed lens tissue (left) and two 2D sections separated in the z-dimension by 30 micron (right).

To minimize acquisition time, one axis of the 2D scan is run continuously at constant velocity for each one-dimensional row scan. The continuously acquired voltage samples of each row are separated into discrete pixels based on sample averaging and the sample acquisition rate. The bottom of Fig. 10.6(a) shows an example of the velocity and position curves for the x- and y-axis stages, where the gray-shaded areas indicate the regions of active pixel acquisition.

The image of fluorescein-dyed lens tissue, shown in Fig. 10.6(b), is from 21 2D planes of  $495 \times 495$  pixels each separated by 3 microns in the z dimension. The 0.6 nJ 1250 nm pulses were the excitation source for the image. Two 2D planes are shown on the right side of Fig. 10.6(b), where the two planes are 30 microns apart and show well resolved dyed fibers at different layers. The data acquisition card (National Instruments NI USB-6363) acquired

analog data from the photomultiplier tube via a current preamplifier (Stanford Research Systems SR570) at 2 MSa/s; averaging every 4000 samples to compose the value of a pixel. The constant x-axis velocity during data acquisition was 0.5 mm/s, and the acquisition time per 2D section was 9.5 minutes. The focusing objective is an aspheric lens (Newport 5721-H-C) with a 1000-1600 nm anti-reflection coating, 2.8 mm effective focal length, and 0.54 numerical aperture (NA). In future work, increasing the NA of the focusing objective should result in higher signal levels, while adding additional color filters and PMT's will extend the microscope into the second- and third-harmonic generation modalities.

As an alternative approach to SSFS, we have built a custom ultrafast laser system to seed a 1250 nm nonlinear fiber cocktail. The dual-ZDW nonlinear fiber does not have the same energy constraints as a single ZDW PCF, nor does it have the same spectral over-shoot problem as it is not a soliton or Raman driven nonlinear conversion process.

In conclusion, using a 37 mm 1250 nm nonlinear fiber cocktail, we generate short pulses at 1250 nm with 0.6 and 2 nJ of energy. The 1250 nm pulse duration out of the fiber depends tightly on the accrued nonlinear spectral phase, with the 0.6 nJ pulse having a FWHM of 26 fs and the shortest reported pulse duration in this spectral band from a nonlinear fiber derived source (to the best of our knowledge). The more energetic pulse has a diminished pulse duration, at 59 fs FWHM. With some improvements to the system, we should be able to continue increasing the pulse energy at 1250 nm to potentially 4.2 nJ with the current seed source.

To demonstrate the utility of our 1250 nm pulse source we took images of fluorescein-dyed lens tissue using a purpose built three-photon excitation fluorescence microscope. The microscope employed a rapid stage-scanning system to raster a  $\sim 0.25 \text{ mm}^2$  area containing

495x495 pixels. As a preliminary result, with room to optimize the microscope side of the system, the three-photon excitation fluorescence image shows the potential of nonlinear fiber derived 1250 nm pulses to play an active role in the continuing development of multiphoton microscopy.

## PART II: THEORETICAL DESIGN OF A ND-DOPED FIBER

## AMPLIFIER FOR 1340 NM ULTRAFAST PULSES

*Aerodynamically, the bumblebee shouldn't be able to fly, but the bumblebee doesn't know that so it goes on flying anyway.*

Mary Kay Ash

## 11.1. INTRODUCTION AND BACKGROUND

In Chapters 9 and 10, we sought to use fiber-based nonlinear frequency conversions stages to directly generate pulses in the second biological imaging window around 1300 nm with sufficient pulse energy for multi-photon microscopy. In this chapter, we instead propose and analyze a fiber amplifier to amplify the low energy  $\sim 1300$  nm seed pulses ( $< 1$  nJ) generated via nonlinear frequency conversion from 1060 nm seed pulses. With the losses intrinsic to a laser scanning microscope, 5 nJ amplified pulses around 1300 nm should reach the fundamental multi-photon image penetration depth at this wavelength.

Past efforts to develop fiber-laser femtosecond sources of 1340 nm pulses have met with limited success. This chapter presents two innovations in the design of the fiber laser source that will enable successful construction of a robust and compact 1340 nm femtosecond fiber laser. The laser pulses produced by this source would contain enough pulse energy ( $\geq 5$  nJ) to reach the fundamental multi-photon image penetration depth limit for 1340 nm excitation of  $\sim 1.5$  mm [53]. The first innovation is the development of an optimum seed pulse for a novel Nd-doped fluorozirconate (ZBLAN) fiber amplifier using soliton self-frequency shifting

(SSFS) to tune a 1060 nm pulse out to 1340 nm [28, 120], as described in Section 9.3. The second, and key, innovation is to design and develop a Nd-doped ZBLAN fiber amplifier (NDFA) with  $> 10$  dB net gain for a bandwidth supporting  $< 100$  fs pulse durations by adapting recently developed ultrafast fiber amplifier technological innovations to and NDFA system.

Currently, the best amplifier performance is a 6 dB net gain after two Nd-doped ZBLAN fiber segments for 300 fs pulses [125]. The NDFA in Ref [125] seems to have been well below the theoretical limit as the measured peak continuous-wave gain with 2 amplifier fibers separated by a 1050 nm ASE filter was only 8 dB. When compared to another continuous-wave NDFA, using a single amplifier fiber, which demonstrated gains as high as 6.5 dB [126], the dual-amplifier fiber in Ref [125] appears to be  $\sim 4$  dB below the maximum attainable performance. Other researchers have calculated that there is a substantial gain penalty, up to 3 dB, when the fiber lengths are not ideal [127], which underscores the critical need for careful modeling.

It is possible to reach the fundamental depth limit of multi-photon imaging in turbid media at 1340 nm with  $\sim 1.5$  nJ of pulse energy incident on the surface of the specimen [53]. Assuming a reasonable laser scanning microscope efficiency of 40% and a pulse compressor efficiency of 80%,  $\geq 5$  nJ of pulse energy must be obtained from the laser system, which is the target pulse energy performance goal of this proposal. Our pulse duration goal is 80 fs, guided by our recent experience with MPM transcorneal eye imaging, where 80 fs pulses were theoretically determined to provide an optimal signal to noise by balancing accumulated dispersion and nonlinear signal generation [34].

Optimization of the seed pulse energy must be balanced with the efficiency of seeding the gain bandwidth of the NDFA. If the seed pulse is too short in duration, the pulse spectrum will span a width much broader than the NDFA gain bandwidth leading to low gain. Because of spectral broadening in the NDFA amplifier, initial estimates suggest a seed pulse duration of 40 fs and an energy of 0.3 nJ launched into an NDFA should produce a net gain of 12.5 dB, sufficient to produce compressed pulses of 5 nJ. With numerical modeling, the SSFS system and subsequent amplification will be designed and optimized to produce  $\geq 5$  nJ, 80 fs pulses centered at 1340 nm, with an architecture that can be commercialized.

There are two other rival fiber dopants, which also exhibit gain around 1340 nm: praseodymium and bismuth. Praseodymium-doped silicate fibers also came out in the early 1990s [128–130], while Bismuth-doped fibers are a relatively new development [131]. The primary problem with Praseodymium-doped fiber amplifiers are the very long active fiber segments, 10s of meters, necessary to achieve high gain, as these are high numerical aperture fibers and possess  $5\times$  the dispersion and nonlinearity as telecom fiber extracting pulse bandwidth supporting  $< 100$  fs would be challenging. Bismuth-doped fiber amplifiers are promising candidates, given their broad emission spectra at 1300 nm and the absence of competing excited state absorption [132], however, again the active fibers are exceptionally long and have very low absorbed pump to output power (slope) efficiency  $< 5\%$  [133] (for comparison ytterbium-doped fibers amplifiers can have slope efficiencies as high as 80% and NDFA have managed 33% [125] even with sub-optimal peak gain). So far, the optical gain from Bismuth-doped fiber amplifiers is limited too, having demonstrated gains of 5-10 dB [134] and as low as 2 dB [135].

The long fiber lengths of Pr- and Bi-doped amplifiers is problematic for pulse durations  $< 100$  fs, since the increased sensitivity to accumulated higher-order dispersion reduces the compressibility and therefore peak intensity of the pulse. Multiphoton interactions are acutely sensitive to the pulse peak intensity as detected signal levels scale with the intensity as  $I^2$  for SHG [79] and  $I^3$  for THG [101]. In the event that an NDFA proves intractable, however, it could be possible to employ one of these other fiber dopants to produce energetic pulses around 1300 nm. Such a system would be quite different though, as the long fiber lengths would require the amplification of pulses with narrow-bandwidth, 500-1000 fs durations, and then a nonlinear pulse compression stage to achieve  $< 100$  fs durations. Additional system complexity is therefore necessary to produce short pulses at 1340 nm and achieve fundamental depth limited imaging. So, we have chosen Nd-doped ZBLAN fiber for our target system.

## 11.2. DESIGNING A ROBUST SELF-FREQUENCY SHIFTING SYSTEM TO PRODUCE 1340 NM PULSES

The desired NDFA seed pulses balance the competing needs for energy, target temporal duration, and low noise. To produce a laser pulse seed for the proposed 1340 nm NDFA amplifier, we will use SSFS of 1060 nm ultrafast pulses propagating in a nonlinear optical fiber as discussed in Section 9.3.

Producing energetic frequency-shifted soliton pulses is challenging for many reasons. Briefly: to maintain coherence and minimize noise, the 1060 nm seed pulse is limited in pulse energy to 0.5–2 nJ ( $N < 10$ ), depending on the seed pulse duration and PCF group

velocity dispersion and fiber nonlinear coefficient [28]. As seen in Table 9.2, there are however, a number of pulse/fiber combinations which yield  $> 0.2$  nJ soliton seed pulses at 1340 nm.

A turn-key system requires the PCF/SSFS sub-system be mechanically stable and have a long lifetime (comparable to standard telecom componentry). To that end, we will construct a highly transmissive, sealed “fiber cocktail” (or segmented fiber) with angled-physical contact connectors. The connectors can then be mated to commercial fiber optic collimators, eliminating the need for day-to-day re-alignment as well as multi-axis stages and highly dispersive objectives. The fiber cocktail is composed of the necessary length of PCF as per the numerical propagator model spliced on either end to telecom fiber. The benchmark for an acceptable fiber cocktail will be 60% power transmission efficiency, including all losses from fiber coupling (in/out) and all splice losses.

The air-hole guiding structure that gives PCF their unique dispersion profiles also pose problems if foreign bodies infiltrate the hole, leading to degradation in the fiber face. To hermetically seal the PCF, we splice the PCF to telecom fiber using an arc fusion splicer. Using repeated low power heating arcs, the micro-hole structure within the PCF undergoes a controlled collapse with increasing arc count allowing for adiabatic electric field mode adaption from the telecom fiber to the PCF. Typical splice losses at the PCF to telecom fiber interface are 0.7 dB, where we routinely achieve 60% total transmission through such fiber cocktails (splice sealed on both ends). Different PCF have different core sizes, and a splice recipe will need to be developed for the chosen PCF and telecom end fibers. The telecom entrance and exit fibers, which can be  $< 1$  cm in length, have the dual advantage of sealing the PCF as well as allowing us to fix the fiber cocktail into angled-physical contact

connectors. With the connector and telecom entrance fiber, we can make use of commercial fiber optic collimators which are very mechanically stable and enable high free-space to fiber coupling efficiencies.

### 11.3. AMPLIFYING 1340 NM PULSES WITH A NEODYMIUM-DOPED ZBLAN FIBER AMPLIFIER

The crux of this chapter proposal is an amplifier for low energy ( $\sim 0.25$  nJ) seed pulses at 1340 nm, capable of  $> 10$  dB gain and generating amplified pulse energies  $\geq 5$  nJ. Such pulse energies will directly enable the implementation of multi-photon imaging platforms with on-sample pulse energies sufficient to reach the fundamental image penetration depth limit at 1340 nm in biological tissue [53].

The amplifier system we propose resurrects the NDFA technology from the early 90s [136, 126, 137, 127, 125] and joins it with one of several techniques to manage the accumulated nonlinearity within the amplifier: chirped-pulse amplification (CPA) [100], divided-pulse amplification (DPA) [138], and negative-CPA [90] to keep gain extraction high while also maintaining pulse bandwidth to support  $< 100$  fs pulses. The system we propose will utilize the 1315-1360 nm gain bandwidth of Nd-doped ZBLAN fiber to amplify pulses at 1340 nm from  $\sim 0.25$  nJ to 5 nJ, and use a counter-pumped pre-amplifier followed by a double-passed, bi-directionally pumped power amplifier. This architecture and the two seed pulse conformations are shown in Fig. 11.1. The filter separated gain fibers will minimize both the gain competition from 1050 nm amplified spontaneous emission and the total amplifier complexity. The single fiber gains will be within the documented 6.5 dB peak gain performance of an NDFA [126], and the total system gain would be superior to previously reported NDFA short pulse amplifier [125].

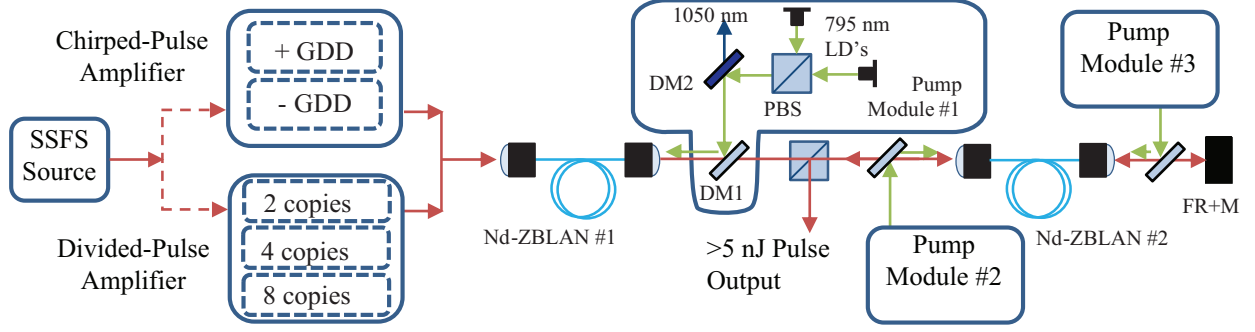


FIGURE 11.1. A schematic of the Nd-doped fiber amplifier: DM1: dichroic mirror reflecting 795 and 1050 nm and transmitting 1340 nm, DM2: dichroic mirror reflecting 795 nm and transmitting 1050 nm, PBS: polarizing beam splitter, LD: laser diodes, FR+M: Faraday rotator and a mirror.

In the same way a numerical propagator model allows us to explore the various nonlinear SSFS systems, an accurate amplifier model will allow us to find an amplifier design without needing to build and test every configuration of fiber length, chirped-pulse, and divided-pulse amplifier. As a preliminary fiber amplifier numerical propagator, we use the same propagator described in Appendix A, but appropriately modified for the material differences between fused silica and ZBLAN fiber along with the inclusion of frequency and fiber length dependent gain. The ZBLAN fiber dispersion was taken from Ref. [125], and is shown in Fig. 11.2 (green curve). Somewhat interestingly, for as different as the Nd-doped ZBLAN fiber is from fused silica and the  $\sim 300$  nm separation between 1060 and 1340 nm, pulses at 1060 and 1340 nm propagate with very similar dispersions in their respective optical fibers. We highlight this similarity in the dashed-dot line in Fig. 11.2.

The ZBLAN Raman response function comes from an intermediate-broadening model of the Raman gain from Ref. [139]. And, the lower nonlinear index of refraction of ZBLAN,  $n_2 = 2.8 \cdot 10^{-20} \text{ m}^2/\text{W}$ , was taken from Ref.s [136, 125] (compared to fused silica,  $n_2 = 3.2 \cdot 10^{-20} \text{ m}^2/\text{W}$ ). The approximate nonlinear coefficient then, is  $\gamma_0 = 0.0034 \text{ 1}/(\text{W m})$ .

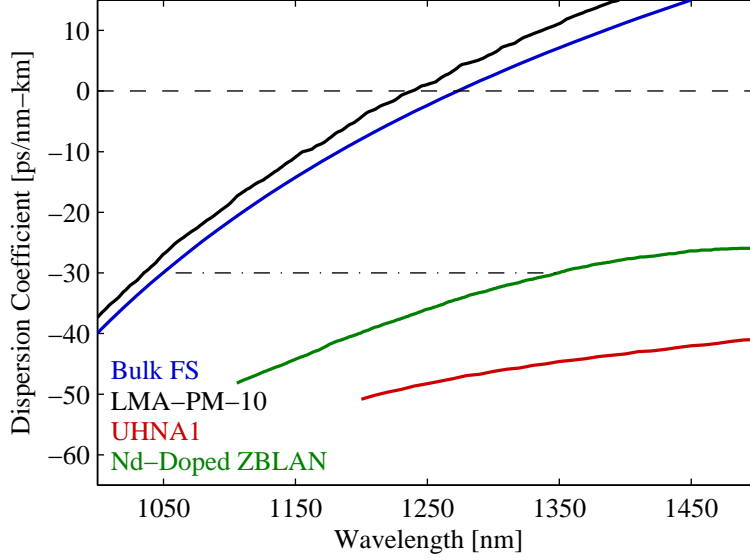


FIGURE 11.2. Dispersion files for bulk fused silica (blue) and the photonic crystal fiber LMA-PM-10 (black), a solid high numerical-aperture fiber UHNA1 (red), and Nd-doped ZBLAN fiber (green).

The gain spectrum,  $g(\omega)$ , was taken from Ref. [136], and is shown in Fig. 11.3 compared to a representative frequency-shifted soliton seed pulse power spectrum. The gain bandwidth supports  $\sim 100$  fs pulse durations. For comparison, the overlap between the frequency-shifted soliton (75 fs 1060 nm seed pulse in a 975 ZDW fiber with  $N = 6$ ) in Fig. 11.3 and the gain bandwidth is 74%. The overlap between frequency-shifted soliton and the Nd-doped ZBLAN gain bandwidth for a number of pulse/fiber combinations are listed in Table 9.2.

The gain coefficient was allowed to vary along the length of the fiber, where we have assumed the gain coefficient is dependent on the pump absorption,  $\sigma'_{\text{pump}} = 150$  dB/m, but independent of the amplified spontaneous emission and 1340 nm amplification (a below gain saturation assumption). We orient the pump intensities for the two gain fibers as counter propagating in the first gain fiber and a symmetric co- and counter-propagating in the second gain fiber. The length dependent gain coefficient was determined by analyzing the differential equation:  $\frac{\partial E}{\partial z} = \alpha E \rightarrow E(z) = E_0 e^{\int_0^z \alpha dz}$ . For a co-propagating pump, the

gain term  $\alpha$  exponentially decays as the pump light is absorbed:  $\alpha = Ae^{-\sigma'_{\text{pump}}z}$ . The net gain in electric field then is,

$$(11.1) \quad E(z) = E_0 e^{\int_0^z Ae^{-\sigma'_{\text{pump}}z'} dz'}$$

Choosing some peak net gain for a fiber section of length  $L$ , e.g.  $G = 4.5$  dB (a gain in energy) over 87 mm of fiber (13 dB pump absorption at 150 dB/m), we can solve for the free parameter  $A$  for the case with co- and counter-propagating pump fields,

$$(11.2) \quad A = -\frac{\log \sqrt{\text{NetGain}} \alpha_{\text{pump}}}{2e^{-(\alpha_{\text{pump}}L)} - 1}$$

$$(11.3) \quad \alpha_{\text{pump}} = -\frac{\log 10^{-\frac{\sigma'_{\text{pump}}}{10}L}}{L}$$

In the numerical model, the gain per step becomes

$$(11.4) \quad E(\omega, z + dz) = E(\omega, z) (g(\omega)(G(z + dz) - 1) + 1)$$

$$(11.5) \quad G(z + dz) = e^{(Ae^{-\alpha_{\text{pump}}z} + Ae^{-\alpha_{\text{pump}}L}e^{\alpha_{\text{pump}}z})dz}$$

The two terms within the exponential in Eqn. 11.5 account for the co-propagating and counter-propagating pump light, respectively, where for counter-propagating pump light only the exponential reduces to  $e^{Ae^{-\alpha_{\text{pump}}L}e^{\alpha_{\text{pump}}z}}$ . This simplistic means of accounting for the gain variation is intended to approximate the laboratory conditions where we can simply turn a knob to adjust the pump power, and therefore net peak gain.

Fig. 11.3 shows the Nd-doped ZBLAN gain bandwidth (red-curve) compared to the frequency-shifted soliton seed pulse produced by the 75 fs FWHM  $N = 6$  pulse at 1060

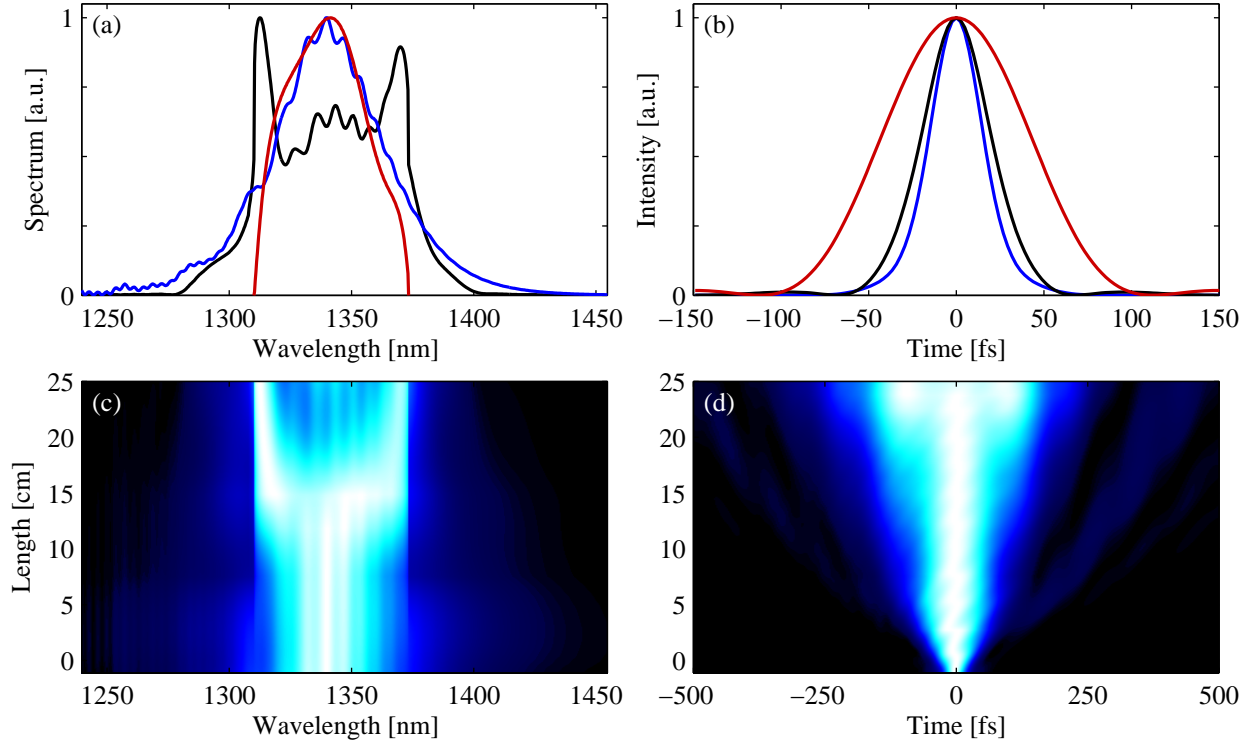


FIGURE 11.3. Frequency-shifted soliton amplification in a Nd-doped fiber amplifier. The (a) power spectra and (b) TL intensities of the frequency-shifted soliton seed pulse (blue), amplified pulse (black), and the gain bandwidth (red). The evolution in (c) normalized power spectrum and (d) normalized intensity as a function of propagation through the amplifier, shown with linear color maps.

nm from Table 9.2 and Fig. 9.5, where we have added a 75% energy loss to the seed pulse to model coupling losses. Clearly, the soliton seed pulse power spectral bandwidth exceeds the gain bandwidth, as seen in Fig. 11.3. Preliminary amplifier modeling indicates some form of peak intensity reduction of the seed pulse is critical to maximize gain extraction, as it allows for some initial gain narrowing of the seed pulse bandwidth. Directly injecting the transform-limited (TL) soliton pulse (by virtue of the soliton propagation leading to its formation) into the amplifier results in low gain extraction. As a conservative model, we set the net gain in each of the three fiber sections (pre-amplifier and double-passed power

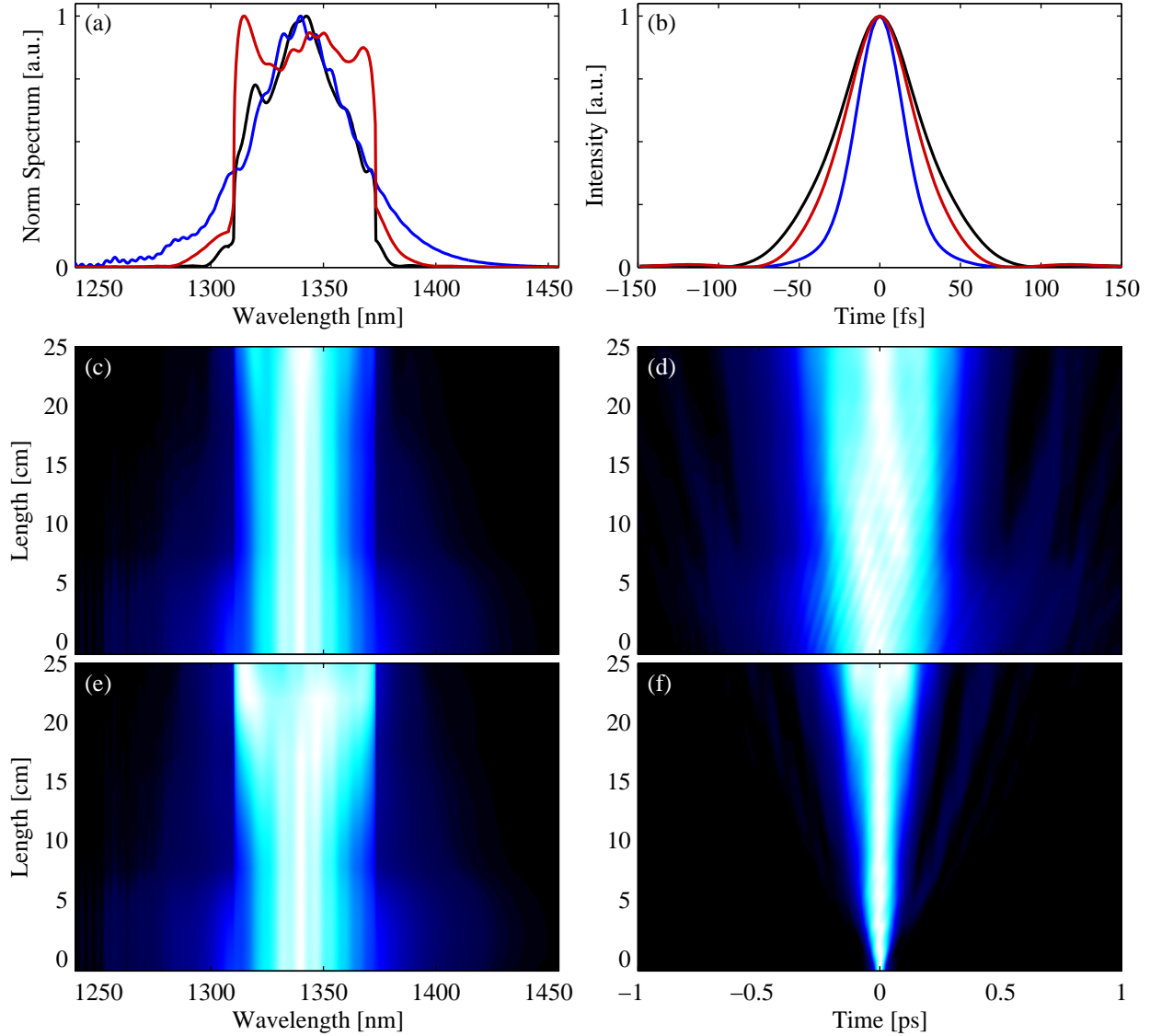


FIGURE 11.4. The (a) power spectra and (b) TL intensities for the frequency-shifted soliton seed pulse (blue), CPA pulse (black), and DPA pulse (red). The evolution in the (c,e) normalized power spectrum and normalized intensity (d,f) with propagation through the NDFA using CPA (c,d) and DPA (e,f), shown with linear color maps.

amplifier, each 87 mm in length) to: 5.5, 5.0, and 4.5 dB. The gain of the un-modified soliton pulse is 11.3 dB, producing a pulse energy of 3.8 nJ.

Positive- and negative-CPA and DPA achieve the necessary peak intensity reduction for efficient energy extraction, but each have different features. Starting with the two more traditional schemes of positive-CPA and DPA, Fig. 11.4 show the amplified pulse power

spectra and TL intensities along with the pulse evolutions through the amplifiers. While the broad bandwidth of the frequency-shifted soliton seed reduces the overlap between seed spectrum and gain, it does allow for an exceedingly simple chirping scheme: bulk material. A double-passed 5 mm ZnSe window tilted to Brewsters angle provides enough group delay dispersion (GDD) to reduce the peak power by an order of magnitude, chirping the soliton seed pulse to 400 fs. Using the same amplifier setting, the gain extraction with this simple CPA setup is 12.7 dB and an amplified pulse output of 5.2 nJ. The CPA output pulse power spectrum is narrower than the amplified un-modified seed pulse from gain narrowing; but the FWHM TL duration is still 60 fs.

Modeling a DPA using a single stage of pulse division (2 pulses) and the same amplifier settings as before, we find the DPA results in less gain narrowing and more nonlinear re-shaping/broadening than the CPA. As there is less gain narrowing, the DPA gain extraction is lower at 12.1 and an amplified pulse energy of 4.6 nJ. The broader amplified output pulse from DPA does however, support a shorter FWHM TL pulse duration than the CPA, at 50 fs.

Another method of mitigating the peak-power of the seed pulse is applying negative GDD, hence negative-CPA. The Nd-doped ZBLAN fiber has normal dispersion at 1340 nm, so the pulse will re-compress with propagation through the fiber. In the presence of negative chirp, self-phase modulation will compress the power spectrum rather than broadening it. The sign of the nonlinear phase accumulation will cancel, or eliminate, the instantaneous frequencies in the extrema of the pulse intensity profile. For the purposes of the NDFA under consideration, a prism compressor (acting as a stretcher) can provide the necessary negative chirp magnitude.

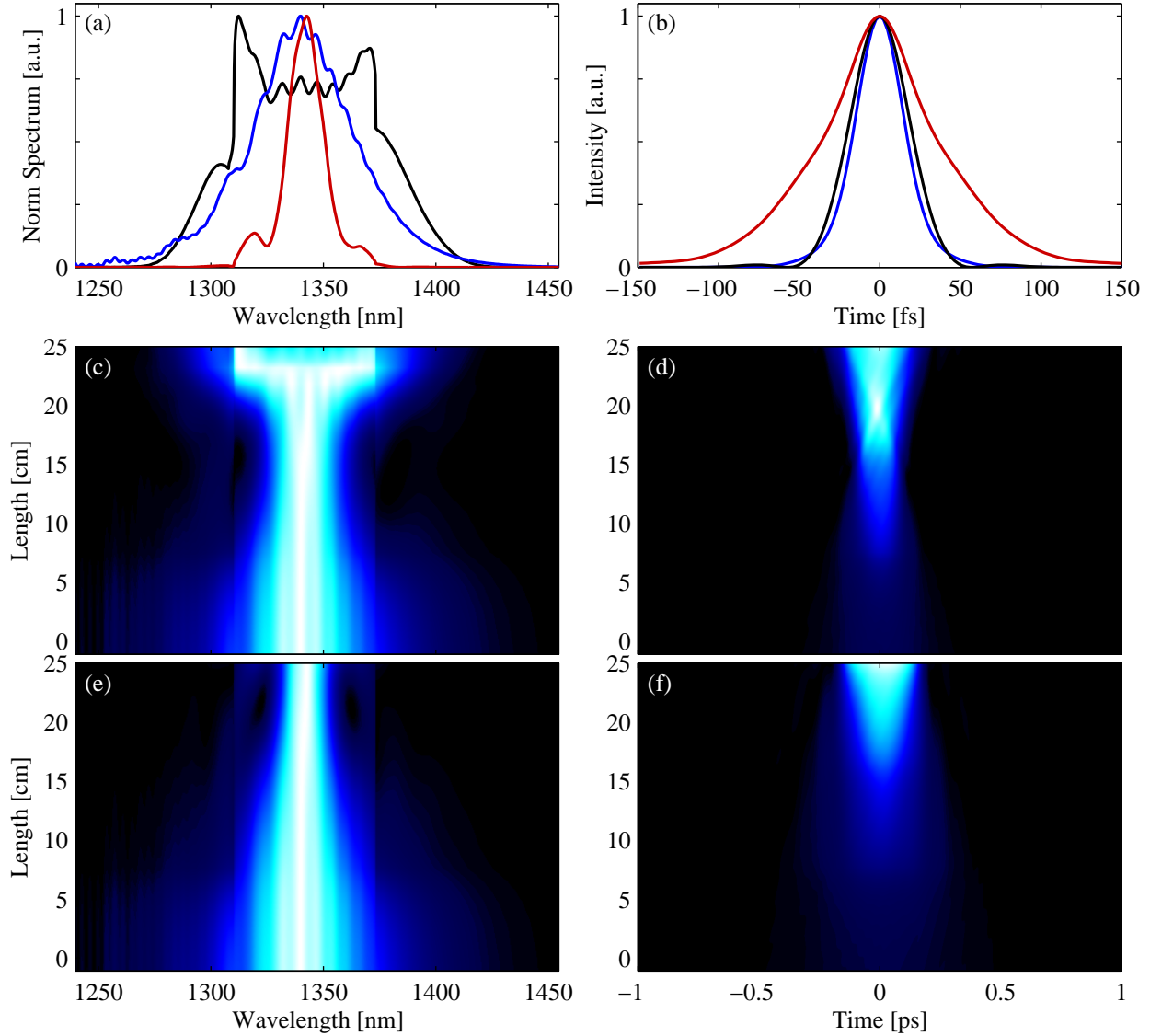


FIGURE 11.5. The (a) power spectra and (b) TL intensities for the frequency-shifted soliton seed pulse (blue), small negative-CPA pulse (black), and large negative-CPA pulse (red). The evolution in the (c,e) normalized power spectrum and normalized intensity (d,f) with propagation through the NDFFA using large (c,d) and small (e,f) negative-CPA, shown with linear color maps with the intensity normalized to the entrance intensity.

We show in Fig. 11.5 amplifier model results for two different GDDs:  $-5.7 \text{ kfs}^2$  (small) and  $-10.2 \text{ kfs}^2$  (large). The smaller negative-CPA is de-chirped within the amplifier at  $\sim 17$  cm, and after additional amplification,  $\sim 20$  cm, the pulse has enough peak power to drive significant spectral broadening. The small negative-CPA case produces the largest spectral

bandwidth of any of the modeled amplifiers, supporting a TL duration of 40 fs. The spectral compression and narrower bandwidths present through most of the amplifier also maintain relatively high gain extraction at 12.5 dB and 5 nJ output pulse energies.

The large negative-CPA amplifier re-compresses only at the very end of the fiber amplifier. The reduced power spectral bandwidth through the final amplifier stage results in the highest gain extraction at 13.1 dB and pulse energies of 5.7 nJ. The 13.1 dB gain is quite close to the full peak gain of 15 dB ( $G$  in the model)! The drawback is the narrowest power spectrum of all the modeled amplifiers, but still supporting a  $< 100$  fs TL duration of 70 fs. The negative-CPA version of the amplifier allows for a wide tuning range in power and bandwidth supported pulse duration. That it requires a more complicated front-end would be offset in the event that more power or  $< 50$  fs pulses were necessary.

For a given pulse energy and spectral bandwidth, the maximum nonlinear signal is typically afforded by the TL (highest possible) peak intensity. For pulses with bandwidths supporting  $< 100$  fs pulse duration generated through nonlinear propagation in optical fiber, it is our experience that it is necessary to compensate both the group-delay dispersion and third-order dispersion to reach better than  $\sim 75\%$ . Uncompensated higher-order dispersion reduces the peak intensity and instead increases the background average power, lowering the signal-to-noise ratio as function of average power. Therefore, it will be critical to design a pulse compressor which can account for even third-order dispersion.

#### 11.4. FEASIBILITY ANALYSIS OF POTENTIAL 795 NM PUMP POWERS

At a repetition rate of 60 MHz, 5 nJ pulse energies equate to 300 mW of average power from the fiber laser source. This is the necessary pulse energy to reach the sample with  $\geq 1.5$  nJ of 1340 nm pulse energy. To reach this number, we assumed the following efficiencies:

pulse compressor (80%), laser scanning hardware (80%), and objective transmission (50%). This 5 nJ pulse goal is predicated on other researchers reaching the fundamental depth limit for multi-photon imaging in turbid media with 1.5 nJ pulses at 1280 nm incident on murine brain [53]. At higher pulse energies, more sophisticated pulse manipulation is possible due to the increase overhead for additional system losses. At  $\sim 10$  nJ pulse energy (and 600 mW of average power), there would be enough pulse energy to employ a pulse shaper [27, 62, 63] to optimize molecular two-photon excitation [81, 82].

Assuming a conservative slope efficiency of 18% (output/input power) [126, 125], our NDFA will require 1.7 W of pumping to reach 5 nJ pulses. Combining three pairs of 400 mW laser diodes at 795 nm, the Nd-doped ZBLAN peak absorption [140], as shown in Fig. 11.1, we could achieve 1.7 W of total pump power if the free-space to fiber coupling losses on the pump intensity into the NDFA are  $< 30\%$ . The best-case performance would be 80% fiber coupling for the pump (1.9 W) and a slope efficiency of 23% from which we could extract 7.4 nJ pulses.

If necessary, a fourth stage of amplification would be possible, by double passing the first gain fiber. Such a configuration would necessitate an additional pump module, bi-directionally pumping the first Nd-doped ZBLAN fiber; increasing the 795 nm pump power to  $> 2.5$  W and potentially producing 10 nJ pulses at 23% extraction efficiency.

Between the conservative estimates of coupling and extracted power and the possibility of adding a fourth amplifier stage, there is good reason to believe we could construct a 13 dB NDFA for SSFS generated seed pulses. We have a diversity of pulse preparation options,  $\pm$ CPA and DPA, allowing a broad tuning range in the output amplified bandwidth and energy. From the range of possible amplified pulses, we have strong confidence in the ability

of an SSFS seeded NDFA to produce pulses highly suited to multi-photon microscopy in the second biological imaging window.

## CHAPTER 12

### PART III: NON-IMPULSIVE STIMULATED RAMAN

#### SCATTERING WITH CHIRPED SUPERCONTINUUM PULSE PAIRS

*There are no rules here – we’re trying to accomplish something.*

Thomas Edison

“Finger-printing” molecules based on coherent Raman scattering is field of high interest to the biomedical community, as it is capable of generating images of molecular concentration without the need to introduce exogenous labels or markers. Coherent Raman scattering techniques such as coherent anti-Stokes Raman scattering [141] and stimulated Raman scattering loss and gain [142] have proven extremely valuable in generating three-dimensional, high-resolution images. But, the signals in these microscopes generally do not encode vibrational spectra, rather they generate contrast based on one to a few Raman bands. In this chapter, we examine non-impulsive stimulated Raman scattering by a chirped, broadband pulse pair to excite coherent molecular vibrations in a manner amenable to rapidly capturing Raman spectra across the entire finger-print region ( $500\text{--}2000\text{ cm}^{-1}$ ).

#### 12.1. THEORETICAL TREATMENT OF NONRESONANT IMPULSIVE VIBRATIONAL EXCITATION

The first component of this chapter, will be to work through the theoretical treatment of the vibrational phase coherence of nonresonant impulsive excitation. Following Dhars et al. [2], I will show how the classical and quantum mechanical treatment give rise to nearly equivalent results. The most interesting component of which is the dependence of the

excitation on the frequency composition of the pump pulse intensity profile, as molecular nuclei can not follow the field oscillations. This dependence makes for a rich environment to tailor the excitation pulse to a particular vibrational resonance.

The first order of business is choosing a Hamiltonian. Expanding the Hamiltonian in terms of applied electric field degree,

$$H = H_0 + H_1 + H_2 + \dots$$

We are interested in maintaining components which describe the isolated system and give rise to light scattering processes, while eliminating the components describing light absorption, and higher order nonlinear interactions. The remaining terms of the Hamiltonian of interest are  $H = H_0 + H_2$ . We will also begin by assuming negligible damping, a seeming weakness of this treatment but which is fixed later.  $H_0$  then, using normal mode displacements and the conjugate momentum, is

$$H_0 = \frac{1}{2} \sum_{q\alpha} P^\alpha(-q)P^\alpha(q) + \omega^\alpha(q)\omega^\alpha(q)Q^\alpha(-q)Q^\alpha(q).$$

where  $q$  is the wavevector and  $\alpha$  labels the material modes. The conjugate momentum is a generalization of the momentum operator, which allows for the description of the momentum in terms of the Lagrangian formalism. Practically, it is very similar to the momentum we typically use except it's defined to have the property,  $\{q_i, p_j\} = \delta_{i,j}$ . Where the  $\{\}$  term is the Poisson bracket and is the classical mechanics analogue to the quantum mechanical commutator.

The term describing first-order light scattering is,

$$H_2 = - \sum_{i,j} \sum_{\mathbf{q}} \delta\alpha(\mathbf{q}, t) F_{i,j}(-\mathbf{q}, t).$$

The force term is,

$$F_{i,j}(\mathbf{q}, t) = \frac{1}{8\pi} E_i(\mathbf{q}, t) E_j(-\mathbf{q}, t).$$

In the Placzek approximation, the change in polarizability is,

$$\delta\alpha_{i,j}(\mathbf{q}, t) = \sum_{\alpha,\xi} \frac{\partial\alpha_{i,j}}{\partial Q_\xi^\alpha} Q_\xi^\alpha(\mathbf{q}, t).$$

Now, of course, let's make some simplifications: dropping the polarization indices ( $\mathbf{q}$ ), neglect the tensorial nature of the dielectric operator ( $H_2 \propto \sum_{i,j} F_{i,j}(t) \rightarrow H_2 \propto F(t)$ ), and consider a single mode ( $\alpha$ ). Substituting  $\partial\alpha/\partial Q = \alpha'$ , the complete Hamiltonian (of interest) is,

$$(12.1) \quad H = \frac{1}{2}(P^2 + \omega^2 Q^2) - \alpha' Q F(t).$$

Defining a seemingly arbitrary variable  $a_c(t)$  (which is clearly related to the ladder operators),

$$a_c(t) \equiv \left(\frac{\omega}{2\hbar}\right)^{1/2} Q + i \frac{P}{(2\hbar\omega)^{1/2}}.$$

The evolution of this variable is found using the Poisson bracket formulation, which is the classical mechanics analogue to the Heisenberg equation (the irony of calling classical mechanical formulations the analogue to a quantum mechanical approach is not lost on me).

As a brief aside, Hamilton's equation of motion describe the time evolution of a system

according to:

$$\frac{d\mathbf{p}}{dt} = -\frac{\partial H'}{\partial \mathbf{q}}$$

$$\frac{d\mathbf{q}}{dt} = \frac{\partial H'}{\partial \mathbf{p}}.$$

where the Hamiltonian here is the usual,  $H' = T + V = \frac{p^2}{2m} + V(q)$ . The second piece we need is the Poisson bracket:

$$\{f, g\} = \sum_{i=1}^N \left( \frac{\partial f}{\partial q_i} \frac{\partial g}{\partial p_i} - \frac{\partial f}{\partial p_i} \frac{\partial g}{\partial q_i} \right).$$

Then the time evolution of a variable,  $f(p, q, t)$  is,

$$\frac{d}{dt} f(q, p, t) = \{f, H\} + \frac{\partial f}{\partial t} = \left( \frac{\partial}{\partial t} - \{H, \cdot\} \right) f.$$

The evolution of  $a_c(t)$ , with  $\partial a_c(t)/\partial t = 0$ , then is

$$\frac{da_c(t)}{dt} = -i\omega a_c(t) + \frac{i}{(2\hbar\omega)^{1/2}} \alpha' F(t).$$

The solution to the inhomogeneous, ordinary differential equation is

$$a_c(t) = e^{-i\omega(t-t')} \left( a_c(t') + e^{-i\omega t'} \frac{i}{(2\hbar\omega)^{1/2}} \alpha' \int_{t'}^t F(\tau) e^{i\omega\tau} d\tau \right)$$

$$= e^{-i\omega(t-t')} (a_c(t') + e^{-i\omega t'} \lambda).$$

Dhar et al. now adds in a small damping term, without much in the way of explanation,

$$\lambda \equiv \frac{i}{(2\hbar\omega)^{1/2}} \alpha' \int_{t'}^t F(\tau) e^{i\omega\tau} d\tau \rightarrow \frac{i}{(2\hbar\omega)^{1/2}} \alpha' \int_{t'}^t F(\tau) e^{-\gamma(t-\tau)} e^{i\omega\tau} d\tau.$$

which assumes  $\gamma \ll \omega$ . A reasonable assumption for vibrations  $\gg 10\text{cm}^{-1}$ . The damping term introduces not only a relaxation of the excited vibrational coherence. A pump intensity profile that has a beat frequency resonant with a vibrational state will not continuously add energy to the resonant oscillation. Instead the oscillator will reach a steady state, where the molecule will “forget” the earlier pump intensity driving oscillations.

Using the definition of  $a_c(t)$ , the real and imaginary components give rise to the normal mode displacements and momenta:

$$Q(t) = \left(\frac{2\hbar}{\omega}\right)^{1/2} |\lambda| \sin(\omega t - \phi)$$

$$P(t) = (2\hbar\omega)^{1/2} |\lambda| \cos(\omega t - \phi)$$

$$E(t) = \hbar\omega |\lambda|^2.$$

where  $\cos(\phi) = \text{Re}\{i\lambda/|\lambda|\}$  and I have assumed the molecules started in the ground state. Notice, the energy term is not what we usually describe as the energy of a vibrational mode, namely the vibrational quanta in a particular vibrational mode. Here, the normal vibrational mode oscillates at angular frequency  $\omega$  with  $E(t)$  describing the amount of energy in the vibrational mode (rather than the energy between the ground state and the vibrational mode).

As the classical treatment relied on formalisms with quantum mechanical analogues, it is unsurprising that we can approach the problem without the need for introducing a perturbation. Like the classical approach, we will start with an un-damped Hamiltonian, and eventually just poach the modified  $\lambda$  to include the damping.

To start, the lowering and raising operators are:

$$a = \left(\frac{\omega}{2\hbar}\right)^{1/2} Q + i\frac{P}{(2\hbar\omega)}^{1/2}$$

$$a^\dagger = \left(\frac{\omega}{2\hbar}\right)^{1/2} Q - i\frac{P}{(2\hbar\omega)}^{1/2} .$$

The Hamiltonian is the same as before (12.1), except it will be rewritten in terms of the raising and lowering operators,

$$H(t) = \hbar\omega(a^\dagger(t)a(t) + 1/2) - \left(\frac{\hbar}{2\omega}\right)^{1/2} \alpha' F(t)(a(t) + a^\dagger(t))$$

To solve for transitions,  $i\hbar\partial/\partial t\langle z, t|z', t'\rangle = 1/(i\hbar)\langle z, t|H(t)|z', t'\rangle$ , we use the Heisenberg equation

$$\frac{da(t)}{dt} = \frac{1}{i\hbar}[a(t), H(t)]$$

which, as mentioned previously, is the quantum analogue to the Poisson bracket in classical Hamiltonian mechanics. The Heisenberg equation results in

$$\frac{da(t)}{dt} = -i\omega a(t) + \frac{i}{(2\hbar\omega)^{1/2}} \alpha' F(t)$$

$$a(t) = e^{-i\omega(t-t')} \left( a(t') + \frac{ie^{-i\omega t'}}{(2\hbar\omega)^{1/2}} \int_{t'}^t F(\tau) e^{i\omega\tau} d\tau \right)$$

which is identical to the classical case. The expectation values are similar to the classical case, but now of course they represent expectation values rather than classical variables.

$$\langle Q(t) \rangle = \left( \frac{2\hbar}{\omega} \right)^{1/2} |\lambda| \sin(\omega t - \phi)$$

$$\langle P(t) \rangle = (2\hbar\omega)^{1/2} |\lambda| \cos(\omega t - \phi)$$

$$\langle E \rangle = \hbar\omega(\langle n \rangle + 1/2) = \hbar\omega(|\lambda|^2 + 1/2)$$

The major difference is in the energy, as the quantum mechanical description is both quantized and has a minimum, ground state energy. The energy calculated though  $\langle E \rangle$ , is still the energy in an oscillator of particular frequency  $\omega$ .

## 12.2. CHIRPED-PULSE EXCITATION IN THE IMPULSIVE-LIMIT

The theoretical formalism developed above holds true for not only transform-limited (TL) pulses (i.e. the impulsive-limit), but also for more complicated pulse profiles such as chirped pulse pairs. While pulse shapers [62, 27] make it possible to deliver TL, or functionally TL, pulses to the focus of a microscope it is not without added challenges such as decreased average power and increased spatial wavefront error. TL pulses also excite all the vibrational modes within the target sample simultaneously, which is either a positive or a negative depending on the particular application. The high peak power of TL pulses can also produce a significant non-resonant background, reducing the possible signal-to-noise ratio depending on the coherent Raman detection scheme. For these reason, we will investigate a chirped pulse pair configuration.

The electric field is taken as a TL Gaussian pulse:  $E_0(t) = \exp(2 \ln(2) \left(\frac{t}{\tau}\right)^2) \exp(-i\omega_0 t)$ , with a full-width at half-maximum (FWHM) of  $\tau$  and a central frequency of  $\omega_0$ . The chirped pulse pair, we represent in the frequency domain

$$E_i(\omega) = E_0(\omega) \exp\left(-i\left(\frac{\beta_2}{2}\omega^2 + \beta_{1,i}\omega\right)\right), \quad \text{where} \quad \beta_{1,i} = \begin{cases} +\frac{\Delta T}{2} & : i = 1 \\ -\frac{\Delta T}{2} & : i = 2 \end{cases}$$

where

$$E(\omega) = \int E_0(t) e^{-i\omega t} dt$$

$$E_0(t) = \int E(\omega) e^{i\omega t} d\omega,$$

$\beta_2$  is the group delay dispersion (GDD),  $\beta_1$  is the group delay, and the total delay between the two pulses is  $\Delta T$ . The pump field then is  $E(t) = E_1(t) + E_2(t)$  and the force term driving the vibrational excitations is  $F \propto |E(t)|^2$ .

We start with the un-damped oscillator approximation to illustrate the major characteristics and best case performance of chirped pulse pair excitation. Fig. 12.1 shows some of the characteristic features of the chirped pulse pair vibrational excitation, using Gaussian 15 fs TL FWHM pulses chirped to several different durations. The GDD spreads the pulse power spectrum out in time; leading to a chirp in the carrier frequency of the electric field, labeled the instantaneous frequency. The temporal overlap of different carrier frequencies between the two pulses produces a so called beat in the total intensity due to temporal interference, as shown in Fig. 12.1(a-c). Unlike the case of TL pump pulses, the beating between the chirped pulse pair can only excite vibrational modes whose period corresponds to the period

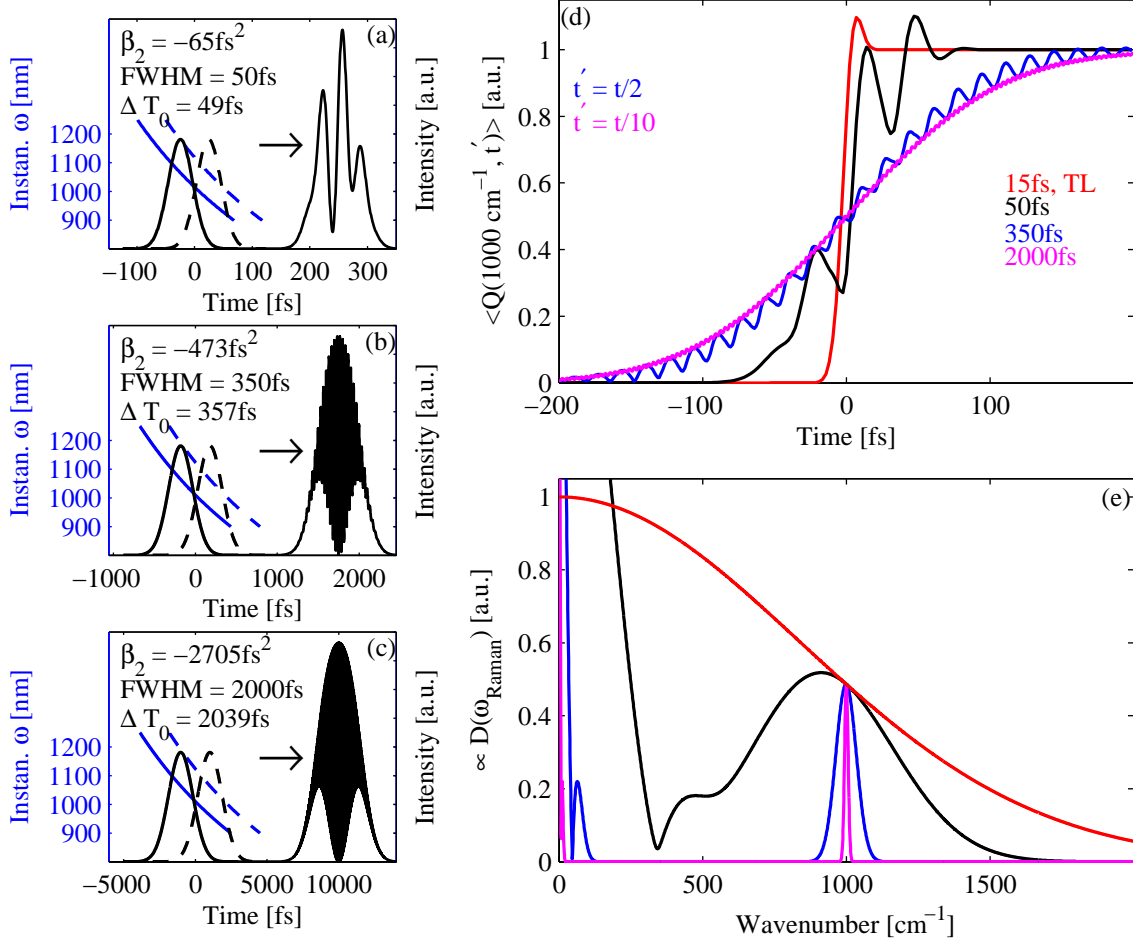


FIGURE 12.1. (a-c) The intensity, instantaneous frequency, and temporal interference between chirped pulse pairs with 15 fs FWHM TL, chirped to 50, 350, and 2000 fs FWHM with the appropriate GDD and each containing equal amounts of energy. (d) The un-damped expectation value of the normal mode displacement of a resonant  $1000\text{ cm}^{-1}$  mode as function of time for the TL 15 fs pulse with energy equal to a single pulse of of a pulse pair (red) and the three chirped pulses pairs: 50 (black), 350 (blue), and 2000fs FWHM (magenta). The plotted temporal axis of the modal displacement for the 350 and 2000 fs chirped pulse pair has been scaled by factors of  $1/2$  and  $1/10$ , respectively, for ease of comparison. (e) The corresponding un-damped vibrational excitation spectra for the same four pulse cases, where  $D(\omega_{\text{Raman}})$  is the maximum vibrational oscillator displacement.

of the intensity beat. In this example, the delays between the three differently chirped pulses give rise to beats at  $1000\text{ cm}^{-1}$ .

The beauty of this pump configuration is the realization of molecular oscillator displacement amplitudes of equal magnitude to the TL pump pulse case, see Fig. 12.1(d) and (e),

without the need to deliver 15 fs pulses to the sample. The TL pump pulse stretches an oscillator with a normal vibrational mode at  $1000 \text{ cm}^{-1}$  to a maximum displacement with a pseudo-instantaneous driving force, as seen in Fig. 12.1 (d), along with all the other normal vibrational modes within the excitation envelope of the TL pulse (Fig. 12.1(e) red-line). The chirped pulse pairs resonantly “kicks” the oscillator with each cycle of the intensity beat, gradually building up the oscillator displacement amplitude. As more chirp is added, the growth in oscillator displacement amplitude requires more kicks, since each kick has a reduced power. In reality perfect equivalence in oscillator displacement magnitude between impulsive and non-impulsive excitation is a figment of the zero-damping approximation. With damping (typical decay times of  $\sim 4$  ps), pulses chirped to 2 ps drive oscillator displacements to a magnitude  $\sim 60\%$  of the impulsive excitation. The reduced oscillator displacement is also present in other ps pulse based coherent Raman scattering modalities, such as stimulated Raman scattering gain/loss, and so if not optimal at least somewhat typical.

We assign the variable  $D(\omega_{\text{Raman}})$  (Fig. 12.1(e)) to be the maximum displacement of an oscillator at frequency  $\omega_{\text{Raman}}$ , as it is the molecular motion which gives rise to an effective transient index of refraction,  $\delta\chi^{(1)} \propto \alpha'\langle Q \rangle$ , where  $\chi^{(1)}$  is the linear optical susceptibility and  $\alpha' = \frac{d\alpha}{dQ}$  is the differential polarizability [143]. It is this transient index which gives rise to the various modalities in coherent Raman measurements (e.g. in stimulated Raman scattering the transient index imparts a sinusoidal temporal phase modulation onto the probe pulse scattering energy into frequency sidebands and modulating the probe pulse energy). The spectrum of  $D(\omega_{\text{Raman}})$  is therefore the vibrational excitation bandwidth. Increasing the chirp reduces the width of the vibrational excitation spectrum of the chirped pulse pairs,

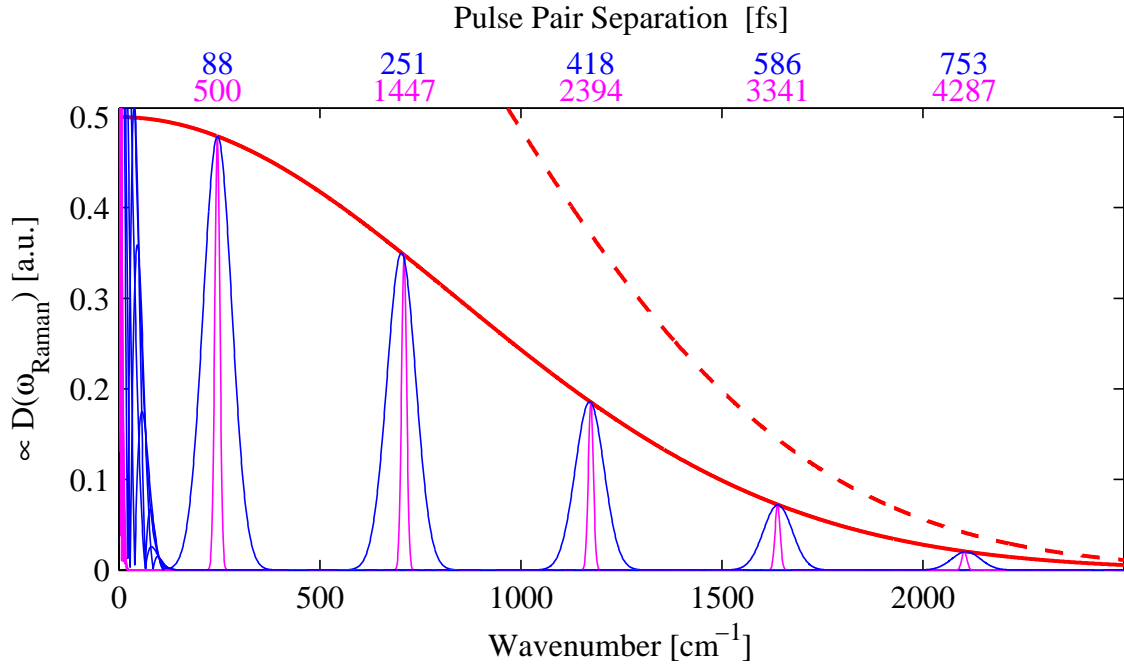


FIGURE 12.2. Examples of vibrational excitation tuning for Gaussian pulse copies chirped to 350 (blue) and 2000 fs (magenta) as compared to the TL cases of total equivalent energy (red-dashed) and single-member energy equivalence (red). The pulse delays for either case, are listed on the upper axis.

where in this example the 2000 fs chirped pulse pair only drives vibrational modes within  $15 \text{ cm}^{-1}$  FWHM around  $1000 \text{ cm}^{-1}$ , Fig 12.1 (3) magenta line.

The intensity beat is tunable in frequency,  $D(\omega_{1,\text{Raman}}) \rightarrow D(\omega_{2,\text{Raman}})$ , by changing the delay between the chirped pulse copies, see Fig. 12.2. The vibration excitation spectra for chirped pulse copies trace out the same excitation spectrum as the TL pulse for changing pulse pair delay. For identical Gaussian pulse copies, the width of the vibrational excitation is independent of pulse pair delay.

Note however, that in the Fig. 12.1 example, the TL pulse was equal in energy to only one pulse from the pulse pair. Experimentally, a 50:50 beam splitter of some kind would generate the chirped pulse pair each with half the energy of the initial pulse. Meaning,

the chirped pulse beating configuration will only excite vibrational excitations to 1/2 the oscillator displacement amplitude as a TL pulse with the energy of both chirped pulses.

To recover the  $2\times$  depreciation in excitation strength from using pulse copies, the seed pulse would need to be split into two pulses, each comprising either the red or blue side of the power spectrum, as shown in Fig. 12.3. For clarity, we will refer to the identical pulse pair configuration as chirped pulse copies. Using a commercial optic as an example: a Semrock longpass filter (LP02-1064RU) could be used as a dichroic mirror to separate a 15 fs FWHM TL pulse centered at 1064 nm into two pulses of nearly equal energy; each comprised of one half of the power spectrum. Defining the longpass filter transmission as  $LP(\omega)$  (and neglecting the filter dispersion), which for the commercial filter is the solid-black curve in Fig. 12.3(a); the pump electric field is then:

$$E(\omega) = \sqrt{2}E_0(\omega) \exp\left(-i\left(\frac{\beta_2}{2}\omega^2 + \frac{\Delta T}{2}\omega\right)\right) \sqrt{LP(\omega)} \\ + \sqrt{2}E_0(\omega) \exp\left(-i\left(\frac{\beta_2}{2}\omega^2 - \frac{\Delta T}{2}\omega\right)\right) \sqrt{1 - LP(\omega)}$$

where the  $\sqrt{2}$  accounts for the increased energy in the spectrally separated pulse pair compared to the identical pulse copies case.

Fig. 12.3(b) shows the increase in potential vibrational excitation for a pulse split using dichroic filters versus a pair of pulse copies, where the same GDD was applied to all three cases. One negative consequence of using a hard-edged filter to generate a red and blue pulses is the addition of structure in the time domain, see Fig. 12.3(d). This temporal structure causes a structured pedestal in the vibrational excitation spectrum. A softer-edged dichroic filter would reduce the ringing, such as the magenta-curve in Fig. 12.3(a), while maintaining the increase in magnitude of the vibrational excitation.

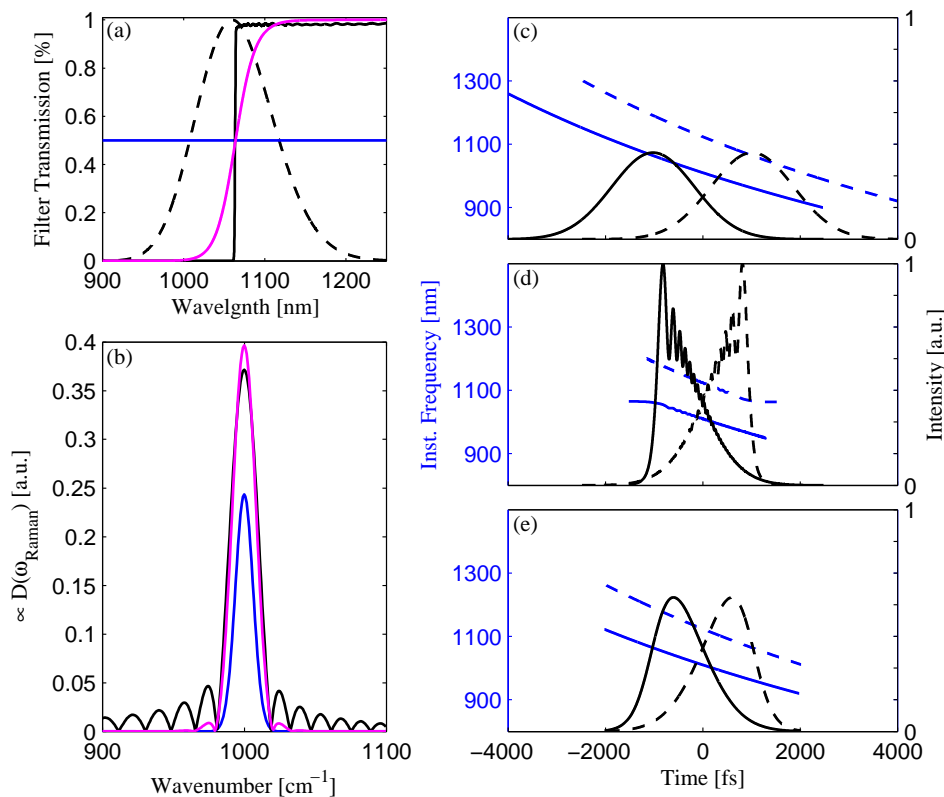


FIGURE 12.3. An alternative pulse pairing concept, using non-identical pulses derived from a dichroic filter to maximize the energy in differing superposed spectral density. (a) The transmission spectrum of a 50:50 beam splitter (blue), an example dichroic longpass filter (LP02-1064RU, black), and a theoretical filter (magenta), along with the power spectrum of a Gaussian 15 fs FWHM TL pulse (black-dashed). (b) The vibrational excitation for pulse delays coupling to a  $1000 \text{ cm}^{-1}$  from each filter in (a). The individual intensities and instantaneous frequencies of the pulse pairs from the filters in (a): pulse copies from the 50:50 beam splitter (c), the LP02-1064RU dichroic filter (d), and the theoretical dichroic filter (e).

Fig. 12.4 shows some example vibrational excitation spectra, along with the curve of the magnitude and width of vibrational excitation as a function of pulse pair time delay for a pulse pair derived from a LP02-1064RU filter. Down to  $\sim 1200 \text{ cm}^{-1}$  the beating in intensity between the time delayed red and blue pulses is nearly equal to the impulsive limit. A negative consequence of the hard-edged filter though, is the changing width of the vibrational excitation as a function of pulse pair delay. As opposed to the case of identical pulse copies, which has a constant vibrational excitation width at all delays (and therefore vibrational

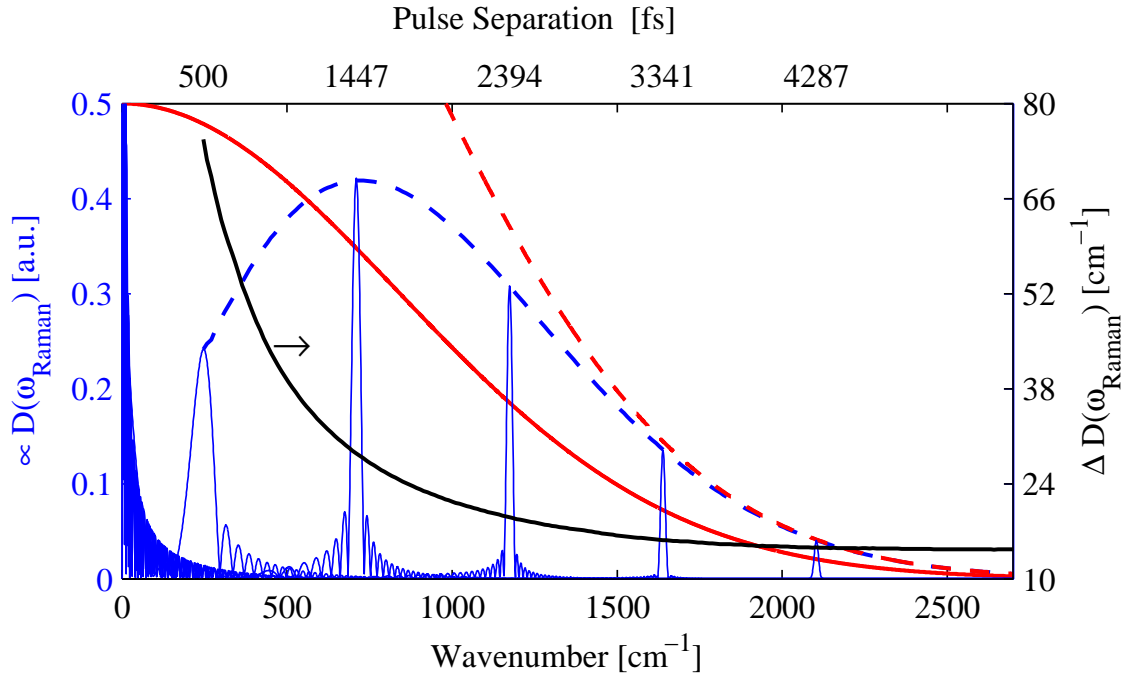


FIGURE 12.4. The vibrational excitation magnitude (blue-dashed) and width (black) from a pulse pair formed by separating a 15 fs Gaussian spectrum into a red and blue pulse via a LP02-1064RU filter, along with a few example excitations (blue) with the corresponding delays listed at the top. The vibrational excitation of the TL Gaussian pulse is also shown (red-dashed) as well as a the excitation spectrum for a TL pulse with half the energy (red).

frequencies), the hard-edged filter generated pulse pair vibrational excitation spectrum increases in width at lower frequencies. This increase in excitation width is accompanied by a reduction in excitation magnitude from the impulsive-limit. Within most of the “fingerprint” region of 500-2000  $\text{cm}^{-1}$  however, the vibrational excitation from red and blue pulses is greater than the 1/2 reduced excitation strength of the identical pulse copies.

One potential means of adding GDD to an ultrafast pulse is through material propagation, notice this is approximately the sort of dispersion accumulated through supercontinuum generation in that it includes higher-order dispersion (HOD) as discussed in Chapter 4. To

account for the HOD, the spectral chirp term becomes

$$\exp\left(-i\frac{\beta_2}{2}\omega^2\right) \rightarrow \exp\left(-i\sum_{j\geq 2}\frac{\beta_j}{j!}\omega^j\right).$$

For comparison, we show in Fig. 12.5 the difference between identical Gaussian pulse copies from a 15 fs FWHM TL pulse, chirped out to 2000 fs FWHM with only GDD and with 250 mm of fused-silica. The difference in the intensity of a single chirped pulse is minimal between the two dispersion cases, as seen in Fig. 12.5(a). The instantaneous frequency however, is sufficiently less linear than the GDD-only chirp as to dramatically alter the excitation spectra, as seen by comparing solid to dashed lines in Fig. 12.5(b). The HOD of the material dispersion, predominantly third-order dispersion, causes a nonlinear instantaneous frequency ramp. The spectrum of temporally interfering carrier frequencies increases, compared to the GDD-only chirp, leading to an increase in the width of the vibrational excitation spectrum (Fig. 12.5(c)). The nonlinear instantaneous frequency ramp also reduces the deposition of energy into narrow vibrational modes, as the intensity beating neither has many individual kicks within a small vibrational frequency window nor the high peak power of a pulse pair with much less chirp. The increase in pump excitation width and reduction in excitation magnitude are dramatic, functionally eliminating this pump configuration as a viable means of selectively exciting vibrational modes.

To further explore the sensitivity of the chirped-beating to HOD, we show in Fig. 12.6 the changes in vibrational excitation magnitude and width as a function of uncompensated fused silica material dispersion added to a Gaussian pulse chirped to 2000 fs with GDD-only. Above 1 cm of material, the magnitude of excitation falls below 75%. The excitation width also increases, where Raman features below  $\sim 30\text{cm}^{-1}$  would be unresolvable. As

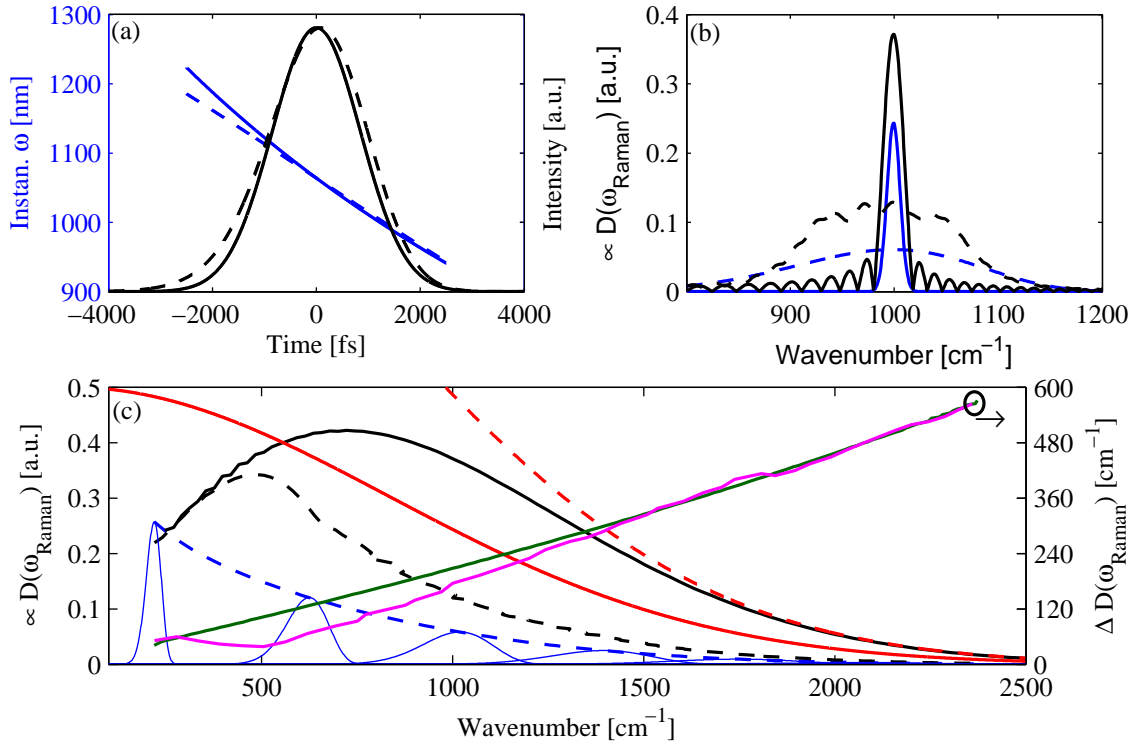


FIGURE 12.5. (a) The intensity and instantaneous frequency with GDD-only (solid) and with the dispersion from 250 mm of fused-silica (dashed). (b) The  $1000 \text{ cm}^{-1}$  vibrational excitation spectrum for identical pulse copies (blue) and LP02-1064RU dichroic filter derived pulse pairs (black) from a 15 fs FWHM TL Gaussian pulse chirped to 2000 fs FWHM with GDD-only (solid-line) and with 250 mm of fused-silica material dispersion (dashed-line). (c) The magnitude and width of the vibrational excitation for a TL 15 fs Gaussian pulse (red-dashed), a TL 15 fs pulse with 1/2 the energy (red-solid), the 15 fs pulse split into two identical pulse copies and pulse chirped to 2000 fs with 250 mm of fused-silica material dispersion (blue-dashed and green), and LP02-1064RU filter separated pulses chirped to 2000 fs FWHM with GDD-only (black-solid, for reference), and 250 mm fused-silica (black-dashed and magenta). Examples of the vibrational excitation spectra from the beating identical pulse copies chirped with fused-silica material dispersion are included (blue-solid).

high numerical-aperture objectives often exceed 1 cm of thickness, to successfully implement chirped-beating excitation in a microscope the entire optical systems HOD, including the objective, would need to be compensated. In practice, this means an evolutionary or genetic algorithm would need to be employed using the second-harmonic generation signal at the focus to construct a phase mask within a pulse shaper to produce purely GDD chirped

pulses within a target sample. This requirement undermines the simplicity of this technique compared to TL excitation.

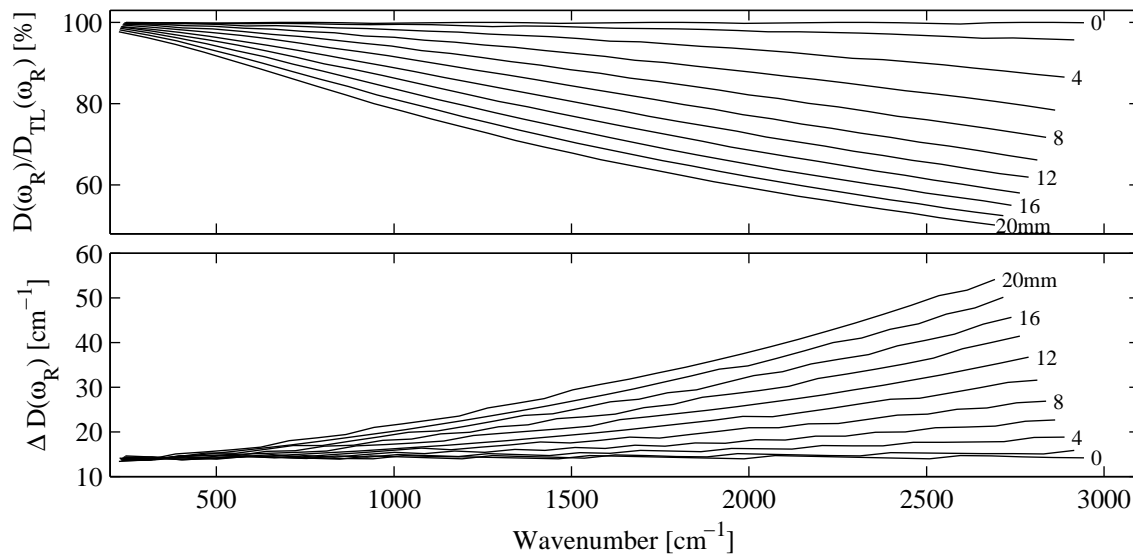


FIGURE 12.6. (a)

Another experimental factor that modifies the achievable vibrational excitation is the actual profile of the power spectrum. Modelocked Ti:sapphire oscillators emit soliton-like pulses that do have smoothly varying power spectra. Above 1000 nm, the gain bandwidth of the possible active ions (Yb and Nd) limits soliton pulses to  $> 30$  fs for truly state-of-the-art Yb systems [23] and is far more typically  $> 100$  fs [144, 21, 86]. To achieve pulse bandwidths supporting TL durations  $< 20$  fs, few 100 fs pulses are injected into optical fiber where the high spatial confinement results in significant nonlinear propagation and spectral broadening [28, 145, 26, 27]. This is precisely the supercontinuum (SC) generation process discussed in detail in Chapters 4, 5, and 6

The power spectrum produced by SC generation is highly dependent on the nonlinearity and the dispersion profile of the optical fiber. A simple option for spectral broadening at  $\sim 1$  W average powers is to use standard, polarization maintaining telecom fiber, as opposed to

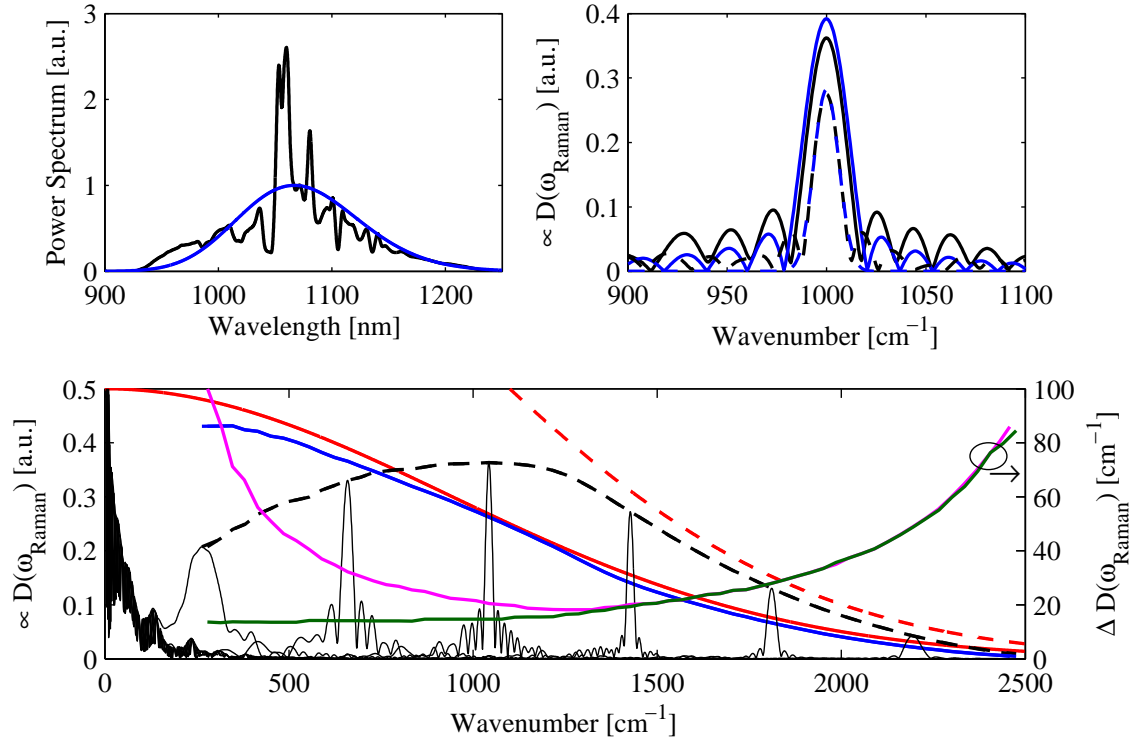


FIGURE 12.7. (a) The power spectra of a SC pulse (black) and a Gaussian pulse (blue) with an equal TL FWHM duration of 13 fs. (b) The  $1000\text{ cm}^{-1}$  vibrational excitation spectrum for SC (black) and Gauss (blue) pulses, for pure GDD chirp (GDD results in a 2000 fs FWHM Gaussian pulse) and either identical pulse copies (dashed) or LP02-1064RU dichroic filter derived pulse pairs (solid). (c) The magnitude and width of the vibrational excitation for a TL 13 fs Gaussian pulse (red-dashed), a TL 13 fs pulse with 1/2 the energy (red-solid), the vibrational excitation from the SC for identical chirped pulse copies (blue and green) and LP02-1064RU filter derived pulses (black-dashed and magenta). Example excitation spectra are also shown for the filter derived SC pulse pairs (black-solid).

“nonlinear” fiber which are designed to have very small mode-field diameters but also have lower damage thresholds. An example of the power spectrum generated in 5 m of PM980-XP (Thorlabs) is shown in Fig. 12.7(a). The vibrational excitation from chirped SC pulse pairs is comparable in magnitude to the ideal Gaussian case (Fig. 12.7(b)), in spite of the structure present in the power spectrum. However, the power spectral structure does cause an increase in the excitation width for increasing vibrational frequencies, even for identical SC pulse copies.

Fig. 12.7(c) indicates SC pulse could be utilized for selective vibrational excitation near the impulsive limit, as the increase in the excitation width within the finger-print region stays below  $40 \text{ cm}^{-1}$ . The current inhibiting technical challenge is the large amount of HOD produced by a prolonged propagation in fiber. 5 m of polarization maintaining fiber imparts more HOD dispersion than can be effectively eliminated, even with a pulse shaper. Shorter fiber lengths result in an even more structured power spectra, and a satisfactory solution has yet to be attained. A broadband Ti:sapphire laser however, in combination with a pulse shaper ought to be able to realize the selective and highly tunable non-impulsive vibrational excitations with oscillator displacement magnitudes near the impulsive limit.

## CHAPTER 13

# PART III: TIME-RESOLVED COHERENT RAMAN SPECTROSCOPY BY HIGH SPEED PUMP-PROBE DELAY SCANNING

*If I had asked people what they wanted, they would have said faster horses.*

Henry Ford

### 13.1. PUMP-PROBE SPECTROSCOPY

Label-free detection of molecular concentrations and dynamics can be performed using pump-probe spectroscopy to capture electronic and vibrational state dynamics. Pump-probe transient absorption spectroscopy (TAS) detects significant information in dynamic behavior from probe amplitude modulations; allowing molecular differentiation between molecules with indistinguishable absorption and emission spectra in addition to concentration [68, 69]. Time-resolved vibrational spectroscopy can identify molecular species and concentration by probing the molecular structure, where amplitude modulations from pump-probe experiments are particularly good at detecting low-frequency vibrational modes [146, 147, 65].

As these amplitude modulation signals are generally very weak, averaging at each delay point in time (point averaging) reduces the signal noise, limiting pump-probe signal detection to low speeds. Flicker noise ( $1/f^\gamma$ ) due to mechanical vibrations, Poynting drift, and gain drift dominates the noise spectrum for this type of averaging, which limits the effectiveness of long time averaging at a single delay. Averaging a set of rapidly acquired delay scans, which we will refer to as scan averaging, improves the signal to noise by the  $\sqrt{\text{number of scans}}$  in

the white noise limit [67]. The challenge then, is to increase the pump-probe delay scan rate to use probe amplitude modulation signals from either TAS or coherent Raman scattering for imaging. The resulting benefits of increasing the pump-probe delay scan rate being either faster averaging of weak signals or pixel dwell time reduction for strong signals.

Using a spinning window, dubbed the *lighthouse* for expediency, to introduce a group delay between pulses is a simple, yet effective means for high speed pump-probe delay scanning. In previous work, we exploited the angularly dependent group velocity in a uniaxial crystal [67] for delay scanning. The detected signal was a harmonic of the fundamental, avoiding interference by small satellite pulses arising from imperfect crystal alignment. Eliminating the degenerate satellite pulses proved nontrivial and led to the new system described here.

In this chapter, which is based on our publication Ref [66], we introduce a new *lighthouse*; utilizing an isotropic optical material, e.g. BK7. The changing path length through the air and glass scans the pump-probe delay. Using an isotropic window, there are four pump-probe delay scans per window rotation; following a nonlinear angle to delay map (shown below).

### 13.2. IMPULSIVE STIMULATED RAMAN SCATTERING WITH THE *lighthouse*

Using impulsive stimulated Raman scattering (ISRS), a pump pulse, with temporal structure shorter than some Raman-active vibrational modes, prepares a vibrational coherence in the ensemble of molecules within the pump volume that travels in the sample with the group velocity of the pump pulse [146]. The vibrational coherence drives a perturbation in the optical response of the medium (linear [64], nonlinear [148]). A time delayed probe pulse propagating through the impulsively-prepared vibrational coherence acquires a phase modulation that allows detection of the Raman excitation through diffraction [146], direct

phase modulation [149], frequency shifting [65, 150, 151, 147], and pulse energy changes [152] in addition to nonlinear scattering such as coherent anti-Stokes Raman scattering.

Here, we demonstrate the capabilities of our rapid delay scanner by measuring low-frequency Raman-active phonon modes of crystal particles. Changes in the linear optical susceptibility following impulsive excitation of a single Raman-active vibrational mode induce frequency modulations in the probe pulse. In the quasi-Gaussian approximation, this can be expressed as,

$$(13.1) \quad \delta\chi^{(1)} \approx \frac{N}{\epsilon_0} \alpha' \frac{1}{\Omega_R} D(\Omega_R) \sin[\Omega_R(t + \tau) + \phi_0] \Phi(\varsigma),$$

where  $\tau$  is the time delay between the pump and probe pulses,  $\Omega_R$  is the angular vibrational frequency,  $\alpha'$  is the Raman mode differential polarizability,  $N$  is the number density of oscillators,  $\epsilon_0$  is the permittivity of free space, and  $\phi_0$  is a phase slip for pump pulses of finite duration. The relative axial excitation strength in the quasi-Gaussian approximation reads:  $\Phi(\varsigma) = A(\varsigma)^{-2}$ , with  $A = 1 - i(\varsigma - z_w)/z_R$ ,  $z_w$  is the focal waist,  $z_R$  is the Rayleigh distance, and  $D(\Omega_R) = \int e^{i\Omega_R t} I(t) dt$ , is the ISRS excitation strength where  $I(t)$  is the intensity profile of the excitation pulse [143]. The modulation of the probe pulse energy is much weaker than the effects of phase modulation. For a small interaction length,  $L$ , in the focal volume, a phase shift of  $\delta\phi(\tau) = \delta\phi_0 \sin[\Omega_R \tau + \phi_0]$  is accumulated by the probe pulse, where the peak phase shift is

$$(13.2) \quad \delta\phi_0 = \frac{\omega_0 L}{2nc} \frac{N}{\epsilon_0} \alpha' \frac{1}{\Omega_R} D(\Omega_R),$$

$\omega_0$  is the angular optical frequency,  $n$  is the index of refraction, and  $c$  is the speed of light. The spectrum of the probe pulse is also modified by the Raman coherence [64], and for a

short enough probe pulse, the center radial frequency of the pulse spectrum is shifted by [146, 147, 150, 151]

$$(13.3) \quad \delta\omega(\tau) = \delta\phi_0\Omega_R \cos(\Omega_R\tau + \phi_0).$$

Frequency shifts smaller than the resolving power of an optical spectrometer can be detected by using a spectral filter to convert the spectral shifts into amplitude changes [147, 65, 151]. We employ that strategy here to detect the coherent Raman induced frequency shift of the probe pulse. Assuming a Gaussian power spectrum with a  $1/e^2$  half width of  $\sigma$ , a Gaussian spectral filter with a  $1/e$  half width of  $\Delta$  centered at  $\sigma/2$  for a maximum signal strength, and also  $\delta\omega \ll \Delta \ll \sigma$ , we find the differential photodiode signal current is approximately  $i_s(\tau) \propto \bar{P} \frac{\delta\omega(\tau)}{\sigma}$ , where  $\bar{P}$  is the probe average power.

The frequency shift varies with pump-probe delay and maps out an oscillatory signal with delay. This delay is introduced by splitting a pulse into pump and probe copies and scanning the probe pulse delay, or equivalently, introducing two lasers with slightly different repetition rates,  $f_r$ , separated by a frequency,  $\delta f$ . The pump-probe delay time is related to the measurement time frame,  $T_m$ , by  $\tau = s(T_m)T_m$ . The most common implementation is a scanning motor with  $s = 2v/c$ , where  $v$  is a linear stage velocity and  $c$  is the speed of light. Here, we make use of a spinning delay crystal, with

$$(13.4) \quad s(\theta) = 2\pi f_{\text{rot}}\tau_0 \frac{d\beta(\theta)}{d\theta}$$

where  $f_{\text{rot}}$  is the window angular velocity and  $\tau_0$  and  $\beta(\theta)$  are discussed below. We also note that in the case of two lasers with repetition rates operating at differing frequencies, the scale factor is given by  $s = \frac{\delta f}{f_r}$ . In each case, the measured Raman frequency,  $\nu_R$ , is scaled

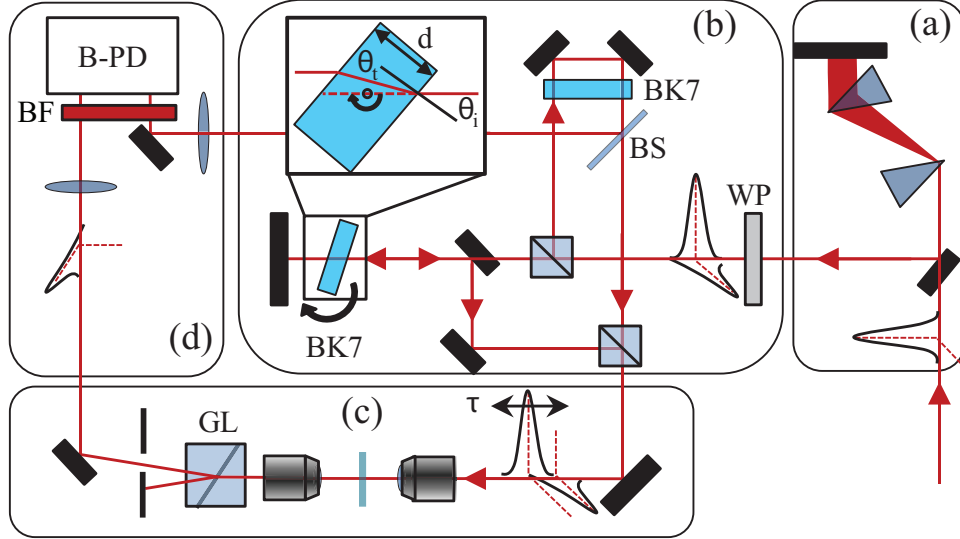


FIGURE 13.1. (a) Pre-compensation compressor, (b) Mach-Zehnder with the lighthouse in one arm, (c) microscope and pump rejection, and (d) detection. B-PD: balanced-photodetector, BF: bandpass filter, GL: Glan-laser polarizer, BK7: BK7 window,  $\tau$ : pump-probe delay, BS: beam splitter, WP:  $\lambda/2$  wave-plate

down to an electronic frequency by the factor  $s$  (where  $s < 1$ ), or  $\nu_s = s\nu_R$ . This is the same scaling factor that is observed in a recent experiment using two synchronized lasers running at slightly different repetition rates [151].

Pump-probe spectroscopy also includes cross phase modulation (XPM) when the pulses temporally overlap. The non-resonant electronic background introduced through XPM is easily removed through a Gabor transform to get the non-instantaneous contribution,  $\psi(T, \omega) = \mathcal{F}\{V(t)g(t - T)\}$  where  $\mathcal{F}\{\}$  is the Fourier transform,  $g(t - T)$  is a Gaussian gate function, and  $V(\tau)$  is the voltage sampled by the DAQ. The Raman spectrum is now calculated by plotting the spectrogram  $\psi$  at a fixed  $T$  that excludes time-zero.

The experiment, shown in Fig. 13.1, uses pulses from a modelocked Ti:sapphire oscillator (90 mW pump and 2 mW probe). After passing a prism compressor, the pulses are split on polarization with a combination of a half wave plate and a polarizing beam splitting cube, allowing the power balance between the arms to be fine-tuned. The transit time of the pump

pulse is rapidly varied by passing the pulse through a thick BK7 window mounted on a motor (the *lighthouse*). The beam is reflected from right angle retro mirrors and recombined with the probe pulse with a second polarizing beam-splitter. A small portion of the probe beam power is taken with a 5% beam-splitter for a reference beam.

The centroid shift of the incident probe spectrum after scattering off of the transient polarizability is estimated by comparing the transmission through a spectral bandpass filter of the probe pulse and the reference probe copy in a Si-based balanced photodetector (Thorlabs PDB450a). For maximal sensitivity, the 7 nm bandpass filter is positioned at the peak slope of the probe pulse's power spectrum at 780 nm.

Time-zero is set at a non-normal incidence angle. Normal incidence then corresponds to the maximum delay between the pump and probe; providing two pump-probe delay scans per window face for a total of four scans per full window revolution. The temporal delay of the pump pulse through the spinning window, relative to the probe pulse, is  $\tau(\theta_i) = \tau_0\beta(\theta_i)$ .  $\tau_0 = 2dn_g/c$  is the group delay through the window at normal incidence, where  $d$  is the window thickness and  $n_g$  is the group velocity index in the window. The nonlinear mapping between incidence angle and delay is

$$(13.5) \quad \beta(\theta_i) = -\frac{n_g + \cos(\theta_t) - \cos(\theta_i - \theta_t)}{n_g \cos(\theta_t)},$$

where  $\theta_{i,t}$  are the incident and transmission angles, respectively. This geometric delay equation predicts the time delay measured by spectral interferometry [Fig. 13.2(a)], as well as accurately producing known vibrational modes of Raman standards such as  $\text{Bi}_4\text{Ge}_3\text{O}_{12}$  (BGO) and  $\text{CCl}_4$ . Fig. 13.2(a) shows a representative half motor cycle, where the chirped vibrational

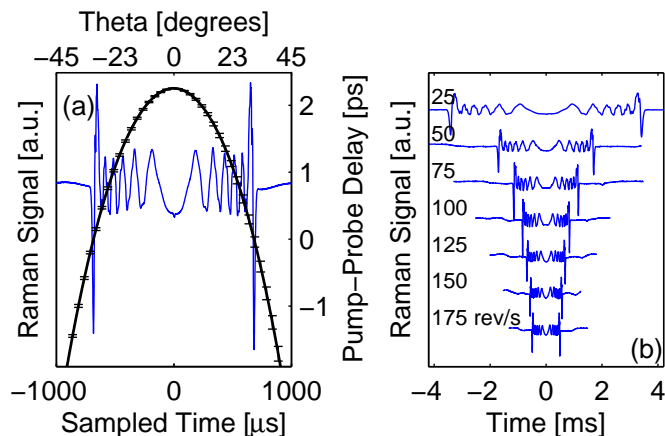


FIGURE 13.2. (a) Vibrational signal from BGO (blue) and the angle to pump-probe delay mapping and error from spectral interferometry measurements (black). (b) Scaling motor velocity.

signal from the  $88\text{ cm}^{-1}$  mode of BGO and the XPM signal at time-zero pump-probe delay ( $\theta_i \approx \pm 30^\circ$ ) are clearly visible.

### 13.3. CHEMICAL IMAGING WITH THE *lighthouse*

Imaging is a major motivator for high speed Raman spectral acquisition, and we have increased the delay scanning speed by  $> 23\times$  to 700 Hz [Fig. 13.2(b)]. This increase was enabled by optimizing the motor drive and mounting as well as by using an isotropic scanner window that further doubled the scan rate.

Because of the nonlinear mapping between window angular velocity and the rate of change in pump-probe delay, it is critical to appropriately choose sampling and detector electronics which have sufficient bandwidth to capture Raman vibrational modes of interest. The angle corresponding to time-zero has the largest delay rate of change and sets the maximum reduced Raman-to-electronic frequency. Evaluating  $s$  at  $\theta_{\max}$  yields the maximum electronic signal for a particular Raman vibration,  $\nu_{s,\max} = s(\theta_{\max})(100c\nu_{R,\text{wn}})$ , where we have converted the Raman frequency  $\nu_R$  to the more convenient wavenumbers,  $\nu_{R,\text{wn}}$ .

As an example, our system uses a  $d = 6.5$  mm thick BK7 window, a maximum pump-probe delay of 2.2 ps ( $\theta_{\max} = \pm 30^\circ$ ), and window angular velocity of 100 rev/s; resulting in a Raman-to-electronic signal frequency de-magnification of  $s = 5.6 \cdot 10^{-9}$ . The maximum electronic signal frequency of the  $459 \text{ cm}^{-1}$  mode of  $\text{CCl}_4$  then is 73 kHz. The *lighthouse* has sufficient clear aperture with 12.7 mm square faces for a maximum angle of  $\pm 60^\circ \rightarrow \tau(\pm 60^\circ) = 10$  ps. Using this maximum delay and a window angular velocity of 175 rev/s, the Raman-to-electronic frequency de-magnification would be  $s = 2.5 \cdot 10^{-8}$ . It is the limited photodetector amplifier bandwidth (300 kHz) that currently limits the maximum pump-probe delay, scan speed, and maximum detectable vibrational mode. For applications with longer time constants (e.g. TAS [69] with temporal dynamics equivalent to Raman vibrations  $< 500 \text{ cm}^{-1}$ ), the current detector bandwidth is entirely sufficient.

By comparison, the frequency de-magnification from two lasers with a 50 Hz difference on a 100 MHz repetition rate, as reported in Ref. [151], is  $s = 5 \cdot 10^{-7}$ , but with the attendant increase in complexity of two repetition rate stabilized, modelocked lasers. Using the more common approach, scanning retro-mirrors, a state-of-the-art voice-coil delay line operating at 60 Hz has a frequency de-magnification factor of only  $s \approx 1 \cdot 10^{-10}$ , far below the *lighthouse*.

The signal generated by the balanced photodetector is sampled with a National Instrument data acquisition board (NI USB-6361) at 1 M-Sa/s. Capturing the swept surface reflection of the *lighthouse* on a photodiode, generates a synchronization signal, which is then filtered through a digital delay generator (Stanford Research Systems, DG535) to tunable digital pulses. The scans of each motor cycle are separated using the synchronization signal.

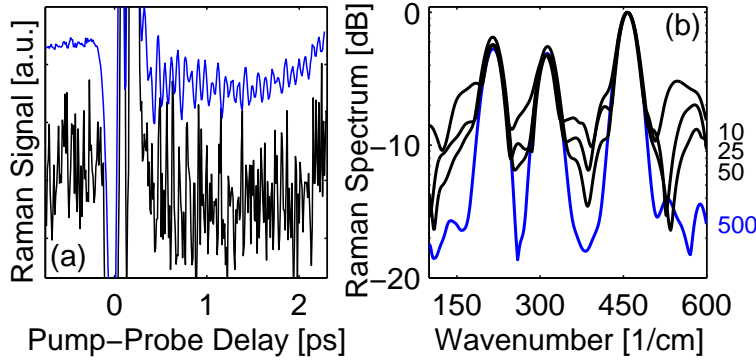


FIGURE 13.3. Measurements of neat  $\text{CCl}_4$  (a) Effects of averaging on frequency modulation signal from 1 pump-probe delay scan (black) to 500 (blue), offset for clarity. (b) The Raman spectra associated with different amounts of scan averaging, with the scan number listed to the right.

The four individual pump-probe delay scans of each motor cycle are independently accumulated and interpolated onto a linear time axis of 2048 points using  $\tau(\theta_i)$ , as the DAQ sampling is linear in  $\theta_i$ . Separating the front and back delay scans serves to minimize the effects of differences in delay calibration and Fresnel reflections. Separating the mirrored scans of each face minimizes the effects of imperfect centering of the beam with respect to the rotation axis. Nearly symmetric XPM peaks occurring at the time-overlap of the pump and probe pulses on each half-cycle scan allow additional refinement in the synchronization. Finally, a Gabor transform is applied to the scan averaged frequency modulation signal, with a Gaussian gate function chosen to minimize the non-resonant background. Line-outs of the spectrogram,  $\psi$ , away from time-zero yield the Raman spectra without the electronic background. All following spectra are plotted for a spectrogram delay of  $T = 1$  ps and 750 fs full-width-half-max (FWHM) gate function.

Using this method of processing the frequency modulation signals into Raman spectra, Fig. 13.3 shows the effects of scan averaging on neat  $\text{CCl}_4$  in a fused silica cuvette with a 1 mm interaction length. Spectra for increasing numbers of delay scans are normalized

to the  $459\text{ cm}^{-1}$  mode. The Raman modes at  $217$ ,  $314$ , and  $459\text{ cm}^{-1}$  appear quickly by averaging only 10 scans. Comparing averages of the noise from  $600$  to  $1000\text{ cm}^{-1}$  (where our system does not resolve any spectral features due to residual pulse chirp) for the 10 and 500 delay scan cases shows an improvement of 8.1 dB. A reduction that is very close to the fundamental white noise limited improvement of 8.5 dB.

As a preliminary demonstration of the system's imaging capability, we constructed a microscope to image crystals with different Raman spectra. The microscope uses an 8 mm focal length asphere and effective numerical aperture (NA) of 0.2 for the focusing objective and a  $20\times$  0.4 NA collection objective; producing a resolution of 13 micron. The focusing asphere minimized material dispersion while the higher NA collection objective minimized signal contributions from non-resonant, nonlinear scattering. We imaged a sample composed of BGO and  $\text{CdWO}_4$  over  $1\text{ mm}^2$  in  $10\text{ }\mu\text{m}$  steps, where Raman spectra were obtained by averaging 430 delay scans at each pixel with a delay scan rate of 500 delays/s (125 rev/s).

A simple peak-comparison algorithm compares the Raman spectra from each pixel to pre-recorded Raman reference spectra, taken with our *lighthouse* of each constituent crystal [Fig. 13.4(a)]. The algorithm compares three peak positions to a null, where the nulls are strategically positioned at the location of a peak from the other constituent crystal. Setting a saturation value for each constituent Raman spectral comparison, a composite image is formed by scaling each pixel value to the saturation level and normalizing. For each pixel, these numbers were used to form an RGB vector:  $R = \text{BGO}$ ,  $G = 0$ , and  $B = \text{CdWO}_4$  for Fig. 13.4(b). The discrimination for the crystal species is 30 and 20 dB for BGO and  $\text{CdWO}_4$  respectively [Fig. 13.4(c) and (d)].

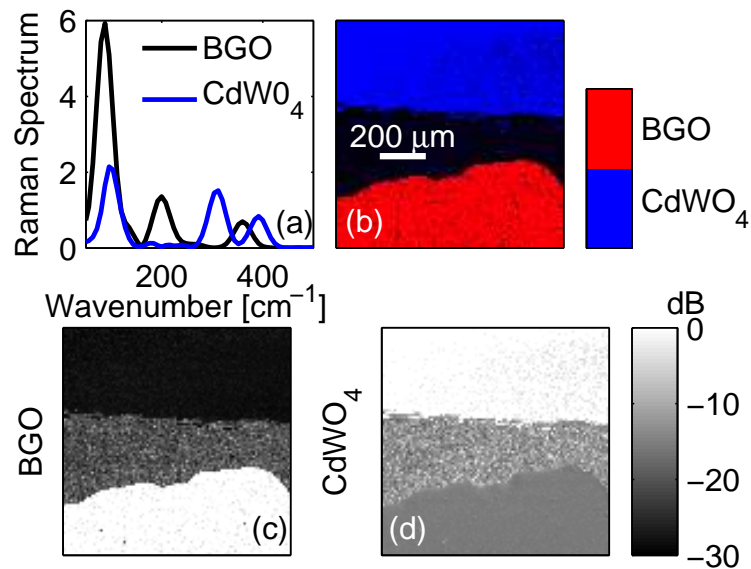


FIGURE 13.4. Raman image. (a) Reference spectra from BGO (black) and CdWO<sub>4</sub> (blue). (b) Composite image from the constituent spectra. Images for each Raman species: (c) BGO and (d) CdWO<sub>4</sub>.

This work demonstrates a simple method for rapidly scanning a pump-probe delay and a route towards the utilization of pump-probe spectroscopy as an imaging modality suited to capturing biological dynamics. Our current *lighthouse* has a scan rate of 700 Hz which we will work to push beyond 1 kHz. The current capabilities of our *lighthouse* will be well suited for attempting TAS experiments where the interactions are often much stronger than coherent Raman interactions, potentially allowing single pump-probe delay scans per pixel.

## CHAPTER 14

# PART III: HYPERSPECTRAL IMAGING VIA LABELED EXCITATION LIGHT AND BACKGROUND-FREE ABSORPTION SPECTROSCOPY

*The way I see it, if you want the rainbow, you gotta put up with the rain*

Dolly Parton

### 14.1. INTRODUCTION

Hyperspectral imaging (HI) generates a three-dimensional data set, a so-called hypercube, composed of two-dimensional (2D) spatially resolved spectroscopic data. Owing to the richness of information contained in the hypercube, HI has found widespread use in a diversity of fields from biomedical applications such as clinical cancer pathology [153, 154] to remote sensing [155], art conservation [156], and crime scene analysis [157]. Within biomedical applications, HI is a noninvasive diagnostic technique [153] using tissue reflectance, absorption, scattering, and fluorescence as indicators for disease progression [158, 159]. Taken together, the different optical characteristics provide a more comprehensive assessment of the specimen; such as quantifying changes in cellular morphology (e.g. nuclear content and epithelial thickening) and metabolism [153].

As HI is a means of adding chromatic information to a spatial imaging system, powerful hybrid systems are possible by combining hyperspectral data acquisition with advanced imaging techniques. For example, spatial frequency domain imaging [160] in conjunction with HI yields depth-sectioned, high spatiotemporal resolutions for quantifiable *in vivo* imaging

of neurophysiology and metabolism [161]. Additionally, there is no wavelength requirement beyond the needs of a particular application, so HI is applicable for illumination sources from the ultraviolet to the mid-infrared [162, 154, 163].

Currently, the dominant HI methods are (much like traditional microscopy): point-, line-, and area-scanning [164]. The first two scanning methods rely on an array detector to capture spatially dispersed spectra from sub-sections of the total field-of-view, whereas area-scanning captures the whole field-of-view while filtering and scanning the illumination spectrum.

In this Chapter, we introduce a new method of performing HI and demonstrate it within a particularly novel application: background-free abortion spectra imaging. Our HI method encodes a wavelength-dependent temporal modulation onto the excitation (or illumination) power spectrum. The temporal modulations shift the spectroscopic wavelength axis into a time-domain measurement, eliminating the need to spatially disperse the light from each pixel within the field-of-view to acquire spectral information. Effectively, we have labeled the power spectrum of the excitation light in the time domain at frequencies far below the optical carrier frequency and typical fluorescent emission rates, allowing us to detect the temporal label imprinted on any subsequent light matter interaction such as broadband fluorescence or absorptive attenuation. Notice, the temporal light labeling (LiLa) method is sufficient to perform spectroscopy on a single element detector at any wavelength; meaning this is an excellent route to inexpensively increase the spectral resolution and speed of spectroscopy in wavelength regions lacking dense array detectors, such as the mid-infrared.

We demonstrate our HI technique in a widefield, epi-fluorescence microscope, where the hypercube contains a 2D micrograph of background-free absorption spectra by virtue of the broad spectrum fluorescence containing the temporal intensity modulation encoded into the

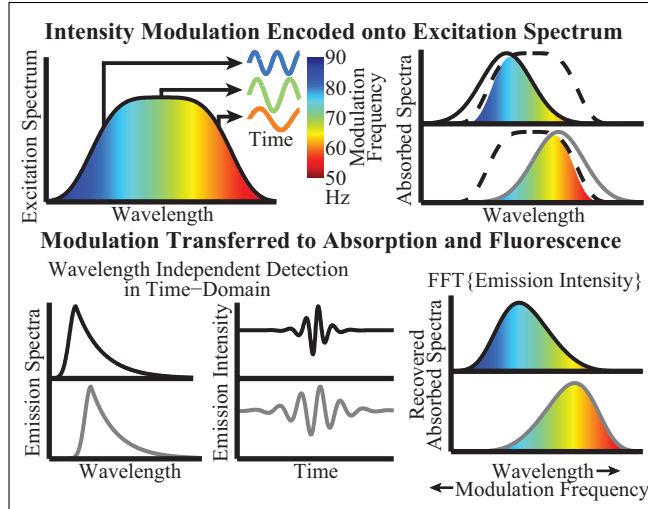


FIGURE 14.1. Concept figure. The intensity modulation encoded onto the excitation power spectrum is transferred to the fluorescence via the absorbed spectrum. A Fourier transform of the temporal dynamics of the emission intensity, across all emission wavelengths, recovers the absorbed spectrum through the unique labeling of excitation wavelength to modulation frequency.

excitation spectrum. We dub this method: HI via excitation labeled fluorescence (ELF). Fig. 14.1 is a concept figure, showing how the unique intensity modulation frequency at each wavelength of the excitation pulse is transferred to absorbers and maintained through fluorescent emission. The net result of HI-ELF is a time-domain encoding of the absorbed spectral energy, detectable through temporal modulations in the emission intensity integrated across the entirety of the fluorescence spectrum. By detecting the absorption spectrum through temporal modulations in the fluorescence spectrum, we drastically lower the noise floor of an absorption measurement as it can be shot-noise limited for small changes to the average of the small fluorescent intensity,  $\langle \Delta I_F \rangle$ , as opposed to small changes on top of the large background excitation intensity,  $\frac{\Delta I_F}{\langle I_E \rangle}$ . Using HI-ELF, we are able to reliably differentiate between absorbed spectra whose centroids differ by only 3 nm.

HI-ELF, and the LiLa method more generally, does not rely on capturing spatially dispersed spectra on an array detector; making it unique among HI techniques in that it is

adaptable to high-speed single element detector based imaging systems such as spatial frequency modulated imaging (SPIFI) [70, 71]. SPIFI performs a similar temporal modulation encoding, but in this case encodes spatial location. Recent SPIFI advances have successfully encoded 2D spatial information into the time-domain, enabling the implementation of a single element detector for 2D image capture [71]. This development will allow for HI-ELF, or other LiLa based HI systems, to acquire complete hypercubes at an order of magnitude beyond the limits of current state-of-the-art high-speed cameras.

Area-scanning alone among the other HI methods would be adaptable to SPIFI style image acquisition. The illumination time per spectral point however, is far below that of LiLa, since LiLa is a multiplexed version of area-scanning. If  $n$  is the number of spectral points sampled, then for a fixed total scan time a LiLa style measurement will increase the illumination by a factor of  $n/2$  over area-scanning, where the factor of 2 assumes a modulation duty cycle of 50%.

## 14.2. LiLa METHOD

The temporal LiLa technique relies on encoding a wavelength dependent temporal intensity modulation onto the excitation power spectrum prior to the microscope. We accomplish this by passing the excitation pulse through a folded  $4f$  Martinez stretcher [75] with a frequency modulated reticle [165] at the focal plane; see Fig. 14.2(a) for a reference schematic. The spinning-disk reticle [Fig. 14.2(a<sub>1</sub>)] modulates the spectral intensity of wavelengths spatially dispersed across the line focus at distinct frequencies, creating a unique mapping between intensity modulation frequency and wavelength.

The spectral resolution,  $\delta\lambda$ , contained in the temporal modulation frequencies is dependent on the focal spot size of the monochromatic wavelets comprising the spectral line focus

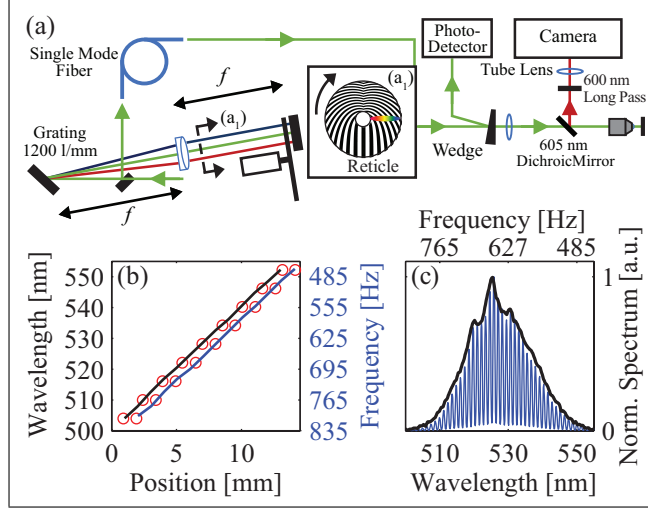


FIGURE 14.2. (a) HI-ELF experimental schematic. (b) The mapping between spatial location in the focal-plane of the Martinez to wavelength (black) and an analogous mapping with modulation frequency (blue), both are compared to theory (red-circles), with the modulation frequency curve offset by 1 mm for visibility. (c) The excitation power spectrum entering the microscope as captured by a spectrometer with the reticle set to an angle with high modulation (blue) and by temporal LiLa (black).

and the smallest reticle feature size, where the larger of the two sets the resolution. The focal spot size of the monochromatic wavelets is estimated using the paraxial approximation, where the intensity distribution of the spectral line focus impinging on the reticle at the focal plane of the Martinez is given by

$$(14.1) \quad I(x, y; \omega) = I_0 \frac{z_{\text{in}}}{f} \exp \left( -2 \left( \frac{\Delta\omega}{\Delta\Omega} \right)^2 \right) \exp \left( \frac{-2((x - \alpha\Delta\omega)^2 + y^2)}{(w_{\text{in}}f/z_{\text{in}})^2} \right),$$

where  $\Delta\omega = \omega - \omega_0$ ,  $\omega_0$  is the central frequency of the excitation pulse,  $\Delta\Omega$  is the angular frequency bandwidth of the pulse, and  $w_{\text{in}}$  is the radius of the electric field of the first-order diffracted beam leaving the grating with an associated Rayleigh length of  $z_{\text{in}} = \pi w_{\text{in}}^2/\lambda$ .

Monochromatic wavelets at  $\Delta\omega$  propagate parallel to the optical axis of the wavelet at  $\omega_0$ ,

but are displaced spatially by  $\alpha\Delta\omega$ , where

$$(14.2) \quad \alpha = \left. \frac{d\theta}{d\omega} \right|_{\omega=\omega_0} \quad f = \frac{2\pi cN}{\omega_0^2 \cos \theta} f,$$

and  $c$  is the speed of light,  $N$  is the grating groove density,  $\theta$  is the first-order diffraction angle of the wavelet at  $\omega_0$ , and  $f$  is the focal length of the achromatic lens in the Martinez.

The reticle feature resolution is determined by its spatial modulation pattern, which is a radially dependent cosine mask expressed as  $m(r, t) = 1/2 + 1/2 \operatorname{sgn}(\cos(\Delta k r \nu_r t))$ , where  $\Delta k$  is the number of cycles per unit radius (i.e. the chirp parameter),  $\nu_r$  is the rotation frequency of the reticle, and  $\operatorname{sgn}()$  enforces binary amplitude modulations. Making the reticle symmetric about the line with polar coordinates  $R(r, \theta) = R(\theta = 0, \pi)$  (the vertical symmetry plane in Fig. 14.1(a<sub>1</sub>) with  $\theta = 0$  oriented downward), has the effect of making the smallest feature on the mask equal to  $1/\Delta k$  [70]. Our mask has a  $\Delta k = 5 \text{ mm}^{-1}$ , making the smallest feature size  $200 \text{ }\mu\text{m}$ . Using  $w_{\text{in}} = 2.1 \text{ mm}$  and  $f = 200 \text{ mm}$ , the monochromatic wavelet focal spots are  $\sqrt{2 \log 2} w_{\text{in}} f / z_{\text{in}} \approx 20 \text{ }\mu\text{m}$  full-width at half-maximum, well below the smallest feature size of the mask. The spectral resolution in this implementation is therefore set by the spatial resolution of the reticle,  $\delta r = 1/\Delta k$ , and is give by

$$(14.3) \quad \delta\lambda = \frac{\delta r}{\alpha} \frac{2\pi c}{w_0^2} = \frac{\cos \theta}{\Delta k N f}.$$

Using our system properties of  $N = 1200 \text{ 1/mm}$ , a grating incidence angle of  $17.5^\circ$ , and  $\omega_0 = 2\pi c/528 \text{ nm}$ , the LiLa spectral resolution is  $\delta\lambda = 0.8 \text{ nm}$ .

The number of spectral points comprising the LiLa spectrum is given by,  $n = \Delta\lambda/\delta\lambda = \Delta\nu/\delta\nu$ , where  $\Delta\lambda$  is the total spectral bandwidth of the excitation source (i.e. the width

encompassing  $\sim 99\%$  of the power spectrum) and  $\delta\nu$  is the modulation frequency resolution and is equal to  $\nu_r$ . The modulation frequency bandwidth encoded across the spectral bandwidth is  $\Delta\nu = \Delta k \Delta r \nu_r$ , where  $\Delta r = \alpha \Delta \lambda \omega_0^2 / 2\pi c$  is the width of the spectral line focus incident on the reticle. Using  $\Delta \lambda = 72$  nm, the number of spectral points in our setup is  $n = 90$ .

To represent the LiLa spectrum in the modulation frequency domain, we need to physically locate the spectral line focus on the reticle. The radial position of the central frequency wavelet on the reticle,  $r_0$ , sets the central modulation frequency. This parameter is adjustable by translating the reticle transverse to the spectral line focus. The spatial location of focused wavelets,  $I(x, y; \omega)$ , becomes  $x = r_0 + \alpha \Delta \omega$ , where we have oriented the Martinez and reticle such that the spectral line focus occurs along the  $x$  dimension. In the limit that the monochromatic wavelet focal spot sizes are much smaller than the smallest feature on the reticle, the mask modulation is transferred directly into the frequency domain,  $m(x, t) \rightarrow m(r_0 + \alpha \Delta \omega, t)$ , as the spatial variations in the mask correspond to spatially isolated (focused) monochromatic wavelets. The excitation intensity after the Martinez, where the power spectrum has been spatially re-compressed, is

$$(14.4) \quad I_E(x, y; \omega, t) = I_0 m(r_0 + \alpha \Delta \omega, t) \exp\left(-2 \left(\frac{\Delta \omega}{\Delta \Omega}\right)^2\right) \exp\left(\frac{-2(x^2 + y^2)}{w_{\text{in}}^2}\right).$$

Capturing the full spatial and spectral extent of the excitation intensity on a photodetector yields a voltage signal

$$(14.5) \quad s(t) = \eta \iiint_{-\infty}^{\infty} I_E(x, y; \omega, t) dx dy d\omega$$

where  $\eta$  accounts for the quantum efficiency of the detector, collection efficiency, and other factors. The first sideband of the Fourier transform of  $s(t)$ ,  $S(\nu) = \mathcal{F}\{s(t)\}$ , is the excitation power spectrum in the modulation frequency domain: the LiLa spectrum.

In using the paraxial approximation to express the spectral intensity through the Martinez, there is the implicit assumption that monochromatic wavelets at all the field angles subtended by the diffracted power spectrum are focused with minimal aberrations, especially Petzval field curvature [27]. This approximation quickly breaks down for a system with large field angles (e.g.  $> 3.5^\circ$  for the achromatic lens in our setup) as the field curvature becomes commensurate with the Rayleigh length of focused wavelets with the highest field angles within the power spectrum. Modeling our system in Zemax, with maximum field angles of  $\pm 2.5^\circ$ , we find the field curvature across the spectral line focus is everywhere less than the respective wavelet Rayleigh lengths.

To calibrate the wavelength to intensity modulation frequency mapping, we step a razor blade through the spectral line focus and co-locate the edge in the transmitted power spectrum between a wavelength domain measurement (a traditional spectrometer and a stationary reticle) and a modulation frequency domain measurement (a single element photodetector and a rotating reticle, i.e. LiLa). Fig. 14.2(b) shows resultant position to wavelength and modulation frequency calibration curves. The theoretical spatial locations of the wavelengths,  $\alpha\Delta\omega$ , are also shown in Fig. 14.2(b) as red circles. The root-mean-squared error between measured wavelengths and the LiLa calibration is 0.2 nm. Fig. 14.2(c) shows the excitation pulse power spectrum captured by temporal LiLa as compared to the power spectrum captured by a spectrometer with a static reticle set to an angle with high modulation ( $\sim 90^\circ$  from the orientation shown in Fig. 14.2(a<sub>1</sub>)). As a redundant check, we can recompute

the number of spectral points using  $\Delta\nu$  as determined from  $S(\nu)$  in Fig. 14.2(c):  $\Delta\nu = 370$  Hz at  $\nu_r = 4.1$  Hz yields  $n = 90$ .

This method of generating a temporal LiLa is related to Fourier transform spectroscopy. The Martinez and reticle constitute a pulse shaper with a rapidly varying amplitude mask. The modulation in the power spectrum in Fig. 14.2(c) (blue-line) is identical to the spectral interferogram generated by a time-delayed coherent pulse pair. A feature of the reticle mask is the constant periodicity of the spatial modulation across the spectral line focus for a fixed angle or time. The spectral modulation shown in Fig. 14.2(c) corresponds to a pulse delay of 800 fs. Increasing the reticle  $\Delta k$  would also increase the pump-probe delay. As the pulses are very nearly common-path, LiLa could prove to be a robust method for performing interferometrically stable, rapid Fourier transform spectroscopy.

### 14.3. HI-ELF RESULTS

For HI-ELF, the captured signal on a camera from a wide-field microscope becomes

$$(14.6) \quad s(M_2x, M_2y; t) = \int_{-\infty}^{\infty} \eta C(x, y) I_E(x/M_1, y/M_1; \omega, t) d\omega,$$

where  $M_1$  is the magnitude of the down-telescope between the input lens and the objective (Zeiss 10x/0.2 numerical aperture),  $M_2$  is the image magnification onto the camera between the tube lens and the objective, and  $M_{1,2} = 7.6$ .  $C(x, y) = \sum C_i(x, y)$  is the spatial distribution of fluorophores, where  $C_i$  represents different fluorophores and includes cross-sections, emission spectra transmission through filters, and other such factors. The captured fluorescent emission intensity retains the encoded excitation frequency modulations, enabling

fluorescent species identification based on the absorbed spectra recovered from the LiLa signal.

We dyed two separate pieces of lens tissue with Alexa Fluor 514 and 546 and situated them in close proximity to one another underneath a cover slip. As an excitation source we frequency-doubled 25 fs pulses at 1075 nm with 10 nJ of pulse energy [83, 27] in a 250  $\mu\text{m}$  potassium-dihydrogen-phosphate crystal. The two dyes' absorption spectra cut-off and -on in roughly the middle of the second-harmonic generation spectrum. HI-ELF images were acquired using the setup in Fig. 14.2(a) with a camera (Andor Neo) operating at a frame rate of 735 Hz over a pixel area of  $240 \times 1000$  px and  $\nu_r = 0.57$  Hz, which keeps the highest frequency in the excitation LiLa spectrum below the Nyquist limit of the camera frame rate. Image processing flowchart and resultant HI-ELF are shown in Fig. 14.3.

To generate the absorbed HI hypercube,  $S(x_i, y_j; \lambda)$ , we Fourier transform the temporal signal at each pixel,  $s(x_i, y_j; t)$ , with a noise reducing gate function. As our excitation spectra did not fully enclose the absorption spectra of the two fluorophores, we use the “un-absorbed” spectra as the contrast mechanism. The difference between an appropriately scaled reference spectrum and the measured absorbed spectrum at each pixel constitutes an un-absorbed spectrum. A surface reflection from a wedge captured on a photodetector generates the reference excitation LiLa spectrum. The reference spectrum is scaled for each pixel such that within modulation frequency windows, black-dashed boxes in Fig. 14.3(c), it circumscribes the absorbed spectrum. Reference un-absorbed spectra for the two dyes are shown in Fig. 14.3(d). Fitting the un-absorbed spectra of each pixel with the reference un-absorbed spectra scaled by coefficients  $a_{514,546}(x_i, y_j)$  generates a species map. The fit parameters  $a_{514,546}(x_i, y_j)$  are found using a least mean-squared-error

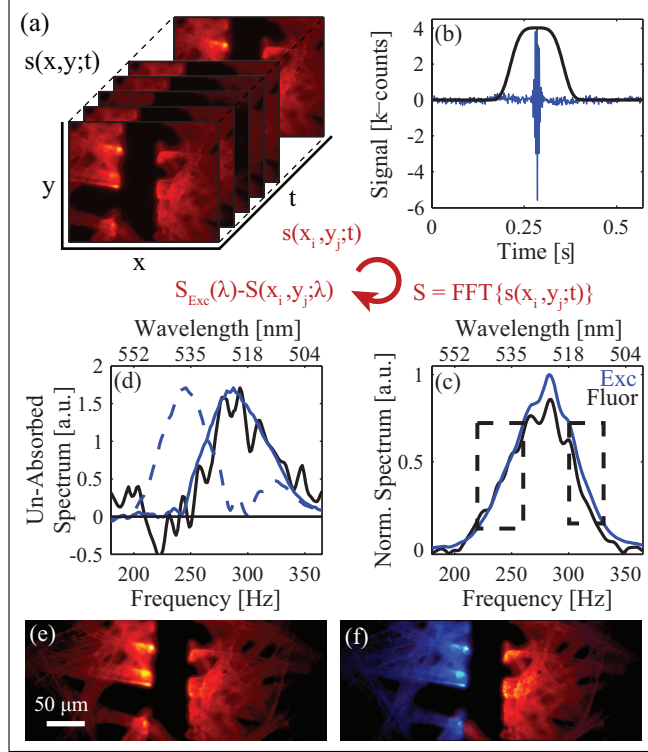


FIGURE 14.3. Image processing: (a) image hypercube in time-domain, (b) single pixel temporal data (blue) and gating filter (black), (c) fast Fourier transform of single pixel temporal data (black) compared to the excitation spectrum (blue), and (d) the single pixel un-absorbed spectrum (black) compared to the reference unabsorbed spectra (Alexa Fluor 514 and 546, blue-dashed and blue-solid, respectively). Widefield micrographs of two lens tissues dyed with Alexa Fluor 514 and 546 using (e) the fluorescent intensity only and (f) HI-ELF, Alexa Fluor 514 and 546 in blue and red, respectively.

search. The integrated absorbed power spectrum of each pixel, Fig. 14.3(e), is then scaled by  $a_{514,546}(x_i, y_j)/(a_{514}(x_i, y_j) + a_{546}(x_i, y_j))$ , creating two fluorescent species labeled micrographs. A combination image is shown in Fig. 14.3(f), with the Alexa Fluor 514 and 546 coefficients taking blue and red color schemes, respectively.

The performance of our LiLa setup could be improved by increasing the reticle  $\Delta k$ , since the pertinent focal spot sizes of monochromatic wavelets are currently much smaller than  $1/\Delta k$ . Increasing  $\Delta k$  from 5 to 50  $\text{mm}^{-1}$  would match the smallest reticle feature size to the focal spot sizes of the the wavelets, increasing the number of spectral points by an order

of magnitude. In terms of pixel count, an  $n \approx 1000$  would compare favorably with many traditional spectrometers in the near-infrared, and it would be a significant improvement in the mid-infrared.

We have introduced a new method of HI using temporal LiLa. The potency of this new technique is demonstrated by performing background-free absorption imaging via ELF. Merging the LiLa method for acquiring spectra with SPIFI will enable a vast increase in frame rate, well beyond the limits of array detectors.

## CHAPTER 15

### A FINAL SUMMARY AND LOOKING FORWARD

*“Begin at the beginning,” the King said, very gravely, “and go on till you come to the end: then stop.”*

Lewis Carroll

We will use this final chapter to summarize some of the thoughts and ideas contained in the previous chapters as well as briefly outline some of the future work we hope to perform. The 1060 nm sources already have their own dedicated summary chapter, Chapter 8, so here, we will restrict ourselves to an overarching summary of the 1060 nm sources.

The 1060 nm fiber sources from Part I of this dissertation are now at the point where we can begin utilizing them for research applications. The ultrafast technology we developed, and detailed in Part I, has proved to be a robust solution for high-quality, energetic pulses at 1060 nm, and importantly, a solution we can now replicate very economically. The current research systems up or under development using ultrafast sources built by us span not only a number of graduate students within the Bartels ultrafast group but multiple universities (University of Colorado Denver and Colorado School of Mines) and include several laser-scanning, multi-modal, multi-photon microscopes [116, 34]; a green pumped multi-photon microscope using a second-harmonic generation pulse; a hyperspectral excitation labeled fluorescence, widefield microscope; a new super resolution method suitable for harmonic generation imaging; a hyperspectral tomographic microscope; a hyperspectral, spatial frequency domain imaging system; and a dichroic, visible transient absorption microscope.

The last experimental system listed above (a dichroic, visible transient absorption microscope) is a good example of the new paths the technology and ideas contained in this dissertation will let us travel. We should be able to use just an ANDi oscillator to generate  $< 20$  fs pulses in a new optical fiber spectral broadening platform without the need for a pulse shaper. The  $< 20$  fs pulses will seed two separate periodically-poled lithium niobate crystals to generate a pulse pair at different central wavelengths between 480–570 nm. The dichroic visible pulse pair will then drive a linear, transient absorption microscope. It is exactly this sort of flexibility which excites us about the future of these sources, driving not only multi-photon microscopes but being able to conceive of systems for a broad diversity of needs (color, pulse duration, chirp requirements, etc.).

In Part II of this dissertation, we demonstrated and proposed fiber-based routes towards producing pulses in the second near-infrared biological imaging window around 1300 nm suitable for multi-photon microscopy. The fiber-based nonlinear wavelength conversion system we demonstrated in Chapter 10, showed promise by generating the shortest fiber-derived 1250 nm pulses published to date. Adding a Faraday isolator and advances in how to construct the nonlinear fiber assembly would enable both higher pulse energies and reduce the destabilizing feedback into the preceding fiber amplifier. As another approach to generating pulses in this wavelength region, our initial modeling seeding a Nd-doped fiber amplifier (Chapter 11) with a soliton self-frequency shifted pulse (Chapter 9) is exceptionally promising in terms of both potential pulse energies and durations. Both conversion routes compare favorably to the current source benchmark at 1300 nm of Ti:sapphire pumped optical parametric oscillators. The amplifier route in particular is enticing; the amplifier would be very

similar to our established master oscillator nonlinear and power amplifier systems (Chapter 3), except in this case the amplifier would open up the highly attractive second biological imaging window to exploration.

Lastly in Part III of this dissertation, we examined and demonstrated just a few of the multitude of nonlinear applications open to our ultrafast sources. Of particular interest are applications involving the subtle use and manipulation of either the short durations or the broad color content of these pulses, such as the tunable, coherent excitation of molecular vibrational modes by a chirped, beating pulse pair (Chapter 12) and the high-speed delay scanner for pump-probe spectroscopy (Chapter 13). We are especially proud of the last chapter in Part III, Chapter 14, as it combined nearly every 1060 nm ultrafast technology we developed with two new technologies developed by the Bartels ultrafast group: light labeling, which down samples the optical angular bandwidth of the pulse to laboratory frequencies well within the bandwidth of square-law detectors, and excitation labeled fluorescence, which captures back-ground free absorbed spectra via the temporal dynamics transferred from the excitation into the fluorescent intensity. As a means of multiplexing spectral signals in the time domain, the possibilities of light labeling are extensive, and we look forward to attempting to capitalize on the technique in a number of upcoming experiments including hyperspectral, spatial frequency domain imaging and hyperspectral, spatial frequency modulated tomographic imaging.

For the readers who have made it the very end, I would like to personally thank you for your perseverance.

## BIBLIOGRAPHY

- [1] W. Denk, J. H. Strickler, and W. W. Webb, “Two-photon laser scanning fluorescence microscopy.” *Science* **248**, 73–76 (1990).
- [2] L. Dhar, J. A. Rogers, and K. A. Nelson, “Time-resolved vibrational spectroscopy in the impulsive limit,” *Chem. Rev.* **94**, 157–193 (1994).
- [3] R. Bartels, S. Backus, E. Zeek, L. Misoguti, G. Vdovin, I. Christov, M. Murnane, and H. Kapteyn, “Shaped-pulse optimization of coherent emission of high-harmonic soft X-rays,” *Nature* **406**, 164–6 (2000).
- [4] A. Chong, J. Buckley, W. Renninger, and F. Wise, “All-normal-dispersion femtosecond fiber laser,” *Opt. Express* **14**, 10095 (2006).
- [5] S. Lefrançois, K. Kieu, Y. Deng, J. D. Kafka, and F. W. Wise, “Scaling of dissipative soliton fiber lasers to megawatt peak powers by use of large-area photonic crystal fiber.” *Opt. Lett.* **35**, 1569–1571 (2010).
- [6] W. H. Renninger, A. Chong, and F. W. Wise, “Giant-chirp oscillators for short-pulse fiber amplifiers.” *Opt. Lett.* **33**, 3025–3027 (2008).
- [7] J. H. Lin, D. Wang, and K. H. Lin, “High energy pulses generation with giant spectrum bandwidth and submegahertz repetition rate from a passively mode-locked Yb-doped fiber laser in all normal dispersion cavity,” *Laser Phys. Lett.* **8**, 66–70 (2011).
- [8] D. Strickland and G. Mourou, “Compression of amplified chirped optical pulses,” *Opt. Commun.* **55**, 447–449 (1985).
- [9] K. Qian, H. Wang, M. Laroche, and A. Hideur, “Mode-locked Nd-doped fiber laser at 930 nm,” *Opt. Lett.* **39**, 267–270 (2014).

- [10] E. J. R. Kelleher, J. C. Travers, Z. Sun, a. C. Ferrari, K. M. Golant, S. V. Popov, and J. R. Taylor, “Bismuth fiber integrated laser mode-locked by carbon nanotubes,” *Laser Phys. Lett.* **7**, 790–794 (2010).
- [11] R. Gumenyuk, J. Puustinen, A. V. Shubin, I. a. Bufetov, E. M. Dianov, and O. G. Okhotnikov, “Operating in Anomalous and Normal Dispersion Regimes,” *Opt. Lett.* **38**, 4005–4007 (2013).
- [12] A. Cabasse, B. Ortaç, G. Martel, A. Hideur, and J. Limpert, “Dissipative solitons in a passively mode-locked Er-doped fiber with strong normal dispersion.” *Opt. Express* **16**, 19322–19329 (2008).
- [13] R. Gumenyuk, I. Vartiainen, H. Tuovinen, and O. G. Okhotnikov, “Dissipative dispersion-managed soliton 2  $\mu\text{m}$  thulium/holmium fiber laser.” *Opt. Lett.* **36**, 609–611 (2011).
- [14] R. Paschotta, J. Nilsson, A. C. Tropper, and D. C. Hanna, “Ytterbium-doped fiber amplifiers,” *IEEE J. Quantum Electron.* **33**, 1049–1056 (1997).
- [15] M. Oheim, E. Beaurepaire, E. Chaigneau, J. Mertz, and S. Charpak, “Two-photon microscopy in brain tissue: parameters influencing the imaging depth,” *J. Neurosci. Methods* **111**, 29–37 (2001).
- [16] M. Balu, T. Baldacchini, J. Carter, T. B. Krasieva, R. Zadoyan, and B. J. Tromberg, “Effect of excitation wavelength on penetration depth in nonlinear optical microscopy of turbid media.” *J. Biomed. Opt.* **14**, 010508 (2009).
- [17] D. Kobat, M. E. Durst, N. Nishimura, A. W. Wong, C. B. Schaffer, and C. Xu, “Deep tissue multiphoton microscopy using longer wavelength excitation.” *Opt. Express* **17**, 13354–64 (2009).

- [18] N. G. Horton, K. Wang, D. Kobat, C. G. Clark, F. W. Wise, C. B. Schaffer, and C. Xu, “In vivo three-photon microscopy of subcortical structures within an intact mouse brain.” *Nat. Photonics* **7**, 1–5 (2013).
- [19] M. T. Asaki, C. P. Huang, D. Garvey, J. Zhou, H. C. Kapteyn, and M. M. Murnane, “Generation of 11-fs pulses from a self-mode-locked Ti:sapphire laser.” *Opt. Lett.* **18**, 977–979 (1993).
- [20] A. Galvanauskas, G. C. Cho, A. Hariharan, M. E. Fermann, and D. Harter, “Generation of high-energy femtosecond pulses in multimode-core Yb-fiber chirped-pulse amplification systems.” *Opt. Lett.* **26**, 935–937 (2001).
- [21] D. N. Papadopoulos, Y. Zaouter, M. Hanna, F. Druon, E. Mottay, E. Cormier, and P. Georges, “Generation of 63 fs 4.1 MW peak power pulses from a parabolic fiber amplifier operated beyond the gain bandwidth limit.” *Opt. Lett.* **32**, 2520–2 (2007).
- [22] K. Kieu, W. H. Renninger, a. Chong, and F. W. Wise, “Sub-100 fs pulses at watt-level powers from a dissipative-soliton fiber laser.” *Opt. Lett.* **34**, 593–5 (2009).
- [23] P. Sévillano, P. Georges, F. Druon, D. Descamps, and E. Cormier, “32-fs Kerr-lens mode-locked Yb:CaGdAlO<sub>4</sub> oscillator optically pumped by a bright fiber laser,” *Opt. Lett.* **39**, 6001 (2014).
- [24] T. Kurita, H. Yoshida, T. Kawashima, and N. Miyanaga, “Generation of sub-7-cycle optical pulses from a mode-locked ytterbium-doped single-mode fiber oscillator pumped by polarization-combined 915 nm laser diodes.” *Opt. Lett.* **37**, 3972–4 (2012).
- [25] H. Tu, Y. Liu, X. Liu, D. Turchinovich, J. Lægsgaard, and S. A. Boppart, “Nonlinear polarization dynamics in a weakly birefringent all-normal dispersion photonic crystal

- fiber: toward a practical coherent fiber supercontinuum laser.” *Opt. Express* **20**, 1113–28 (2012).
- [26] S. R. Domingue and R. A. Bartels, “Overcoming temporal polarization instabilities from the latent birefringence in all-normal dispersion, wave-breaking-extended nonlinear fiber supercontinuum generation.” *Opt. Express* **21**, 13305–21 (2013).
- [27] S. R. Domingue and R. A. Bartels, “Nearly transform-limited sub-20-fs pulses at 1065 nm and 10 nJ enabled by a flat field ultrafast pulse shaper,” *Opt. Lett.* **40**, 253 (2015).
- [28] J. M. Dudley and S. Coen, “Supercontinuum generation in photonic crystal fiber,” *Rev. Mod. Phys.* **78**, 1135–1184 (2006).
- [29] C. Finot, B. Kibler, L. Provost, and S. Wabnitz, “Beneficial impact of wave-breaking for coherent continuum formation in normally dispersive nonlinear fibers,” *J. Opt. Soc. Am. B* **25**, 1938 (2008).
- [30] P. J. Campagnola and C.-Y. Dong, “Second harmonic generation microscopy: principles and applications to disease diagnosis,” *Laser Photon. Rev.* **5**, 13–26 (2011).
- [31] P. T. So, C. Y. Dong, B. R. Masters, and K. M. Berland, “Two-photon excitation fluorescence microscopy.” *Annu. Rev. Biomed. Eng.* **2**, 399–429 (2000).
- [32] P. Campagnola, “Second harmonic generation imaging microscopy: Applications to diseases diagnostics,” *Anal. Chem.* **83**, 3224–3231 (2011).
- [33] P. J. Campagnola, A. C. Millard, M. Terasaki, P. E. Hoppe, C. J. Malone, and W. a. Mohler, “Imaging of Endogenous Structural Proteins in Biological Tissues,” *Biophys. J.* **82**, 493–508 (2002).

- [34] O. Masihzadeh, T. C. Lei, S. R. Domingue, M. Y. Kahook, R. A. Bartels, and D. A. Ammar, “Third harmonic generation microscopy of a mouse retina,” *Mol. Vis.* **21**, 538–547 (2015).
- [35] C. Xu, W. Zipfel, J. B. Shear, R. M. Williams, and W. W. Webb, “Multiphoton fluorescence excitation: new spectral windows for biological nonlinear microscopy.” *Proc. Natl. Acad. Sci. U. S. A.* **93**, 10763–10768 (1996).
- [36] W. R. Zipfel, R. M. Williams, R. Christie, A. Y. Nikitin, B. T. Hyman, and W. W. Webb, “Live tissue intrinsic emission microscopy using multiphoton-excited native fluorescence and second harmonic generation.” *Proc. Natl. Acad. Sci. U. S. A.* **100**, 7075–7080 (2003).
- [37] K. W. Dunn and T. A. Sutton, “Functional studies in living animals using multiphoton microscopy.” *ILAR J.* **49**, 66–77 (2008).
- [38] C. Stosiek, O. Garaschuk, K. Holthoff, and A. Konnerth, “In vivo two-photon calcium imaging of neuronal networks.” *Proc. Natl. Acad. Sci. U. S. A.* **100**, 7319–7324 (2003).
- [39] K. Svoboda and R. Yasuda, “Principles of Two-Photon Excitation Microscopy and Its Applications to Neuroscience,” *Neuron* **50**, 823–839 (2006).
- [40] N. Olivier, M. a. Luengo-oroz, L. Duloquin, E. Faure, T. Savy, I. Veilleux, X. Solinas, D. Débarre, P. Bourguin, A. Santos, N. Peyriéras, and E. Beaurepaire, “Cell Lineage Reconstruction of Early Zebrafish Embryos Using Label-Free Nonlinear Microscopy,” *Science* **70**, 967–971 (2010).
- [41] M. Mogensen, B. M. Nürnberg, J. L. Forman, J. B. Thomsen, L. Thrane, and G. B. E. Jemec, “In vivo thickness measurement of basal cell carcinoma and actinic keratosis

- with optical coherence tomography and 20-MHz ultrasound,” *Br. J. Dermatol.* **160**, 1026–1033 (2009).
- [42] J. Paoli, M. Smedh, A.-M. Wennberg, and M. B. Ericson, “Multiphoton laser scanning microscopy on non-melanoma skin cancer: morphologic features for future non-invasive diagnostics.” *J. Invest. Dermatol.* **128**, 1248–1255 (2008).
- [43] S.-J. Lin, S.-H. Jee, C.-J. Kuo, R.-J. Wu, W.-C. Lin, J.-S. Chen, Y.-H. Liao, C.-J. Hsu, T.-F. Tsai, Y.-F. Chen, and C.-Y. Dong, “Discrimination of basal cell carcinoma from normal dermal stroma by quantitative multiphoton imaging.” *Opt. Lett.* **31**, 2756–2758 (2006).
- [44] R. Cicchi, A. Sturiale, G. Nesi, D. Kapsokalyvas, G. Alemanno, F. Tonelli, and F. S. Pavone, “Multiphoton morpho-functional imaging of healthy colon mucosa, adenomatous polyp and adenocarcinoma.” *Biomed. Opt. Express* **4**, 1204–13 (2013).
- [45] J. N. Rogart, J. Nagata, C. S. Loeser, R. D. Roorda, H. Aslanian, M. E. Robert, W. R. Zipfel, and M. H. Nathanson, “Multiphoton Imaging Can Be Used for Microscopic Examination of Intact Human Gastrointestinal Mucosa Ex Vivo,” *Clin. Gastroenterol. Hepatol.* **6**, 95–101 (2008).
- [46] T. Makino, M. Jain, D. C. Montrose, A. Aggarwal, J. Sterling, B. P. Bosworth, J. W. Milsom, B. D. Robinson, M. M. Shevchuk, K. Kawaguchi, N. Zhang, C. M. Brown, D. R. Rivera, W. O. Williams, C. Xu, A. J. Dannenberg, and S. Mukherjee, “Multiphoton tomographic imaging: A potential optical biopsy tool for detecting gastrointestinal inflammation and neoplasia,” *Cancer Prev. Res.* **5**, 1280–1290 (2012).
- [47] M. J. Katz, D. M. Huland, and R. Ramasamy, “Multiphoton microscopy: applications in Urology and Andrology,” *Transl. Androl. Urol.* **3**, 77 (2014).

- [48] D. M. Huland, B. D. Robinson, D. S. Harya, M. M. Shevchuk, C. Xu, and A. K. Tewari, “Multiphoton gradient index endoscopy for evaluation of diseased human prostatic tissue ex vivo of diseased human prostatic tissue ex vivo,” *J. Biomed. Opt.* **19**, 116011 (2014).
- [49] X. Wu, G. Chen, J. Lu, W. Zhu, J. Qiu, J. Chen, S. Xie, S. Zhuo, and J. Yan, “Label-Free Detection of Breast Masses Using Multiphoton Microscopy,” *PLoS One* **8**, 1–7 (2013).
- [50] I. Pavlova, K. R. Hume, S. a. Yazinski, J. Flanders, T. L. Southard, R. S. Weiss, and W. W. Webb, “Multiphoton microscopy and microspectroscopy for diagnostics of inflammatory and neoplastic lung,” *J. Biomed. Opt.* **17**, 036014 (2012).
- [51] C.-C. Wang, F.-C. Li, R.-J. Wu, V. a. Hovhannisyan, W.-C. Lin, S.-J. Lin, P. T. C. So, and C.-Y. Dong, “Differentiation of normal and cancerous lung tissues by multiphoton imaging.” *J. Biomed. Opt.* **14**, 044034 (2009).
- [52] M. Oheim, E. Beaurepaire, E. Chaigneau, J. Mertz, and S. Charpak, “Two-photon microscopy in brain tissue: parameters influencing the imaging depth.” *J. Neurosci. Methods* **111**, 29–37 (2001).
- [53] D. Kobat, N. G. Horton, and C. Xu, “In vivo two-photon microscopy to 1.6-mm depth in mouse cortex,” *J. Biomed. Opt.* **16**, 106014 (2011).
- [54] S.-W. Chu, S.-Y. Chen, T.-H. Tsai, T.-M. Liu, C.-Y. Lin, H.-J. Tsai, and C.-K. Sun, “In vivo developmental biology study using noninvasive multi-harmonic generation microscopy.” *Opt. Express* **11**, 3093–3099 (2003).

- [55] D. M. Huland, K. Charan, D. G. Ouzounov, J. S. Jones, N. Nishimura, and C. Xu, “Three-photon excited fluorescence imaging of unstained tissue using a GRIN lens endoscope.” *Biomed. Opt. Express* **4**, 652–658 (2013).
- [56] Y. Fu, H. Wang, R. Shi, and J.-X. Cheng, “Characterization of photodamage in coherent anti-Stokes Raman scattering microscopy.” *Opt. Express* **14**, 3942–3951 (2006).
- [57] I. H. Chen, S. W. Chu, C. K. Sun, P. C. Cheng, and B. L. Lin, “Wavelength dependent damage in biological multi-photon confocal microscopy : A micro-spectroscopic comparison between femtosecond Ti : sapphire and Cr : forsterite laser sources,” *Opt. Quantum Electron.* **34**, 1251–1266 (2002).
- [58] J. M. Squirrell, D. L. Wokosin, J. G. White, and B. D. Bavister, “Long-term two-photon fluorescence imaging of mammalian embryos without compromising viability.” *Nat. Biotechnol.* **17**, 763–767 (1999).
- [59] K. König, P. T. So, W. W. Mantulin, and E. Gratton, “Cellular response to near-infrared femtosecond laser pulses in two-photon microscopes.” *Opt. Lett.* **22**, 135–136 (1997).
- [60] C. Xu and F. W. Wise, “Recent advances in fibre lasers for nonlinear microscopy,” *Nat Phot.* **7**, 875–882 (2013).
- [61] S. W. Chu, I. H. Chen, T. M. Liu, P. C. Chen, C. K. Sun, and B. L. Lin, “Multimodal nonlinear spectral microscopy based on a femtosecond Cr:forsterite laser.” *Opt. Lett.* **26**, 1909–11 (2001).
- [62] a. M. Weiner and I. Introduction, “Femtosecond pulse shaping using spatial light modulators,” *Rev. Sci. Instrum.* **71**, 1929 (2000).

- [63] J. W. Wilson, P. Schlup, and R. A. Bartels, “Ultrafast phase and amplitude pulse shaping with a single, one-dimensional, high-resolution phase mask.” *Opt. Express* **15**, 8979 (2007).
- [64] R. a. Bartels, T. C. Weinacht, S. R. Leone, H. C. Kapteyn, and M. M. Murnane, “Nonresonant control of multimode molecular wave packets at room temperature.” *Phys. Rev. Lett.* **88**, 033001 (2002).
- [65] A. M. Weiner, D. E. Leaird, G. P. Wiederrecht, and K. A. Nelson, “Femtosecond multiple-pulse impulsive stimulated Raman scattering spectroscopy,” *J. Opt. Soc. Am. B* **8**, 1264 (1991).
- [66] S. R. Domingue, D. G. Winters, and R. A. Bartels, “Time-resolved coherent Raman spectroscopy by high-speed pump-probe delay scanning,” *Opt. Lett.* **39**, 4124 (2014).
- [67] J. W. Wilson and R. A. Bartels, “Rapid birefringent delay scanning for coherent multiphoton impulsive raman pump-probe spectroscopy,” *IEEE J. Sel. Top. Quantum Electron.* **18**, 130–139 (2012).
- [68] M. Bauer, C. Lei, K. Read, R. Tobey, J. Gland, M. Murnane, and H. Kapteyn, “Direct Observation of Surface Chemistry Using Ultrafast Soft-X-Ray Pulses,” *Phys. Rev. Lett.* **87**, 025501 (2001).
- [69] D. Fu, T. Ye, T. E. Matthews, B. J. Chen, G. Yurtserver, and W. S. Warren, “High-resolution in vivo imaging of blood vessels without labeling.” *Opt. Lett.* **32**, 2641–3 (2007).
- [70] G. Futia, P. Schlup, D. G. Winters, and R. A. Bartels, “Spatially-chirped modulation imaging of absorbtion and fluorescent objects on single-element optical detector.” *Opt. Express* **19**, 1626–1640 (2011).

- [71] D. G. Winters and R. A. Bartels, “Two-dimensional single-pixel imaging by cascaded orthogonal line spatial modulation,” *Opt. Lett.* **40**, 2774 (2015).
- [72] E. D. Diebold, B. W. Buckley, D. R. Gossett, and B. Jalali, “Digitally synthesized beat frequency multiplexing for sub-millisecond fluorescence microscopy,” *Nat. Photonics* **7**, 806–810 (2013).
- [73] E. Hecht, *Optics 4th edition* (Addison Wesley Longman Inc, 1998).
- [74] O. E. Martinez, J. P. Gordon, and R. L. Fork, “Negative group-velocity dispersion using refraction,” *J. Opt. Soc. Am. A* **1**, 1003 (1984).
- [75] O. Martinez, “3000 times grating compressor with positive group velocity dispersion: Application to fiber compensation in 1.3-1.6  $\mu\text{m}$  region,” *IEEE J. Quantum Electron.* **23**, 59–64 (1987).
- [76] S. Kane and J. Squier, “Grism-pair stretcher-compressor system for simultaneous second- and third-order dispersion compensation in chirped-pulse amplification,” *J. Opt. Soc. Am. B* **14**, 661 (1997).
- [77] L. Nugent-Glandorf, T. a. Johnson, Y. Kobayashi, and S. a. Diddams, “Impact of dispersion on amplitude and frequency noise in a Yb-fiber laser comb.” *Opt. Lett.* **36**, 1578–1580 (2011).
- [78] D. J. Kane, “Principal components generalized projections: a review [Invited],” *J. Opt. Soc. Am. B* **25**, A120 (2008).
- [79] R. W. Boyd, *Nonlinear optics* (Academic press, 2003).
- [80] C. Mertz Jerome, *Introduction to Optical Microscopy* (Roberts and Company Publishers, 2009).

- [81] B. Kohler, V. Yakovlev, J. Che, J. Krause, M. Messina, K. Wilson, N. Schwentner, R. Whittell, and Y. Yan, “Quantum Control of Wave Packet Evolution with Tailored Femtosecond Pulses,” *Phys. Rev. Lett.* **74**, 3360–3363 (1995).
- [82] N. Dudovich, B. Dayan, S. Gallagher Faeder, and Y. Silberberg, “Transform-Limited Pulses Are Not Optimal for Resonant Multiphoton Transitions,” *Phys. Rev. Lett.* **86**, 47–50 (2001).
- [83] S. R. Domingue and R. A. Bartels, “Nonlinear fiber amplifier with tunable transform limited pulse duration from a few 100 to sub-100-fs at watt-level powers.” *Opt. Lett.* **39**, 359–62 (2014).
- [84] T. Eidam, S. Hanf, E. Seise, T. V. Andersen, T. Gabler, C. Wirth, T. Schreiber, J. Limpert, and A. Tünnermann, “Femtosecond fiber CPA system emitting 830 W average output power.” *Opt. Lett.* **35**, 94–6 (2010).
- [85] M. E. Fermann, V. I. Kruglov, B. C. Thomsen, J. M. Dudley, and J. D. Harvey, “Self-similar propagation and amplification of parabolic pulses in optical fibers.” *Phys. Rev. Lett.* **84**, 6010–3 (2000).
- [86] Y. Zaouter, D. N. Papadopoulos, M. Hanna, J. Bouillet, L. Huang, C. Aguergaray, F. Druon, E. Mottay, P. Georges, and E. Cormier, “Stretcher-free high energy nonlinear amplification of femtosecond pulses in rod-type fibers.” *Opt. Lett.* **33**, 107–109 (2008).
- [87] L. Shah, Z. Liu, I. Hartl, G. Imeshev, G. Cho, and M. Fermann, “High energy femtosecond Yb cubicon fiber amplifier.” *Opt. Express* **13**, 4717–22 (2005).
- [88] H. G. Winful, “Polarization instabilities in birefringent nonlinear media: application to fiber-optic devices.” *Opt. Lett.* **11**, 33 (1986).
- [89] G. P. Agrawal, *Nonlinear fiber optics* (Academic press, 2007).

- [90] S. Wang, B. Liu, C. Gu, Y. Song, C. Qian, M. Hu, L. Chai, and C. Wang, “Self-similar evolution in a short fiber amplifier through nonlinear pulse preshaping.” *Opt. Lett.* **38**, 296–8 (2013).
- [91] A. Sullivan, W. E. White, K. C. Chu, J. P. Heritage, K. W. DeLong, and R. Trebino, “Quantitative investigation of optical phase-measuring techniques for ultrashort pulse lasers,” *J. Opt. Soc. Am. B* **13**, 1965 (1996).
- [92] B. E. Lemoff and C. P. Barty, “Cubic-phase-free dispersion compensation in solid-state ultrashort-pulse lasers.” *Opt. Lett.* **18**, 57–59 (1993).
- [93] A. M. Heidt, J. Rothhardt, A. Hartung, H. Bartelt, E. G. Rohwer, J. Limpert, and A. Tünnermann, “High quality sub-two cycle pulses from compression of supercontinuum generated in all-normal dispersion photonic crystal fiber,” *Opt. Express* **19**, 13873 (2011).
- [94] A. M. Heidt, A. Hartung, G. W. Bosman, P. Krok, E. G. Rohwer, H. Schwoerer, and H. Bartelt, “Coherent octave spanning near-infrared and visible supercontinuum generation in all-normal dispersion photonic crystal fibers.” *Opt. Express* **19**, 3775–87 (2011).
- [95] P.-A. Champert, V. Couderc, P. Leproux, S. Février, V. Tombelaine, L. Labonté, P. Roy, C. Froehly, and P. Nérin, “White-light supercontinuum generation in normally dispersive optical fiber using original multi-wavelength pumping system.” *Opt. Express* **12**, 4366–4371 (2004).
- [96] L. E. Hooper, P. J. Mosley, A. C. Muir, W. J. Wadsworth, and J. C. Knight, “Coherent supercontinuum generation in photonic crystal fiber with all-normal group velocity dispersion.” *Opt. Express* **19**, 4902–4907 (2011).

- [97] Y. Liu, H. Tu, and S. a. Boppart, “Wave-breaking-extended fiber supercontinuum generation for high compression ratio transform-limited pulse compression,” *Opt. Lett.* **37**, 2172 (2012).
- [98] D. L. Marks, A. L. Oldenburg, J. J. Reynolds, and S. a. Boppart, “Study of an ultrahigh-numerical-aperture fiber continuum generation source for optical coherence tomography.” *Opt. Lett.* **27**, 2010–2012 (2002).
- [99] K. L. Corwin, N. R. Newbury, J. M. Dudley, S. Coen, S. a. Diddams, K. Weber, and R. S. Windeler, “Fundamental noise limitations to supercontinuum generation in microstructure fiber.” *Phys. Rev. Lett.* **90**, 113904 (2003).
- [100] S. Backus, C. G. Durfee, M. M. Murnane, and H. C. Kapteyn, “High power ultrafast lasers,” *Rev. Sci. Instrum.* **69**, 1207 (1998).
- [101] G. O. Clay, A. C. Millard, C. B. Schaffer, J. Aus-der Au, P. S. Tsai, J. a. Squier, and D. Kleinfeld, “Spectroscopy of third-harmonic generation: evidence for resonances in model compounds and ligated hemoglobin,” *J. Opt. Soc. Am. B* **23**, 932 (2006).
- [102] S. F. Feldman, D. A. Weinberger, and H. G. Winful, “Observation of polarization instabilities and modulational gain in a low-birefringence optical fiber.” *Opt. Lett.* **15**, 311 (1990).
- [103] H. G. Winful, “Self-induced polarization changes in birefringent optical fibers,” *Appl. Phys. Lett.* **47**, 213–215 (1985).
- [104] S. Wabnitz, “Modulational polarization instability of light in a nonlinear birefringent dispersive medium,” *Phys. Rev. A* **38**, 2018–2021 (1988).
- [105] Z. Zhu and T. G. Brown, “Polarization properties of supercontinuum spectra generated in birefringent photonic crystal fibers,” *J. Opt. Soc. Am. B* **21**, 249 (2004).

- [106] H. Tu, D. L. Marks, Y. L. Koh, and S. a. Boppart, “Stabilization of continuum generation from normally dispersive nonlinear optical fibers for a tunable broad bandwidth source for optical coherence tomography,” *Opt. Lett.* **32**, 2037 (2007).
- [107] S. G. Murdoch, R. Leonhardt, and J. D. Harvey, “Polarization modulation instability in weakly birefringent fibers.” *Opt. Lett.* **20**, 866–868 (1995).
- [108] P. Tournois, “New diffraction grating pair with very linear dispersion for laser pulse compression,” *Electron. Lett.* **29**, 1414 (1993).
- [109] S. Kane and J. Squier, “Grating compensation of third-order material dispersion in the normal dispersion regime: sub-100-fs chirped-pulse amplification using a fiber stretcher and grating-pair compressor,” *IEEE J. Quantum Electron.* **31**, 2052–2057 (1995).
- [110] F. V. Hartemann, S. G. Anderson, D. J. Gibson, C. a. Hagmann, M. S. Johnson, I. Jovanovic, M. J. Messerly, J. a. Pruet, M. Y. Shverdin, a. M. Tremaine, D. P. McNabb, C. W. Siders, and C. P. J. Barty, “Gamma-ray compton light source development at LLNL,” *PPPS-2007 - Pulsed Power Plasma Sci. 2007* **2**, 1382–1386 (2007).
- [111] S. Zhou, L. Kuznetsova, A. Chong, and F. Wise, “Compensation of nonlinear phase shifts with third-order dispersion in short-pulse fiber amplifiers.” *Opt. Express* **13**, 4869–4877 (2005).
- [112] B. Metzger, A. Steinmann, and H. Giessen, “High-power widely tunable sub-20 fs Gaussian laser pulses for ultrafast nonlinear spectroscopy.” *Opt. Express* **19**, 24354–60 (2011).
- [113] S. R. Domingue and R. A. Bartels, “Three-photon excitation source at 1250 nm generated in a dual zero dispersion wavelength nonlinear fiber,” *Opt. Express* **22**, 2665–2673 (2014).

- [114] A. Negrean and H. D. Mansvelder, “Optimal lens design and use in laser-scanning microscopy,” *Biomed. Opt. Express* **5**, 1588 (2014).
- [115] J. W. Wilson, P. Schlup, M. Lunacek, D. Whitley, and R. a. Bartels, “Calibration of liquid crystal ultrafast pulse shaper with common-path spectral interferometry and application to coherent control with a covariance matrix adaptation evolutionary strategy.” *Rev. Sci. Instrum.* **79**, 033103 (2008).
- [116] D. R. Smith, D. G. Winters, and R. a. Bartels, “Submillisecond second harmonic holographic imaging of biological specimens in three dimensions.” *Proc. Natl. Acad. Sci. U. S. A.* **110**, 18391–6 (2013).
- [117] D. G. Ouzounov, F. R. Ahmad, D. Müller, N. Venkataraman, M. T. Gallagher, M. G. Thomas, J. Silcox, K. W. Koch, and A. L. Gaeta, “Generation of megawatt optical solitons in hollow-core photonic band-gap fibers.” *Science* **301**, 1702–4 (2003).
- [118] J. P. Gordon, “Theory of the soliton self-frequency shift.” *Opt. Lett.* **11**, 662–4 (1986).
- [119] J. Knight, J. Arriaga, T. Birks, A. Ortigosa-Blanch, W. Wadsworth, and P. Russell, “Anomalous dispersion in photonic crystal fiber,” *IEEE Photonics Technol. Lett.* **12**, 807–809 (2000).
- [120] D. G. Winters, P. Schlup, and R. a. Bartels, “Subpicosecond fiber-based soliton-tuned mid-infrared source in the 9.7-14.9 microm wavelength region.” *Opt. Lett.* **35**, 2179–2181 (2010).
- [121] A. Aguirre, N. Nishizawa, J. Fujimoto, W. Seitz, M. Lederer, and D. Kopf, “Continuum generation in a novel photonic crystal fiber for ultrahigh resolution optical coherence tomography at 800 nm and 1300 nm.” *Opt. Express* **14**, 1145–60 (2006).

- [122] H. Wang and A. M. Rollins, "Optimization of dual-band continuum light source for ultrahigh-resolution optical coherence tomography." *Appl. Opt.* **46**, 1787–1794 (2007).
- [123] J. van Howe, J. H. Lee, S. Zhou, F. Wise, C. Xu, S. Ramachandran, S. Ghalmi, and M. F. Yan, "Demonstration of soliton self-frequency shift below 1300 nm in higher-order mode, solid silica-based fiber." *Opt. Lett.* **32**, 340–2 (2007).
- [124] J. H. Lee, J. van Howe, C. Xu, S. Ramachandran, S. Ghalmi, and M. F. Yan, "Generation of femtosecond pulses at 1350 nm by Cerenkov radiation in higher-order-mode fiber." *Opt. Lett.* **32**, 1053–5 (2007).
- [125] H. Ammann, W. Hodel, and H. Weber, "Experimental and numerical investigation of short pulse propagation and amplification around 1.3  $\mu\text{m}$  in a Nd<sup>3+</sup>-doped fluoride fiber," *Opt. Commun.* **113**, 39–45 (1994).
- [126] J. Pedersen and M. Brierley, "High saturation output power from a neodymium-doped fluoride fibre amplifier operating in the 1300 nm telecommunications window," *Electron. Lett.* **26**, 819 (1990).
- [127] O. Lumholt, M. Ø bro, A. Bjarklev, T. Rasmussen, B. Pedersen, J. E. Pedersen, J. r. H. Povlsen, and K. Rottwitt, "Optimum placement of filters in 1300 nm Nd-fibre amplifiers," *Opt. Commun.* **89**, 30–32 (1992).
- [128] Y. Ohishi, T. Kanamori, T. Kitagawa, S. Takahashi, E. Snitzer, and G. H. Sigel, "Pr(3+)-doped fluoride fiber amplifier operating at 1.31 microm." *Opt. Lett.* **16**, 1747–1749 (1991).
- [129] D. Peter, W. Hodel, and H. Weber, "Efficient distortion-free amplification of 1.3  $\mu\text{m}$  femtosecond pulses in a Pr<sup>3+</sup>-doped fluoride fiber amplifier," *Opt. Commun.* **130**, 75–80 (1996).

- [130] T. Whitley, R. Wyatt, D. Szebesta, S. Davey, and J. R. Williams, “Quarter-watt output at 1.3  $\mu\text{m}$  from a praseodymium-doped fluoride fiber amplifier pumped with a diode-pumped Nd:YLF laser,” *IEEE Photonics Technol. Lett.* **5**, 399–401 (1993).
- [131] V. V. Dvoyrin, V. M. Mashinsky, L. I. Bulatov, I. A. Bufetov, A. V. Shubin, M. A. Melkumov, E. F. Kustov, E. M. Dianov, A. A. Umnikov, V. F. Khopin, M. V. Yashkov, and A. N. Guryanov, “Bismuth-doped-glass optical fibers—a new active medium for lasers and amplifiers.” *Opt. Lett.* **31**, 2966–2968 (2006).
- [132] I. Bufetov, M. Melkumov, S. Firstov, and K. Riumkin, “Bi-doped optical fibers and fiber lasers,” *IEEE J. Sel. Top. Quantum Electron.* **20**, 0903815 (2014).
- [133] I. a. Bufetov and E. M. Dianov, “Bi-doped fiber lasers,” *Laser Phys. Lett.* **6**, 487–504 (2009).
- [134] E. M. Dianov, S. V. Firstov, V. F. Khopin, A. N. Gur’yanov, and I. A. Bufetov, “Bi-doped fibre lasers and amplifiers emitting in a spectral region of 1.3  $\mu\text{m}$ ,” *Quantum Electron.* **38**, 615–617 (2008).
- [135] S. Norizan, W. Chong, and S. Harun, “O-Band Bismuth Doped Fiber Amplifier with Double-pass Configuration,” *Photonics Technol.* **23**, 1860–1862 (2011).
- [136] J. Pedersen, M. Brierley, S. Carter, P. France, and J. Pankove, “Erratum: Amplification in the 1300 nm telecommunications window in a Nd-doped fluoride fibre,” *Electron. Lett.* **26**, 555 (1990).
- [137] M. Obro, B. Pedersen, A. Bjarklev, J. Povlsen, and J. Pedersen, “Highly improved fibre amplifier for operation around 1300 nm,” *Electron. Lett.* **27**, 470 (1991).
- [138] S. Zhou, D. G. Ouzounov, and F. W. Wise, “Divided-pulse amplification of ultrashort pulses,” *Opt. Lett.* **32**, 871–873 (2007).

- [139] X. Yan, C. Kito, S. Miyoshi, M. Liao, T. Suzuki, and Y. Ohishi, “Raman transient response and enhanced soliton self-frequency shift in ZBLAN fiber,” *J. Opt. Soc. Am. B* **29**, 238 (2012).
- [140] M. Kwaśny, Z. Mierczyk, R. Stpie, and K. Jdrzejewski, “Nd<sup>3+</sup>-, Er<sup>3+</sup>- and Pr<sup>3+</sup>-doped fluoride glasses for laser applications,” *J. Alloys Compd.* **300**, 341–347 (2000).
- [141] C. L. Evans, E. O. Potma, M. Puoris’haag, D. Côté, C. P. Lin, and X. S. Xie, “Chemical imaging of tissue in vivo with video-rate coherent anti-Stokes Raman scattering microscopy.” *Proc. Natl. Acad. Sci. U. S. A.* **102**, 16807–16812 (2005).
- [142] C.-S. Liao, M. N. Slipchenko, P. Wang, J. Li, S.-Y. Lee, R. a. Oglesbee, and J.-X. Cheng, “Microsecond scale vibrational spectroscopic imaging by multiplex stimulated Raman scattering microscopy,” *Light Sci. Appl.* **4**, e265 (2015).
- [143] J. W. Wilson and R. a. Bartels, “Coherence-modulated third harmonic generation for vibrational spectroscopy: a theoretical treatment,” *J. Opt. Soc. Am. B* **29**, 1875 (2012).
- [144] G. Machinet, P. Sevillano, F. Guichard, R. Dubrasquet, P. Camy, J.-L. Doualan, R. Moncorgé, P. Georges, F. Druon, D. Descamps, and E. Cormier, “High-brightness fiber laser-pumped 68 fs-2.3 W Kerr-lens mode-locked Yb:CaF<sub>2</sub> oscillator.” *Opt. Lett.* **38**, 4008–10 (2013).
- [145] A. M. Heidt, J. Rothhardt, A. Hartung, H. Bartelt, E. G. Rohwer, J. Limpert, and A. Tünnermann, “High quality sub-two cycle pulses from compression of supercontinuum generated in all-normal dispersion photonic crystal fiber.” *Opt. Express* **19**, 13873–9 (2011).

- [146] Y.-X. Yan, E. B. Gamble, and K. a. Nelson, “Impulsive stimulated scattering: General importance in femtosecond laser pulse interactions with matter, and spectroscopic applications,” *J. Chem. Phys.* **83**, 5391 (1985).
- [147] J. K. Wahlstrand, R. Merlin, X. Li, S. T. Cundiff, and O. E. Martinez, “Impulsive stimulated Raman scattering: comparison between phase-sensitive and spectrally filtered techniques.” *Opt. Lett.* **30**, 926–8 (2005).
- [148] K. Hartinger and R. a. Bartels, “Modulation of third-harmonic generation conversion in the presence of a rotational wave packet.” *Opt. Lett.* **33**, 1162–1164 (2008).
- [149] R. Bartels, T. Weinacht, N. Wagner, M. Baertschy, C. Greene, M. Murnane, and H. Kapteyn, “Phase Modulation of Ultrashort Light Pulses using Molecular Rotational Wave Packets,” *Phys. Rev. Lett.* **88**, 1–4 (2001).
- [150] K. Hartinger and R. a. Bartels, “Pulse polarization splitting in a transient wave plate.” *Opt. Lett.* **31**, 3526–8 (2006).
- [151] T. Ideguchi, S. Holzner, B. Bernhardt, G. Guelachvili, N. Picqué, and T. W. Hänsch, “Coherent Raman spectro-imaging with laser frequency combs.” *Nature* **502**, 355–8 (2013).
- [152] D. Kupka, J. W. Wilson, O. Masihzadeh, and R. a. Bartels, “Distinguishing bulk and interface modulation of optical third harmonic generation due to coherent optical phonon excitation,” *Chem. Phys. Lett.* **490**, 97–101 (2010).
- [153] D. G. Ferris, R. A. Lawhead, E. D. Dickman, N. Holtzapple, J. A. Miller, S. Grogan, S. Bambot, A. Agrawal, and M. L. Faupel, “Multimodal hyperspectral imaging for the noninvasive diagnosis of cervical neoplasia.” *J. Low. Genit. Tract Dis.* **5**, 65–72 (2001).

- [154] Y. Zhang, Y. Chen, Y. Yu, X. Xue, V. V. Tuchin, and D. Zhu, “Visible and near-infrared spectroscopy for distinguishing malignant tumor tissue from benign tumor and normal breast tissues in vitro.” *J. Biomed. Opt.* **18**, 077003 (2013).
- [155] Z. Lee, K. L. Carder, C. D. Mobley, R. G. Steward, and J. S. Patch, “Hyperspectral remote sensing for shallow waters. 2. Deriving bottom depths and water properties by optimization.” *Appl. Opt.* **38**, 3831–3843 (1999).
- [156] H. Liang, “Advances in multispectral and hyperspectral imaging for archaeology and art conservation,” *Appl. Phys. A Mater. Sci. Process.* **106**, 309–323 (2012).
- [157] J. Kuula, I. Pölönen, H.-H. Puupponen, T. Selander, T. Reinikainen, T. Kalenius, and H. Saari, “Using VIS/NIR and IR spectral cameras for detecting and separating crime scene details,” *SPIE Defense, Secur. Sens.* **8359**, 83590P–83590P (2012).
- [158] T. Vo-Dinh, *Biomedical Photonics Handbook: Biomedical Diagnostics*, vol. 2 (CRC press, 2014).
- [159] D. A. Boas, C. Pitris, and N. Ramanujam, *Handbook of biomedical optics* (CRC press, 2011).
- [160] J. R. Weber, D. J. Cuccia, W. R. Johnson, G. H. Bearman, A. J. Durkin, M. Hsu, A. Lin, D. K. Binder, D. Wilson, and B. J. Tromberg, “Multispectral imaging of tissue absorption and scattering using spatial frequency domain imaging and a computed-tomography imaging spectrometer.” *J. Biomed. Opt.* **16**, 011015 (2011).
- [161] D. Abookasis, C. C. Lay, M. S. Mathews, M. E. Linskey, R. D. Frostig, and B. J. Tromberg, “Imaging cortical absorption, scattering, and hemodynamic response during ischemic stroke using spatially modulated near-infrared illumination,” *J. Biomed. Opt.* **14**, 024033 (2009).

- [162] R. Salzer, G. Steiner, H. H. Mantsch, J. Mansfield, and E. N. Lewis, "Infrared and Raman imaging of biological and biomimetic samples." *Fresenius. J. Anal. Chem.* **366**, 712–6 (2000).
- [163] C. Gendrin, Y. Roggo, and C. Collet, "Pharmaceutical applications of vibrational chemical imaging and chemometrics: A review," *J. Pharm. Biomed. Anal.* **48**, 533–553 (2008).
- [164] G. Lu and B. Fei, "Medical hyperspectral imaging: a review," *J. Biomed. Opt.* **19**, 10901 (2014).
- [165] J. S. Sanders, R. G. Driggers, C. E. Halford, and S. T. Griffin, "Imaging with frequency-modulated reticles," *Opt. Eng.* **30**, 1720 (1991).
- [166] K. Blow and D. Wood, "Theoretical description of transient stimulated Raman scattering in optical fibers," *Quantum Electron. IEEE J.* **25**, 2665–2673 (1989).

## APPENDIX A

# SPLIT-STEP FIBER PROPAGATOR FOR THE GENERALIZED NONLINEAR SCHRÖDINGER EQUATION

*Before I came here, I was confused about this subject. Having listened to your lecture, I am still  
confused – but on a higher level.*

Enrico Fermi

### A.1. THE SPLIT-STEP PROPAGATOR

The generalized nonlinear Schrödinger equation (GNLSE) [28, 99] accurately describes the propagation of ultrafast optical pulses in the tightly confined cores of optical fibers, as verified by Corwin et al. in Ref. [99]. The evolution of the electric field,  $A(z, t)$ , according to the GNLSE is

$$(A.1) \quad \frac{\partial A}{\partial z} + \sum_{k \leq 2} \frac{i^{k+1}}{k!} \beta_k \frac{\partial^k A}{\partial t^k} = -i\gamma \left( 1 + i\tau_{\text{shock}} \frac{\partial}{\partial t} \right) \left( A(z, t) \int_{-\infty}^{\infty} R(t') \times |A(z, t - t')|^2 dt' \right).$$

The  $\beta_k$ 's are the dispersion coefficients of a Taylor expansion of the propagation constant  $\beta(\omega)$ .  $\gamma$  is the fiber nonlinear coefficient. The third-order response function is  $R(t) = (1 - f_R)\delta(t) + f_R h_R(t)$ , where  $\delta(t)$  is the Dirac delta function and  $h_R(t)$  is an analytic representation of the Raman response function. Following Ref [28]  $f_R$  is the relative strengths of the instantaneous (Kerr) and non-instantaneous (Raman) interactions and  $\tau_{\text{shock}} = 1/\omega_0$ .

To model the electric field propagation along the length of the fiber, we implement a split-step fiber propagator following Ref. [89]. This type of numerical propagator separates the GNLSE into independent dispersion and nonlinear operators,  $\frac{\partial A(z, t)}{\partial z} \approx (\hat{D} + \hat{N})A(z, t)$ .

In the simplest approximation, the change in electric field over a short distance can then be approximated by  $A(z + \Delta z, t) = e^{\hat{D}\Delta z} e^{\hat{N}\Delta z} A(z, t)$ . The operators are alternately applied as though the other is negligible to perform one step:

$$(A.2) \quad A_1(t) = e^{\hat{N}\Delta z} A(z, t)$$

$$(A.3) \quad A(z + \Delta z, t) = e^{\hat{D}\Delta z} A_1(t)$$

The dispersion operator accounts for the terms:

$$(A.4) \quad \hat{D} = - \sum_{k \geq 2} \frac{i^{k+1}}{k!} \beta_k \frac{\partial^k A}{\partial t^k}$$

and is most easily applied in the frequency-domain, where  $\tilde{A}(z, \omega)$  is the Fourier transform of  $A(z, t)$ . Analyzing the  $k = 2$  component of the sum,

$$(A.5) \quad \frac{\partial A(z, t)}{\partial z} = - \frac{i^3 \beta_2}{2!} \frac{\partial^2 A(z, t)}{\partial t^2}$$

$$(A.6) \quad \int \frac{\partial}{\partial z} \tilde{A}(z, \omega) e^{i\omega t} d\omega = \frac{i\beta_2}{2} \frac{\partial^2}{\partial t^2} \int \tilde{A}(z, \omega) e^{-i\omega t} d\omega$$

$$(A.7) \quad = \int \frac{i\beta_2}{2} (i\omega)^2 \tilde{A}(z, \omega) e^{-i\omega t} d\omega$$

Equating the integrands and solving the differential equation, the evolution due to dispersion is

$$(A.8) \quad \tilde{A}(z + \Delta z, \omega) = e^{\frac{-i\beta_2 \omega^2}{2} \Delta z} \tilde{A}(z, \omega),$$

which is the group-delay dispersion associated with the Taylor series expansion of the propagation constant  $\beta$ . The higher order  $k$  terms in the sum of  $\hat{D}$  represent the higher order

terms in the Taylor series expansion. The dispersion operator is then,

$$(A.9) \quad e^{\hat{D}\Delta z} A(z, t) = \mathcal{F}^{-1}\{e^{-i\beta'(\omega)\Delta z} \tilde{A}(z, \omega)\},$$

where  $\mathcal{F}^{-1}$  is the inverse Fourier transform and  $\beta'(\omega) = \sum_{k \geq 2} \frac{\beta_k}{k!}$  or equivalently is taken from the measured profile of the group-velocity dispersion as a function of frequency. Notice, in the absence of a nonlinear interaction,

The nonlinear operator,

$$(A.10) \quad \hat{N}A(z, t) = -i\gamma \left(1 + i\tau_{\text{shock}} \frac{\partial}{\partial t}\right) \left(A(z, t) \int_{-\infty}^{\infty} R(t') \times |A(z, t - t')|^2 dt'\right),$$

is applied in a two step process. First, the non-instantaneous component from the Raman response function,  $\int h_R(t - t')|A(z, t')|^2 dt$ , is transformed into the frequency-domain where the convolution becomes

$$(A.11) \quad \int h_R(t - t')|A(z, t')|^2 dt = \mathcal{F}^{-1}\left\{\mathcal{F}\{h_R(t)\}\mathcal{F}\{|A(z, t)|^2\}\right\}.$$

The real and imaginary parts,

$$(A.12) \quad \hat{N}A(z, t) = (-i\gamma + \gamma\tau_{\text{shock}}) \left( (1 - f_R)|A(z, t)|^2 + f_R \mathcal{F}^{-1}\left\{\mathcal{F}\{h_R(t)\}\mathcal{F}\{|A(z, t)|^2\}\right\} \right) A(z, t),$$

are approximately propagated over a  $\Delta z$  step using the second-order Runge-Kutta method.

The midpoint value is

$$(A.13) \quad A\left(z + \frac{\Delta z}{2}, t\right) = \frac{\Delta z}{2} \left( (-i\gamma + \gamma\tau_{\text{shock}}) \right. \\ \left. \left( (1 - f_R)|A(z, t)|^2 + f_R \mathcal{F}^{-1} \left\{ \mathcal{F}\{h_R(t)\} \mathcal{F}\{|A(z, t)|^2\} \right\} \right) A(z, t) \right).$$

The endpoint value is then,

$$(A.14) \quad A(z + \Delta z, t) = \Delta z \left( (-i\gamma + \gamma\tau_{\text{shock}}) \right. \\ \left. \left( (1 - f_R)|A(z, t)|^2 + f_R \mathcal{F}^{-1} \left\{ \mathcal{F}\{h_R(t)\} \mathcal{F}\{|A(z, t)|^2\} \right\} \right) A\left(z + \frac{\Delta z}{2}, t\right) \right).$$

The dispersion and nonlinear operators are applied separately to the electric field at  $A(z, t)$  to propagate the pulse along  $\Delta z$ . The step-size is set to be some small fraction of the nonlinear length, defined in Chapter 4.2: e.g.  $\Delta z = \frac{L_{\text{NL}}}{300}$ .

## A.2. FIBER PROPERTIES

There are two types of fibers modeled within this dissertation: silica and fluorozirconate (ZBLAN) based. The dispersion, nonlinear coefficient, ratio between instantaneous and non-instantaneous contributions to the third-order optical susceptibility, and Raman response function.

For silica fibers, we use dispersion vs wavelength maps provided by the fiber manufacturers. Generally these maps are plotted in  $D(\lambda)$  with units of ps/nm-km and must be converted to a group-velocity dispersion map using:  $\beta_2(\lambda) = -((D \cdot 10^{-6})\lambda^2)/(2\pi c)$ .

The nonlinear coefficient is taken either from either the fiber manufacturer or by  $\gamma = \omega_0 n_2(\omega_0)/cA_{\text{eff}}(\omega_0)$ , where  $\omega_0$  is the central frequency of the pulse,  $n_2$  is the intensity dependent index of refraction,  $c$  is the speed of light, and  $A_{\text{eff}}(\omega_0)$  is the effective mode area at the central frequency. For silica,  $n_2 = 3.2 \cdot 10^{-20} \text{ m}^2/\text{W}$  [79].

The ratio parameter  $f_R$  is 0.18 in silica, following Ref [28].  $h_R$  is an analytic representation of the measured Raman response function:

$$(A.15) \quad h_R(t) = \frac{T_1^2 + T_2^2}{T_1 T_2^2} e^{-t/T_2} \sin(t/T_1) H(t),$$

where  $T_1 = 12.2 \text{ fs}$ ,  $T_2 = 32 \text{ fs}$ , and  $H(t)$  is the Heaviside function to enforce causality [166].

For neodymium-doped ZBLAN fibers, the dispersion curve and nonlinear refractive index are taken from Ref [125], with  $n_2 = 2.8 \cdot 10^{-20}$ . The ratio  $f_R = 0.24$  and Raman response function are taken from Ref [139]. There the Raman response function is approximated using an intermediate-broadening model for the Raman gain spectrum:

$$(A.16) \quad h_R(t) = \sum_{i=1}^8 a_i e^{-\alpha_i t - \rho_i^2 t^2/4} \sin(\omega_{\nu,i} t),$$

where  $a_i$ 's are amplitudes,  $\alpha_i$ 's are Lorentzian widths,  $\rho_i$ 's are Gaussian widths, and  $\omega_{\nu,i}$ 's are oscillator frequencies (see Ref [139] for numerical values).